CRANFIELD UNIVERSITY

THE DEVELOPMENT OF A LASER DETONATOR SYSTEM

DEFENCE COLLEGE OF MANAGEMENT AND TECHNOLOGY

PhD THESIS

MIKE BOWDEN

CRANFIELD UNIVERSITY

DEFENCE COLLEGE OF MANAGEMENT AND TECHNOLOGY

DEPARTMENT OF MATERIALS AND APPLIED SCIENCES

PhD THESIS

Mike Bowden

The Development of a Laser Detonator System

Supervisor: Professor J Akhavan

Industrial Supervisor: Dr R. C. Drake

January 2014

ABSTRACT

Laser detonators offer several advantages over traditional electrical detonators, such as exploding bridgewire and slapper detonators, in terms of both safety and performance. Laser detonators remove the electrical conduction path to the energetic material, providing immunity from threats such as electrostatic discharge and lightning. A larger separation between the initiating energy source and the explosive devices is possible, up to several tens of metres, compared to a few metres for electrical slapper detonators.

A laser detonator system has been developed, with laser-driven flyer plates used to shock initiate the explosive. All aspects of the system, including coupling into an optical fibre, used to transmit the laser energy to the detonator, the optical fibre, the flyer plate launch and acceleration and subsquent shock into the explosive, and the explosive initiation have been investigated, with an understanding of the underlying principles and processes developed. Shock initiation of two secondary explosives, hexanitrostilbene and pentaerythritol tetranitrate, has been studied at extremely high shock pressures, comparable to the detonation pressure, and the critical energy fluence required for initiation establised.

The laser detonator system is robust and optimised, with design tools developed to enable efficient design of future systems.

ACKNOWLEDGEMENTS

I would like to thanks Sarah Knowles and Matthew Cheeseman (AWE) for experimental assistance for flyer and initiation experiments, Matthew Maisey (AWE) for advice on shock physics, Steven Clarke (LANL) and Ted Strand (LLNL) for technical discussions and advice on PDV, Adrian Akinci (LANL), Steven Harris (SNL), Eric Welle (AFRL), Alan Frank and Paul Wilkins (LLNL) for many invaluable technical discussions and debates on explosive initiation, Arnie Duncan and BWTX Pantex for HNS supply, Ray Everest and Roger Quant (AWE) and their staff for pellet pressing, Chris Hall and David Holder (AWE) for funding and John Richardson (AWE) for being the ultimate Devil's advocate and technical sounding board. I would also like to thank my amazing wife Dondra and son David, for their love and understanding during my studies.

TABLE OF CONTENTS

TABLE OF FIGURES

TABLE OF TABLES

GLOSSARY

- Detonator: a device used to convert non-explosive energy (such as optical or electrical) into explosive energy, typically used to initiate successive components in an explosive train.
- Equation of state: an equation describing the relationship between various parameters of a material, such as pressure, volume and temperature.
- Exploding Bridgewire (EBW) detonator: a detonator that uses a high current electrical signal to explode a small diameter metallic wire placed in intimate contact with a low density explosive fill, such as pentaerythritol tetranitrate. The explosion of the wire initiates the explosive fill.
- Fresnel reflection: the reflection of light from an interface between two materials with differing refractive indices, given by the Fresnel equations.
- Hexanitrostilbene: 1,3,5-Trinitro-2-[2-(2,4,6-trinitrophenyl)ethenyl]benzene, a secondary explosive typically used in slapper detonators.
- Hugoniot: the relationship between sound velocity, particle velocity and shock velocity for a material.
- Lenslet array: an optical element comprising many small (smaller than the optical aperture) lenses, which act to produce multiple images of the incident light.
- Numerical aperture: a measure of the acceptance angle of an optical fibre. Light which exceeds the acceptance angle cannot be coupled into the fibre.
- Optical fibre: a flexible, transparent fibre, capable of transmitting light along the length of the fibre.
- Pentaerythritol tetranitrate: [3-Nitrooxy-2,2-bis(nitrooxymethyl)propyl] nitrate, a secondary explosive typically used in EBW and slapper detonators.
- Q-switch: an optical element that acts as a variable attenuator. When placed into a laser cavity, it acts to inhibit laser until the attenuation is removed. This enable the creation of short duration, high power laser pulses.
- Slapper detonator: a detonator that uses a high current pulse to explode a metallic foil. The explosion of the foil accelerates a plastic flyer across an air

gap into a high density explosive pellet, where the shock imparts to the explosive causes initiation.

CHAPTER 1: INTRODUCTION

Laser initiation of energetic materials has been a topic of interest almost since the invention of the first laser in 1960. Since then, a wide range of lasers, and an even wider range of energetic materials, ranging from sensitive primary explosives such as lead azide, to very insensitive explosives such as Triamino Trinitrobenzene (TATB) have been investigated. With the continuous reduction in laser size, and increase in laser energies and powers, the use of lasers to initiate energetic materials is becoming more practical to implement in a space-limited system.

Laser initiation offers several advantages over traditional electrical initiation systems, in terms of both safety and performance. Laser initiation removes the electrical conduction path to the energetic material, providing immunity from threats such as electrostatic discharge and lightning. Laser initiation allows a larger separation between the initiating energy source, i.e. the fireset, and the explosive devices, up to several tens of metres, compared to a few metres for electrical slapper detonators. Beyond this length, non-linear effects act to degrade the quality of the laser pulse.

A laser detonator system is the practical realisation of laser initiation, typically comprising an optical energy source i.e. a laser, a method to transport the optical energy to the explosive device, such as an optical fibre, and the explosive device, or detonator.

Laser detonators can be considered the optical analogue of electrical detonators, with variants comparable to both Exploding Bridgewire (EBW) and Exploding Foil Initiators (EFI). This study focuses on laser slapper detonators, the optical equivalent of EFI detonators, for the following reasons: firstly, EBW detonators require a low-density explosive fill in intimate contact with the exploding wire (or foil in optical EBWs), which complicates manufacture and does not isolate the explosive fill from the initiating mechanism, secondly, the functioning of laser slapper detonators can be separated into two parts: the launch of the flyer plate and subsequent shock generated upon impact with an inert witness material, and the initiation of the high-density explosive fill by this shock. This allows a detailed study of the two processes, and provides shock initiation data that can be directly related to the development of EFI detonators.

This thesis details the development of a laser slapper detonator system, using commercially available laser systems. It studies the scientific principles behind each component of a laser detonator system, examining the prior art and building on this to develop a robust, optimised system with a scientific understanding of the processes involved. A laser slapper detonator has not been reported in the literature, and key aspects of the processes and interactions have not been investigated. The work reported within has been performed exclusively by the author, except where noted and general experimental assistance.

CHAPTER 2: LITERATURE REVIEW

It is necessary to identify prior art relevant to the development of a laser detonator system in order to both optimise the research required for development and to identify where this study has advanced the current understanding of this area. A thorough literature search is required to identify and critique any prior art, and to guide the subsequent research.

2.1. Optical Fibre Delivery of High Energy Laser Pulses

The majority of laser initiation systems cable of use outside of a laboratory use optical fibres to transport the laser radiation from the laser to the initiating device. For the initiation of energetic materials, typically requiring high peak laser powers, this presents a challenge, as optical fibres do not readily transmit high powers without damage. Optical fibres were developed in the 1900's, though serious development was limited until the advent of the laser. Most early work on laser initiation of energetic materials focused on free-space delivery of the beam. Using optical fibres to deliver the laser light did not begin in earnest until the 1970's.

An optical fibre is a transparent dielectric waveguide, which can transmit light from one end to the other. Optical fibres typically comprise of a transparent core surrounding by a transparent cladding with a lower refractive index. Light is reflected from the core/cladding interface by total internal reflection and is thus transmitted along the axis of the fibre, as shown in Figure 1.

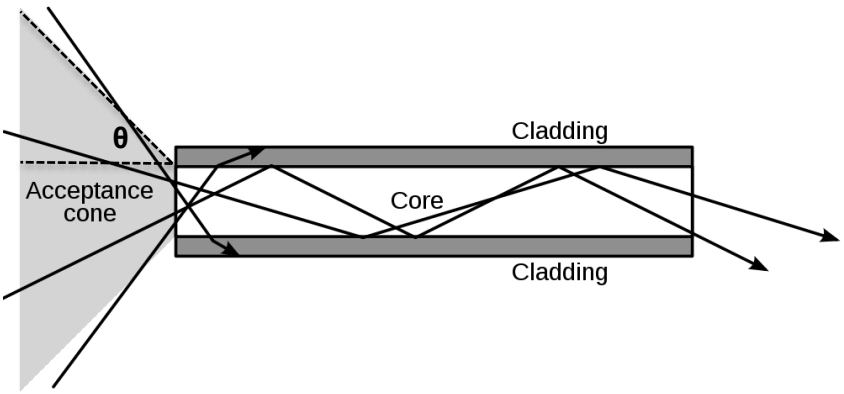

Figure 1 - Illustration of optical transmission through a multi-mode optical fibre [1]

Light which exceeds the critical angle for total internal reflection at the core/cladding interface escapes the core, and this defines the acceptance angle, or cone, for the optical fibre, the angle within which light is coupled into and transmitted by the fibre. The acceptance angle is generally characterised by the Numerical Aperture (NA), given by:

$$NA = n.sin\theta = \sqrt{n_{core}^2 - n_{cladding}^2}$$

Equation 1

where n is the refractive index of the medium the light is transmitted from (typically air, $n = 1$), θ is the half acceptance angle, n_{core} the refractive index of the core, and $n_{cladding}$ the refractive index of the cladding.

The three most common types of optical fibre are shown in Figure 2. A step index fibre typically has a large diameter core, capable of propagating multiple transverse modes, and is known as a multi-mode fibre. A graded index fibre has a gradual decrease in refractive index between the core and the cladding and typically has a smaller diameter core than a step index fibre. A single mode fibre has a very small diameter core, which can propagate a single mode for a given wavelength. Step index fibre are the type most commonly used for power transmission, due to the large diameter cores available.

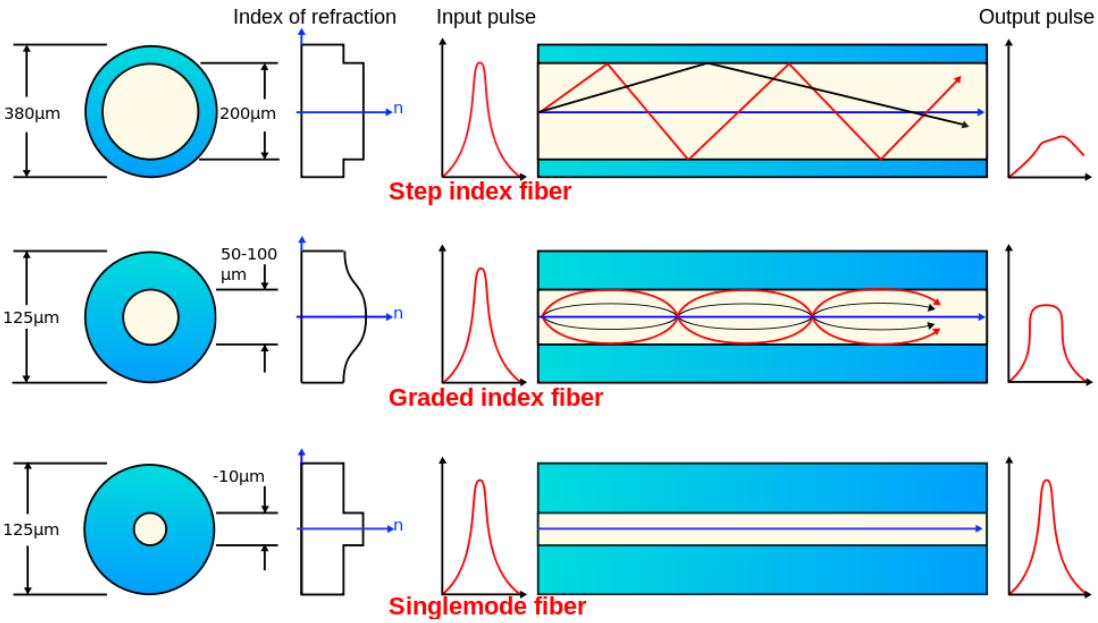

Figure 2 - Types of optical fibre [1]

Optical fibre power delivery is a widely studied field with a vast array of literature sources. In the interest of brevity, this literature study is limited to a selection of those sources most directly relevant to the application of laser initiation, i.e. high power transmission.

Allison et al [2] examined laser damage to step-index, multimode fibres using a pulsed dye ultraviolet laser producing pulses of 5 ns duration. The fibres had 400 – 1000 μm diameter pure fused silica cores, with either plastic or hard polymer claddings. The fibres were prepared by mechanically polishing the end faces until scratch-free when viewed under 20X magnification. The input beam of the fibre was focused with a lens, and the entry face of each fibre was placed beyond the beam waist (to avoid focussing within the fibre). In all of the tests, damage occurred initially at the core/cladding interface, within the first 10 mm. However, when a shorter focal length lens was used, higher damage thresholds were attainable. Energy densities, or fluences, at the point of damage varied from 1 to >6 $J.cm^{-2}$, depending upon the type of cladding and the focal length of the lens used. Damage mechanisms were ascribed to the formation of local regions of high intensity caused by initial beam reflections at the core/cladding interface. The effect was escalated if the beam collimation was improved at the injection point, or if the beam was misaligned with the fibre.

Allison et al [3] published a further paper in 1986 that investigated some crucial issues for quantifying the damage and power handling characteristics of optical fibres. Non-uniform light distributions, where the localised fluence significantly exceeds the average fluence, and laser-fibre misalignment were identified as key factors in causing damage, as well as the surface properties of the fibre ends; a “flawless surface” was described as being most desirable. A typical value of the surface damage threshold of Quartz fibres was stated as 10 $J.cm^{-2}$, though it was emphasized that the power handling capability of a fibre could not be determined solely by the bulk material damage threshold. The focal length of the focussing lens, and hence beam waist size, was found to affect the level at which damage occurred, and hence the pulsed power handling capability. A simple experimental setup was used to image the light profile at the output face of short lengths of fibre, in order to investigate the light distribution. This is one of

the earliest pieces of evidence of this being performed. Nonlinear phenomena were identified as important contributors to fibre damage.

Trott and Meeks [4] experimented with a Nd:Glass Q-switched infrared laser (16 – 45 ns pulse width) in conjunction with multimode, step index fibres of several different core diameters, ranging from 200 μm up to 1000 μm. The cores of the fibres were pure fused silica, whilst the claddings were either fluorine-doped silica or hard polymer. Energy densities greater than 90 $J.cm^{-2}$ (for a 25 ns pulse width) could be transmitted through fibres with even the smallest core (200 μm) before catastrophic damage occurred. In most cases damage was observed initially at the rear/exit face of the fibre. Trott and Meeks also tested tapered optical fibres, which could achieve a higher fluence at the output, whilst the input alignments were less stringent. Two different kinds of taper were tested in the paper, a long taper and a short taper. Good coupling efficiencies were achieved for both types, and damage thresholds were acceptable, though the short taper was found to be more sensitive to misalignment of the input beam. Beam homogenization and uniformity was found to be an important factor in reducing fibre damage. Multiple loops of the fibre served to increase the uniformity of the emergent laser beam, and a "top-hat" shaped beam profile was the goal. Additionally, fibres were bent through 90 degrees close to the output end so that the emergent beam was at 90 degrees to the propagation direction, sometimes with more than one loop and sometimes beyond the recommended minimum radius. No significant effect on either the coupling efficiencies or damage thresholds were noted.

Setchell et al [5] used 16 ns pulses from a Q-switched Nd:YAG infrared laser to test damage thresholds of a variety of batches commercially available radiation-hardened silica fibres. The fibres were multimode, step index, with 400 μm core diameters. A variety of mechanical polishing techniques were employed, in order to prepare the end faces. Plasma formation at the front face was observed in many cases, though this was found to actually aid the transmission of subsequent shots, due to a surface improvement phase termed "laser conditioning". It was observed that damage occurred initially at the exit face of the fibre, and that this damage was usually more severe. The reason for this was due to the guided light undergoing constructive interference at the exit face, resulting in higher electric field strengths capable of exceeding the damage

threshold of the fibre at that point. Unlike in previous experiments, there were no occurrences of damage at the core/cladding interface, however internal damage was observed at points where the fibres were looped through 360^{o}. This was attributed to high mechanical tensile stresses, which were exasperated at defects within the silica. 83 J.cm^{-2} was the highest energy density that could be transmitted, corresponding to 5.2 GW.cm^{-2}.

In 1992, Su et al [6] used a similar ND:YAG laser to test different input conditions, such as beam diameter and lateral alignment, of a step-index silica fibre with a 600 μm core. The effect of these conditions on the output profile was discussed and a successful theoretical model was developed, which closely followed the experimental results. It was found that when the input beam diameter was substantially less than the core diameter, meridional modes were preferentially excited. The output profile was roughly Gaussian, with a diameter less than the core. However, if the input beam was laterally misaligned, the quality of the output profile was reduced. Conversely, when a large input beam diameter was used, the concentration of skew modes was increased and an output beam size roughly the size of the core was the result. Its profile had a sharp-edged distribution and a local minimum on axis. Any lateral misalignment of the input beam had no effect on the output profile. In agreement with previous works, it was found that bending the fibres around a fairly tight radius served to enhance mode coupling within the core, which consequently improved the quality of the output beam profile.

In the same year, continuing from the work of Setchell et al, Klingsporn [7] investigated extensively the importance of rigorous cleaning and preparation of fibre end faces, using mechanical polishing techniques. It was found that the polishing process itself could create problems such as angling of the fibre face, and sub-surface damage. To verify this, the surfaces of a selection of fibre faces were etched with hydrofluoric acid after polishing to reveal the sub-surface layer. Subsequent examination under a microscope showed that in most cases damage, in the form of scratches, was present despite the fact that the surfaces had a very good initial finish.

Carlson and Johnson [8] tested short (200 mm) silica fibres with very large 1 mm diameter cores, using 10 ns pulses from a frequency-doubled Nd:YAG laser operating at 532 nm. They identified the critical parameters in coupling high power pulsed lasers into a fibre optic delivery system as follows: fibre composition and diameter, laser mode, surface preparation, fibre holding fixture, focal length of the input lens, position of the fibre relative to the focal spot, input laser power, fibre type and sheathing type. In one experiment, an energy of 16.3 mJ was successfully injected; the output power was 14.3 mJ, and after roughly 72,000 shots this dropped to 12.3 mJ. No damage to the faces of the fibre was visible upon inspection with an optical microscope, suggesting that gradual damage was occuring within the fibre, absorbing a fraction of the incident energy. The maximum output energy achieved with no observable damage was 26 mJ (3.3 $J.cm^{-2}$). This could be obtained even after 100 000 shots, though higher energies caused visible damage at the front face.

Sweatt and Farn [9] experimented with a system of diffractive optics for injecting high power, multimode laser pulses into an optical fibre with a 400 μm core. The purpose of the injection system was to create an even distribution of energy across the face of the fibre, in order to keep the peak fluence below the damage threshold. It was intended to smooth the laser beam prior injection to avoid breakdown in either air or the fibre, and avoid focusing at any point. Ideally, it was intended to cancel the ambient effects that can alter a laser cavity, and utilize all of the modes provided by the laser. Sweatt and Farn's system used a lens in conjunction with a binary optics element (a diffractive axicon), in order to create multiple concentric rings on the fibre face. Short focal lengths were used in order to minimize movement of the ring pattern foci. The ratio between the peak intensity on the fibre face to the average over the fibre face was found to be 3.7:1, when a well-aligned laser was used. As a result, approximately 60% of the fibres tested were able to deliver pulses of 40 mJ (31.8 $J.cm^{-2}$), before permanent damage occurred, and no damage occurred to the axicon itself.

In 1994, Reng et al [10] compared a selection of different fibres for use with Nd:YAG lasers. Step index and graded index fibres with 400 μm and 600 μm core diameters were tested, along with different core to cladding ratios and different coatings. The graded index fibre (600 μm core) was able to transmit the highest power, due to its

larger numerical aperture. Spherical aberrations were observed due to the beam injection system and these were found to cause losses in transmission, because light was coupled into both the core and the cladding. A CCD camera was used to record the intensity distribution of the beam before and after transmission through a step index fibre. The beam profile was said to correspond to a "top-hat" shape, which was desirable. Two different end face preparation techniques, cleaving and mechanical polishing, were employed and pictures were taken of the interference fringes resulting from these. Images of the faces were taken with a scanning electron microscope in order to examine the quality of the surface finish. Cleaving was favoured as a means of end face preparation due to the smoothness achieved.

The following year, Setchell [11] published a detailed overview of high intensity transmission systems. The importance of the output beam profile of the laser was discussed, and how the effects of non-uniformity such as "hotspots" could lower the threshold of fibre breakdown. Careful design and alignment of the laser cavity, in conjunction with injection optics and beam profiling techniques were described as ways to mitigate these breakdowns. A laser with a broad spectral line width was more desirable due to lower temporal coherence and hence a higher quality beam profile i.e. a finer speckle pattern with a reduced intensity variation. The importance of beam injection into the fibre core was summarized from previous works and it was found that certain damage processes could be inhibited if the beam was diverging when entering the fibre, as this limits focussing within the fibre. Diffractive optics were thought to be the key to creating the best beam characteristics in an optical injection system. Fibre routing was found to affect the onset of internal damage mechanisms. If injection lenses of relatively long focal length were used, consistent internal damage was observed near the start of bends and at the outside edge of loops in the fibre. It was found that "whispering gallery" ray propagation, a result of filling only a few of the fibre modes, was the cause of this. However, broadening the mode power distribution could alleviate the problem. Finally, fibre end face preparation was examined, where different finishing techniques including mechanical polishing, cleaving and laser polishing were tested for entrance face breakdown. The fibres that had been polished with a CO_2 laser withstood the highest incident fluence of over 250 $J.cm^{-2}$ for an 11.5 ns pulse. It should be noted that this fluence is the peak fluence incident upon the fibre face, not the fluence

averaged across the fibre face. It is more usual to report fluence as an average fluence, which in this case would be 57 J.cm^{-2}.

In a continuation of his previous work, in 1996 Setchell [12] used a Q-switched Nd:YAG laser, operating at 1064 nm, with 14 ns pulse-widths to test commercially available fibres. The fibres were high OH^- fused silica cores, with F-doped claddings and 365 μm diameter cores. The end faces of a selection of the fibres were prepared by 10.6 μm CO_2 laser polishing. The CO_2 laser radiationis absorbed by the fibre face, causing partial melting, removing surface imperfections. It was found that the fibres that had not been conditioned with the CO_2 laser could transmit a maximum of 71.1 J.cm^{-2}, and results were dominated by entrance face breakdown. The fibres that had been conditioned were superior in performance; they could transmit 85.0 J.cm^{-2}, allowing higher energies to pass beyond the entrance face, resulting in other damage mechanisms within the fibre bulk. To date, a fibre-to-fibre injection technique (using lenses to image the first fibre onto the second) was the most successful method for mitigating entry damage. However, continual developments in the field of diffractive optics were thought to provide a superior injection system, which would dispense with the need for the mechanical mode scrambler used in these experiments.

Setchell reported further damage threshold comparisons on a batch of commercial fibres (the same as previously studied) whose end faces had been cleaved [13]. Some of the batch had been subsequently flame polished, and some had been CO_2 laser polished. Despite the very high quality of the cleaved finish, it was discovered that they were rarely inert. In most cases they were electrostatically charged, which attracted dirt, and were quite often chemically active. Cleaved fibres frequently suffered from exit face damage as a result of unseen sub-surface defects, inherent in the cleaving process. The laser and flame polished cleaved ends did not prevent this from happening, suggesting that faults extended beyond the surface. The cleaved fibres were able to transmit 73.8 J.cm^{-2}, which could be improved to 81.7 J.cm^{-2} by laser polishing the cleaved fibres before use. Flame polishing the cleaved fibres reduced the damage threshold to 73.6 J.cm^{-2}.

Frank et al [14] described the coupling of a 10 J laser into 16 independent fibres by using a 4 by 4 binary diffraction grating. This system was a further development of Honig's 1 J Nd:YLF laser that was successfully used to initiate PETN[15] in a previous set of experiments. The fibres for the 10 J laser were 400 μm high OH^- fused silica, whose end faces were prepared by the mechanical polishing technique developed by Setchell in previous publications. The bulk damage threshold of the fibres was stated as 38 $J.cm^{-2}$; energy densities exceeding this were reported to result in catastrophic failure. The mechanism of this was attributed to the mode of the imaged spot of the beam not propagating far enough to uniformly fill the mode volume of the fibre, causing a failure at the core-cladding interface. However, the damage threshold of the entire system was always limited by the diffraction grating, whose threshold was about 12 $J.cm^{-2}$ due to coherence effects at the grating step edges. At the time of publication, the system was successful and had become the prototype for a 200-point system that was yet to be fully integrated and tested.

Greenaway et al [16] tested several batches of 400 μm fused-silica fibres to assess their damage thresholds. Eight different methods of mechanical polishing were employed using different abrasives and polishing compounds, and Atomic Force Microscopy (AFM) was used to measure the resultant surface roughness. The formation of a visible plasma flash at the front face of almost all fibres was observed. In agreement with previous work by Setchell, microscopic examination showed that the surface finish was improved as a result ("front face conditioning"). However, critically damaged fibres persistently formed plasma, and microscopic inspection showed that pits had formed on the face; these would worsen with successive shots. The rear face was by far the most common site for catastrophic failure, and the threshold for damage was lower than that for the front face. Again, in agreement with previous studies, the cause of this was constructive interference at the rear face between the incident field and the Fresnel reflection, but the interference at the front face was destructive due to a phase reversal. Equations for these interference conditions were derived. The paper concludes with the fact that end face preparation is extremely important in high power transmissions. Further advances in the polishing technique enabled energy densities in excess of 55 $J.cm^{-2}$ in an 8 ns pulse without damage. Mechanical polishing was found to be an

important means of removing sub-surface cracks and damage introduced from cleaving. Without polishing, the damage thresholds were found to be much lower.

Clarkin et al [17] of Polymicro Technologies published a paper on specially shaped fibre tips in 2004. The tips, which could replicate a variety of optical components, included lenses, diffusers, tapers, collimators and "side fires" (where the beam exits the fibre perpendicular to the fibre core), and were made from the glass of the fibre itself, meaning no joins or additional components were required. Tapers were the main focus of the investigation, owing to their special properties and potential useful applications. However, they can suffer from transmission losses. Thirty different tapers were tested, and it was found that a lower input numerical aperture (NA), relative to the allowed output NA, gave better transmission. Different lengths of taper were tested, but were found to have minimal effect on the transmission. Computer software was used to model a variety of tapers using ray trace analysis, and it was found that this was in close agreement with the experimental findings. Interestingly, the modelling also showed that very long tapers had little effect in reducing losses, but helped in smoothing the output profile when a highly non-uniform beam was injected.

D M Brown et al [18] developed an optical injection system for use with seven fibres, using a multimode YAG laser operating at 1064 nm. It was shown that a highly non-uniform input beam from the laser could be successfully transformed into multiple, equally spaced, uniform output beams for injection into fibres. This was achieved with an integrator beam-shaping system, in which a refractive microlens array in a hexagonal pattern was used in conjunction with a focusing lens and diffractive beam splitter. The system showed good beam homogenization and beam splitting uniformity, even when the input laser beam profile was unknown or changed with time. Some optical aberration was desirable in order to reduce interference effects, though too much was found to reduce coupling efficiency. The lens system was compact, with a total length of 16 mm.

2.2. Summary of Optical Fibre Delivery of High Energy Laser Pulses

A summary of the published literature is shown in Table 1, in order of increasing damage threshold, given as intensity, to allow comparison of different pulse lengths.

2.2.1. Injection method

Two methods were used to couple the laser into the optical fibres: a simple plano-convex lens, and diffractive optics.

Diffractive optics offer two advantages. Firstly, the energy intensity variation across the fibre face can be minimised, limiting any "hot-spots" that may cause plasma formation. Secondly, the numerical aperture of the injection optics can be maximised without focussing down to a minimum beam waist, either in the air before the fibre face or inside the fibre. Maximising the numerical aperture of the injection optics results in a rapid filling of the possible propagation modes within the fibre, lowering the energy density. However, diffractive optics do not offer an improved damaged threshold over a simple plano-convex lens, although no direct comparison has been made. Therefore, both methods were investigated to determine the optimal method.

2.2.2. Fibre Face Preparation Method

Setchell's work [11-13] provides a comparison of different fibre face preparation methods (cleaving, mechanical polish, flame polish and laser polish) for a similar injection method. There is little difference between the four methods (71-85 $J.cm^{-2}$), though it should be noted that other considerations dictate the choice of preparation method. Cleaving tends to be quite variable, and is not suitable for use with connectorised fibres, as the fibre must be flush with the ferrule. Flame polishing is rarely used, and appears to reduce damage thresholds when used on cleaved fibres. Laser polishing with a CO_2 laser results in the highest, most consistent damage threshold, but is only available from a few vendors, at increased cost. Mechanical polishing is comparable to laser polishing, albeit with a slightly reduced damage threshold. Mechanical polishing is the most common fibre face preparation method, and is widely available. The optimal method for mechanical polishing a fibre to maximise the damage threshold has not been widely studied, and may offer a means to improve

the performance of a mechanical polish. Therefore, mechanical polishing was chosen as the baseline fibre face preparation method.

2.2.3. Fibre Core Diameter

The fibres in this literature review range from 200 to 1000 μm core diameter. There is no correlation between core diameter and damage threshold, but as the core diameter, and hence the diameter of the flyer launched, approach the critical diameter of the explosive, it is likely that initiation threshold energies will rise. Therefore, the fibre diameter should exceed the critical diameter of the explosive, around 200-300 μm for typical detonator explosives. However, the larger the fibre diameter, the greater the laser energy required to achieve a given flyer velocity. The most common fibre diameter published was 365-400 μm, and therefore this was chosen as the baseline fibre core diameter.

2.2.4. Laser Pulse Length

The most commonly reported pulse length is 11.5-14 ns. This is slightly longer than the typical pulse length of a standard Nd:YAG Q-switch laser, around 8-10 ns, though easily achievable by reducing the flashlamp energy. Although increasing the pulse length will reduce the intensity and hence increase the damage threshold, it is also linked to the acceleration of the flyer plate, unlike most other fibre parameters. The baseline pulse length was therefore chosen to be 11.5-14 ns.

The research published to date has either used bare fibres (i.e. not mounted in ferrules) or has not reported this detail. Any practical application of a laser detonator system must use connectorised fibres, to enable assembly and ease handling. The connector and ferrules may impact the performance, as fibre ferrules typically have the fibre ferrule in close proximity to the fibre itself.

Fibre Core, μm	Fluence, $J.cm^{-2}$	Pulse Length, ns	Intensity, $GW.cm^{-2}$	Wavelength, nm	Fibre Finish	Injection Method	Reference
400	31.8			1064		Diffractive optic	[9]
400	38			1057	Mechanical polish	Diffractive optic	[14]
1000	3.3	10	0.33	532			[8]
400-1000	10	5	2.00	1064	Mechanical polish	Plano-convex lens	[3]
200	90	25	3.60	1060	Mechanical polish	Plano-convex lens	[4]
400	57	11.5	4.96	1064	Mechanical polish	Diffractive optic	[11]
365	71.1	14	5.08	1064	Mechanical polish	Plano-convex lens	[12]
400	83	16	5.19	1064	Mechanical polish	Plano-convex lens	[5]
365	73.6	12.2	6.03	1064	Flame polish	Diffractive optic	[13]
365	73.8	12.2	6.05	1064	Cleaved	Diffractive optic	[13]
365	85	14	6.07	1064	Laser polish	Plano-convex lens	[12]
365	81.7	12.2	6.70	1064	Laser polish	Diffractive optic	[13]
400	55	8	6.88	1060	Mechanical polish	Plano-convex lens	[16]

Table 1 - Summary of published research into high-energy fibre injection

2.3. Laser-Driven Flyers

There are three published methods of initiating energetic materials with laser radiation. The first, and simplest, is direct irradiation of the energetic material. Secondly, the laser irradiates a thin foil, typically metal, placed in intimate contact with the energetic material. The third method, a laser-driven flyer plate, is the most amenable for use in a detonator system based upon secondary explosives, such as hexanitrostilbene (HNS), as it can generate shocks in the explosive in excess of 20 GPa. This method uses a short pulse length (typically 10-40 ns), moderate energy (<1 J) near-IR laser (Nd:YAG or similar). A short pulse length ensures that the energy is deposited before significant thermal diffusion can occur, and therefore a plasma can be formed. Near-IR lasers are used primarily due to availability and efficiency. Visible lasers can be used, but normally require frequency-doubling a near-IR laser, reducing efficiency.

The laser is incident upon a thin coating on a transparent substrate, generally a window or the output end of an optical fibre. The laser fluence is sufficient to ionize the coating at the interface between the substrate and the coating, and plasma comprised of the substrate material and the coating is formed. This plasma is confined between the substrate (which can be considered massive and immobile) and the remainder of the coating. The plasma subsequently expands, accelerating the remainder of the coating away from the substrate as a flyer plate. Velocities of several $km.s^{-1}$ are easily reached, over a very short distance, less than 100 μm.

2.3.1. Experimental Studies of Laser-driven Flyer Plates

2.3.1.1. Flyer plates Launched Using Free-space Lasers

Sheffield and Fisk [19] reported the first experiments on the launch of flyer plates using a Nd:YAG laser with a wavelength of 1064 nm, with an energy of 700 mJ and a pulse length of 10 ns. A 310 mm focal length lens was used to produce a 1.5 mm diameter spot on an aluminium foil, 2 to 200 μm in thickness. The motion of the side of the foil away from the laser was probed using a velocity interferometer.

The aluminium foil was held in tension by a plastic fixture to ensure it was flat and smooth. In some experiments the foil was confined by water on both sides; in this case,

fused silica windows were used. This is in contrast to later experiments where the aluminium foil was coated onto a transparent window. Energy was lost in reflections at the uncoated lens and silica window, along with absorption in the water. It was estimated that 500 mJ reached the foil for the water-confined foils and 600 mJ for the freestanding foils, corresponding to fluences of 30 and 40 $J.cm^{-2}$.

The resulted velocities measured are shown in Table 2. It can be seen that velocity decreases with foil thickness, with the water confinement offering a threefold increase in velocity, due to the plasma being constrained during the energy deposition process, enabling a higher temperature and hence pressure to be reached.

Foil Thickness, μm	12	25
Water confined	0.6 $km.s^{-1}$	0.1 $km.s^{-1}$
No confinement	0.2 $km.s^{-1}$	

Table 2 – Flyer velocities reported by Sheffield and Fisk [20]

These velocities (both confined and unconfined) were reached in around 60 ns, many times longer than the driving laser pulse. This indicates that the pressure in the plasma was maintained after the energy was deposited. It was estimated that a plasma pressure of around 200 MPa was required for the observed acceleration.

For the thicker foils, in excess of 12 μm, steps in the velocity profile were observed. Assuming the time between steps to be a double transit time through the foil, a velocity of 6.4 $km.s^{-1}$ was obtained for this wave. This is equal to the speed of longitudinal elastic waves in aluminium. As the estimated plasma pressure is below the elastic limit of aluminium, it was concluded that an elastic wave was induced, the reverberation of which produces the foil acceleration. It was postulated that this was not observed in the thinner foils due to averaging of the velocity record by the interferometer delay.

A shorter acceleration period of 15 ns was observed for the confined foils, again due to the increased pressure, with no evidence of any shock reverberation. However, some correlation between the temporal profile of the drive pulse and the velocity record was

noted. Finally, a foil confined on the drive side only achieved the highest velocity, 1.5 $km.s^{-1}$.

Paisley [21] made significant improvements to the technique developed by Sheffield and Fisk, increasing the flyer plate velocity to greater than 5 $km.s^{-1}$, and using the flyer plates to initiate HNS. An Nd:YAG laser with an energy of 30-300 mJ at a wavelength of 1064 nm with a pulse length of 10 ns was used, with flyer plates of 2-10 μm of aluminium and copper, 0.4 to 1.0 mm in diameter being used.

The water confinement used by Sheffield and Fisk was replaced with a transparent solid substrate such as fused quartz, with the flyer material being coated onto this substrate. A 250 mm focal length lens was used to focus the laser beam to spots of 400, 600 and 1000 μm in diameter. Efficiencies of greater than 50% (i.e. coupling of laser energy to flyer kinetic energy) were obtained by depositing a dielectric layer, typically 0.25 μm thick, between two metal layers. The first layer (on the substrate) is converted to the driving plasma, with the inhibited thermal diffusion intended to preserve the second layer, which forms the flyer plate.

A similar velocity interferometer to that used by Sheffield and Fisk was used to measure the flyer plate velocity. Velocities in excess of 5 $km.s^{-1}$ were reported with 90% of the peak velocity obtained within 20 ns, corresponding to accelerations greater than 10^9 g.

To investigate the integrity and planarity of the flyer plates, they were impacted into PMMA windows separated from the substrate by 25 to 250 μm. The adiabatic compression of the air between the window and the flyer plate produces an intense flash of light, recorded by a streak camera. Impact time variations of less than 4 ns were obtained over 70% of the flyer diameter.

Paisley initiated HNS with a surface area of 14 $m^2.g^{-1}$ at densities of 1.55 and 1.6 $g.cm^{-3}$ with these flyer plates, with minimum velocities of 1.8 $km.s^{-1}$, equating to a shock pressure of 8 GPa and a shock duration of less than 1 ns. This is the first reported initiation of an energetic material using laser-driven flyer plates. This research arguably paved the way for the further development of laser-driven flyers over the next twenty years.

Paisley [22] built upon his previous work by reporting the use of several optical diagnostics for investigating the dynamic behaviour of laser-driven flyer plates: velocity interferometry, streak photography and stereo photography. The details of the velocity interferometry and streak photography are essentially identical to his earlier papers and hence they will not be discussed here. It was reported that LASNEX (a 1-dimensional hydrocode model) calculations supported the experimental results showing around 50 nm of the metal forms the plasma in this case, equating to only a few per cent, with 30-60% of the laser energy converted to flyer kinetic energy.

Pulsed-laser stereo photography uses a short-duration (typically 1-10 ns) laser pulse to illuminate a dynamic experiment. By using band pass filters to selectively pass the illumination wavelength, high temporal resolution equal to that of the laser pulse length is obtained. Since the flyer plates were laser-driven, Paisley used a portion of the drive beam, frequency doubled to 532 nm, to illuminate the shape of the flyer plates in flight. A time delay of 80 ns was introduced by means of turning mirrors, and then the illumination laser pulse was focused into a quadfurcated[1], pseudo-random fibre optic bundle. The four outputs were then used to illuminate the flyer plate during flight. Two cameras, equally spaced from the flyer plate axis of flight were used to produce a stereo view. Unfortunately, experimental results from this technique are somewhat sparse, with discussion being limited to the observation that the results agree with the streak photography, showing the flyer plates to be intact and symmetrical.

Paisley was granted a patent [23] in 1991, with free-space coupling of the laser energy to the flyer plate, with the flyer coated upon a transparent substrate. The advantages of the multilayer flyer were detailed (with an alumina insulating layer), reporting a 16% increase in the attained velocity for a given energy, or a 34% increase in kinetic energy. Velocities reported for a laser energy of 30 mJ are around 2.3 $km.s^{-1}$ for free-standing (i.e. no confinement) foils and 3.3 $km.s^{-1}$ for single and multilayer flyers on substrates.

[1] Four fibres assembled into a single input connector.

Paisley [24] again used velocity interferometry to study the velocity profiles of laser-driven flyer plates. In this case, the flyers were impacted into a PMMA window, and the impact was also recorded on a streak camera, along with the velocity interferometry traces, a portion of the launch pulse, and a 100 MHz laser diode (for temporal calibration of the streak record). The flight and subsequent impact into the window were recorded. This is an elegant technique that records all the experiment data on a single camera. Paisley reported that the flyer plates could be planar over the central 80% to within 200 ps, a flatness of around 1 μm, an impressive figure given the free-space beam launch of the flyers. This implies good control over the spatial intensity profile of the beam.

Paisley reported further experimental characterisation of laser-driven flyers [25]. This paper is similar to Paisley's other papers. The flyer plates used were somewhat thicker, 3-50 μm; with the majority of the flyers being a rolled metal foil adhered to a thinner deposited layer on a quartz substrate.

ORVIS was again used for velocity measurement, with a modification to enable longer record lengths. The optical fibres carrying the signal are split three ways into varying length fibres, to delay each set of fibres relative to the others. This allows longer record lengths to be recorded on a single streak camera.

The flyer plates were used for material characterization, by impacting a material with unknown shock properties into a window such as lithium fluoride with known shock properties. This allowed the shock properties of the material under test to be determined.

Watson [26] probed the depth to which the plasma ablates the flyer material using embedded tracer layers. An estimation of the ablation depth could be made by embedding thin layers with a distinct spectroscopic signature within the flyer material, and then varying the depth of these tracer layers. If emission lines corresponding to the tracer layer were observed, then ablation had occurred at that depth.

An Nd:YAG laser with a wavelength of 1064 nm, a pulse length of 10 ns and an energy of up to 1 J was focussed onto a substrate coated with the flyer material using a lens,

resulting in a spot size of 1 mm. The flyer was of 4 μm total thickness, either aluminium or an unspecified (though it appears to refer to an alumina / aluminium composite) multi-layer coating. The substrate could be translated relative to the beam to allow multiple flyers to be launched from a single substrate.

A temporally gated spectrometer was used to record the emission lines from the plasma driving the flyer, with a minimum gate window of 100 ns. A delay generator was used to provide a variable delay between the laser and the spectrometer gate.

Yttrium was chosen as a tracer layer as its spectral emissions are notably different to those of aluminium and silica, the other materials likely to contribute to the plasma. The yttrium layer was embedded at a depth of between 300 and 1300 nm.

Firstly, the plasma produced by a flyer with an yttrium layer at a depth of 100 nm was studied. Four emission lines were attributed to the plasma at 360, 414, 437 and 600 nm. The delay between the laser and spectrometer was varied from 0 to 770 ns, with the emission lines remaining at all delays, indicating that the emission lines remain as the plasma expands and cools.

A gradual reduction in the intensity of the observed yttrium lines was observed as the depth of the layer was increased to 400 nm. A reduction in the overall level of plasma emission was also noted with increasing tracer layer depth. As yttrium has a lower thermal conductivity than aluminium, it was postulated that the presence of the yttrium layer delayed thermal diffusion into the flyer material. This effect appeared to be constant past a depth of 400 nm.

By examination of the reduction in the intensity of the 600 nm tracer line with increasing yttrium layer depth, Watson was able to estimate the ablation depth variation with energy, shown in Table 3.

Laser Pulse Energy, mJ	Ablation Depth, nm
51 ± 1	350 ± 70
101 ± 1	450 ± 70
155 ± 1	1000 ± 100

Table 3 - Ablation depths for three laser pulse energies [26]

The main limitation of Watson's experiments was the free-space coupling of the laser energy to the flyer material, resulting in a non-uniform spatial energy profile, likely to cause uneven ablation of the flyer.

He et al [27] studied the motion of aluminium, gold and platinum flyers, launched by an Nd:YAG laser with a pulse length of 10 ns. The laser had a maximum energy of 100 J, resulting in an irradiance of up to 400 $GW.cm^{-2}$ over the 1-2 mm diameter flyer plates. This is substantially higher than any other research discussed here. The application appears to be inertial confinement fusion, i.e. impacting several flyer plates onto a fuel pellet to generate extreme pressures.The flyers used ranged from 5 to 50 μm in thickness, and appear to be single-layer. No significant analysis of the results is given. The maximum velocity reported is around 9 $km.s^{-1}$ for a 10 μm aluminium flyer launched at 280 $GW.cm^{-2}$.

Rupp [28] detailed a camera system to calibrate the planarity of flyer plates, using a pair of cameras and pulsed laser illumination. The flyer was comprised of three layers: a carbon ablation layer to form the plasma, an insulating alumina layer to protect the flyer, and an aluminium impact layer. The flyer was required to be flat upon impact, to permit one-dimensional models to be used. The flyer planarity can be affected by both the spatial profile of the launch beam, and plasma leakage around the edges, reducing the pressure, causing curvature towards the edges. It is therefore necessary to be able to measure the planarity of the flyer in flight.

An Nd:YAG laser, frequency doubled to 532 nm, with an 8 ns pulse width, was passed through a carbon disulphide cell, inducing spectral broadening (due to phase modulation induced by the non-linear refractive index of carbon disulphide [29]), which reduced laser speckle. The beam then passed through a 345 μm square grid, imaging it onto the flyer plate. Two Pulnix TM-1300 cameras with Navitar Zoom 6000 lenses were

positioned at a 20 degree angle from the axis of flyer motion, one either side, or one to the side and one above. Two filters protected the cameras, firstly a filter to prevent any light from the launch laser reaching the camera, and secondly, a 532 nm band-pass filter to eliminate the plasma light. The camera system is shown in Figure 3.

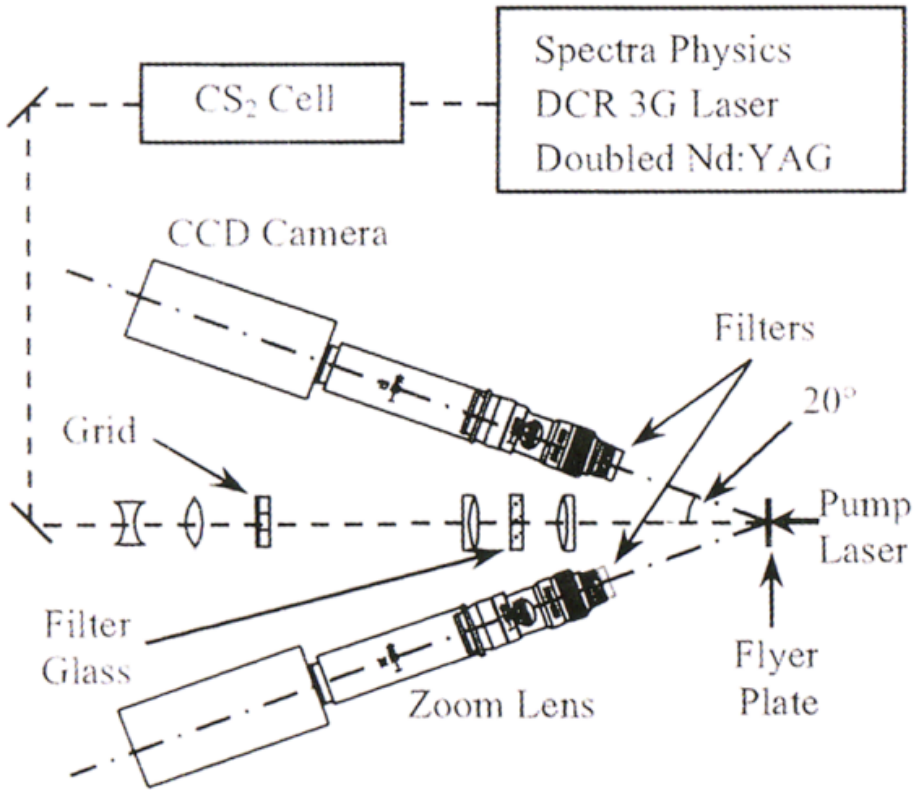

Figure 3 - Stereo camera system as reported by Rupp [28], used to determine flyer shape in flight

The system was tested on 50 μm thick copper and 100 μm thick titanium flyers. Though not apparent, it is believed these formed a fourth layer on top of those described earlier. These were accelerated to between 200 and 550 $m.s^{-1}$, with 1.0 to 3.5 J of laser energy. For the titanium flyers, around 20 μm of bowing across the 3 mm diameter flyer was observed.

On some shots with thin (0.5 μm thick) aluminium coatings, significant plasma "blow-by" was observed. This was reduced by increasing the flyer thickness to 3 μm.

2.3.1.2. Flyer Plates Launched Using Fibre Optically Coupled Lasers

Paisley was granted a second patent [30] in 1991 for fibre optic mounted laser driven flyer plates. The two patents were filed on the same date, 2nd April 1990. This patent offers little further information beyond Paisley's papers, except that the flyer material is coated onto the end of an optical fibre. The reported advantages are primarily simplicity and versatility, with the coupling lens being located remote from the flyer, and the fibre allowing increased flexibility as to the positioning of the flyer plate. Although the patent claims there is no need for a coupling lens, the laser energy must still be focussed into the optical fibre. This patent reports the first use of optical fibres to transmit the laser energy from the laser to the flyer plate, greatly increasing the practical applications of laser-driven flyer plates.

Trott [31] investigated flyer plates launched from optical fibres, focussing on the effect of laser fluence, pulse duration and flyer thickness. An Nd:Glass laser was used with a wavelength of 1054 nm, with a pulse duration varied from 16-50 ns by adjustment of the flashlamp voltage. An electro-optic modulator was used to obtain shorter pulses down to 3 ns. As before, velocity interferometry was used to record flyer velocity.

A small portion of the drive pulse was coupled into a second fibre and imaged onto the streak camera alongside the velocity interferometry record. By characterisation of the light propagation times throughout the system it was possible to determine the delay between the onset of the drive pulse and flyer motion. The light reflected and backscattered from the fibre/flyer interface was collected by the fibre, and then recorded by a fast photodiode, enabling the difference between the launch beam and reflected beam to be investigated.

Trott found that above fluences of 10-15 J.cm^{-2} (12-19 mJ for a 400 μm fibre), the flyer velocity scales as the square root of fluence, suggesting a simple kinetic energy relationship assuming a small ablated thickness and constant efficiency of coupling laser energy to flyer kinetic energy, with the relationship:

$$V_f \propto \sqrt{\frac{kE_l}{m_f}}$$

Equation 2

where V_f is the flyer velocity, E_l is the laser energy, m_f the flyer mass and k is a constant. For a given flyer diameter, this becomes:

$$V_f \propto \sqrt{\frac{kF_l}{\rho x_f}}$$

Equation 3

where F_l is the laser fluence, ρ the flyer material density and x_f the flyer thickness. Trott observed that the coupling efficiency fell rapidly at lower fluences, with flyer motion not occurring below 3 J.cm^{-2}. This relationship was found to be valid over a range of flyer thicknesses and fibre diameters.

For fluences significantly in excess of the threshold for flyer motion, there was a mild dependence of peak velocity on pulse duration, with shorter pulses inducing a much more rapid acceleration to a peak velocity somewhat higher than that for longer pulses. The efficiency dropped from around 40% for the shorter pulses to 21% for the 48 ns pulses. Below around 8 ns, there appeared to be little dependence on pulse length, both in terms of acceleration and peak velocity. This would suggest a limit to the rate at which energy can be coupled into the flyer kinetic energy. It is useful to note that pulse durations of 8-12 ns are typically obtained from COTS (commercial off-the-shelf) Nd:YAG lasers. For low fluences, less than 10 J.cm^{-2}, shorter durations have substantially lower threshold fluences for flyer motion. It is encouraging that simple relationships appear to govern flyer behaviour, making models of the processes easier to develop.

The pulses reflected from the flyer displayed a pronounced reduction in intensity, corresponding to the formation of the plasma. As the fluence is lowered, this drop was seen progressively later in the pulse. Near the threshold, the majority of the energy appeared to be required for plasma formation, suggesting only the energy delivered after this intensity reduction contributes to sustaining the plasma and subsequent flyer motion.

Paisley [32] used an 1064 nm Nd:YAG laser with a 8 ns pulse length to launch flyers coated onto the end of 0.2-2 mm diameter optical fibres. The flyer plates were 0.5 to 20 μm thick aluminium, although other materials were suggested. Power densities of 0.3 – 3 $GW.cm^{-2}$ were described as sufficient for plasma formation, with around 30% of the laser energy being converted to flyer plate kinetic energy.

As in previous papers, velocity interferometry was used to record flyer plate velocities, with velocities in excess of 5 $km.s^{-1}$ measured. The LASNEX hydrocode was used to predict flyer plate velocity profiles, with good agreement between the predictions and the experimental data.

The use of laser-driven flyer plates for spall strength determination was proposed, and the results of experiments to confirm this were reported. 6 μm thick copper flyers were impacted into a 25 μm thick copper target, with velocity interferometry being used to measure the free-surface velocity of the rear of the copper target. The results of spall strength for aluminium and copper for strain rates in excess of 10^7 s^{-1} were presented, an extension of previously published data up to 10^6 s^{-1}. This report does not build extensively upon Paisley's earlier work, but does offer an additional application, i.e. materials property determination.

Frank investigated pure aluminium flyers [33], investigating the boundary between thin (where the coating is completely ablated) to thick (where a flyer is launched) coatings. The aluminium was coated onto the end of optical fibres.

A Nd:Cr:GSGG laser with a wavelength of approximately 1060 nm with a 12 ns pulse length was used, focussed into a 2 m length optical fibre tapering from 1000 to 400 μm diameter. A 400 μm diameter fibre was then coupled to the output. This fibre was either coated with the flyer material, or uncoated, with a calorimeter used to measure the transmitted energy and a beam profiler used to examine the spatial intensity profile. The laser and fibre system is shown in Figure 4 (where PMT is a photomultiplier tube).

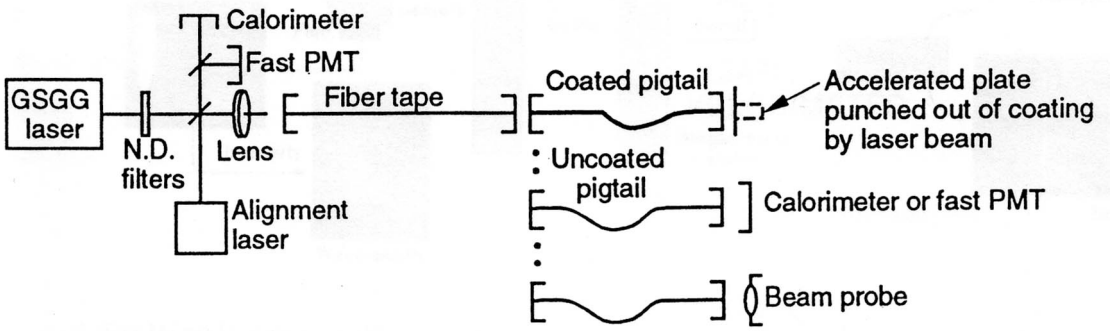

Figure 4 - Laser and fibre injection system as used by Frank [33]

The flyers were examined using the Micro Detonics Facility at the Lawrence Livermore National Laboratory (LLNL). This is a highly diagnosed facility for examining the dynamic properties of explosive and other such high-speed events. Three main diagnostics were used: a fast framing camera, a streak camera[2] and a streak spectrometer. A CW argon laser at 514 nm was used to illuminate the streak camera, and a 1 ns duration pulsed dye laser at 570-630 nm illuminated the framing camera.

The input face of a 100 μm diameter optical fibre was placed around 1 mm from the experiment to gather the light produced by the plasma, and the output connected to a spectrometer. The output of the spectrometer was recorded by a streak camera to provide time-resolved spectra.

The flyers were typically launched with 30 mJ of laser energy, with some experiments being performed at 7.5 and 15 mJ. The flyers were 0.25, 1 and 4 μm in thickness.

Images taken immediately after the laser pulse, viewing the oncoming flyer, showed a complex pattern in the flyer, which appeared to correlate to the spatial intensity profile of the fibre output. However, the limited depth of field and experimental timing jitter prevented examination of the flyer more than a few ns after launch.

[2] A streak camera views the image through a narrow slit. The image of the slit is then swept across a recording medium, producing a continuous time record of a portion of the image.

The framing camera was then used to image the flyer travelling across the field of view, using shadowgraphy. The flyer could be seen driven by the plasma, and appeared to be flat to within 8 μm, with this being maintained for at least 50 ns of flight, seen in Figure 5. This was believed to be due to residual strength in the flyer.

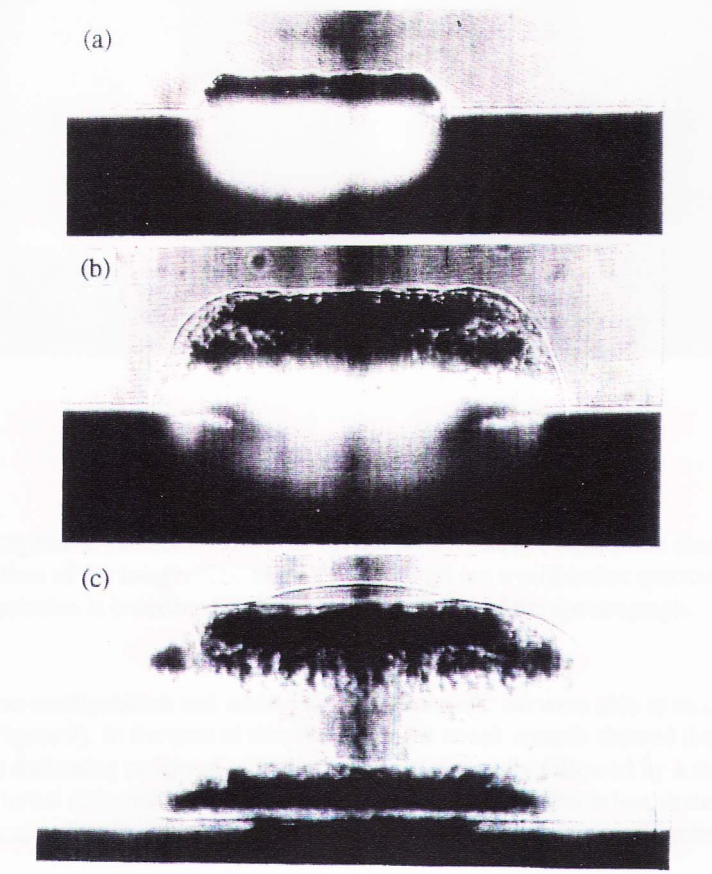

Figure 5 - Flyers shown at various times after launch, photographed in the LLNL Micro Detonics Laboratory [33]. The images are arranged in order of increasing delay after the laser pulse, from (a) to (c). The flyer is travelling vertically upwards.

The streak spectrometer showed a rapidly decaying broadband emission lasting around 75 ns. A strong aluminium emission line was observed, with four additional, unidentified lines. These may have been due to the silica from the fibre, as seen by Trott [34]. A late time flash at around 80-120 ns was also seen. This was proposed as being due to the radial expansion of the plasma interacting with the fibre ferrule producing additional plasma.

The streak camera was then used to observe the oncoming flyer. For the thin flyers, the initial deformation was seen, followed by a significant loss of reflectivity, then an expanding self-luminosity. For the thick flyers, the initial deformation appeared stable until the flyer moved out of the field of view. The expanding self-luminosity of the driving plasma was again seen.

These phenomena were explained by aluminium plasma being formed at the fibre/flyer interface, driving the remainder of the aluminium from the fibre. The fibre spatial profile induces deformations in the flyer, which are arrested by the strength of the aluminium. If the flyer is sufficiently thin, the flyer then vaporises (when the reflectivity drops) and ionises (when the flyer becomes self-luminescent). For the thick flyers, the flyer appeared to remain solid, with no evidence of breakup or melting.

Stahl described a flyer system [35] based upon either a substrate or a fibre, comprising of a 2 μm thick carbon layer, followed by a metal layer of unspecified thickness, typically aluminium. The advantages are given as a higher peak velocity, and a flatter flyer, due to the higher sound speed in carbon plasma compared to most metal plasma, allowing any pressure gradients to equalize faster. Whilst no evidence is provided to support a flatter flyer plate, the carbon layer is stated as producing a flyer of higher velocity (3 $km.s^{-1}$ compared to 2 $km.s^{-1}$ without), with this velocity achieved in a shorter timescale.

Trott [34] investigated the driving plasma for flyer plates launched from optical fibres, using both aluminium and composite flyer plates, using spectroscopy. He also used thin tracer layers to probe the ablation depth. An Nd:Glass laser at 1054 nm with a pulse duration of 18 ns was focussed into a 1000 to 400 μm tapered optical fibre using a 100 mm focal length lens. The output end was coupled to either a thin substrate coated with the flyer material, or a 1 m length fibre coated with the flyer material.

The diagnostics focussed on the light coupled “backwards” by the optical fibre, hence favouring the detection of the fibre material in the plasma. A fast-gated spectrometer with a 60 ns gate was used to examine the plasma emission, with a fast photodiode used to examine the temporal profile.

For 8 μm thick aluminium flyers, an alumina layer (0.25 μm thickness, 0.25 μm from the fibre interface) produced plasma with a longer emission time than that of a pure aluminium flyer. It was proposed that the thermal confinement of the alumina layer results in the plasma temperature being maintained for longer.

The spectrometer results indicated a broadband emission at early times, with discrete emission lines from the ablated material appearing later. Identified features included Al (308.2, 309.3, 394.4, 396.2 nm), Si (252.0, 288.2 nm), and Si^+ (290.6, 413.1 nm). The spectrometer data also showed the increased persistence of plasma emission for composite flyers.

The presence of silica features indicated a significant contribution to the plasma from the fibre or substrate material, in agreement with Farnsworth's [36] predictions.

Flyers with embedded layers 0.01 μm in thickness of copper, silver and tin were also tested, positioned at 0.1, 0.21 and 0.32 from the fibre interface. Strong emission from the copper and silver were observed, suggesting ablation to a depth of at least 0.21 μm. The emission from the tin was weaker, perhaps suggesting less ablation at this depth. Flyers with copper and silver layers at 0.25 and 0.5 μm also showed strong copper and very weak silver emission, supporting the conclusion that ablation involves less than 0.5 μm of the flyer, for these "pure" aluminium flyers.

It would be useful to repeat these experiments with tracer layers on composite flyers, to assess the impact of the alumina layer. A layer placed after the alumina layer would allow determination of whether the alumina layer is fully ablated. Streak spectroscopy would allow time-resolved measurements of the emission features to be made.

Trott [37] used velocity interferometry, streak photography and high-speed framing photography to investigate flyer behaviour. The laser used was a multimode Nd:Glass laser with a wavelength of 1054 nm and an 18 ns pulse length. The laser was coupled into 400 μm diameter optical fibres, with the flyer material coated directly onto the end of the optical fibre. Fluences of between 2.5 and 25 $J.cm^{-2}$ (equating to 3 to 30 mJ) were used. Trott noted that 2.5 $J.cm^{-2}$ was near the threshold for flyer motion.

Two flyer compositions were examined, a 4 μm aluminium coating, and a 4 μm composite coating, with a thin (sub-μm) layer of alumina between two aluminium layers.

The composite flyers were found to be more efficient than the pure aluminium flyers, with the difference most pronounced at fluences below 6 $J.cm^{-2}$ and decreasing at higher fluences. An analytic model was used to predict the flyer velocity, with excellent agreement for the composite flyers. For pure aluminium flyers, the predicted velocity was in excess of the experimental results at low fluences and below them at high fluences. As the alumina layer was intended to prevent ablation of the flyer by the driving plasma, Trott suggested that at the higher fluences, significant flyer ablation results in a thinner, lighter flyer, accounting for the discrepancies observed. Near threshold, he proposed the lack of insulating layer resulted in deep thermal diffusion, depriving the driving plasma of energy, resulting in lower than expected velocities.

Streak photography was used to image the flyers "edge-on", i.e. with the flyer travelling across the field of view. Firstly, the flyers were observed after travelling 75 μm. In both cases, a thin opaque object (the flyer) crosses the image plane, followed by the luminous driving plasma. However, after a distance of 300 μm, the aluminium flyer appears as an extended, diffuse image with a non-planar leading edge. In comparison, the composite flyer is much more compact and planar, implying it is substantially more intact.

A high-speed framing camera with a frame rate of 75 million frames per second (a frame every 13 ns) was used to examine the flyer "face on" i.e. travelling towards the camera. The flyer surface was not observed due to the intensity of the plasma, though the flyer could be seen silhouetted against the plasma. The diameter of the plasma can be seen to increase over time. The plasma begins to emerge within a single inter-frame time (13 ns) of the laser energy arriving at the flyer.

Finally, the flyers were impacted into lithium fluoride windows coated with 50 nm of aluminium. By recording the motion of the aluminium / LiF interface, it is possible to determine the shock duration imparted to the window. For a flyer launched at 27.5 mJ, a peak particle velocity of 1.23 $km.s^{-1}$ (for an aluminium flyer) and 1.298 $km.s^{-1}$ (for a

composite flyer) were predicted. The experimental values were 1.219 $km.s^{-1}$ and 1.268 $km.s^{-1}$ respectively, a close match. Assuming no significant flyer ablation, a pulse duration of 2.4 ns was expected. For the composite flyer this was found to be accurate; for the aluminium flyer, the pulse duration was 10% shorter, implying significant flyer ablation.

This technique of impacting flyers into LiF windows offers a useful way of studying flyer thickness at impact, a vital parameter for flyer initiation of energetic materials. It also provides further evidence that composite flyer offer significant performance advantages over aluminium flyers.

The composite flyers had higher peak intensities with longer emission times, suggesting the alumina layer provides thermal confinement. Significant emission was observed from silica i.e. the optical fibre from which the films were launched, supporting Farnsworth's earlier calculations. Thin (0.01 μm) layers of various metals were embedded at various depths within the flyers. By examining the emission from these layers at various depths, the extent of ablation could be measured. For a 4.0 μm pure aluminium flyer, this was seen to be around 0.5 μm.

Labaste [38] investigated the time-dependent reflectivity, flyer velocity and impact pressure for several materials. An Nd:YAG laser at 1064 nm with an 8 ns pulse width and an energy of up to 850 mJ was used to irradiate samples at varying irradiances, with the reflected energy being reflected by an elliptical mirror to a calorimeter. The experimental results presented are limited to a single plot of reflectivity versus irradiance for copper, showing a substantial drop in reflectivity above $1x10^{8}$ $W.cm^{-2}$ (roughly 1 mJ for a 400 μm diameter, 8 ns pulse length). No significant discussion is presented. The velocity data is similarly sparse, with a single plot of velocity versus irradiance for an unspecified aluminium flyer. This paper does not contain any significant information, save for a technique for measuring reflectivity of films at varying irradiances.

Hatt [39] studied a variety of single and multi-layer flyer plates, using a Time Of Arrival (TOA) technique to determine flyer velocity, using the model published by Lawrence [40]. An Nd:YAG laser with a pulse length of 6 ns at 1064 nm was focussed

to a 1 mm diameter spot on a fused silica substrate coating with the flyer material. A PMMA impact window was placed either 0.2 or 0.5 mm from the substrate. A fibre optic probe viewing the rear of the substrate collected light from the plasma, whilst a second fibre optic probe collected the light produced by the impact. Both fibres were recorded by a PMT, with the flight time defined as the time between the times of maximum light intensity of each trace. As similar flyers achieve 90% of peak velocity within 0.05 mm of travel, it was deemed that the TOA method produces a reasonable measure of peak velocity.

Three varieties of aluminium flyer plates were studied: a single 4 μm thick layer of aluminium, a 4 μm thick layer of aluminium with a 0.25 μm thick alumina layer, and a 0.25 μm thick aluminium layer with 3.35 μm of alumina. The third flyer plate provided the highest velocity at all fluences, with the aluminium multilayer flyer plate performing better than the pure aluminium flyer plate at fluences below around 15 $J.cm^{-2}$. Above this, the aluminium flyer plate performed better. It was postulated that above the fluences, the alumina insulating layer was compromised, resulting in a loss of pressure and hence velocity. The flyer plate with an alumina impact layer is a curious choice, as no other researcher has used alumina for an impact layer. The motivation behind this is not clear.

Two flyer plates with magnesium ablation layers and copper impact layers were tested, one with an MgF_2 insulating layer and the second with a ZnS layer. The flyer plate with the MgF_2 layer gave a velocity some 27% higher than an equivalent aluminium flyer, though the ZnS layer gave poorer performance.

Evidence of flyer plate breakup was observed, indicated by multiple light emissions on impact. This is contrary to other researchers observations at comparable fluences. It is likely that the free-space nature of the coupling of the laser energy is the cause; if the laser had a poor spatial intensity, the localised “hot spots” may have caused premature failure. This indicates the importance of maximising the spatial uniformity of the launch beam.

Paisley’s interest in laser-driven plates appears to shift from explosive initiation to dynamic material characterization [41], with the flyer plates becoming somewhat larger

(3 mm diameter by 50 μm thick). Results of impacts on copper are reported, with VISAR being used to monitor the free-surface velocity of the copper target. The results are used to determine the equation of state for copper, with a close match to existing experimental data observed.

The flyer plates used are not detailed, but a sapphire window is described, along with a sapphire/carbon interface. It seems likely the flyer plates are comparable to those described in Paisley's earlier patent [35]. The advantages of sapphire are unfortunately not stated.

Labaste [42] defined the acceleration of a flyer plate by laser irradiation into three distinct phases. Firstly, the deposition of the laser energy into the target. Secondly, the creation of a plasma and subsequently vaporisation of a small thickness of the flyer material. Finally, the expansion of this plasma resulting in acceleration of the remainder of the flyer plate. Considering these as three distinct phases may aid in the development of models of the flyer acceleration process.

A standard three-layer flyer was defined, consisting of an ablation layer, a thermal insulation layer, and an impactor layer, coated onto a silica substrate. The thermal insulation layer is an unspecified thickness of alumina (Al_2O_3), with 7 μm of aluminium as the impactor layer. By varying the material and thickness of the ablation layer it is possible to increase the flyer velocity for a given energy or fluence.

An Nd:YAG laser with a wavelength of 1064 nm and a pulse length of 8 ns was used for the experiments, with fluences ranging from 10 to 50 $J.cm^{-2}$. The method of beam delivery is not stated, but assuming a 400 μm fibre diameter, this equates to energies of 12 to 63 mJ. A laser Doppler interferometer was used to measure flyer velocities, though the distance at which the velocity was measured is not given.

Firstly, the optimum ablation layer thickness was determined for a reference aluminium layer. Over the thickness range of 0.3 to 2.0 μm, the maximum velocity was obtained for a thickness of 1 μm. The results are shown in Table 4.

Labaste noted that other researchers found the optimal efficiency of laser to flyer energy coupling was for singly ionised plasma. He then postulated that material with low

reflectivity and a large skin depth (i.e. volume absorption) would prove to be efficient. This led him to investigate germanium, carbon, hafnium and titanium.

The maximum velocity for each ablation layer material was then measured. The thickness of each material is different to that for aluminium, though it is not stated that these thicknesses were optimised like the aluminium layer.

Ablation Layer Material	Thickness, μm	Velocity, $km.s^{-1}$	Cold Reflectivity, %
Germanium	0.15	4.13	28
Carbon	0.5	4.11	29
Hafnium	0.3	3.80	46
Titanium	0.3	3.75	51
Aluminium	1	3.75	93

Table 4 - Maximum flyer velocity at 30 $J.cm^{-2}$, as reported by Labaste [42]

Labaste calculated the vaporisation depth for each material assuming a single ionisation, shown in Table 5. It is obvious that there are significant differences between the calculated ablation depth and the optimal thickness, which Labaste concluded implied a more complicated relationship between efficiency and layer thickness. It may be that the model used to calculate the absorption thickness is not time-dependant, i.e. early-time plasma formation will cause energy absorption preferentially towards the substrate, reducing the actual absorption depth.

Ablator	Optimum test thickness, μm	Singly-ionized Plasma thickness, μm
Aluminium	1	0.86
Titanium	0.3	0.78
Hafnium	0.3	0.9
Carbon	0.5	0.4
Germanium	0.15	1

Table 5 - Comparison at 30 $J.cm^{-2}$ of optimum test thickness with singly-ionized thickness [42]

Labaste then examined how the plasma energy is transmitted into the impactor layer. The pressure of the plasma produced a shock propagating into the remainder of the

ablation layer then transmitted into the alumina layer and the aluminium projectile. It is possible to calculate the shock pressure imparted to the impactor layer. For a pressure of 3 GPa (most likely in the ablation layer), pressures of 2.6 GPa in the impactor for an aluminium ablator and 1.7 GPa for hafnium were obtained. The shock impedance is linked to the material density, hence Table 6 is arranged in order of density.

Labaste concluded that for ablator materials with a density lower than alumina, the optimal thickness was given for the singly-ionized condition, whereas for denser materials, the shock impedance optimisation dominates, requiring a thin ablation layer. This is supported by Table 6, where it can be seen the lower density materials (aluminium, carbon) are a much better match to the experimental data than the higher density materials (titanium, germanium, hafnium).

Alumina density ρ = 3.9 g.cm^{-3}					
Ablator	Aluminium	Carbon	Titanium	Germanium	Hafnium
Density, g.cm^{-3}	2.2	2.2	4.5	5.3	11.7
Optimum thickness	Nominal for singly-ionized plasma		Very low / impedance mismatch		

Table 6 - Optimal thickness of ablators as a function of their mechanical properties [42]

Trott [43] used velocity interferometry to determine the Hugoniot of 6061-T6 aluminium, by impacting the aluminium flyers into a well-characterised window, in this case fused silica. A Nd:Glass laser at 1053 nm was focussed using a variety of beam shaping and focussing techniques; the method used is not detailed, but it stated that the flyer planarity is relatively insensitive to the laser spatial profile. Fluences up to 50 J.cm^{-2} for a 2.5 mm flyer diameter were used. The flyer plates consisted of 5 μm thick aluminium deposited onto fused silica windows, with a 100 μm thick disc of 6061-T6 aluminium diffusion bonded to the aluminium layer. This allowed the pressure-particle velocity curve to be determined, and the results obtained were in close agreement to published values. This technique is described in greater detail later.

Trott [44] continues the development of a method for determination of dynamic material properties using laser-driven flyer plates, by investigating a method for improving the spatial profile of the beam used to launch the flyers.

To simplify the analysis of such experiments, it is necessary to launch flyers with a high degree of planarity. Two such techniques are discussed: firstly, transmitting the laser pulse through an optical fibre to smooth the intensity profile; secondly, directly manipulating the beam profile by using beam-shaping optics. For the flyer diameter of interest here, up to 2.5 mm, using optical fibres is impractical due to the lack of available fibres of this diameter. Therefore, a method for producing a uniform spatial profile was developed.

The laser used is an Nd:Glass laser, operating in either an oscillator-only or oscillator and amplifier configuration. The respective energies are 4.5 and 20 J, with a pulse duration of 20 ns.

A beam shaping system was developed consisting of a diffractive lenslet array and a primary lens shown in Figure 6. The diameter of the lenslet array was 30 mm, with a thickness of 1 mm. Each hexagonal lenslet measured 2.5 mm flat-to-flat with a focal length of 95.2 mm. The plano-convex primary lens had a focal length of 76.2 mm. The system was designed to produce a spot diameter of 2 mm.

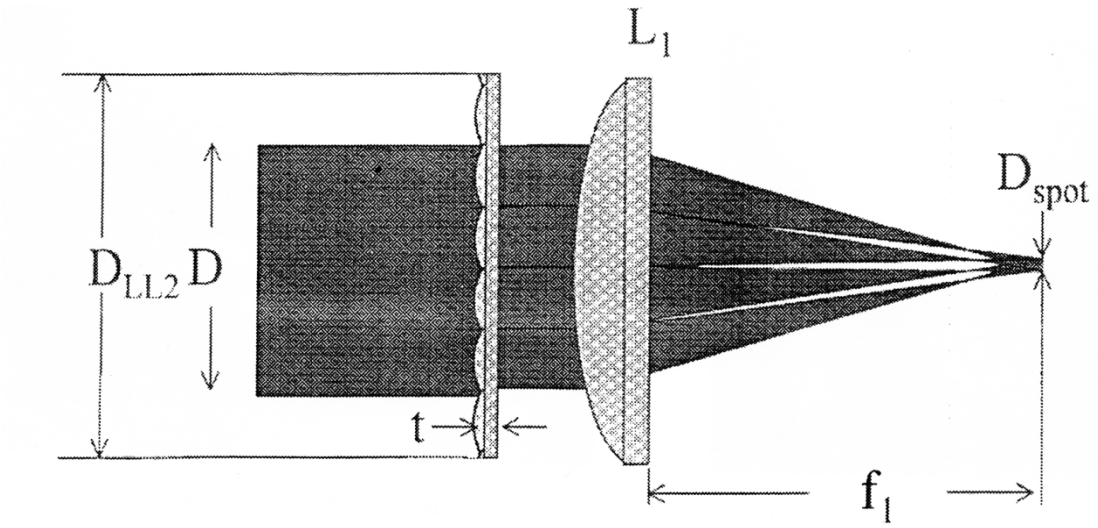

Figure 6 - Beam shaping configuration as used by Trott [44]

CCD cameras coupled to beam-profiling software were used to analyse the intensity profiles produced. The uniformity was measured by applying the following relation, where a perfectly uniform profile would yield a value of 1:

$$\frac{Peak\ intensity}{Average\ intensity} = \frac{Peak\ total\ fluence.Aperture\ area}{Total\ energy\ incident\ on\ aperture}$$

Equation 4

The beam shaper was first evaluated using an Nd:YAG laser and a 77.4 mm focal length primary lens. The beam profiles obtained at the focal plane (a), 5.0 mm beyond the focal plane (b) and 10.0 mm beyond the focal plane (c) are shown in Figure 7. It can be seen that a significant amount of un-diffracted light produces a significant intensity "spike" in the centre, seen in Figure 7 (a). Though it can be seen that moving the image plane beyond the focal plane reduces this spike, the amount of energy contained within the 2 mm diameter aperture reduces also. Similar results were obtained with the Nd:Glass laser and a 75 mm focal length lens.

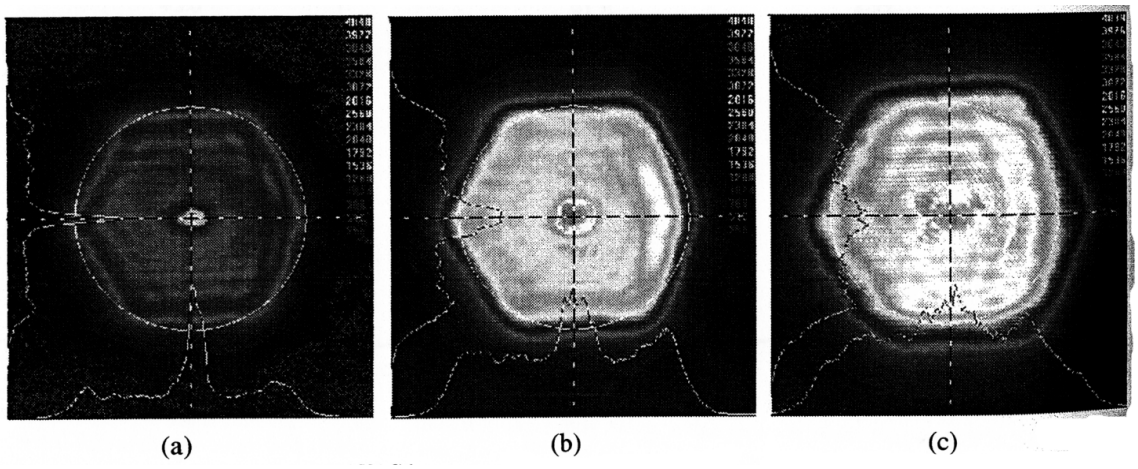

Figure 7 - Beam profiles produced by beam shaper [44]

Velocity interferometry was then used to evaluate flyer velocity across the central 0.5 mm of a 2.5 mm diameter, 100 μm thick aluminium flyers. The flyer was positioned at two locations, at the focal plane, and 4 mm before the focal plane. The peak/average values (as per Equation 4) at each position were 13.56 and 2.31 respectively. At the focal plane, a velocity peak corresponding to the intensity spike seen in the beam profiles was observed. With the flyer positioned before the focal plane, a significantly smoother velocity profile was seen, with little evidence of a central velocity peak.

This highly planar flyer is suitable for dynamic material characterisation, permitting a one-dimensional analysis of the results. The beam shaping technique presented offers significantly greater performance compared to the unshaped beam.

Greenaway et al [45] investigated the impact of flyers into a window. It is suggested in the abstract that velocities approaching 10 $km.s^{-1}$ were attained, though the main article does not support this. The application of the flyer system is not detailed, though possible applications are given as micrometeorite simulation, materials testing and detonics.

The laser used was an Nd:YAG laser with a pulse length of 9 ns at 1064 nm. This is somewhat shorter than the typical 12-15 ns used for laser-driven flyer plates. A 400 μm fibre conducts the laser energy to a metallic coating on a transparent substrate. The flyer plates produced are stated as achieving terminal velocity within 100 ns, with destruction of the flyer by thermal effects occurring after a few hundred μm.

Streak photography was used to characterise the flyer plates, with the camera observing the oncoming flyer. The flyer is impacted into a transparent window, and the resulting adiabatic compression of the air between the flyer and window causes a bright flash then recorded on the streak camera. A stand-off of 100 μm was used between the substrate and window. By adjustment of this standoff, time of flight measurements between varying stand-offs were made and average velocities calculated. This technique has poor velocity resolution in comparison to velocimetry but offers a basic understanding of flyer performance.

Finally, a brief description of research into an unspecified ablation layer, between the substrate and flyer, is given. The details of this layer are not given for unknown reasons, but a threefold increase in flyer kinetic energy is claimed. This is somewhat at odds with the claimed increase in velocity from 2.26 $km.s^{-1}$ to 3.67 $km.s^{-1}$. It is claimed in the conclusion that launching flyers in a vacuum would be expected to increase flight length by a factor of up to 10^4 i.e. from 500 μm to 5 m. This claim seems highly dubious and there is no evidence supplied to qualify this claim.

2.3.2. Summary of Experimental Results for Laser-Driven Flyer Plates

A significant body of work has been reported for laser-driven flyer plates, using both free-space laser beams and fibre optic coupling. There has been no direct comparison made between the two methods, although the main difference is that fibre optic coupling offers a convenient method to control the spatial intensity uniformity of the beam used to launch the flyer plate, which determines the planarity of the flyer plate launched. Free-space laser beams allow greater fluences and hence velocities to be reached, by avoiding the limited damage threshold of optical fibres. Optical fibres are also limited in diameter to around 1 mm, limiting flyer diameter. However, optical fibre coupling allows for flexibility in the experimental setup and can increase the separation between the laser and the flyer, desirable for explosive initiation.

Explosive initiation has not been reported using fibre optic coupling, although the literature is sparse. The velocity required for initiation by Paisley [21], 1.8 $km.s^{-1}$, is achievable by using fibre optic coupling, as shown by Paisley [32] , Stahl [35], Trott [37] and Greenaway [45].

The majority of published literature has reported the use of multi-layer flyer plates, with the use of a dielectric layer, used to insulate the flyer from the accelerating plasma and increase the temperature of the plasma. Multi-layer flyer plates offer both an increase in efficacy [30; 37; 39] and a reduction in the ablation of the flyer by the plasma [37].

2.3.3. Theoretical and Computation Studies of Laser-driven Flyer Plates

2.3.3.1. Analytical Models

Farnsworth [46] and Lawrence [40] reported both analytic and numerical models of laser-driven flyer plates, comparing the predicted results with experimental data.

The analytical model used the following assumptions and is based upon the Gurney equations [47]:

1. An exponential laser energy deposition profile
2. Deposition depth much less than the initial flyer thickness
3. Complete tamping of the foil by the optical fibre
4. A constant fraction of the laser energy lost by radiation and reflection
5. A linear velocity profile in the plasma between fibre and foil

If x_d is the deposition depth and x_0 is the original thickness, then the energy equation in 1 dimension was given by:

$$\rho x_d E = \frac{\rho}{2}(x_0 - x_d)v_0^2 + \frac{\rho}{2}\int_0^{x_d}\left(v_0 \frac{x}{x_d}\right)^2 dx$$

Equation 5

where ρ is the flyer density, E is the laser energy and v_0 the terminal flyer velocity.

The left side of the equation represents the Gurney energy available for driving the flyer, the first term on the right gives the flyer kinetic energy and the second term gives the plasma kinetic energy. The Gurney energy is the energy remaining after reflection, radiation and conduction losses, and vaporisation and ionization. The deposition depth is given by:

$$x_d = k\sqrt{\alpha\tau}$$

Equation 6

where k is a fraction, to account for energy losses, α the thermal diffusivity and τ the laser pulse duration.

The ratio of foil kinetic energy to incident laser energy is given by (where F_o is the laser fluence):

$$\frac{KE_f}{E_l} = \frac{\rho(x_0 - x_d)v_0^2}{2F_0}$$

Equation 7

Equation 5 can be solved for the flyer velocity v_o (where E is the Gurney energy i.e. the energy remaining after losses and vaporisation, x_0 the original flyer thickness and x_d the ablated thickness):

$$v_0 = \sqrt{\frac{3E}{\frac{3x_0}{2x_d} - 1}}$$

Equation 8

These relationships were used to predict flyer velocity, normalised impulse and coupling efficiency as a function of fluence. Close matches to experimental data are found, with both normalised impulse and efficiency dropping at low fluences. Figure 8 shows the match between experimental and predicted flyer velocity as a function of fluence, with good agreement.

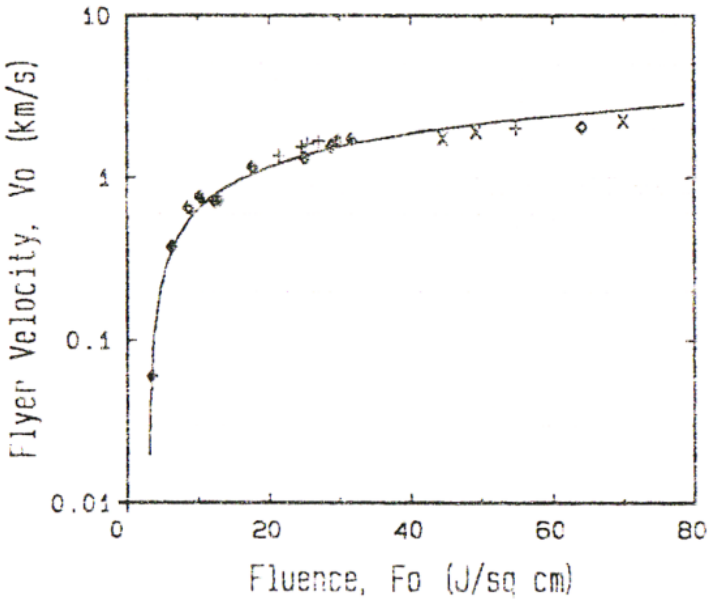

Figure 8 - Experimental vs. predicted flyer velocity [46]

2.3.3.2. Numerical Models

The numeric model developed by Farnsworth [46] reported in Section 2.3.3.1 was implemented in a hydrocode, LASNEX, again in 1 dimension. LASNEX did not include laser deposition in solid, liquid or neutral gas phase, so an artificial energy source was used until ionisation occurs.

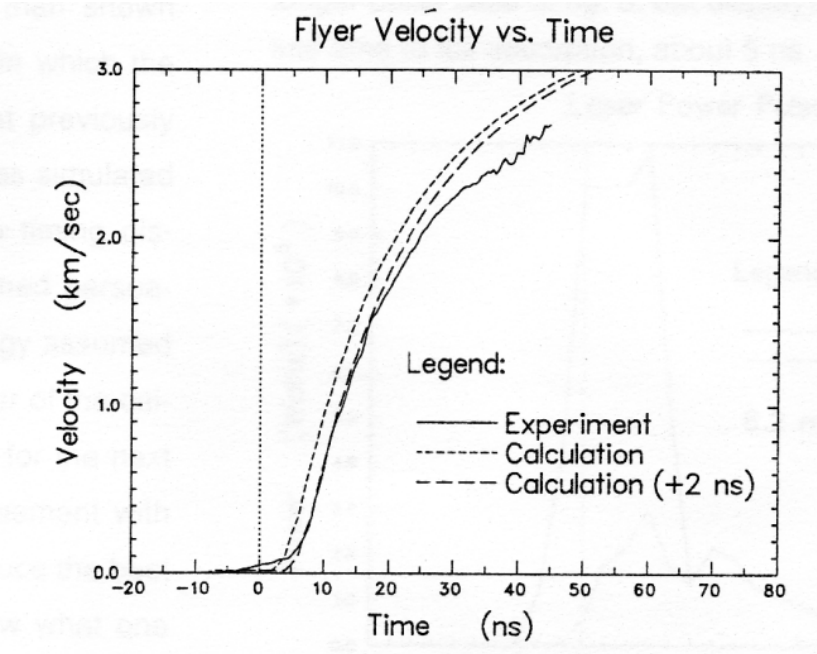

Figure 9 – Comparison of experimental and modelled flyer velocity vs. time [46]

The predicted flyer velocity is shown in Figure 9, where a close match can be seen. There appears to be an offset of some 2 ns, believed to be due to the artificial energy source used to model the early laser deposition. The over-prediction at later times was believed to be due to 2 dimensional effects, such as the lateral expansion of the plasma.

The incident laser pulse is shown in Figure 10, along with the calculated absorbed (or deposited) pulse. The energy not absorbed at early times was reflected back into the fibre and was measured, where it compared well to the predicted values.

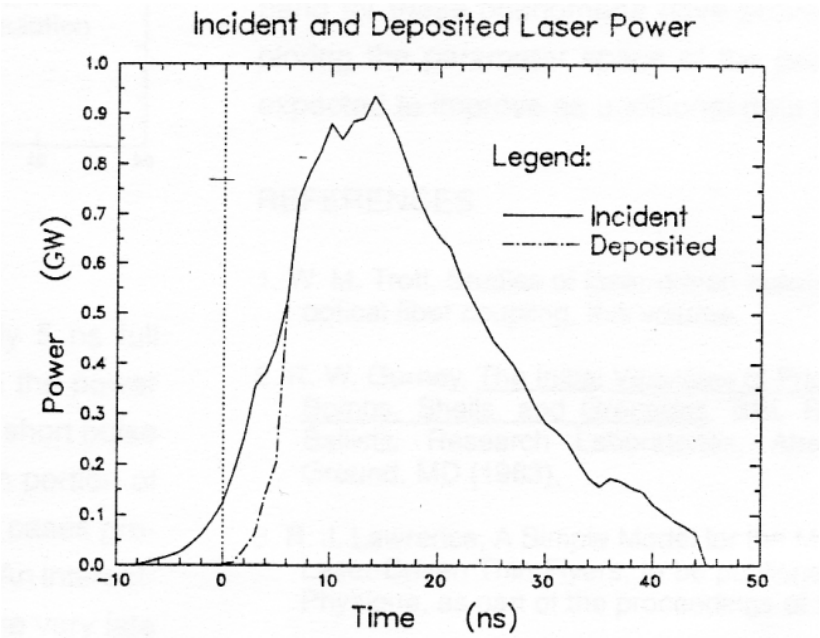

Figure 10 – Comparison of measured incident and deposited laser pulse [46]

Farnsworth [36] used the CTH hydrocode to model the flyer launch, flight and impact processes, with the aim of optimising the flyer design for explosive initiation. The CTH hydrocode was modified with routines to allow laser interaction and transport to be modelled.

The results indicated a substantial contribution to the plasma from the silica substrate. The aluminium plasma produces a small quantity of silica plasma, which then begins to absorb the laser energy. The point of absorption was predicted to recede into the silica substrate during the laser pulse. It was found that the majority of the absorption actually

occurs in the silica, to a depth of around 0.4 μm, confirmed by post-shot examination. This is also confirmed by Trott's [37] spectroscopic data. As a result of this discovery, different substrate materials were examined for their effect on performance. Silica, quartz and polyethylene were modelled. Quartz was found to be significantly inferior, whilst polyethylene gave a lower velocity at early times but showed some recovery relative to silica at later times. It was concluded that no benefit was gained by changing the substrate material.

Trott reported that composite flyers performed substantially better for explosive initiation, stating Harris was unable to initiate explosives with pure aluminium flyers even at high laser energies.

The temperature distribution for each flyer was modelled for a time corresponding to impact. For pure aluminium flyers, the temperature was above the melting point of aluminium throughout the entire flyer thickness during flight. For the composite flyers however, the impact surface was found to remain below the melting point. This compromising of the pure aluminium flyers agrees with the reduced shock width measured by Trott [37].

It was proposed that selection of a flyer material with a higher melting point could improve the flyer performance. To investigate this, the aluminium impactor layer was replaced with an equal mass of titanium. However, whilst the melting point of titanium is higher, the temperatures reached were actually higher relative to the melting point than for aluminium, resulting in poorer performance.

Following Labaste's experimental paper, Cazalis [48] reported numerical modelling of laser-driven flyer plates. The model is implemented in a one-dimensional hydrocode. Labaste's technique for determined reflectivity as a function of irradiance is used to provide data for aluminium reflectivity at varying irradiances.

The model was used to evaluate metallic flyers (copper, aluminium, magnesium) and multilayer flyers. The model was able to predict the temperature distribution across the flyer, and for a copper/alumina/copper flyer, whilst the plasma temperature approaches 10^5 K, the impactor layer thickness on impact remains below the melt temperature.

Flyer velocity profiles for 1 μm thick copper flyer plates were calculated, with velocities in excess of 5 $km.s^{-1}$ being reached in less than 50 ns for a fluence of 70 $J.cm^{-2}$.

The model was also used to predict shock pressures and durations imparted to a range of target materials. Unfortunately, little comparison to experimental data is made, so the physical applicability of the model is unknown.

Lee [49] used the LASNEX hydrocode to model the experimental results reported by Trott [31], Frank [33] and Labaste [42]. A flyer plate comprising three layers was modelled: a 0.25 μm thick aluminium ablation layer, a 0.25 μm thick alumina insulator layer and an aluminium impactor layer of variable thickness. A 30 ns pulse length laser was modelled, at a fluence of 25 $J.cm^{-2}$. Two important results were noted. Firstly, the insulator layer increased the pressure accelerating the flyer, as the increased temperature vaporised some of the glass substrate, resulting in an increase in flyer velocity of approximately 25%. Secondly, the insulator layer increased the time at which the temperature of the impactor layer exceeded the melt temperature of aluminium, at which point flyer integrity would be compromised. Without the insulator layer, melt occurred at 35 ns (for reference, a 100 μm flight distance corresponds to a flight time of 40 ns). A 0.25 μm insulator layer increased this time to 70 ns, whilst a 0.5 μm insulator layer increased this time to 80 ns, with a reduction in velocity, due to the additional mass, of 5%. Whilst the predicted flyer velocities were in reasonable agreement to the experimental flyer velocities, experimental data on flyer integrity were not available.

Farnsworth [50] used the modified CTH hydrocode described earlier [36] to model flyer plates used for equation of state studies. A flyer plate consisting of a 5 μm thick deposited aluminium layer with a 92 μm thick 6061 T-6 aluminium impact layer was launched using a 1.6 J, 20 ns laser pulse, and impacted into a fused silica window. It can be seen in Figure 11 that the calculated and experimentally measured flyer velocities are closely matched. It can be seen that the calculated velocity profile displays deeper valleys than the experimental profile, most likely due to two-dimensional effects across the 100 μm diameters measured.

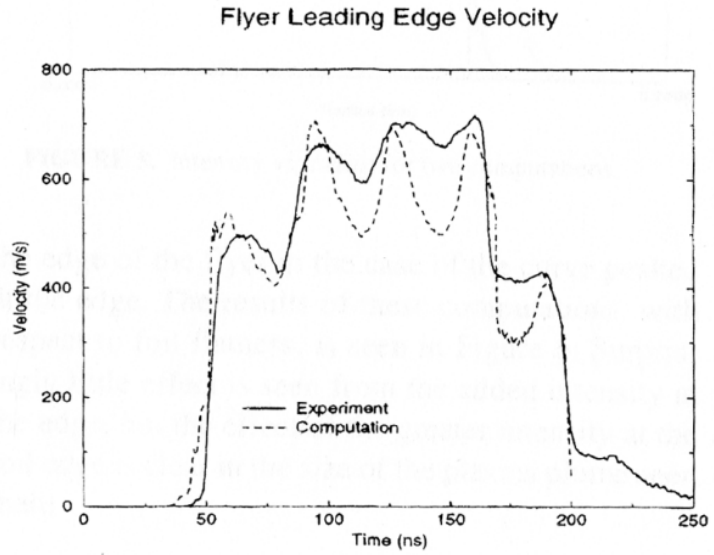

Figure 11 - Calculated and experimental flyer velocity profiles [50]

Two-dimensional calculations were also performed to assess the effects of the laser spatial profile. Pressure relief around the edges of the flyer plate can cause the edges of the plate to lag behind the centre. Two profiles were assessed: a flat-topped profile with a Gaussian decrease towards the edge, and a significantly higher intensity at the edge, to drive the edges of the plate harder. Little difference was found in the flyer flatness, though a larger quantity of plasma was found ahead of the flyer for the second profile.

In agreement with earlier papers, CTH appears to be a valuable tool to model complex time-dependant processes, such the flyer launch and motion.

Swift [51] modelled flyer launch and acceleration using the hydrocode HYADES, and made comparisons to experimental data. The flyers were larger than that used by other researchers, with a diameter of 5-6 mm and thicknesses up to 250 μm, although the multi-layer construction was similar, with a carbon ablation layer, an alumina insulator layer and a aluminium impactor layer. The laser had a pulse length of 600 ns, with an energy of up to 24 J. This corresponds to a fluence of approximately 2.5 $J.cm^{-2}$, below that used by of most researchers. Experimental velocities of up to 0.6 $km.s^{-1}$ were obtained, for a 55 μm thick flyer.

Unlike earlier research however, the calculated flyer velocities consistently exceeded the experimental flyer velocities, with the error increasing with flyer thickness. This was believed to be due to inaccuracies in the material properties, particularly those for the carbon ablation layer.

2.3.3.3. Summary of Theoretical and Computation Studies of Laser-driven Flyer Plates

Theoretical and computation studies of laser-driven flyer plate launch can be grouped into two areas. Firstly, those investigating simple, analytical models, such as those reported by Farnsworth [46] and Lawrence [40]. These produce a prediction of the terminal velocity of the flyer plate, and are not time-dependant. However, they are useful for quickly assessing the effect of parameters such as laser fluence, flyer thickness and flyer material. To be useful as a design tool, time-dependence is needed, to determine the flyer velocity and position as a function of time.

Time-dependant models are typically implemented in hydrocodes, and have been reported by Farnsworth [36; 50], Cazalis [48], Lee [49] and Swift [51]. Hydrocode models are able to investigate parameters that are difficult or impossible to measure experimentally, such as flyer temperature. They are however, computationally intensive and hard to validate, as only limited comparison to experimental parameters, such as flyer velocity, can be made. Lee [49] predicted the time of flyer melt, and hence loss of flyer integrity as a function of insulator layer thickness. This prediction has not been tested experimentally, but is possible to investigate using velocity interferometry. This is a possible area for experimental research.

Swift's results [51] highlight the difficulties in numerical modelling of laser-driven flyer plates. Most material data available is applicable to two regimes: ambient, or close to ambient, conditions, and warm, dense conditions, such as those found in laser fusion experiments. Laser-driven flyer velocity conditions fall between these two regimes, and hence applicable material properties are lacking.

Time-dependant analytical models, capable of predicted velocity histories, have not been reported in the literature. Such a model, if developed, could allow rapid

assessment of changes to experimental parameters, such as laser fluence, or flyer thickness, without the computational expense of a hydrocode.

2.4. Laser-induced Explosive Initiation

There are three published methods of initiating energetic materials with laser radiation. The first, and simplest, is direct irradiation of the energetic material. Secondly, the laser irradiates a thin foil, typically metal, placed in intimate contact with the energetic material.

The third method, a laser-driven flyer plate, is the most amenable for use in a detonator system based upon secondary explosives, such as HNS. As this study focuses on the shock initiation by a flyer plate, the other two methods have been omitted.

Whilst there exists a large body of literature regarding laser-driver flyer plates, little has been published on the shock initiation of energetic materials using laser-driven flyer plates.

Paisley reported the first initiation of an energetic material, HNS using 2 μm thick aluminium flyers launched by a free-space beam [52]. He reported that a 0.25 μm thickness alumina layer deposited within an aluminium flyer could increase the efficiency of the flyer by up to 30%. Flyer velocities as low as 1.8 $km.s^{-1}$ were required for detonation in high density (1.6 $g.cm^{-3}$), high surface area (14 $m^2.g^{-1}$) HNS powders.

Chengwei et al [53] presented a model in 1999 for both the flyer motion and shock initiation of explosives impacted by the flyer. Large diameter fibres, 0.7 mm were used, with a 15 μm thick aluminium foil attached to the output end. The initiation of PBX9404, an HMX-based composition, was discussed, but it is not apparent if this was achieved. It is the author's opinion that this was not achieved, as the failure diameter (>1 mm) is likely to preclude this.

Watson et al [54] reported the initiation of Pentaerythritol Tetranitrate (PETN) using 1 mm diameter, 3-5 μm thick aluminium flyers launched with a free-space laser beam. Course PETN, with a particle size of 135 μm, could not be initiated with flyer velocities up to 6 $km.s^{-1}$, though some reaction was observed. Fine PETN with a particle size of 1

μm, pressed to 75% theoretical maximum density (TMD) was initiated at flyer velocities of around 4.3 $km.s^{-1}$. The flyer velocity was estimated from time of flight measurements using streak photography.

Greenaway et al [55] investigated the shock sensitivity of HNS to laser-driven flyer plates. Fine particle HNS IV, fine particle HNS IV with pressing additives, and coarse HNS II were investigated. Pure HNS IV at 70% TMD was found to have the lowest threshold, at 250 mJ (laser energy). Reducing the density to 65% TMD increased the threshold to 350 mJ, and the addition of pressing additives at 65% TMD resulted in a threshold of 350 mJ. HNS II could not be initiated. This work is of limited use, as the results are reported in terms of laser energy, not flyer velocity. As a result, it is not possible to evaluate the shock pressure or duration required for initiation.

Zhuowei [56] initiated PETN using aluminium flyer plates launched with an Nd:YAG laser with pulse duration of 10 ns and a maximum energy of 1 J. The flyer plates were 5.5 or 10 μm in thickness, and 1 mm in diameter. They were accelerated across a 100 μm stand-off into PETN pellets with a density of 1.2 $g.cm^{-3}$. This is substantially lower than the PETN and HNS densities used by other researchers, typically 1.6 $g.cm^{-3}$. The motivation behind this choice is not clear.

Nine explosive shots were performed, eight with the 10 μm thickness flyers and one with the 5.5 μm thickness flyers. The detonation pressure threshold was found to be 7.1 ± 0.2 GPa, at shock pulse duration of 3.8 ns, for the 10 μm flyers. The critical energy criteria $P^2\tau$ (where P is imparted shock pressure, and τ is imparted shock duration) was evaluated and found to be equal to $23x10^{10}$ $Pa^2.s$, though this is essentially calculated from a single value, and may therefore be somewhat dubious. Had more than one experiment with the 5.5 μm thickness flyer been performed, a more satisfactory calculation of $P^2\tau$ could have been performed.

Numerical simulations of the initiation were performed using a one-dimensional hydrocode. The detonation pressure of PETN at 1.2 $g.cm^{-3}$ was set at 12 GPa. The calculated threshold was 8.7 GPa, some 20% than the experimental value. The discussion appeared to suggest that as soon the shock within the explosive begins to be attenuated by the rarefaction wave travelling from the rear of the flyer, the growth to

detonation will be interrupted and detonation will not propagate. Whilst simplistically this is true, this is a gradual process, and the growth to detonation can be extended and still grow to full detonation and propagate. This may be the cause of the discrepancy between the experimental and modelled threshold.

Parker [57] continued the work of Greenaway [55] to initiate HNS. Unfortunately, the experimental details are very sparse, with the flyer thickness, diameter or velocity not reported. The threshold is stated in terms of laser energy (181 mJ) and cannot be correlated to a pressure. Parker reported that 2,6-diamino-3,5-dinitropyrazine (ANPZ) and 2,6-diamino-3,5-dinitropyridine-1-oxide (DADNPO), insensitive explosives, could not be initiated.

2.4.1. Summary of Laser-induced Explosive Initiation

Using flyer plates to initiate energetic materials has several advantages over other methods. It is the only method in which HNS can be initiated; HNS cannot be initiated by an exploding bridgewire (EBW). HNS is thermally stable, and does not degrade significantly over time. Furthermore, high-density (90% theoretical maximum density (TMD)) explosive pressings can be used, resulting in a single fill or pellet, and can withstand shock loading better than a low-density (50% TMD) pressing.

Little has been published on the laser-driven flyer plate initiation of explosives. Two explosives have been reported to have been initiated: HNS [21; 55; 58] and PETN [54; 56]. Of these studies, none have used fibre-optic coupling of the laser. Only three studies [21; 54; 56] have reported the flyer velocity required for a 50% probability of initiation, required for the calculation of the imparted shock pressure and evaluation of critical energy criteria.

There is a clear void in the literature on laser-driven flyer plate initiation of explosives. The literature confirms that initiation is possible, but a comprehensive scientific study of the processes involved, or the practicality of a system using laser-driven flyer plates, has not been reported.

2.5. Summary of Literature Review

There is a reasonable quantity of literature regarding the major components of a laser detonator system: coupling into an optical and subsequent transmission; flyer plate launch and acceleration; and the initiation of the explosive. However, there are no published studies of such a system in its entirety. Further, there are voids in the literature in several areas.

Coupling the optical energy into an optical fibre, and the subsequent transmission of this energy has been reasonably well studied. However, the research has been limited to laboratory investigations, with little investigation of the practicalities of implementing fibre optic energy delivery in a system context. All the fibres investigated have omitted the fibre connector and associated ferrule, required for handling and connection to the laser and detonator. Additionally, no thorough studies of a robust fibre-to-fibre connection, required for practical applications, have been performed. Further work is needed to investigate the effect of connectorising the optical fibre, along with development of a fibre-to-fibre connection method, to eliminate the need for frequent alignment of the free-space laser beam to the optical fibre. Whilst laser polishing of the fibre faces is reported to achieve the highest damage thresholds, this polishing method is complex, uncommon and expensive. In contrast, mechanical polishing, whilst offering similar performance, has not been adequately studied, and the effect of the mechanical polishing process and surface smoothness remains unknown. Investigation of the optimal mechanical polishing method would provide a specification for the polish and resulting surface finish that could be met by many fibre assembly vendors.

The flyer launch process has been adequately studied, with a variety of flyer compositions investigated. However, few studies of the shock imparted by thin (<10 μm) laser-driven flyer plates have been reported. It is critical to know the thickness of the flyer at impact, as this controls the duration of the shock imparted to the explosive. Little has been published on the relative performance of these flyers when applied to explosive initiation. It would be prudent to apply modern diagnostics, such as PDV, to the flyer launch, flight and impact process, and to determine the optimal flyer composition for explosive initiation. Analytical and numerical models of the flyer plate launch and acceleration process have been report. However, a time-dependant analytical

model of the process, capable of predicting time-varying flyer velocity and position has not been reported. Development of such a model would provide a rapid means to evaluate the effect of parameters such as laser fluence and flyer thickness, and would provide a valuable design tool.

The initiation of explosives by laser-driven flyer plates is sparsely reported in the literature, with approximately five papers published. Laser-driven flyer plates impart extremely high shock pressures to the explosive, on the order of the detonator pressure within the explosive itself, and no comparison of this inert shock to the reactive shock of a detonation wave has been made. The short duration of the shock imparted is also comparable to the reaction zone length in common detonator explosives, such as PETN and HNS, and this relationship would be interesting to study.

Common critical energy criteria, such as $Pn\tau$ or the James Criterion may not be extensible to this extreme pressure regime.

To summarise, the following topics are not, or sparsely, reported in the literature:

1. The interaction between optical fibre core and ferrule for high-energy transmission.
2. A method for connecting two high-energy optical fibres together.
3. The interaction between the methods used to mechanically polish the optical fibre faces and the damage threshold of the optical fibre.
4. The shock generated in materials by thin laser-driven flyer plates.
5. Shock initiation of explosives by laser-driven flyer plates.

It is clear that a substantial contribution to the scientific knowledge may be made in these areas.

2.6. A Baseline Laser Detonator System

From a review of the literature, it is possible to define a baseline laser detonator system. Whilst these parameters should produce a usable system, it will not be optimised, nor will a full understanding of the processes involved be available. The baseline system, derived from the literature review, is detailed in Table 7.

Parameter	Specification	Justification
Laser type	Nd:YAG, 1064 nm	Most common laser type reported in literature. Commercially available. Fundamental wavelength (1064 nm) as highest radient efficiency.
Laser energy	>100 mJ	Assuming 400 μm core diameter fibre, provides adequate energy for explosive initiation (estimated at 20 $J.cm^{-2}$ [59])
Laser pulse width	11.5 – 14 ns	Most commonly reported in literature for fibre injection
Injection method	Plano-convex lens	Commercially available.
Fibre core diameter	400 μm	Exceeds critical diameter of HNS [60] and PETN [61].
Flyer plate composition	0.5 mm fused silica window 0.25 μm aluminium ablation layer 0.25 μm alumina insulator layer 3-5 μm aluminium impactor layer	Ablation layer and insulator layer reported to initiate HNS [21]. Impactor layer reported to initiate PETN [54] and HNS [55]
Barrel length[3]	75-100 μm	90% of terminal velocity attained by 75 μm, 100% by 100 μm [49]
Explosive material	HNS or PETN	Successful initiation reported by laser-driven flyer plates [21; 54-57]
Explosive density	90% TMD	Successful initiation reported by laser-driven flyer plates [21; 54-57]
Explosive surface area or particle size	1 μm particle size (PETN) 14 $m^2.g^{-1}$ surface area (HNS)	PETN particle size [54]. HNS surface area [21].

Table 7 - Baseline laser detonator system parameters

[3] Separation between flyer plate and explosive

CHAPTER 3: FUNCTIONAL DESCRIPTION AND EXPERIMENTAL CONFIGURATION

3.1. Functional Description of a Laser Detonator System

A laser detonator system consists of three sub-systems, illustrated in Figure 12: the laser; fibre-coupling optics; and the detonator. For this functional description, the laser considered is that designed by Honeywell Federal Manufacturing & Technologies, designated the FY07 Baseline System [62]. This laser was chosen as it was developed specifically for laser detonation systems, and several papers [62-66] have been published detailing the laser development and characteristics.

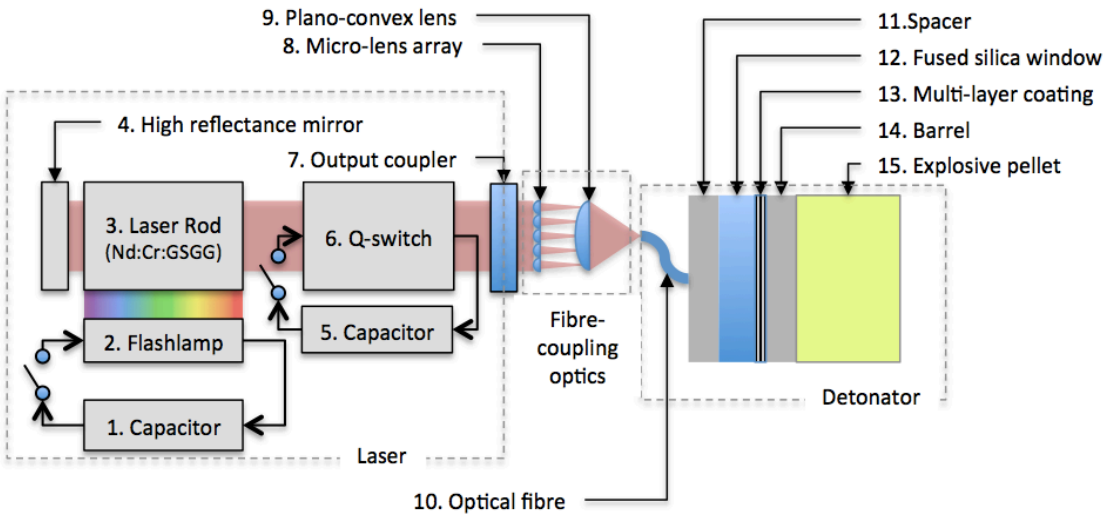

Figure 12 – Schematic of a Laser Detonator System

3.1.1. Laser Operation

The firing operation begins with the discharge of the flashlamp capacitor (1) through the xenon flashlamp (2). The capacitor discharge circuit has a capacitance of 21.3 μF, and an inductance of 36 μH. The capacitor is charged to a voltage of 855 V, corresponding to a stored electrical energy of approximately 7.8 J. The resulting pulse has a duration of 80 μs.

The flashlamp produces an intense pulse of broadband light, which is absorbed by the laser rod (3). The flashlamp and laser rod are housed within a diffusely-reflective

enclosure which acts to efficiently couple the flashlamp energy into the laser rod. The laser rod is Nd:Cr:GSGG (Gallium Scandium Gadolinium Garnet, co-doped with Neodymium and Chromium ions); 5.0 mm in diameter and 46.5 mm long, with end faces polished plane and parallel. The broadband light is absorbed by the Neodymium ions, which are then promoted to an excited state. Laser operation at this point is inhibited by the active Q-switch (Lithium Niobate), which acts to prevent feedback within the laser cavity.

At the point of maximum population inversion (i.e. maximum proportion of excited atoms), approximately 80 μs after the flashlamp pulse begins, the Q-switch capacitor (5) is discharged, switching the voltage across the Q-switch (6) from zero to -3 kV in around 75 ns. Feedback (i.e. stimulated emission) can then occur, and the Neodymium ions transition to a lower state, releasing the energy built up within the laser cavity in a single pulse at a wavelength of 1061 nm, approximately 12 ns in duration with an energy of around 100 mJ. The radiant efficiency is approximately 1% for a flashlamp-pumped system as described here, rising to approximately 10% for laser diode-pumped system.

3.1.2. Fibre Optic Coupling and Transmission

The laser pulse exits the laser cavity through the output coupler (7), typically 20% transmission (a compromise between optical efficiency and the desired pulse duration), and is separated into an array of multiple images by the micro-lens array (8). A short focal length (15-20 mm) plano-convex primary lens (9) (selected for reduced spherical abberations), placed before the focal plane of the micro-lens array, focuses the multiple images to a single spot at the focal plane of the primary lens. This arrangement produces a uniform spatial energy distribution at the entrance plane of the optical fibre (10), with a spot size of around 80% of the fibre core diameter, typically 300-400 μm (to allow for tolerances). The cone angle of the focused pulse (a function of the beam diameter and primary lens focal length) is less than the acceptance angle of the fibre (to allow the pulse to be efficiently coupled into the fibre), but higher than that of a simple lens injection method.

The pulse is guided through the fibre by total internal reflection between the fused silica core and the fluorine-doped silica cladding. Any bends in the fibre routing promote the population of higher-order modes (light paths that travel at a higher angle relative to the fibre axis. High order modes result in a uniform energy distribution at the fibre exit plane due to superposition of the modes, desirable for the flyer launch process. The optical fibre can transmit light within a characteristic angle, typically described by the numerical aperture (a function of the refractive indices of the core and cladding). Light that exceeds this angle escapes the fibre and is lost.

The laser pulse exits the fibre at the exit face (or plane), which is separated from the fused silica window, or substrate (12) by a spacer (11), typically 75 μm in thickness. If the fibre and window were in intimate contact,then theoretically there would be no Fresnel reflections at this interface. However, the non-perfect surface of the fibre and window will result in regions of locally increased fluence, due to constructive interference between the reflections from each interface. The seperation maximises the uniformity of these reflections, minimising the riskof optical damage.

3.1.3. Flyer Launch and Acceleration

The laser pulse is transmitted by the fused silica window (12), and is incident upon the interface between the window and the multi-layer coating deposited upon the far side (relative to the optical fibre) of the window.

The multi-layer coating (13) is comprised of four layers, as shown in Figure 13. Firstly, a thin layer (10-50 nm) of titanium, which acts to effectively absorb the laser pulse. Secondly, a layer of aluminium (100-500 nm), which forms the bulk of the plasma (also known as an ablation layer). Thirdly, a layer of aluminium oxide (100-500 nm), which insulates the fourth layer from the plasma (by virtue of a low thermal conductivity). Fourthly, a layer of aluminium (3000-10000 nm), which forms the final flyer plate and impactor.

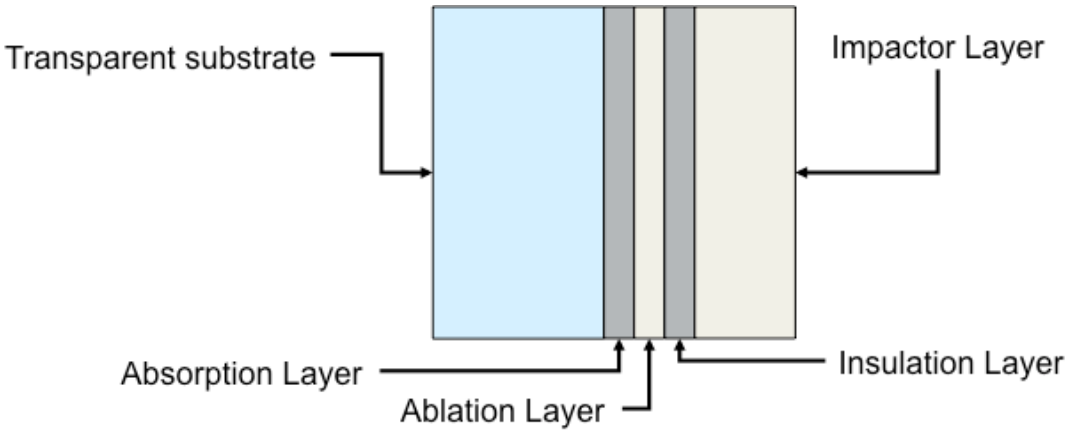

Figure 13 - Illustration of multi-layer coating on transparent substrate

The laser pulse is absorbed by the absorption layer, causing rapid heating, vaporization and ionization. The resulting warm dense plasma begins to expand, whilst heating, vaporizing and ionizing the silica window and the ablation layer. The expansion of the plasma accelerates the remainder of the coating away from the window as a flyer plate, across an air gap defined by the barrel (14), typically 50-200 μm in length. The flyer reaches a velocity of 3-5 $km.s^{-1}$ in around 20-30 ns, with a total flight time of around 50-75 ns.

3.1.4. Explosive Initiation

The flyer plate impacts the explosive pellet (15), imparting a shock wave propagating into the explosive with an initial pressure of 20-30 GPa. The shock imparted to the explosive initiates decomposition within the explosive, resulting in the release of energy, which acts to reinforce the shock. This process accelerates until complete decomposition of the explosive occurs, resulting in a steady-state shock wave propagating through the explosive at a characteristic detonation velocity, given by the explosive material and density.

A shock is also generated within the flyer plate, which upon reflection from the free rear surface of the flyer plate, moves in the same direction as the initial shock wave in the explosive, as a rarefaction wave. This moves faster through the material compressed by the initial shock, and begins to attenuate the shock. The initial pressure is maintained for around 500-1000 ps, and if the explosive has not transited to a steady-state detonation

when the rarefaction wave begins to attenuate the initial shock, the transition to detonation can be delayed or fail entirely.

A summary of the function of a laser detonator system is shown in Figure 14.

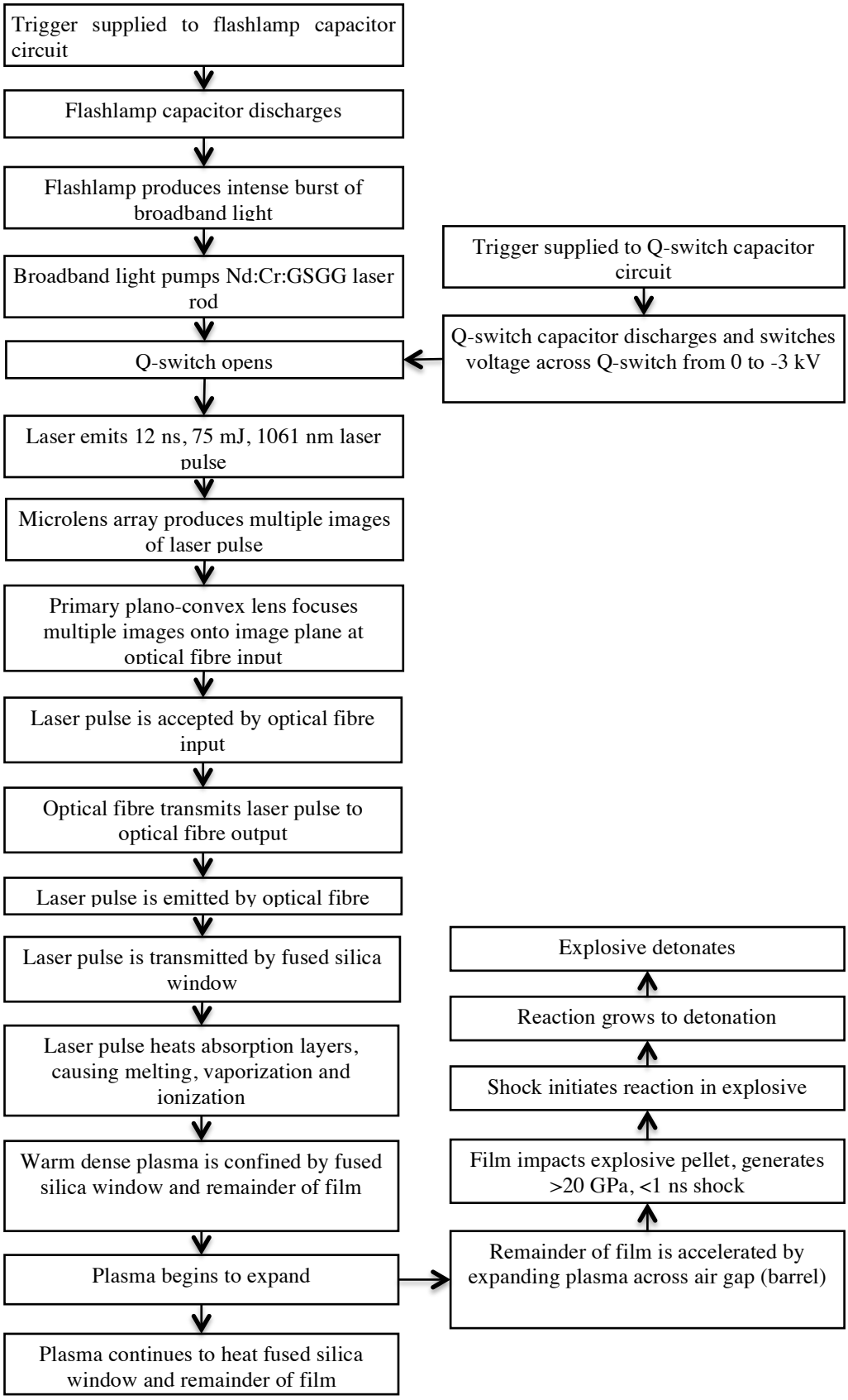

Figure 14 - Summary of functional description

3.2. Typical Experimental Configuration

The experiments reported here can be separated into three distinct types. Firstly, those investigating the coupling of the optical energy into, and subsequent transmission by, the optical fibre. Secondly, the launch of the flyer plate, focusing on flyer velocity, planarity and integrity. Thirdly, those investigating the explosive initiation and output. Common to both experiments is the need to couple the laser energy into optical fibres. To aid the reader's understanding of this thesis, a description of each experimental type and the configuration used is presented. Where significant deviations from these descriptions occur, this is detailed in the relevant section.

A variety of Nd:YAG (yttrium aluminium garnet, doped with neodinium ions) lasers were used, operating at the fundamental wavelength of 1064 nm. These had maximum pulse energies ranging from 50 mJ to 400 mJ, and pulse lengths, tuneable by flashlamp energy, of 8-14 ns.

Where axes are referred to, the Z axis corresponds to the propagation direction of the laser, the X axis is horizontal, and the Y axis is vertical, as shown in Figure 15.

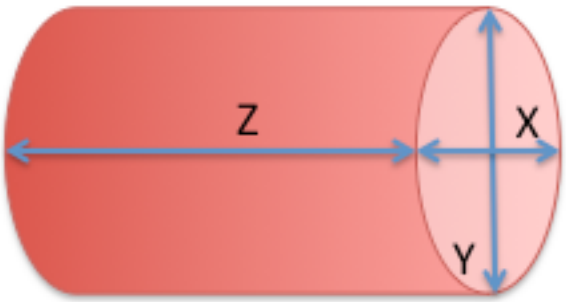

Figure 15 - Optical axes

Certain laser diagnostics are used throughout all experiments. These are detailed here to ease the reading of subsequent sections.

3.2.1. Imaging of Laser Beam

A Dalsa CCD camera, connected to a desktop PC running Spiricon beam profiling software was used to image the beam profile. This produces a spatial map of beam intensity and allows the uniformity of the beam to be measured. It can be used both on raw (unfocussed) laser beams, focussed beams and fibre outputs. For measurement of focussed beams and fibre outputs, a 40x microscope objective was used to image the beam. For measurement of unfocussed laser beams, the beam was imaged directly onto the CCD sensor. Neutral density (ND) filters were used in all cases to reduce the optical intensity below the level at which damage to the sensor would occur. Figure 16 illustrates a typical beam profile, as measured at the laser output.

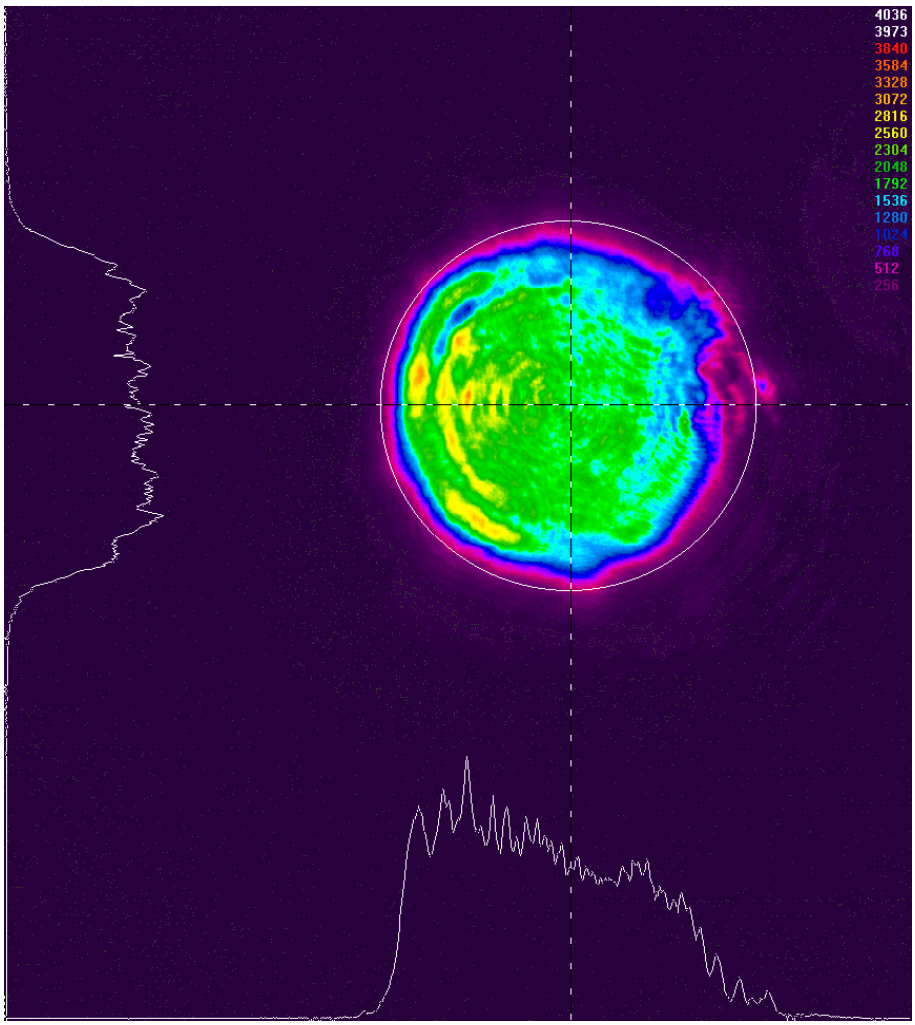

Figure 16 – Typical laser beam spatial profile measured at laser output

3.2.2. Measurement of Laser Energy

Ophir 3A-P thermal sensors were used to record the laser pulse energy. These measure energy by recording the voltage produced by the temperature differential between a "cold" thermopile junction and a "hot" thermopile junction upon which the laser energy is incident. The thermal sensors were connected to either a Ophir Laserstar energy meter, a standalone meter capable of displaying the energy incident upon two thermal sensors, or a Ophir Pulsar interface connected to a desktop PC running Ophir Starlab software, allowing the recording of the energy incident upon up to four thermal sensors.

3.2.3. Measurement of Laser Temporal Profile

Laser pulse width was measured using silicon photodiodes with a bandwidth of approximately 1 GHz, the output of which was recorded using Tektronix digitising oscilloscopes. These were located where a small amount of laser light scattered from optical elements could be recorded. For experiments that did not use Photonic Doppler Velocimetry (PDV), DPO7104 oscilloscopes were used with a bandwidth of 1 GHz and a sampling rate of $5x10^{9}$ samples.s.$^{-1}$ For experiments using PDV, DPO71254 and DPO71604 oscilloscopes were used, with bandwidths of 12 GHz and 16 GHz respectively, and sampling rates of 50-100 GS.s^{-1} (dependant on the number of channels used).

3.2.4. Triggering and Syncronisation

Stanford DG535 or DG645 delay generators were used to trigger the lasers and diagnostics, ensuring accurate timing and synchronisation of experiments. These provide 4-8 channels of variable voltage trigger outputs, with adjustable delays between outputs, and sub-ns jitter (variability) between outputs.

3.2.5. Laser to Fibre Coupling

This section details the experimental configuration used for most flyer and explosive experiments. Optical fibre coupling experiments used a variety of methods to focus the laser beam into the optical fibre; these are discussed separately. The typical experimental configuration used to fibre coupling is shown in Figure 17.

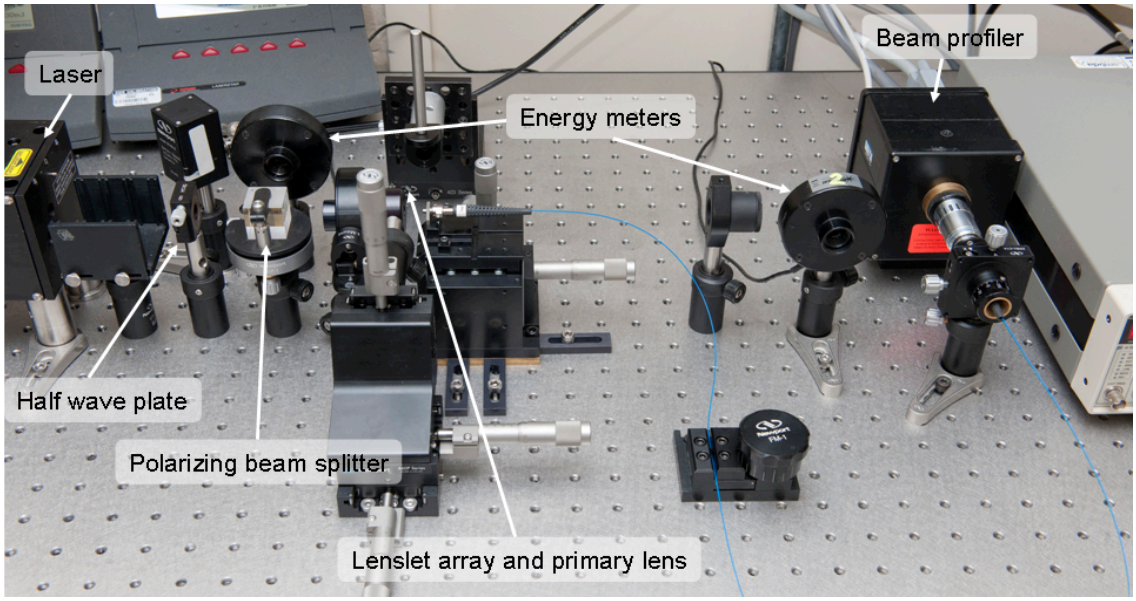

Figure 17 – Typical experimental configuration used for fibre injection

A half wave plate was used in conjunction with a polarising beam splitter cube to attenuate the laser energy without affecting the beam profile. As the lasers were linearly polarised, rotation of the half wave plate rotated the polarisation axis and varied the split ratio between the two outputs of the beam splitter cube.

Thermal energy sensors were positioned at the two outputs of the beam splitter cube to record the reflected and transmitted energies. The thermal energy sensor on the transmitted output was mounted on a kinematic "flip" mount to allow it to be removed from the beam path.

A micro-lens, or lenslet array was used with a 19 mm focal length lens to obtain a beam diameter of 320 μm, approximately 75-80% of the fibre core diameter to prevent inadvertent exposure of the fibre cladding and jacket to the laser beam. The microlens array produced multiple images of the incident beam, which were then collapsed to a

single focussed spot by the primary lens. The spatial intensity uniformity of the focussed spot was relatively independent of the spatial intensity profile of the incident beam. The focussed spot is shown in Figure 18. A improvement in uniformity can be observed, relative to Figure 16.

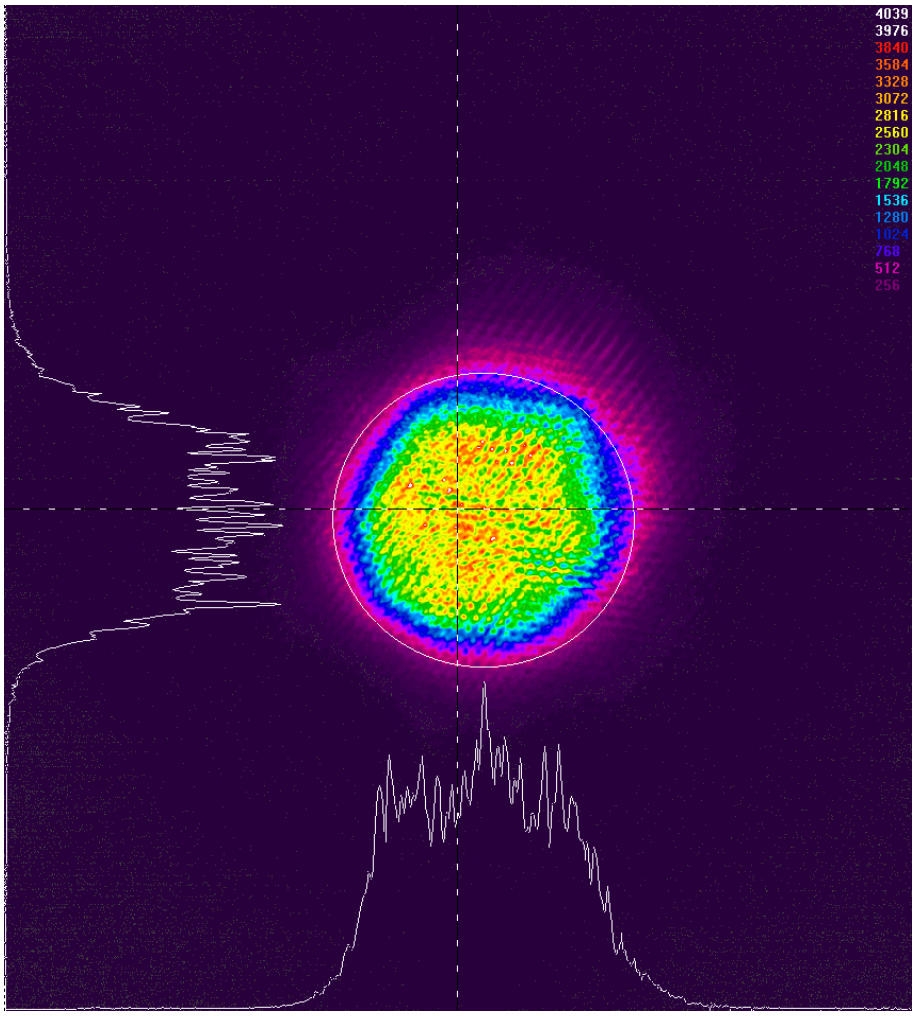

Figure 18 - Beam Focussed with Lenslet Array

The optical fibre was aligned to the focussed spot in several stages.

Firstly, the laser pulse was attenuated using ND filters, and a coherent fibre bundle, consisting of approximately 10,000 single mode optical fibres, placed at the image plane of the primary lens. The bundle transmitted an image from the input face to the output face, which allowed the beam profiling system to be remotely located from the image plane. The beam profiling system was then used to image the spatial uniformity of the pulse at the output face of the bundle, corresponding to the spatial uniformity at

the image plane of the primary lens lenslet array. A 3-axis fibre alignment stage was then used to align the bundle with the focussed spot at the image plane i.e. along the propagation axis of the laser pulse.

Secondly, the bundle was replaced with the test optical fibre, and coarsely aligned using the 3-axis stage to maximise the intensity recorded by the beam profiler at the fibre output.

Finally, the ND filters were removed, the output of the fibre connected to the thermal energy sensor, and the fibre finely aligned to the focussed spot by adjusting the 3-axis stage to maximise the transmission efficiency of the fibre. This was performed with an incident energy of approximately 5 mJ, to minimise the possibility of damage to the fibre. A typical beam profile is shown in Figure 19. It can be seen that the beam profile exhibited a high degree of spatial intensity uniformity.

The half wave plate was adjusted to obtain the desired transmitted energy required and three measurements made of the energy transmitted through the fibre. The energy recorded for the experiment was taken as the average of these three measurements. The output of the fibre was then connected to the relevant experiment.

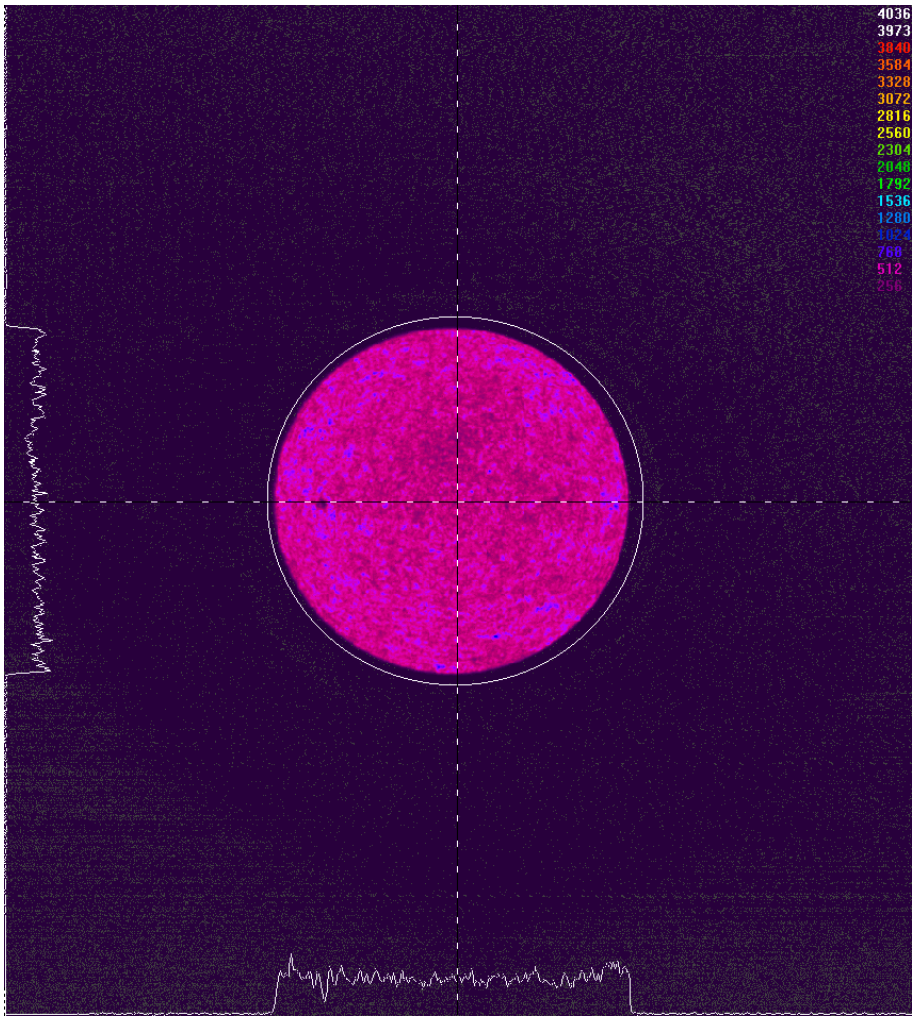

Figure 19 - Typical Output Beam Profile

3.2.6. Flyer Plate Studies

The optical fibre used to launch the flyer plate was connected to one of two fixtures. The first is shown in Figure 20, with a schematic in Figure 21. This fixture is known as the “Revolver”, as it allowed 6 flyer plates to be launched from a single 10 mm diameter coated substrate via an indexed mount. The Revolver was mounted into a gimbal mount with θX and θY adjustment via a custom mount. This allowed the tip and tilt of the flyer plate relative to the probe beam to be adjusted without translating the flyer plate.

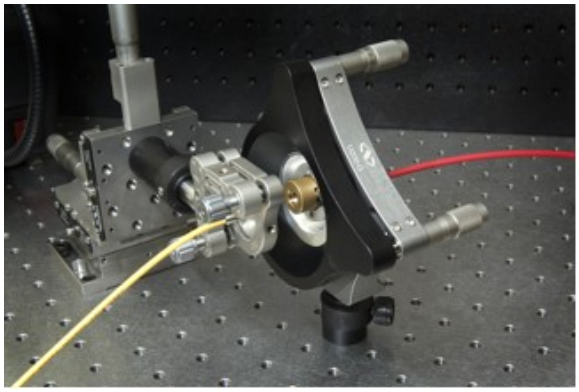

Figure 20 - Flyer Launch and Probe Assembly

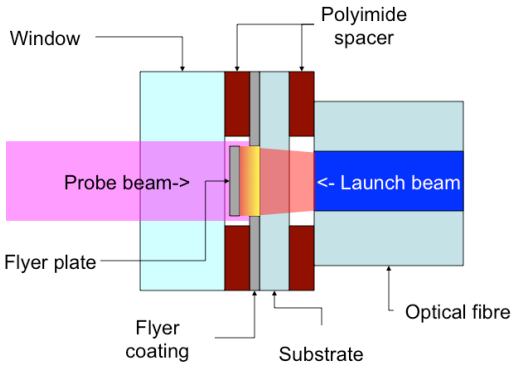

Figure 21 - Probing Schematic

Photonic Doppler Velocimetry (PDV) was used to measure the flyer plate velocity. The development of the PDV systems used in this study is reported in Chapter 4:and is not discussed further in this section.

A single mode PDV fibre collimator, connected to the PDV system, was mounted into a stage with X, Y and Z adjustment. This allowed the probe beam to be aligned relative to the flyer, by removing the substrate, and aligning the probe beam to the launch fibre. A phosphor card (to image the IR probe beam) was placed at the opposite end of the launch fibre to achieve this.

The PDV fibre collimator produced a collimated beam of approximately 0.250 mm diameter, a good match to the flyer size. The collimator was placed as close as possible to the flyer, to maximise the collection efficiency of the reflected beam. The flyer was impacted into a 5 mm thickness polymethylmethacrylate (PMMA) window. This both protected the collimator from damage and provided a definite end point, allowing validation of the data obtained, by comparison of the measured flyer displacement to the measured separation of the initial flyer position and the impact window.

Once assembled, the tip and tilt of the flyer assembly was adjusted to ensure the specular reflection from the flyer was not aligned with the probe. As the flyer was believed to change from a specular reflector to a diffuse reflector during the launch process, this ensured a consistent return signal.

This experimental arrangement is also used to investigate the flyer planarity and integrity. Adiabatic compression of the air between the impacting flyer and the window produced an intense flash of light, which was recorded using an Optronis SC-10 streak camera, typically operating at a sweep speed of 10 $ns.mm^{-1}$. A GEC diode laser operating at 100 MHz (one pulse every 10 ns) provided a calibration source in case of a nonlinear sweep speed. A typical impact is shown in Figure 22 with pertinent features labelled. In this shot, a portion of the Nd:YAG laser beam was separated prior to injection into the optical fibre used to launch the flyer plate, frequency-doubled to 532 nm using a KD*P (potassium dideuterium phosphate) crystal and imaged onto the streak camera to record the launch time of the flyer plate.

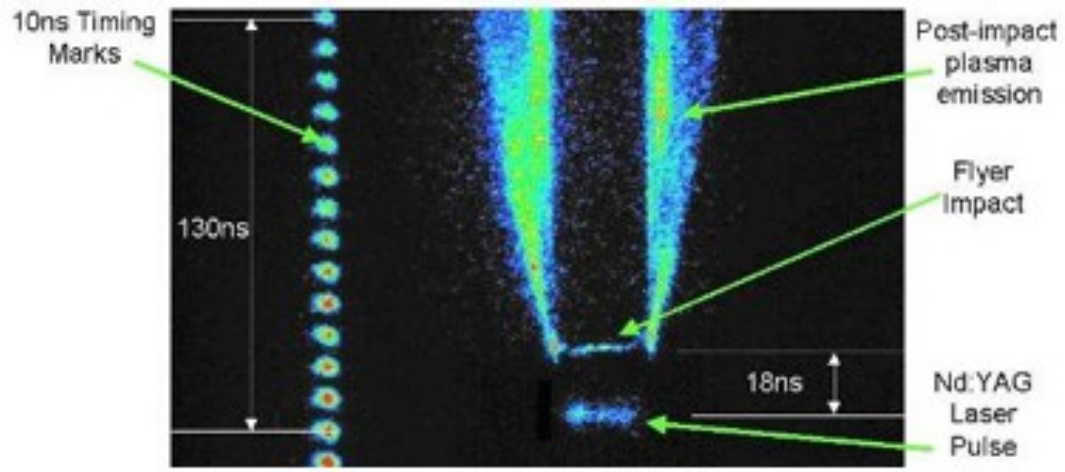

Figure 22 - Flyer Impact

Figure 22 indicates that the flyers produced by this system are extremely planar, with a variation in impact time across the flyers of less than one nanosecond, corresponding to a positional variance of 3-5 μm across the flyer plate. Earlier experiments indicated a direct correlation between fibre output profile and flyer planarity, and hence it is important to ensure a uniform beam profile across the fibre output.

The second fixture was an evolution of the Revolver fixture, and was dubbed the Minigun, as it allowed a large number (10-20) of flyers to be launched from a single 10 mm diameter substrate, shown in Figure 23. The launch fibre was secured in a fibre fixture, aligned vertically, and a focussing single mode PDV fibre probe with a 30 mm focal length, was located 30 mm above the launch fibre face. This probe was specified

to produce a 55 μm diameter focussed spot. The substrate, coated with the flyer, was then simply placed over the output of the launch fibre. The tip and tilt of the PDV probe was then adjusted, as before, ensuring the specular reflection from the flyer was not aligned with the probe. The substrate was then removed, and the launch fibre aligned with the PDV probe by translating in the X and Y axes (where Z is the direction of light propagation) using a visible laser coupled into the PDV probe. The substrate was then replaced.

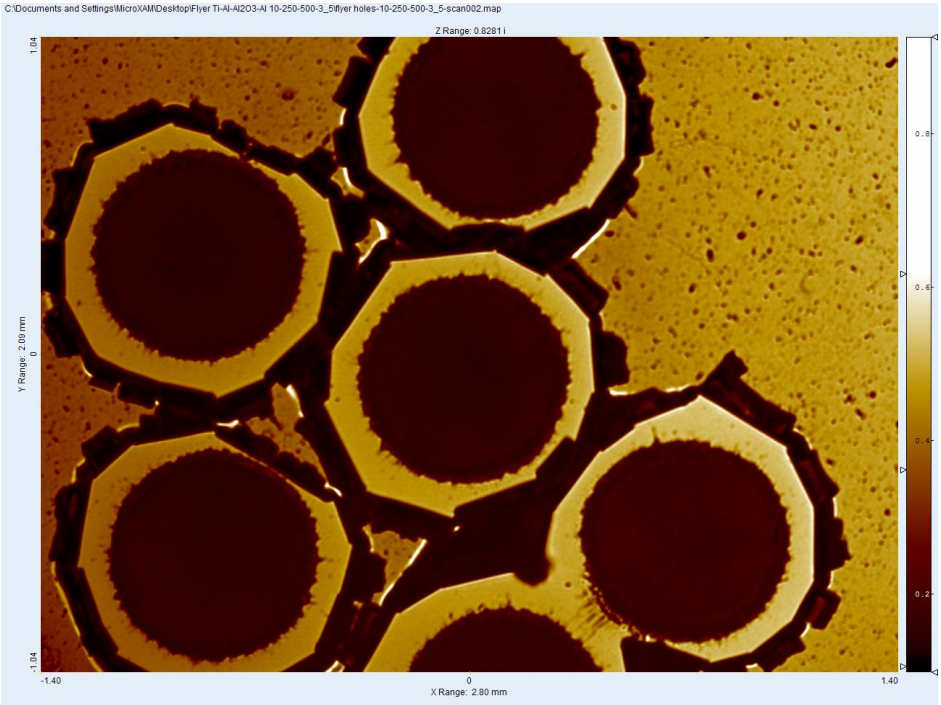

Figure 23 - Multiple flyer plates launched from the Minigun fixture

For simple flyer velocity measurements, the flyer was launched into free space. Degradation of the PDV probe performance was observed after a few dozen shots due to deposition of the flyer material onto the probe.

To measure the duration and amplitude of the shock generated by the flyer impact, a spacer was placed onto the substrate, and a lithium fluoride (LiF) window was placed onto the spacer, ensuring a known separation between the flyer launch position and the LiF impact window. The LiF window was aligned with the [100] crystal plane perpendicular to the flyer impact. LiF is a transparent material with a well-characterised U_s-U_p (U_s is shock velocity, U_p is particle velocity) relationship for pressures in excess

of 100 GPa. By impacting the flyer into a window with known behaviour under shock loading, and monitoring the motion of the interface formed between the flyer and the window, the amplitude and duration of the pressure pulse generated in the LiF window could be determined, using the Rankine-Hugoniot relations.

The LiF windows used were 25 mm diameter, 2 mm nominal thickness, with a 2 degree wedge between front and back faces, to eliminate spurious reflections from the back face, and an anti-reflection coating on the front face, impacted by the flyer, again to eliminate spurious reflections from the front face prior to flyer impact.

3.2.7. Explosive Initiation

A standard test body was developed for explosive testing, injection moulded from Nylon 12, shown in Figure 24. This test body allowed prototype detonators to be easily assembled without complex tooling.

The optical fibre is coupled to the test body using a standard ST connector. A coated substrate was then placed over the fibre end, separated by a 75 μm thickness polyimide spacer. A polyimide barrel separated the coated substrate from the explosive pellet. A 1 mm diameter PMMA optical fibre was proximity coupled to the output face of the pellet to provide time-of-arrival data. A digitizing oscilloscope recorded the output of a photodiode located prior to the launch fibre and a photodiode connected to the PMMA fibre. This provided a record of when the laser pulse arrived at the detonator, and when the pellet detonated. From this, the function time of the detonator can be calculated.

Approximately 10-15 shots were performed for a threshold measurement; with the threshold energy calculated using the Langlie or Neyer method.

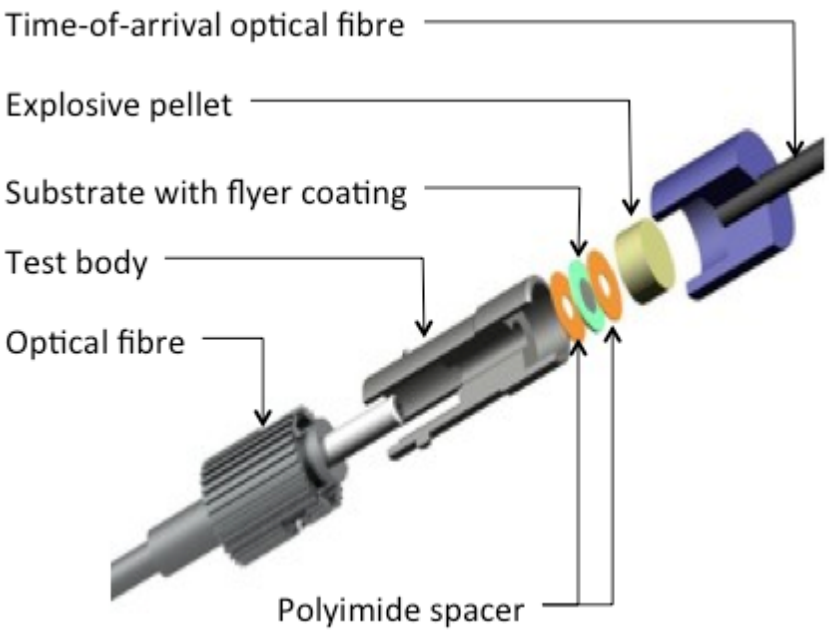

Figure 24 - Illustration of Explosive Test Fixture

CHAPTER 4: DEVELOPMENT OF A PHOTONIC DOPPLER VELOCIMETER

Initiation train development, especially detonator design, requires the capability to measure velocities in excess of 5 $km.s^{-1}$, on objects typically less than 1 mm in diameter, such as laser-driven flyer plates (see Section 2.3). These velocities are reached in times as short as 20 ns. This presents a significant challenge. Historically laser velocimetry has been the only practical method to achieve this.

VISAR [67] (Velocity Interferometer System for Any Reflector) and its higher time resolution sibling, ORVIS [68](Optically Recorded Velocity Interferometer System), is the most widely used method. It typically uses a single line, single mode, Nd:YAG laser operating at 532 nm, with several watts of power. An optical fibre is used to deliver the laser light, with a second fibre being used to collect the scattered light from the surface of interest. This return light is then split, one half delayed, and then recombined. If the target is moving, the difference in frequencies between the delayed and non-delayed light produces interference. From the frequency produced, the velocity of the surface can be calculated. As the return signal is interfered with a time-shifted version of itself, relatively low frequencies for a given velocity are produced. VISAR & ORVIS cannot resolve multiple velocities, and for a target containing a spread of velocities, an average velocity is recorded. Due to their size, VISAR & ORVIS systems are not easily portable, and the free-space optics employed can be liable to misalignment.

Strand et al [69] reported a new type of velocity interferometer in 2004, based upon the heterodyne principle. The Photonic Doppler Velocimeter (PDV) is contained entirely within fibre, except where the beam is incident upon the surface of interest. This allows for an exceptionally portable and robust system; the entire system, including laser, oscilloscope and interferometer, is mounted within a commercially available compact, shock-mounted 19” width rack enclosure.

The system relies upon the interference between the original beam and the return beam. This produces a higher frequency for a given velocity than other methods, but electronic technology is now sufficiently mature to resolve these frequencies.

Figure 25 shows the velocimeter concept. The fibre-coupled laser is connected to a circulator. This device has the property of separating bi-directional light, which allows the return light to be separated from the original light. Of course, a portion of original light is required to interfere with the return light, and this is obtained from the back-reflectance of the probe. This is then matched to the return light intensity from the experiment. The interference between original and return beams is measured by a high-bandwidth photodiode, connected to a digitizing oscilloscope.

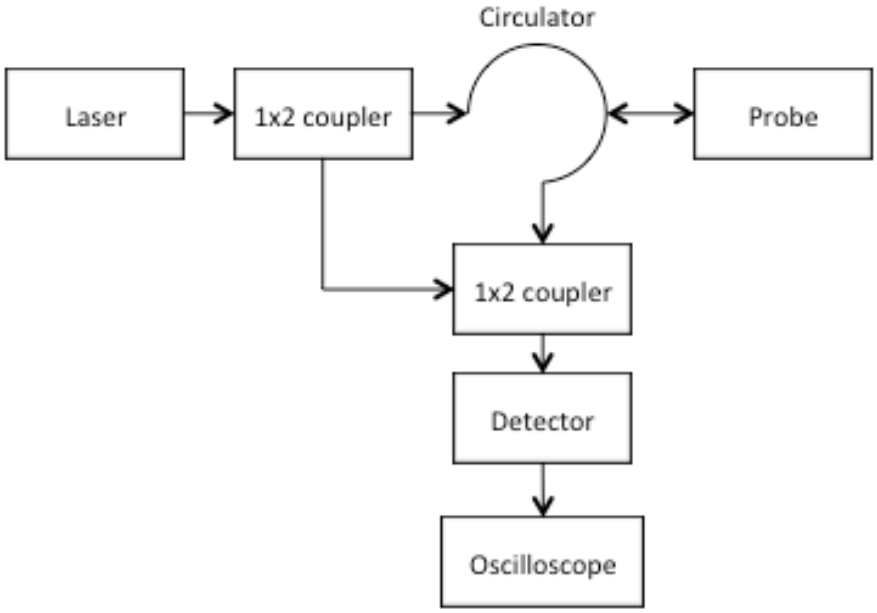

Figure 25 - PDV Concept

A PDV system has several advantages over more traditional methods of velocimetry. It is capable of resolving multiple velocities simultaneously. Further, as it is constructed from standard telecommunications optical fibre components, it is relatively inexpensive, with a cost per channel of approximately £20,000 (including laser and oscilloscope) for a 4 channel high-bandwidth system as presented here. For comparison, a VISAR system typically costs £50,000 per channel (excluding laser and oscilloscope).

A full description of the physics of PDV is given in Annex A.

4.1. System Design and Construction

4.1.1. 4 Channel PDV System

Strand's original design [69] was been modified to better suit the requirements. The reflectivity of laser-driven flyers tends to drop substantially during the flyer launch process [70], so the amount of light returned to the interferometer must be maximized. Additionally surfaces of varying reflectivity are investigated, and hence it must be possible to vary the level of the reference signal, to balance the return signal.

An NP Photonics fibre laser was used, operating at 1550 nm with a power of 2 W. This was specified with a line width of <3 kHz, resulting in a very clean signal. This was coupled to the interferometer chassis using a standard single-mode optical fibre.

A 1:4 splitter was used to split the laser power four ways, driving a 4-channel system with a nominal power of 500 mW per channel. All components after this splitter are duplicated on a per channel basis, as shown in Figure 26.

The reference signal was obtained from a 10%/90% split ratio coupler inserted prior to the circulator. This then passed through an attenuator before being combined with the return signal after the circulator by a 2:1 coupler. This allowed the level of the reference signal to be tuned on a shot-by-shot basis. This modification has since been reported in the literature, though the implementation reported here is believed to be the first reported [71]The probe design was also optimised for maximum efficiency, in comparison to the relative inflexibility of the original PDV.

A fibre optic power meter was used to monitor the level of the return signal, allowing for optimal probe alignment. This was located between the circulator and the 2:1 coupler.

The interferometer was mounted into a 19" rack enclosure, approximately 8" in height. This contained the fibre optics, the power meter, the displays for the power meter, and all electronics. All fibres were single-mode, employing angle-polish FC/APC connectors to minimize back-reflectance. The components used in the system are

commercially available, excepting some of the mounts used to secure components inside the interferometer chassis.

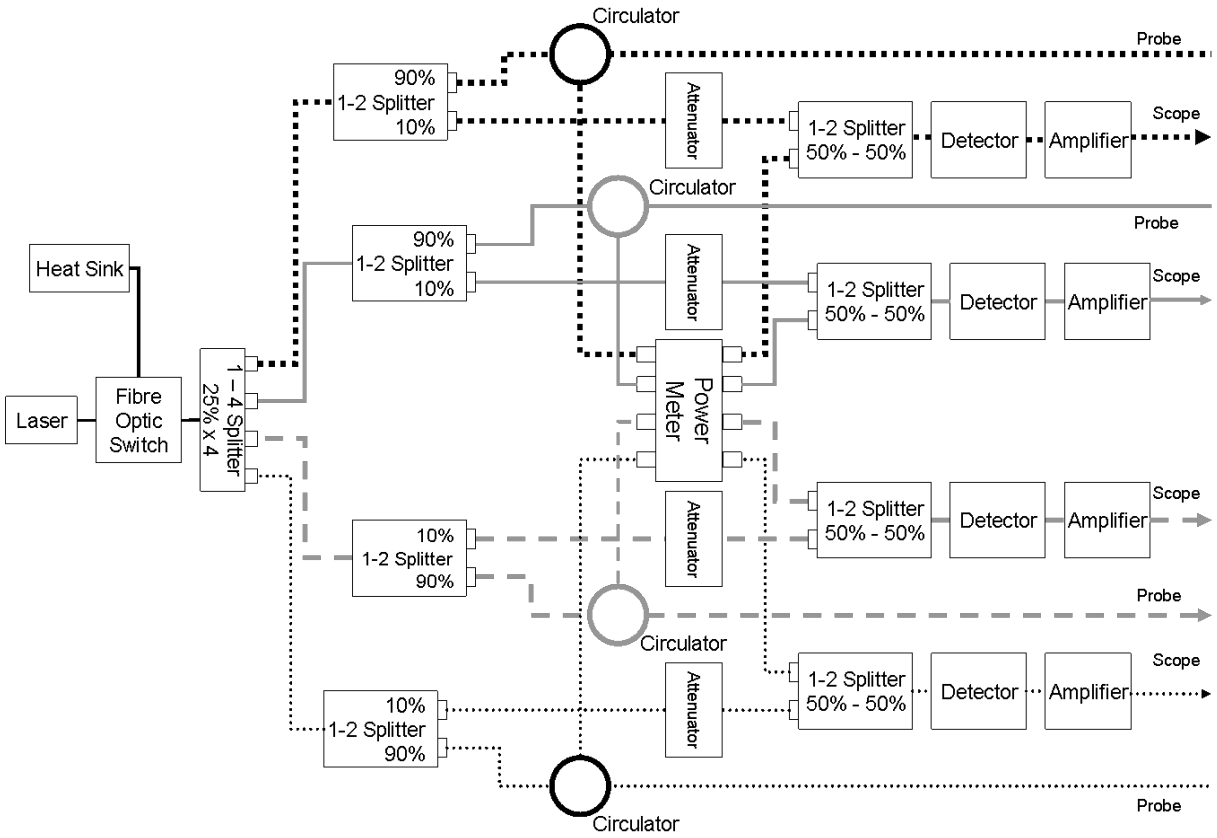

Figure 26 - System Schematic

4.1.2. Optically Upshifted PDV System

A recent modification to PDV replaces the reference signal, originally obtained from a portion of the probe laser, with a separate reference signal obtained from a second laser [72]. This laser is set to a frequency differing from that of the probe laser, resulting in the signal being shifted to a differing frequency. In the original PDV implementation, the signal increases from zero frequency. By optically-upshifting the signal to a higher frequency, typically 2-8 GHz, the low frequency noise floor can be avoided. Additionally, it is now possible to resolve directional velocity as opposed to absolute velocity magnitude. The data is analysed as discussed previously, with the exception that the upshifted-frequency must be subtracted to give the true velocity. A schematic of an optically upshifted PDV system is shown in Figure 27

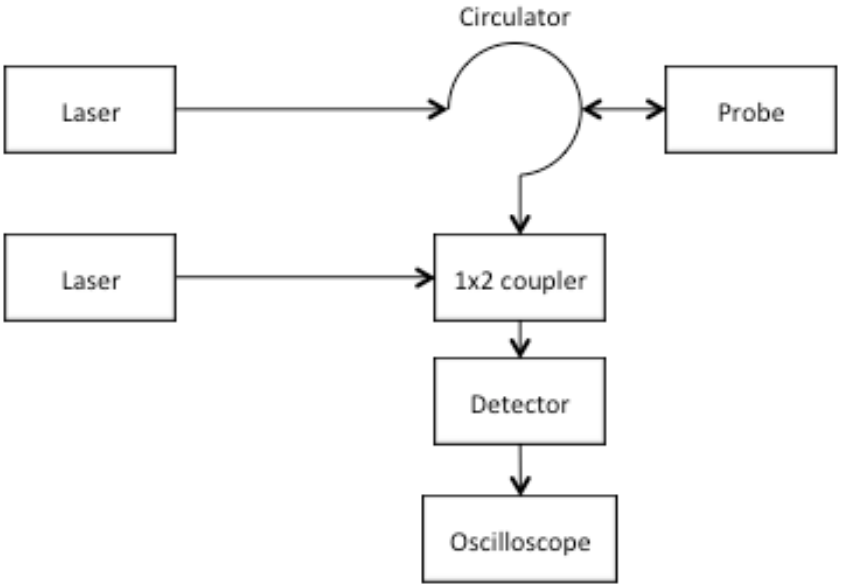

Figure 27 - Optically-upshifted PDV concept

A single-channel, compact, optically-upshifted PDV system was constructed specifically for flyer velocity measurements. This system was much simpler than the 4-channel system constructed previously and essentially identical to the concept shown in Figure 27.

An NP Photonics Rock laser, with a power of 150 mW and a linewidth of >3 kHz was used for the main laser. An NP Photonics Rock laser, with a power of 25 mW and a linewidth of >3 kHz was used for the reference laser. The reference laser was thermally-tuned to a frequency 2-8 GHz less than that of the main laser, resulting in the signal being upshifted by this offset.

The return signal and reference signal were combined using a 10%/90% split ratio coupler, with the resulting signal comprising 90% of the return signal and 10% of the reference signal. Given the greater power of the reference signal to the return signal, this resulted in a reference to return ratio of 10-100:1 at the detector. Miteq DR-125G-A 12.5 GHz bandwidth fibre optic receivers were used to convert the optical signal to an electrical signal, and Tektronix oscilloscopes (models DPO71254C, DPO71604B and DPO71604C) with a bandwidth of 12.5 to 16 GHz were used to record the signal.

This configuration was implemented in 2010 and has been used on all experiments since then.

4.2. PDV Data Analysis

The recorded signal is simplistically a time-varying sine wave, and must be processed to yield velocity information. The signal was analysed using SIRHEN [73], an analysis routine implemented in MATLAB, kindly provided by Daniel Dolan (Sandia National Laboratories). An example signal is shown in Figure 28.

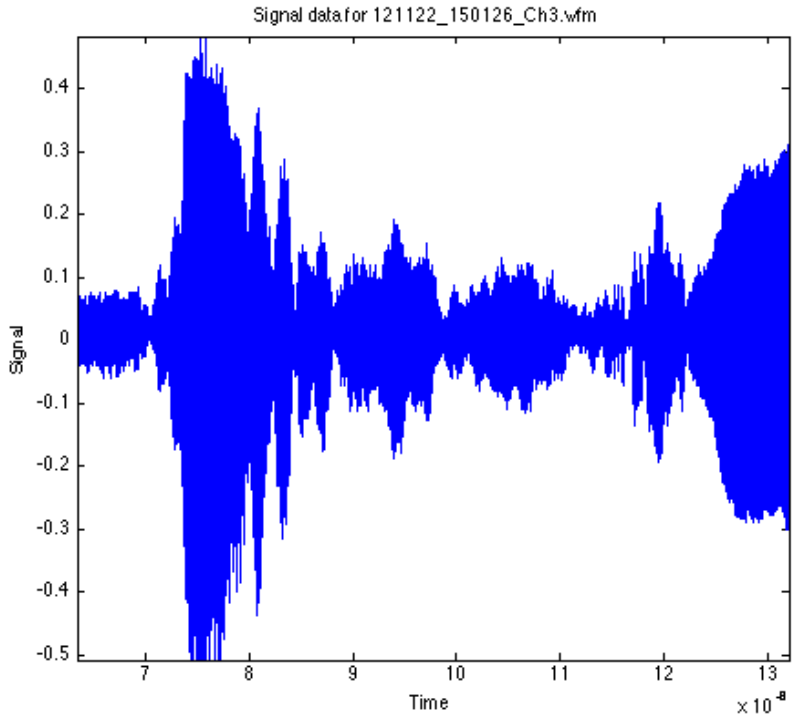

Figure 28 - Example PDV signal

The signal was analysed using a Short Time Fourier Transform (STFT). The STFT operates by breaking a time resolved signal into a number of fixed width subdivisions. Each subdivision then has a window function applied to it, and is then Fourier transformed, yielding frequency component data. The STFT results in a series of windows, each spanning an equal subdivision of time, each containing frequency data for that subdivision. The highest power frequency component, in a well constructed and diagnosed experiment, will be the Doppler shifted frequency of the target reflector. The

output of the SFFT is viewed in the form of a spectrogram, a frequency-time-power plot. An example spectrogram is shown in Figure 29.

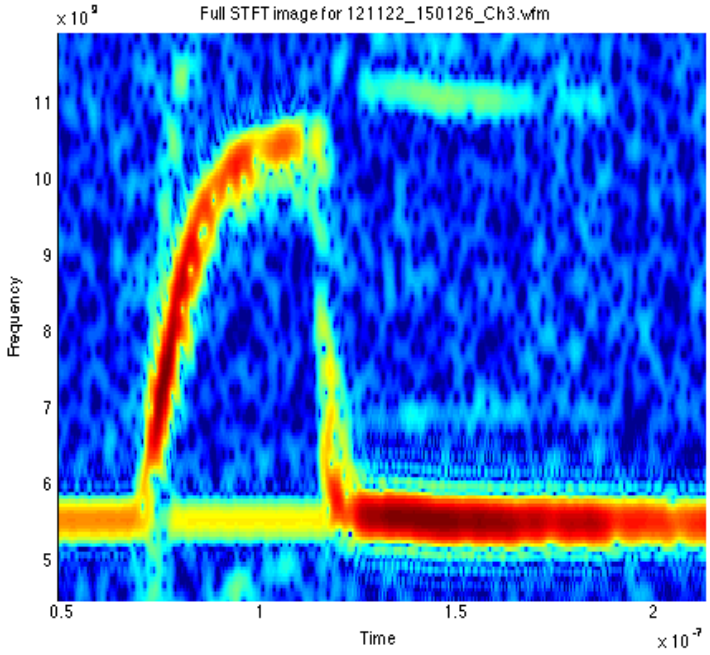

Figure 29 - Example spectrogram of PDV data

A centroid integration routine is then used to extract the peak frequency for each time window. The analysis process is illustrated in Figure 30. The resulting peak frequency vs. time data is then converted to velocity vs. time.

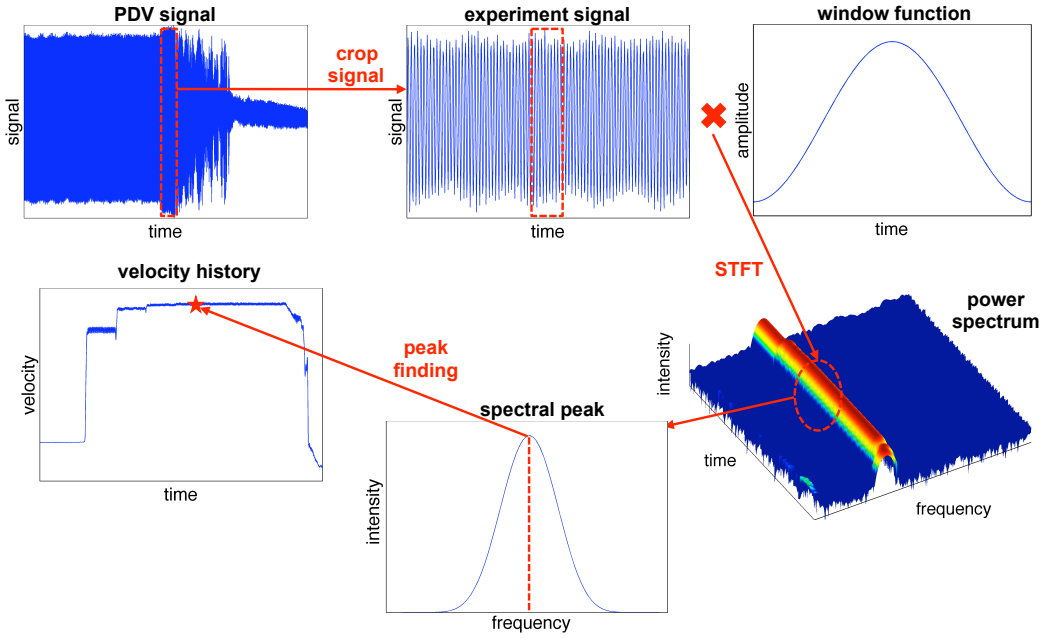

Figure 30 - Summary of SIRHEN PDV analysis process [73]

Photonic Doppler Velocimetry was used to measure all velocities reported in this investigation, with the majority of the resulted obtained using the optically upshifted system reported in Section 4.1.2

CHAPTER 5: OPTICAL FIBRE COUPLING AND TRANSMISSION

5.1. Introduction to Optical Fibre Coupling and Transmission

An integrated and optimised optical fibre for a laser detonator has not been reported in the literature. This chapter aims to develop such a fibre, whilst investigating the processed involved in the coupling into, and transmission by, the optical fibre. An understanding of several parameters are critical to this aim.

5.1.1. Fibre Coupling

There are two different methods of coupling high power laser pulses into optical fibres. The first entails the direct focusing of the laser beam into the optical fibre by a lens system: therefore, the power density required at the input face is more than or equal to that of the output face. In the second method, an optical fibre taper is positioned between the lens system and the delivery fibre. This taper may be part of the delivery fibre or a separate fibre. A tapered optical fibre has a large input core diameter and a reduced output diameter and relies on the gradual narrowing of the optical fibre to concentrate the power density of the pulse. Thus the energy density needed at the input face to achieve the required energy density at the output face is reduced. These fibres have the potential to drastically increase the margin between firing energies and the damage threshold of the optical fibre.

5.1.2. Damage Threshold

The fluence that an optical fibre can transmit without damage is known as the damage threshold. It is typically measured in fluence, $J.cm^{-2}$, or intensity, $W.cm^{-2}$. Optical fibres can be damaged by high energy laser pulses in several ways. The laser pulse can ablate material from the input face of the fibre, resulting in plasma formation and a loss of transmission efficiency. Flaws in the surface finish of the fibre can cause localised focussing of the pulse, resulting in an increase in intensity which can initiate material ablation. Alternatively, contaminants can provide absorption sites for the laser energy. This generally results in permanent damage to the fibre face, reducing the damage threshold for subsequent pulses.

Once coupled into the fibre, bends in the fibre can couple energy into the cladding, where it can be absorbed, causing damage. This can cause mechanical failure of the fibre.

Fresnel reflections at the fibre output can increase the intensity of the laser pulse adjacent to the fibre output to above the damage threshold of the bulk material, resulting in material ablation and removal from the fibre output.

The damage threshold of the fibre must exceed the fluence required for reliable initiation of the explosive.

5.1.3. Transmission Efficiency

The transmission efficiency of an optical fibre is determined by a number of factors including surface finish (e.g. scratches, pits and flatness) of the input and output faces, levels of impurity in the fibre and chemical content. For short fibres, attenuation within the fibre may be neglected, and hence the theoretical transmission is limited by Fresnel reflections at each air/glass interface, approximately 4% at each, giving a theoretical maximum transmission of 92.2% for a single fibre.

5.1.4. Bend Radius

Optical fibres have a minimum bend radius to which they can be bent. Below this diameter, induced stress in the fibre can cause micro cracks, which can propagate and result in mechanical failure of the fibre. For a typical fibre, the minimum bend radius is approximately 40 mm [74].

Bends in optical fibres can also reduce the transmission efficiency, due to higher order modes, which propagate through the fibre at higher angles, exceeding the critical angle for total internal reflection and escaping the fibre core.

5.1.5. Spatial Profile

In conventional flyer plate initiation of explosives the thresholds increase with flyer curvature, as a curved flyer reduces the area over which a uniform shock is imparted. The planarity of a laser driven flyer is determined by the spatial energy distribution

across the beam profile. Energy hot spots within the beam profile will result in rippling of the flyer and possibly flyer break up [70].

Uniform beam profiles can be generated by a number of means including using multimode lasers, incorporating optical fibres of several metres or introducing ~100 mm diameter coils into the fibre. These have the effect of promoting the higher order modes within the fibre, causing an increased uniformity in the beam profile. The beam profile is generally measured by imaging the beam using a CCD camera coupled to beam profiling software. It is possible to quantify the spatial profile by a Top Hat Factor, defined as [75]:

$$F = \frac{\sum_{f=1}^{pk-1} \frac{E(f) + E(f+1)}{2}}{pk}$$

Equation 9

where: $E(f) = \sum_{i=pk}^{f} \frac{iN}{total}$ and E = the fraction of energy contained between the fluence value and the peak value, f = fluence, pk = peak fluence, $total$ = total energy, N = the number of pixels that have the value of I, F = the Top Hat factor. For a perfectly uniform profile, $F = 1$, referred to as a Top Hat profile, illustrated in Figure 31.

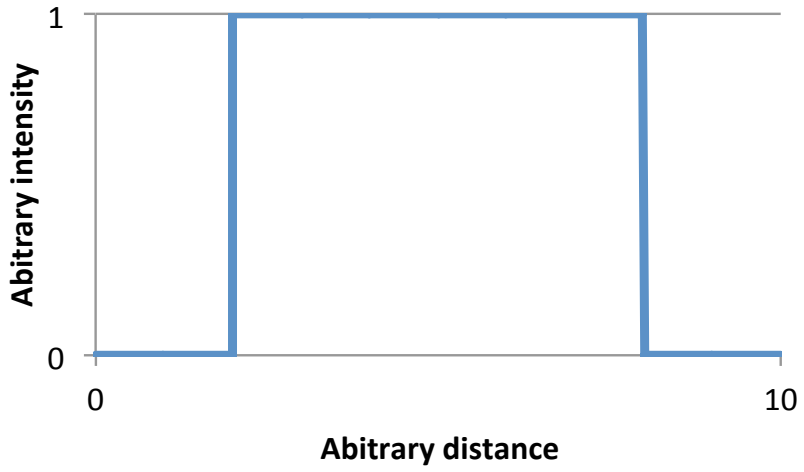

Figure 31 - Illustration of Top Hat profile

5.1.6. Axial and Radial Fibre Coupling

Optical fibres, by their design and transmission mechanism, lend themselves to being axially coupled into the detonator body: the light exits the fibre axially. However, this does constrain the detonator integration options as the optical fibre must enter the detonator from the rear. “Side fire” fibres are now commercially available and potentially provide the means to extend the integration options to provide compact detonator designs. “Side-fire” fibres have a bevel micro-machined onto the output face. This results in the beam exiting the fibre at approximately 90 degrees to the core. This offers a method for designing a laser detonator in which the fibre enters from the side, as opposed to the rear.

5.2. Optimal Polishing Methods for High Energy Optical Fibres

Energy densities in the region of 35 $J.cm^{-2}$ are required for initiation, significantly above the damage threshold of typical optical fibres (approximately 8 $J.cm^{-2}$ [76]). Laser-induced damage is typically caused by laser absorption at the input face due to imperfections in the surface polishing. The imperfections in the fibre face cause localization focusing, raising the energy density above the bulk damage threshold. This process induces plasma formation which can ablate the fibre face, degrading the quality of the finish and preventing successful transmission of the energy [77]. To successfully transmit energy densities of this magnitude, a high quality fibre end face finish is required.

To date, the majority of research has focused upon the injection method, with a wide variety of injection methods examined, from simple plano-convex lenses to diffractive optical elements and microlens arrays. Relatively little research has been published into the most suitable optical fibre polishing method. Setchell [13] compared the performance of flame polished, CO_2 laser polished and mechanically polished fibres, but the mechanical polish was not specified. High damage thresholds were reported for laser polished fibres, >70 $J.cm^{-2}$, but this polishing method is highly specialized and expensive. An economical, repeatable mechanical polishing method, suited to mass production is desirable.

Optical fibre assemblies for laser detonator research at AWE have been sourced from C Technologies Inc., NJ, USA for several years, using a standard steel ferrule and mechanical polish. It was observed during collaborative experiments [78] that fibre assemblies also manufactured by C Technologies, but with zirconia ferrules and a different polish, had a higher laser-induced damage threshold than the AWE fibre assemblies. This motivated the study of the effect of ferrule material and polishing method to determine the optimal polishing method for high energy optical fibres.

Fibre assemblies were prepared by C Technologies Inc., NJ, USA, with Innovaquartz FG365UEC optical fibre, using a variety of polishing methods (shown in Table 8, detailing the polishing material and grit size in microns. Particle shape and polishing medium i.e. grit or dry, were not known), and both steel and zirconia ferrules. Batches B & F are representative of the fibre assemblies used in the collaborative experiments. The quality of the fibre end faces was assessed using non-contact optical profilometry. The damage threshold for each polishing method was determined using a Q-switched Nd:YAG laser, and the optimal polishing method determined.

Batch	1st Step	2nd Step	3rd Step	4th Step	5th Step	6th Step	Polishing Method	Ferrule
A	3	1	0.5	0.1	0.05		Machine	Zirconia
	Diamond	Diamond	Diamond	Diamond	Aluminium Oxide			
B	15	9	6	3	1	0.3	Machine	Zirconia
	Diamond	Diamond	Diamond	Diamond	Diamond	Cerium Oxide		
C	15	2	0.3				Hand	Zirconia
	Diamond	Diamond	Cerium Oxide					
D	15	9	6	3	1	0.3	Machine	Steel
	Diamond	Diamond	Diamond	Diamond	Diamond	Cerium Oxide		
E	15	3	0.3				Hand	Steel
	Aluminium Oxide	Aluminium Oxide	Cerium Oxide					
F	15	3	0.3				Machine	Steel
	Aluminium Oxide	Aluminium Oxide	Cerium Oxide					

Table 8- Polishing methods investigated. Polishing media for each step is detailed, along with grit size in microns.

5.2.1. Assessment of Polish Quality

An ADE Phase Shift MicroXAM optical surface profilometer was used to examine the fibre end faces. This allowed quantitative analysis of the quality of the end face finish. 2D and 3D surface maps of the fibre end faces were obtained. This characterization was repeated both before and after the damage threshold testing.

The fibre under test was mounted on the profilometer using a fibre holder attached to the profilometer 3-axis stage. The fibre was then positioned beneath the microscope objective lens, and the focus adjusted so that the fibre input face was clearly visible.

An initial surface map was acquired to accurately record the condition of the fibre face 'out of the packet', i.e. the original condition on arrival from the manufacturer. Maps were produced that displayed a clear picture of the fibre core and an accurate topography of its surface, allowing dimension measurement and determination of roughness using the tools provided in the software analysis package. The maps were inspected, and if the fibre face showed contamination it was removed from the profilometer and cleaning of the face was attempted using a Cletop optical fibre cleaner. The map was then repeated and changes in appearance and roughness were recorded.

The input end of the fibre was then disconnected and replaced with the output end, which was then profiled in the same manner as outlined above.

This procedure was performed on each batch in this study. Based upon the profiling results, three fibres from each batch of four fibres were selected for testing. Fibres with damage or contamination were rejected and not tested.

5.2.2. Determination of Damage Threshold

The fibre was first aligned as described in Section 0, and then subject to multiple laser pulses, with the incident energy increased by 1-5 mJ between shots. Once a loss of transmission was observed (defined as a reduction in transmitted energy of greater than 3 standard deviations from the average of the first 5 shots), the incident energy was reduced by approximately 50%, and again gradually increased. This process was repeated until a permanent loss of transmission was observed.

5.2.3. Results of Damage Threshold Testing

The damage thresholds were assessed against two metrics. Firstly, the maximum energy transmitted before significant plasma formation occurred (defined as a reduction in transmitted energy of greater than 3 standard deviations from the average of the first 5 shots), and secondly, the maximum energy transmitted without significant plasma formation. The results are tabulated in Table 9. The energy fluence and power density were calculated for the 290 μm diameter focused laser beam and a 10.5 ns pulse length.

		Energy transmitted before significant plasma formation			Maximum without significant plasma formation		
Fibre	Batch	Energy / mJ	Energy Fluence / $J.cm^{-2}$	Power Density / $GW.cm^{-2}$	Energy / mJ	Energy Fluence / $J.cm^{-2}$	Power Density / $GW\ cm^{-2}$
A2	A	25.3	38.3	3.6	25.3	38.3	3.6
A3		31	46.9	4.5	31	46.9	4.5
A4		22.8	34.5	3.3	22.8	34.5	3.3
B1	B	36.5	55.3	5.3	36.5	55.3	5.3
B2		29.4	44.5	4.2	29.4	44.5	4.2
B3		38.3	58.0	5.5	38.3	58.0	5.5
C2	C	33.4	50.6	4.8	33.4	50.6	4.8
C3		37.8	57.2	5.4	37.8	57.2	5.4
C4		29.5	44.7	4.3	29.5	44.7	4.3
D1	D	24.7	37.4	3.6	34.5	52.2	5.0
D2		28.1	42.5	4.1	31	46.9	4.5
D3		26.9	40.7	3.9	30.8	46.6	4.4
E1	E	29.2	44.2	4.2	29.2	44.2	4.2
E2		31.4	47.5	4.5	39	59.0	5.6
E3		31.9	48.3	4.6	41.8	63.3	6.0
F2	F	32	48.4	4.6	36.5	55.3	5.3
F3		28.8	43.6	4.2	34.5	52.2	5.0
F4		33.5	50.7	4.8	41.3	62.5	6.0

Table 9 - Damage threshold testing results for various polishing methods

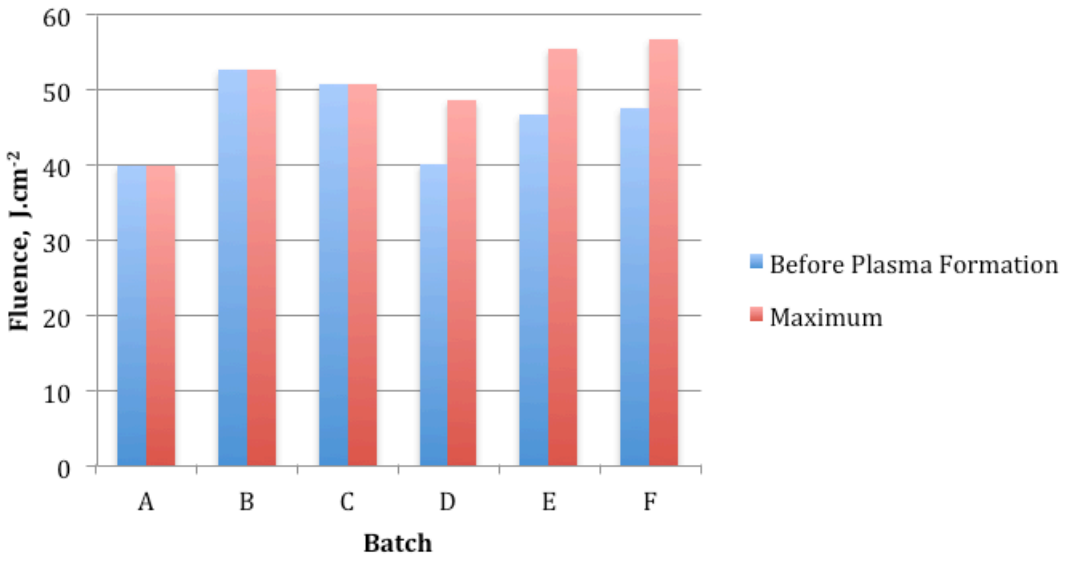

Figure 32 - Average damage thresholds for various polishing methods

5.2.4. Surface Profilometry of Optical Fibre Faces

The 3D surface maps of the input face of a representative fibre assembly from each batch are shown in Figure 33. The initial map is shown on the left, with the post-damage threshold testing map shown on the right. All the fibre assemblies had smooth, high quality finishes with no signs of scratches or pitting on the fibre core. Post-testing, damage was visible in all assemblies, exhibited as pitting, where material was vaporised by the laser pulse.

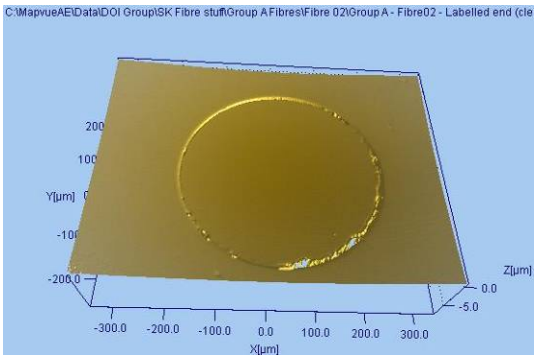

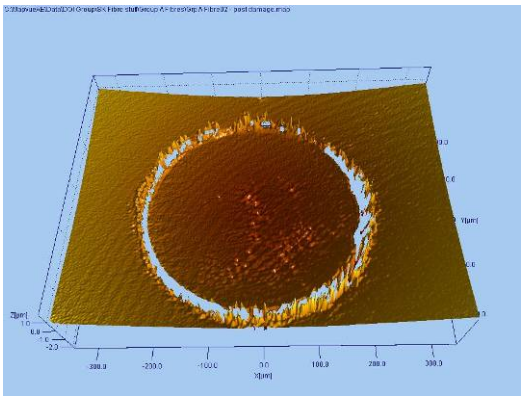

Group A Fibre 2

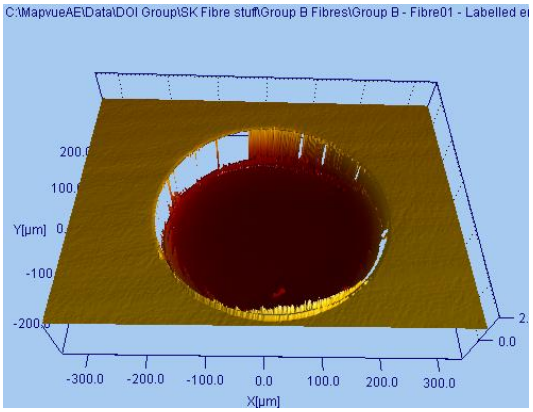

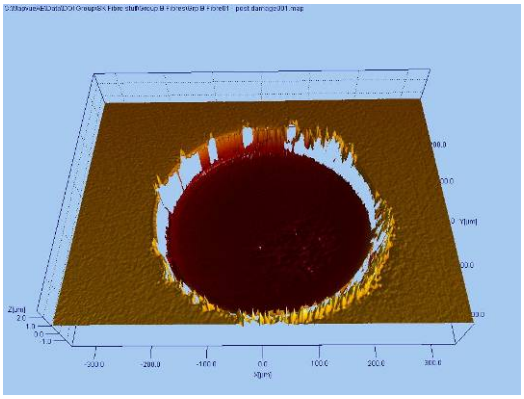

Group B Fibre 1

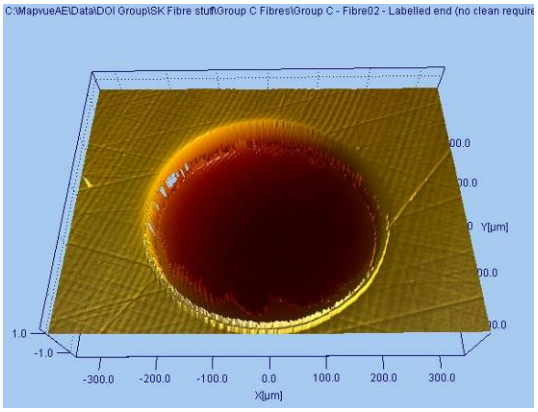

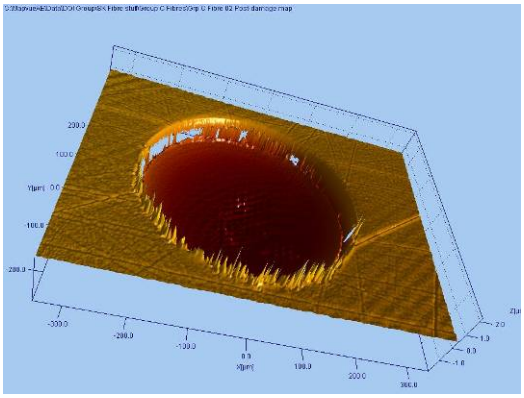

Group C Fibre 2

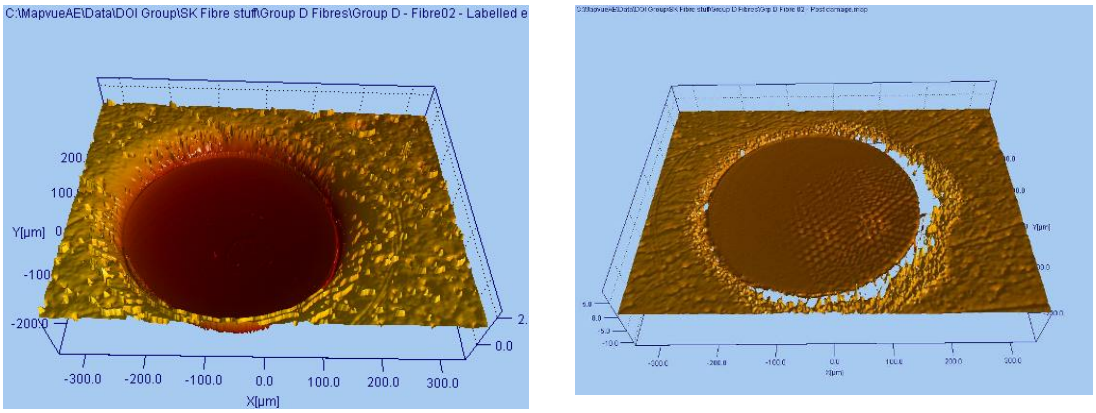

Group D Fibre 2

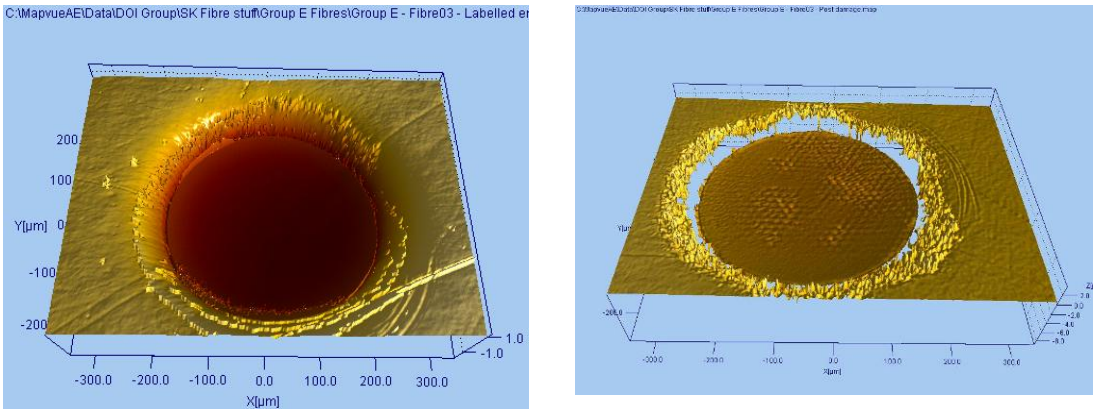

Group E Fibre 3

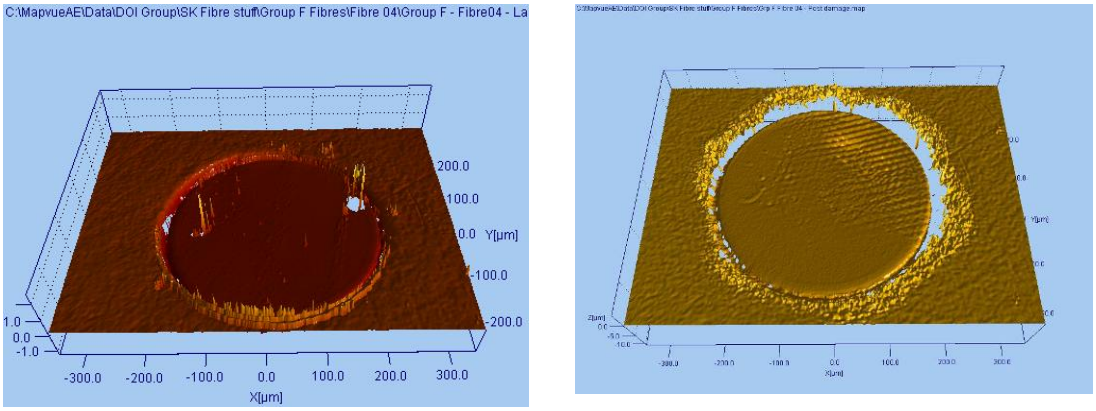

Group F Fibre 4

Figure 33 – Example surface maps for each polish method

5.2.5. Damage Mechanisms and Annealing

5.2.5.1. Steel Ferrules

Annealing of optical fibres has been reported previously [77], where successive plasma formations acted to anneal surface defects, and subsequently permitted the transmission of higher energies. As the present study included zirconia ferrules in addition to the steel ferrules previously tested, the fibre assemblies were examined for evidence of annealing. Figure 34 shows the annealing of a typical steel ferrule fibre assembly. It can be seen that four significant plasma formations were observed (shown as green triangles), indicated by the losses in transmission. Plasma formation was also observed without a loss in transmission, believed to be due to damage to the steel fibre ferrule (shown as purple triangles). Following the first significant plasma formation, higher energies were able to be transmitted (given by the product of the incident energy and the transmission values shown in Figure 34) before a final plasma formation that caused permanent damage. This behaviour was observed for every steel ferrule fibre assembly (except Fibre E1), with an average of 22% higher energy being transmitted after annealing.

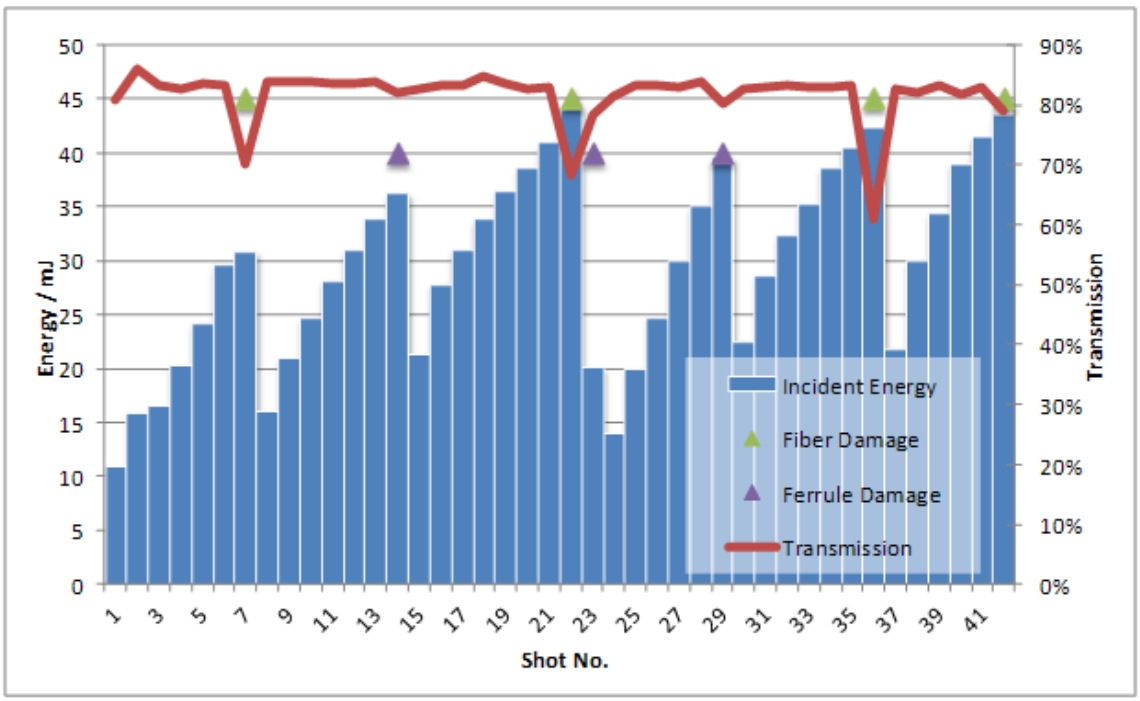

Figure 34 – Annealing of fibre face shown for a typical steel ferrule (Fibre D1)

In addition to this annealing behaviour, plasma formation was observed without a loss in transmission, relative to the previous pulse. Upon examination of the surface maps of damage threshold-tested fibres, following the completion of testing, damage to both the fibre face and ferrule was evident, as seen in Figure 35. The damage on the ferrule, observed as a raised area around the fibre core, is not present prior to testing. The damage to the fibre core can be seen as areas of pitting on the fibre face. The damage was similar to the intensity pattern of the focused laser beam (shown in Figure 18), suggesting that the damage on the ferrule was due to the laser beam directly impinging the fibre ferrule, as opposed to sideways expansion of the plasma formed on the fibre face. This is supported by the hexagonal outer shape observed on the fibre ferrule, similar in shape to the focussed laser pulse spatial profile. To test this hypothesis, a section of ferrule was irradiated with the focused laser beam, seen on the right in Figure 35. The pattern is very similar to that observed around the ferrule. This suggests that despite the majority of the laser energy being contained within a 290 µm diameter spot, sufficient energy exists outside the 365 µm diameter fibre core to damage the fibre ferrule at higher energies, resulting in the observed plasma formations without a loss of transmission.

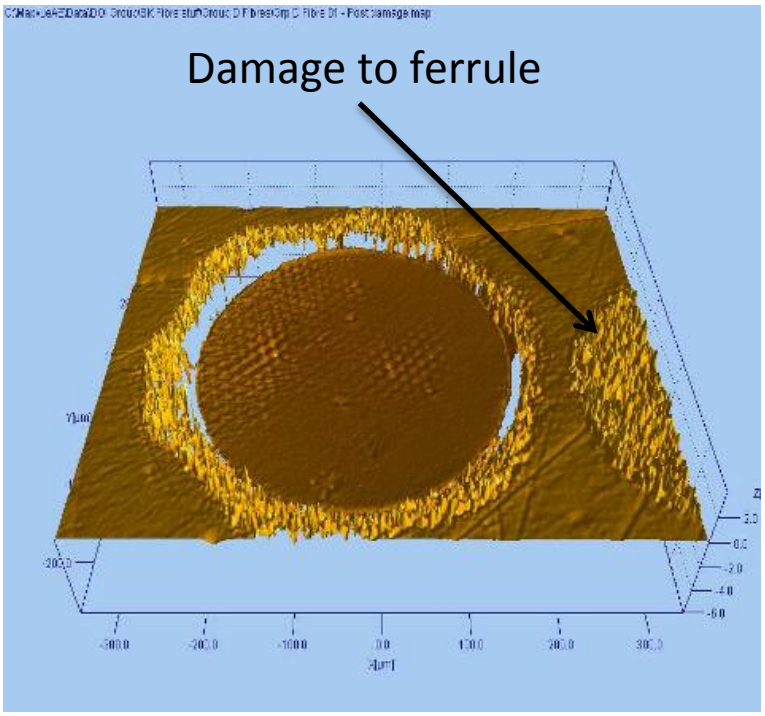

Figure 35 - Surface map of fibre D1 illustrating damage to ferrule

5.2.5.2. Zirconia Ferrules

In contrast, the zirconia ferrule fibre assemblies did not display this behaviour. Following the first significant plasma formation, successive plasma formations were observed at lower energies. This behaviour was observed for every zirconia ferrule, where the first plasma formation appeared to cause permanent damage to the fibre end face.

Upon examination of the zirconia ferrule fibre end faces, damage was observed on both the fibre core and the ferrule. Distortion was evident to the surface of fibre, localized adjacent to the region of greatest damage to the ferrule (seen in Figure 36). Zirconia is often used in a tetragonal crystal structure phase, though an applied stress or heating to approximately 1000 °C can cause a transformation to a monoclinic crystal structure, with an associated volume change [79]. Although the crystal phase used in these zirconia ferrules is not known, it is believed that the action of forming plasma within the zirconia induces a transformation to a monoclinic crystal structure, and the corresponding volume change results in distortion to the fibre face. If the transformation is induced by heating, as opposed to plasma formation, it is possible that the distortion occurs on the shot immediately prior to plasma formation, with the distortion itself the cause of the plasma formation.

The distortion induced in the fibre core results in catastrophic damage to zirconia ferrule fibre assemblies following the first formation of plasma, differing from the behaviour of steel ferrule fibres, where several plasma formations can be tolerated without significant damage.

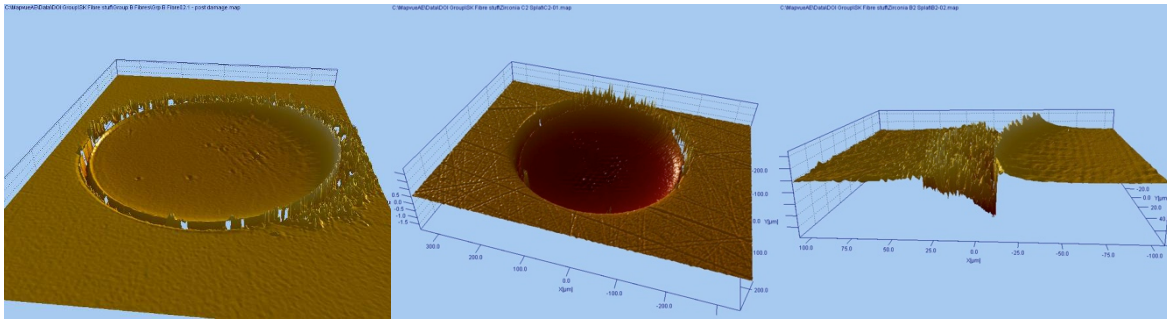

Figure 36 – Surface maps illustrating damage induced to fibre core by Zirconia ferrule. Maps show alternate views of the same fibre assembly. Distortion of the fibre face and ferrule can be seen.

5.2.5.3. Zirconia Ferrules vs. Steel Ferrules

Fibre batches B & D were polished using identical steps, with batch B using zirconia ferrules and batch D using steel ferrules. It can be seen in Table 10 that whilst the zirconia fibre assemblies exhibited higher variance in the maximum energy transmitted before a significant plasma formation, all zirconia fibre assemblies transmitted higher energies than the steel fibre assemblies. The steel fibre assemblies were able to transmit higher energies following a plasma formation, but on average these energies were still below that transmitted by the zirconia fibre assemblies. The zirconia ferrules could not transmit higher energies following a plasma formation; permanent damage was observed.

Batch	Average energy transmitted before plasma formation, ± σ 1 / mJ	Average energy transmitted without significant plasma formation, ± σ 1 / mJ
B	34.7 ± 4.7	34.7 ± 4.7
D	26.6 ± 1.7	32.1 ± 2.1

Table 10 – Damage testing results for zirconia (batch B) and steel (batch D) ferrules. See Section 5.2.2 for details of metrics.

Examination of the surface maps (Figure 33) indicate that the fibre face is more recessed on the zirconia ferrules. Table 11 details the Mohs hardness values for the polishing compounds and the fibre assembly materials. It is evident that during the final polishing step, with cerium oxide, the steel ferrule will be abraded, whereas the zirconia

ferrule may not be. This is supported by Batch A, which had a final 0.05 μm aluminium oxide polish, resulting in abrasion of the zirconia ferrule, as seen in Figure 33, where Batch A exhibits very little recession of the fibre face.

Material	Mohs Hardness
Diamond	10
Aluminium Oxide (Alumina)	9
Cerium Oxide	8
Zirconia	8
Fused Silica	7
Steel	6.5

Table 11 - Mohs Hardness values for polishing materials and fibre ferrules

Two outcomes are possible from this ferrule abrasion. Firstly, the fibre face may be contaminated with small particles of the ferrule material embedded in the fibre face. The final polishing step on the zirconia ferrules will remove this contaminated layer whilst not adding further contamination from the ferrule. The final polishing step for the steel ferrules abrades both the fibre face and the ferrule, resulting in small steel particles embedded in the fibre face. Secondly, the material removed from the ferrule may cause surface damage (below the resolution of the profilometer) that is not removed by polishing. This contamination or damage is removed during the first plasma formations, with the resulting annealing allowing steel ferrule fibres to approach the performance of zirconia ferrule fibres. These postulations may be tested by examining the performance of well-tip steel ferrules, where the ferrule is not present next to the fibre core (see Figure 53). This may also explain the poor performance of batch A, where the final polishing step continues to abrade the zirconia ferrule. Whilst this results in a high quality finish (as seen in the surface maps), due to the finer grit size used (0.05 μm compared to 0.3 μm) it results in poorer performance. Replacing the final step with a cerium oxide polish may improve the performance of this polishing method.

5.2.5.4. Machine Polishing vs. Hand Polishing

Fibre batches E & F were polished using identical steps, as detailed in Table 8, with batch E using a manual hand polish and batch F using an automated polish. The hand fibres were polished singly, and the automated fibres were polished in batches of four.

Fibre E1 had contaminants, most likely abrasive media, on the surface that could not be removed by cleaning, seen on the left in Figure 37. It can be seen from the surface map on the right in Figure 37 that damage has been sustained at these sites, and it is considered that these contaminants induced premature permanent damage. This fibre is therefore not included in this discussion.

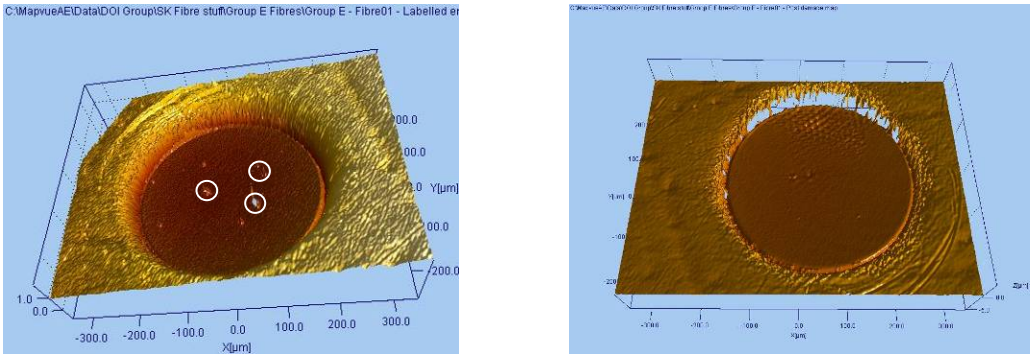

Figure 37 - Fibre E1 Surface Maps. Contaminants are indicated by white circles.

The performance of machine polished and hand polished fibres are similar, as shown in Figure 38. Excluding fibre E1, as discussed above, the machine polished fibres appear to be less variable than the hand polished fibres, as could be expected from the inherent variability of a hand polishing method. Hand polishing incurs additional expense due to the labour requirement, and does not offer any advantage, based on this admittedly small sample size.

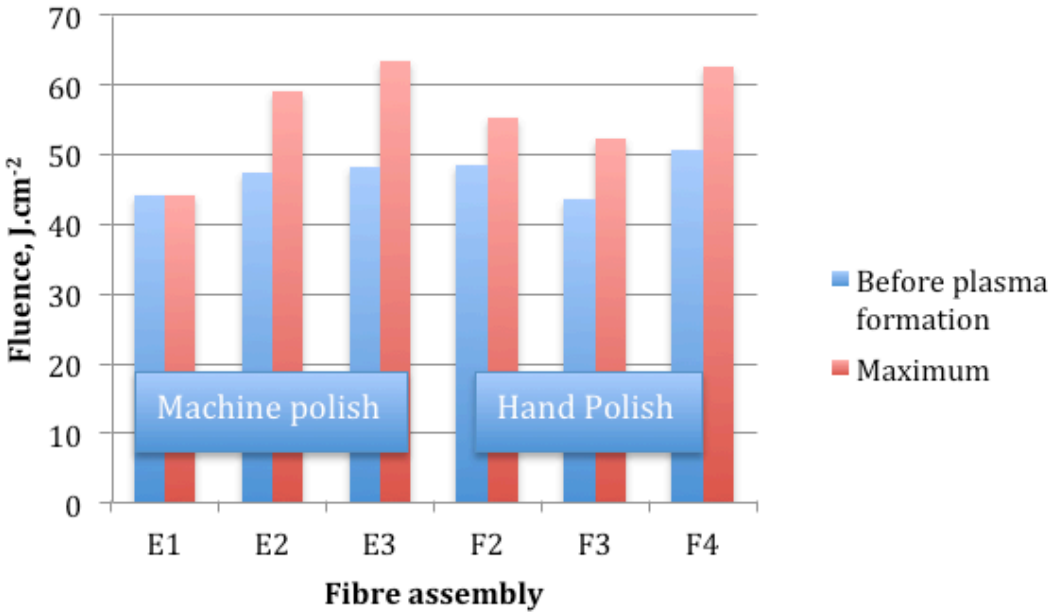

Figure 38 – Damage testing results for hand polish vs. machine polish

5.2.6. Recommendation for Optimal Polishing Method

There are several considerations for selecting an optical polishing method. Given the significant differences between steel ferrules and zirconia ferrules, it is sensible to consider them separately, and identify an optimal polish for each material.

For zirconia ferrules, there is little difference in performance between batches B & C (see Figure 32). The expense of the additional polishing steps for batch B may be offset by the additional labour cost in the hand polish of batch C. Batch B has a smoother finish to the ferrule, probably due to the additional steps allowing the scratches and grooves caused by the initial coarser polishing material to be removed. Whilst no significant effect can be attributed to this in this study, it is felt a smoother finish is more desirable for long-term usage as the ferrule may be in physical contact with a second ferrule, and abrasion between the two surfaces would lead to contamination of the fibre faces by abraded ferrule material. Therefore, the polishing method used for batch B is recommended for zirconia ferrules. The polishing method for batch A should be investigated further, as this polish is intended to minimize sub-surface damage [80] (not studied here), but with the final step replaced with a cerium oxide polish to minimize abrasion of the ferrule.

Alumina ferrules may be worthwhile investigating, as the phase transformation upon plasma formation observed for zirconia may be avoided, and the high Mohs hardness value should allow for a final polishing step that avoids abrasion of the ferrule.

The polishing method used for batch B appears to have a deleterious effect when applied to steel ferrules, with poorer performance than that used for batches E & F. Batches E & F have similar performance, with the difference in the polishing method being hand versus machine polishing. Given the significant cost saving of machine polishing, the polishing method for batch F is the recommended polish for steel ferrules.

The optimal polishing methods determined for each ferrule material are shown in Table 12, with the damage thresholds shown in Table 13.

Regardless of the ferrule material, it appears important that the final polishing step is chosen to minimize abrasion of the ferrule material, to prevent damage or contamination of the fibre face. Steel has a lower Mohs hardness value than fused silica, and in practice this may be impossible to achieve without a well-tip ferrule, to separate the fibre face and ferrule.

Plasma formation on zirconia ferrules is clearly catastrophic, and further work is needed on a larger number of fibre assemblies to quantify this effect. It is proposed that a significant number of shots be performed at or above the proposed design energy to examine the reliability of zirconia ferrules.

The effect of the mechanical polishing method and interaction between the fibre core and the ferrule has not been investigated in this detail before.

Batch	1st Step	2nd Step	3rd Step	4th Step	5th Step	6th Step	Polishing Method	Ferrule
B	15	9	6	3	1	0.3	Machine	Zirconia
	Diamond	Diamond	Diamond	Diamond	Diamond	Cerium Oxide		
F	15	3	0.3				Machine	Steel
	Aluminium Oxide	Aluminium Oxide	Cerium Oxide					

Table 12 - Optimal polishing methods for zirconia and steel ferrules

Batch	Ferrule	Fluence transmitted before significant plasma formation, ± 1σ, J.cm^{-2}	Maximum fluence transmitted without significant plasma formation, ± 1σ, J.cm^{-2}
B	Zirconia	52.6 ± 7.1	52.6 ± 7.1
F	Steel	47.6 ± 3.6	56.7 ± 5.3

Table 13 - Damage thresholds for optimal polishing methods for zirconia and steel ferrules

5.3. Novel Optical Fibres

All fibres tested in this section were manufactured from Polymicro Technologies FIP series fibre. This fibre was chosen as a number of papers have reported usage of FIP series fibre for high power or energy applications.

Our initial studies were performed on bare fibres i.e. no connectors or sleeving. These studies allowed the definition of a baseline fibre. The baseline fibre has a 400 μm diameter core, 440 μm diameter cladding and 480 μm diameter jacket. Input and output faces are mechanically polished, then polished using a CO_2 laser, to ensure the highest quality finish. The fibre is typically protected by a 3 mm diameter PVC/Kevlar sleeve. A number of these fibres were tested to provide a benchmark. In addition, a number of similar fibres finished solely by mechanical polishing were tested to assess the need for laser polishing.

Three types of novel fibres were investigated, to assess their suitability for use in a laser detonator system. These were side fire fibres, tapered fibres and a fibre splitter. The tapered fibres consist of a short fibre taper fusion bonded to a constant core diameter fibre. The fibre splitter comprised two fibres fusion bonded to a tapered fibre.

Two methods were used for coupling the light into the fibre, both using a 100 mm focal length plano-convex lens. The first method placed the fibre after the focal point, so that the beam waist occurred in the air. In the second method, the fibre was before the focal point, i.e. the focal point occurred within the fibre. An input beam diameter of approximately 80% of the core diameter was chosen, to ensure the beam was not coupled into the cladding in the event of misalignment. The fibre was aligned in the X and Y axes to maximize transmission at energies of a few mJ, as measured by a calorimeter at the fibre output.

Two lasers were used for these experiments, detailed in Table 14.

Used For:	Laser Type	Manufacturer	Wavelength / nm	Energy / mJ	Pulse Width / ns
Bare Fibres	Nd:Glass	Lumonics	1053	1000	19
Connectorised Fibres	Nd:YAG	Litron	1064	180	12

Table 14 - Lasers used for testing of novel fibres

The beam waist positioned before the fibre i.e. in the air. The effect of moving the beam waist inside the fibre was also investigated, and discussed separately in Section 5.3.4. The experimental results are summarised in Table 15.

Fibre type	Input diameter, µm	Output diameter, µm	Length, m	Polish method	Average transmission, %	Fluence transmitted before damage, J.cm^{-2}	Maximum fluence transmitted, J.cm^{-2}	Typical Top Hat factor[4]
Bare fibre	400	400	3	Laser	60.9	79.6	183.8	0.769
Bare fibre	400	400	0.5	Laser	78.4	72.4	113	0.508
Bare fibre	400	400	2	Laser	83.3	95.5	107.4	0.612
Bare fibre	400	400	1	Laser	86.0	44.5	100.3	0.539
Bare fibre with 40mm loop	400	400		Laser	84.6	113.8	113.8	0.840
Bare fibres, average	400	400		Laser	78.6	81.2	123.7	0.654
Baseline, laser polish	400	400	5	Laser	71.1	48.1	50.5	0.211
400/200 taper	400	200	5	Laser	45.3	72.1	72.1	0.635
400/300 taper	400	300	5	Laser	56.8	71.3	77.5	0.540
400/300 tapered side fire	400	300	5	Laser & mechanical	31.0	34.4	34.4	
400/200 tapered side fire	400	200	5	Laser & mechanical	32.6	20	20	
Baseline, mechanical polish	400	400	5	Mechanical	76.9	40.7	51.5	0.273
533/400 taper	533	400	5	Laser	75.8	49.1	54	0.215
533/400 tapered side fire	533	400	5	Laser	74.5	40.9	50.9	0.119
533/400 tapered splitter	533	400	5	Laser	32.5	24.1	24.1	0.579
900/300 taper	900	300	2	Laser	70.6	36.1	55.3	0.544

Table 15 - Summary of results for novel optical fibres

[4] As measured at output of fibre, and defined by Equation 9

5.3.1. Damage Threshold of Novel Optical Fibres

In the majority of cases, damage was initially observed at the front face. Once this face had been preconditioned, damage was then observed at the rear face. It was found that if catastrophic damage occurred at the front face, it was not normally possible to obtain a transmitted beam profile, and the fibre would not transmit energy. However, if catastrophic failure occurred at the rear face, it was generally possible to obtain a beam profile. Eventually, a fluence level was reached at which catastrophic damage occurred, generally at the back face, where the fibre would either fail to transmit on subsequent shots or do so with a drastically reduced transmission. No damage was observed in the bulk fibre.

Figure 39 shows the maximum fluence transmitted for each fibre type tested after pre-conditioning. It should be noted that the bare fibres were tested with a longer pulse length than the connectorized fibres, and these results should not be directly compared. Due to the high cost and scarcity of the fibre splitter, this fibre was not tested to destruction. All other fibres were tested until either catastrophic failure occurred, or the laser energy could not be increased further. This was due to the maximum laser energy being reached or repeated non-catastrophic damage at similar energies.

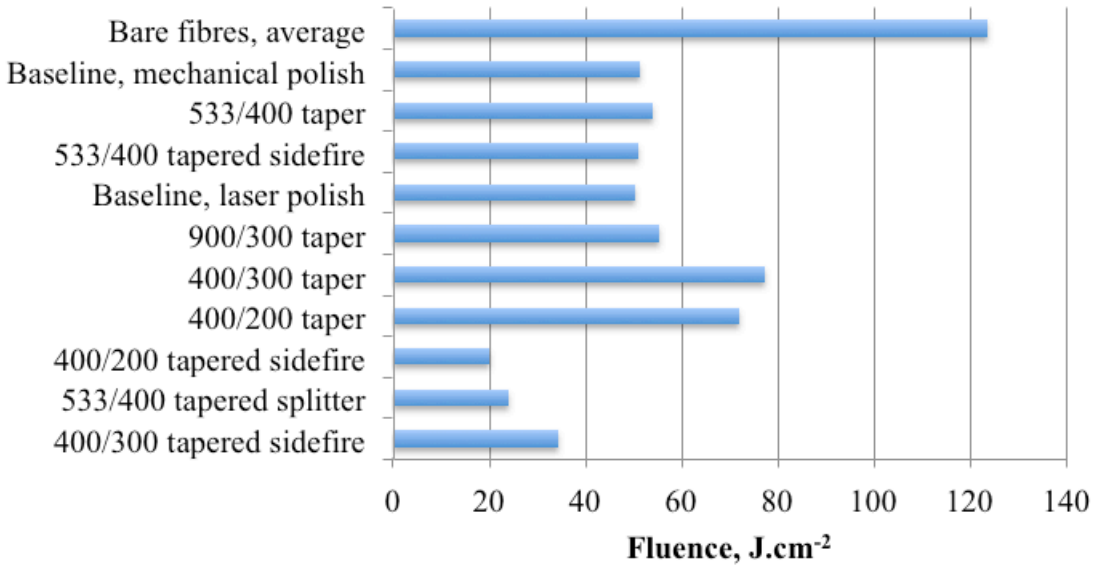

Figure 39 - Damage thresholds of novel optical fibres

The baseline fibre (laser polished) transmitted an average of 43.8 J.cm^{-2}. In comparison, the mechanically polished fibres tested transmitted 50.7 J.cm^{-2}. This limited testing suggests there is no significant advantage gained by laser polishing fibres, in agreement with Section 5.2. This is due to the annealing effect of non-catastrophic plasma formation. The difference may be due to the small numbers of fibres available for test, or due to a difference in mechanical polishing methods. Setchell [3] reported a 19% increase in damage thresholds following CO_2 laser polishing.

The bare fibres transmitted an average fluence before damage of 81.2 J.cm^{-2}, with a average maximum of 123.7 J.cm^{-2}. The fibre with the maximum transmittance was reached with no pre-conditioning evident and is in excess of all other fibres tested, as seen in Figure 39.

The effect of fibre length and fibre loops on output beam quality and damage threshold was investigated. As Figure 40 shows, no systematic effect can be observed from either of these factors. This is not unexpected, as no damage or events occurred in the bulk fibre.

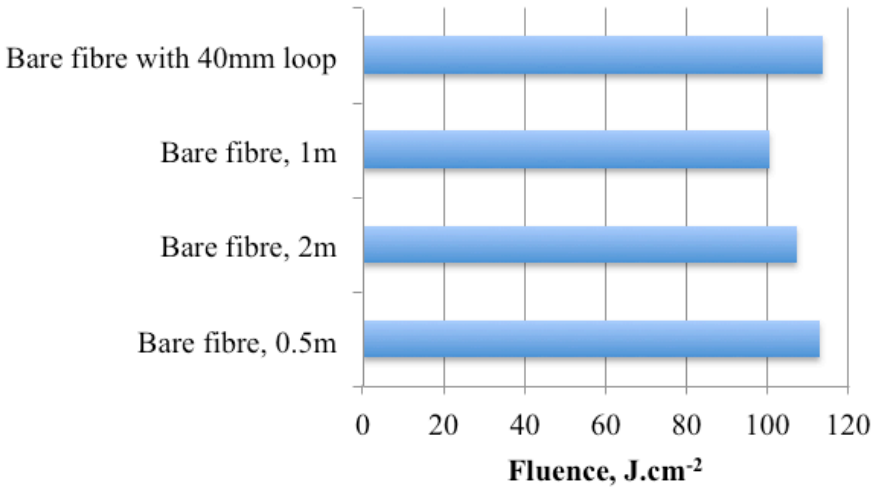

Figure 40 - Effect of fibre length and loop on damage threshold after fibre conditioning

A 40 mm diameter loop was introduced to a bare fibre. This is 6 mm below the specified long-term failure threshold for this fibre type. This may be expected to reduce damage thresholds due to stress-induced micro-fractures in the loop. However, no

reduction in damage threshold was observed, and hence this effect, over the short timescales used in this study, is not significant.

Initially a 533 μm input face, tapering down to a 400 μm core was evaluated. Essentially this fibre is the baseline fibre with a tapered input. It was hoped that higher fluences could be delivered by a fibre with a nominally identical output face as the baseline fibre. However, the damage threshold of 53.9 J cm^{-2} is not substantially higher than the baseline fibre. This is very similar to the fluence transmitted before any damage. This suggests that the limiting factor in these fibres is the output face and any associated imperfections or contaminants.

To confirm this, two further diameters of tapered fibres, 300 μm and 200 μm, both with a 400 μm diameter input face were tested. On the basis of the above, it was expected that these would fail at similar fluences to the larger taper. This would therefore provide an approximate limit for fibre transmission, for an idealized beam profile. However, of the seven fibres tested, only one suffered catastrophic damage at the output face, the rest damaging at the input face. The maximum fluence delivered by these two diameters is similar at approximately 75 J cm^{-2}. As the majority of these fibres failed at the input face, at fluences (incident on the input face) less than the baseline fibre, this suggested the limit for transmission through the output face was not reached, and that the taper design is causing rejection of some of the energy, causing input face damage.

The final tapered fibre evaluated was a 900 μm to 300 μm taper, to investigate the possibility of using it as a beam conditioning fibre, to which a disposable fibre would be connected. However, the damage threshold was lower than expected, around 60 J cm^{-2}.

The results of the taper studies described here have highlighted some issues that are not fully understood, for example, the effect of the taper length and position within the fibre i.e. at the input, or the output. These are explored further in Sections 5.4 and 5.5

The side fire fibres were based on the tapers described above. The tapered fibre designs were modified by micro-machining a bevel onto the output end. This results in an output at approximately 90 degrees to the fibre core axis, due to total internal reflection from the bevel. The 533 μm to 400 μm diameter fibres had an additional taper on the

output end, which was then laser-polished, as shown in Figure 41. The 400 µm to 300 µm and the 400 µm to 200 µm diameter were mechanically polished on the output end, as shown in Figure 42.

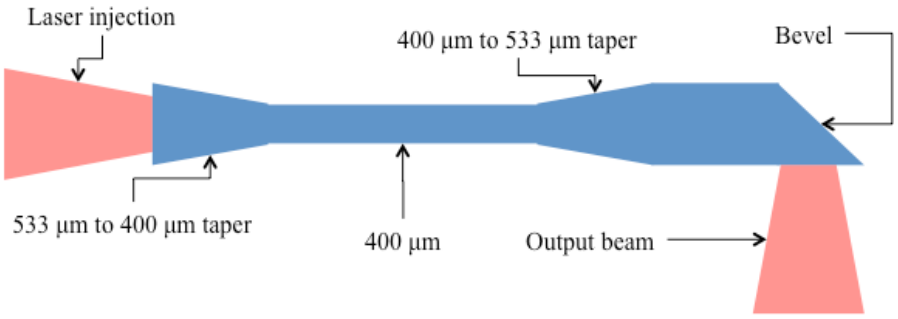

Figure 41 - Illustration of 533 µm side fire fibre

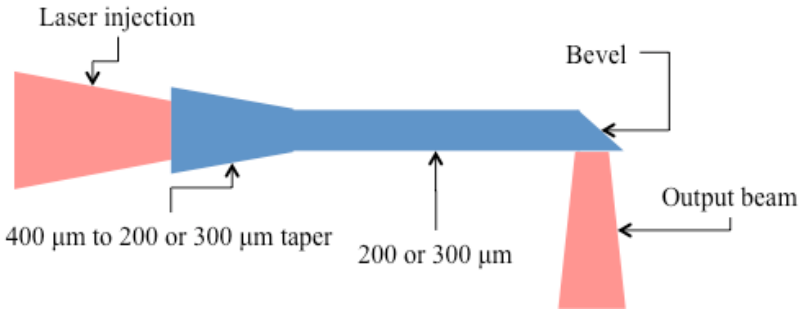

Figure 42 - Illustration of 300 and 400 µm side fire fibre

The 533 µm to 400 µm side-fire fibre had a damage threshold similar to the baseline fibre. As these fibres damaged primarily at the output end, it can be concluded that the side-fire method does not inherently reduce the damage threshold. It should be noted however, that these fibres had a larger than expected output diameter, of approximately 700 µm, due to a taper on the output end

The 200 µm and 300 µm side-fire fibres were not laser-polished, and hence a direct comparison is not possible. These fibres have the lowest damage threshold of all the fibres tested, with the 300 µm fibres averaging 18 $J.cm^{-2}$ and the 200 µm fibres averaging 30 $J.cm^{-2}$. This is not adequate for initiation, and hence further refinement of this fibre design would be necessary before they could be considered a viable candidate.

The final fibre tested was a 1:2 fibre splitter. This consisted of a 533 µm to 400 µm tapered fibre, fusion bonded to two 400 µm fibres. No previous research on this type of fibre splitter has been reported at these energy levels. This fibre was not tested to destruction due to its high cost and scarcity, but it transmitted up to 24 $J.cm^{-2}$ with no sign of damage.

5.3.2. Transmission of Novel Optical Fibres

Transmission is defined as the ratio of output energy to input energy. It is not a critical parameter, as a low transmission can generally be overcome by increasing the laser energy. However this will increase the required laser energy, and increase the probability of fibre damage. Figure 43 shows the typical transmission for the fibres evaluated.

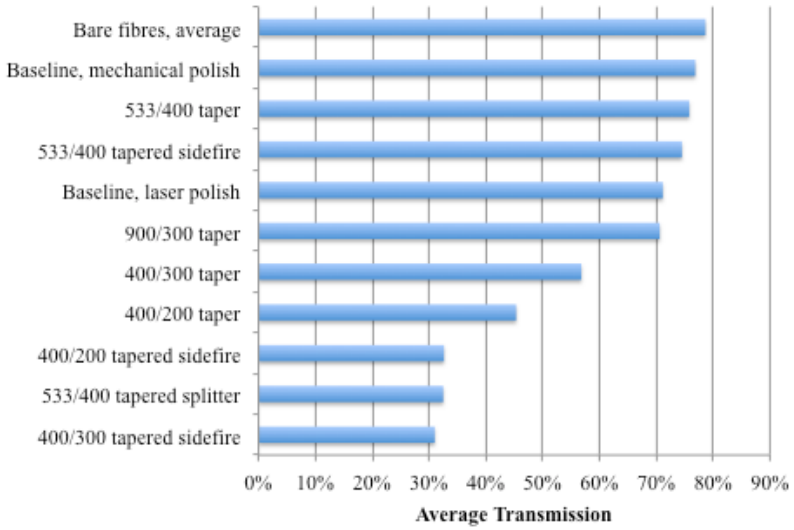

Figure 43 - Average transmission of novel optical fibres

Irrespective of the length and configuration, the bare fibres consistently have the higher transmission (approximately 86%) than all other types of fibres considered in this study. The transmission values do not appear to be strongly dependent on fibre length and implies that the transmission characteristics are dominated by the characteristics of the input and output faces. Optical fibres are designed and manufactured to have very high transmissions and so it is not surprising that no systematic changes in the transmission with fibre length were observed for the lengths considered in this study.

Loops in the fibre are used to improve the beam quality (see Section 5.3.3), thus the effect of a 40 mm diameter loop on transmission was investigated. The input and output fluences were recorded for fibres in straight and coiled configurations and the transmission determined from these values. A typical result is shown in Figure 44. The fibre was tested uncoiled, to measure its transmission, shown as 'A', at fluences below the damage threshold. It was then coiled, with a 40 mm loop, and tested for damage threshold, see 'B'. The fibre did not suffer permanent damage. It was then re-straightened and measured for transmission again at fluences below the damage threshold, shown as 'C'. No significant reduction in transmission is seen due to the looping.

If a fibre is fully filled (in terms of modes), then any curvature will cause the higher-order modes to be lost as the angle the light rays make with the core/cladding interface exceeds the critical angle. This would be observed as a loss of transmission. However, for a fibre with a small number of modes filled, curvature will promote lower order modes, and hence induce mode mixing. The injection method used does not initially fill a large number of modes, and hence a loss in transmission is not observed. There will be a diameter at which even these lower order modes will be lost. It is suspected that for these fibres, the fibre would fail mechanically before this diameter was reached. A 40 mm loop is below the long-term failure diameter of 46 mm for these fibres.

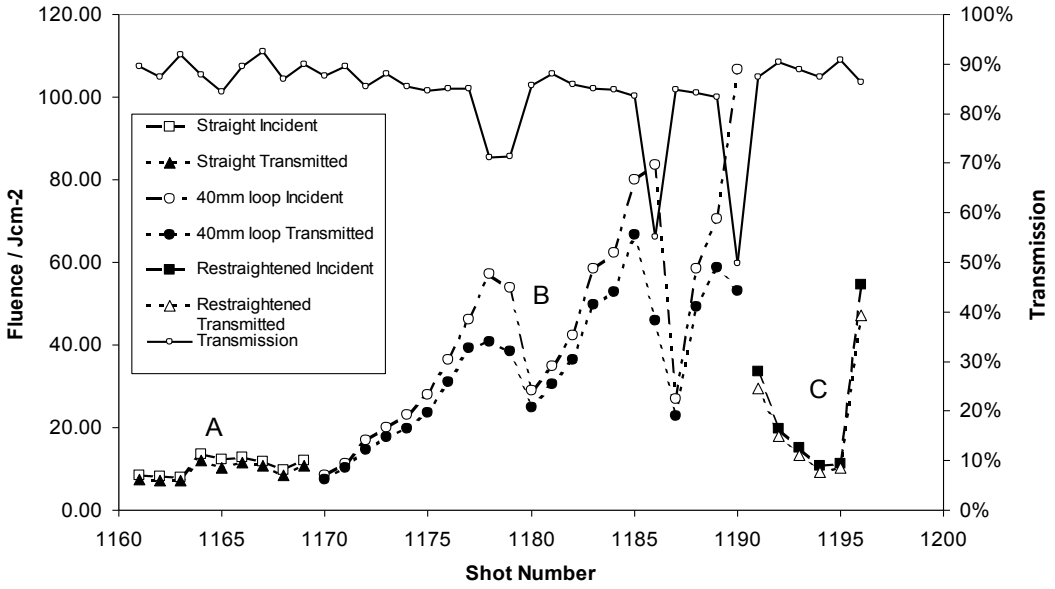

Figure 44 - Effect of 40 mm loop on transmission

The laser polished baseline fibres typically transmitted 72%, in comparison to the mechanically polished fibres, which transmitted 75%. The mechanically polished fibres are comparable to the bare fibres. Apart from the polishing method, the main difference between these fibres is the connector. The laser-polished fibres use a glass sleeve around the fibre end to aid heat dissipation. The mechanically polished fibres utilize a well-tip ferrule, where the fibre is not in contact with any material at the input end. It is believed the glass sleeve may be increasing losses in the fibre by inducing coupling into the cladding and hence the sleeve. This could potentially also reduce the damage threshold. The bare fibres were laser polished, suggesting that the polishing method does not have a strong effect on transmission.

The transmission characteristics range from around 48% for the 400-200 μm taper to 74% for the 533-400 μm and 900-300 μm taper with the highest transmitting taper comparable in performance to the baseline fibre. As the beam is diverging into the fibre, it would be expected that the transmission would be reduced as the ratio of input diameter to output diameter increases. This is due to the angle the beam makes with the taper walls exceeding the critical angle to remain within the fibre for some light rays, reducing the transmission. This trend is generally observed, with the exception of the 900 to 300 μm taper. This fibre is believed to have a significantly longer taper than the

other fibre. This would reduce the angle the beam makes with the taper walls, thus reducing the loss in transmission. Clarkin et al [12] reported substantial losses in fibre tapers when the input numerical aperture matched the bulk fibre numerical aperture. It was shown that the numerical aperture of the fibre is reduced by the ratio of the two diameters i.e. core diameter and input diameter. However, for the system reported here, the numerical aperture of the input beam is much less than that of the fibre, so this effect was not observed.

The transmission from the fibre splitter is obviously lower as each fibre was recorded separately. If these are summed however, we can see the transmission is some 10% lower than the closest comparable fibre, the 533 μm tapered fibre. This is evidently due to losses at the fibre splitter interface. Whilst this is not a critical loss, it is expected that there would be a fluence at which these losses would cause damage at this interface.

Figure 43 shows the transmission of the side-fire fibres. It can be seen there are two distinct populations. Firstly, The fibre with a 533 μm diameter input face has a transmission only slightly less than that of its tapered analogue. This fibre had an up taper (i.e. increase in diameter) before the micro-machined bevel. Whilst a small proportion of energy was observed exiting this fibre axially, this taper evidently makes for a very efficient (i.e. low loss) turn. Secondly, the fibres with 400 μm input faces did not have an up taper before the micro-machined bevel. This results in drastically reduced efficiency, as a large proportion of the energy exits the fibre axially.

5.3.3. Output Beam Quality of Novel Optical Fibres

The “top hat” figures of merit (as defined in Equation 9) for the beam profiles for all the fibres studied are summarized in Table 16. A value of 1 represents a perfectly uniform beam profile spatial intensity. There is a large variability in the results. The Nd:YAG laser has a significantly greater spatial coherence than the Nd:Glass laser, and this is manifested as speckle in the beam profiles of the fibres tested with this laser. The connectorized fibres do not show significant differences between the laser polished and the mechanically polished fibres.

Fibre Type	Typical Top Hat Factor
400-200 µm Taper	0.635
400-300 µm Taper	0.540
400 µm Mechanical Polish	0.273
400 µm Laser Polish	0.211
533-400 µm Taper	0.215
533-400 µm Tapered Side fire	0.119
533-400 µm Tapered Splitter	0.579
900-300 µm Taper	0.544
Bare Fibres	0.654

Table 16 - Top Hat Factors for novel optical fibres

The effect of looping the fibre, to improve the beam profile, was investigated. Loop diameters of 40, 80, 120 and 240 mm were tested. It should be noted that 40 mm is below the recommended bend diameter of 46 mm for these fibres. The results are shown in Figure 45. A 240 mm loop does not have a significant effect upon the beam profile, quantified here using the top hat factor. There does not seem to be any strong correlation between loop diameter, number of loops and top hat factor for all small (<120 mm) loop diameters. For subsequent experiments, three 80 mm loops were used, as this was above the recommended bend diameter for these fibres, whilst giving a significant increase in beam profile relative to a straight fibre or larger (240 mm) loops.

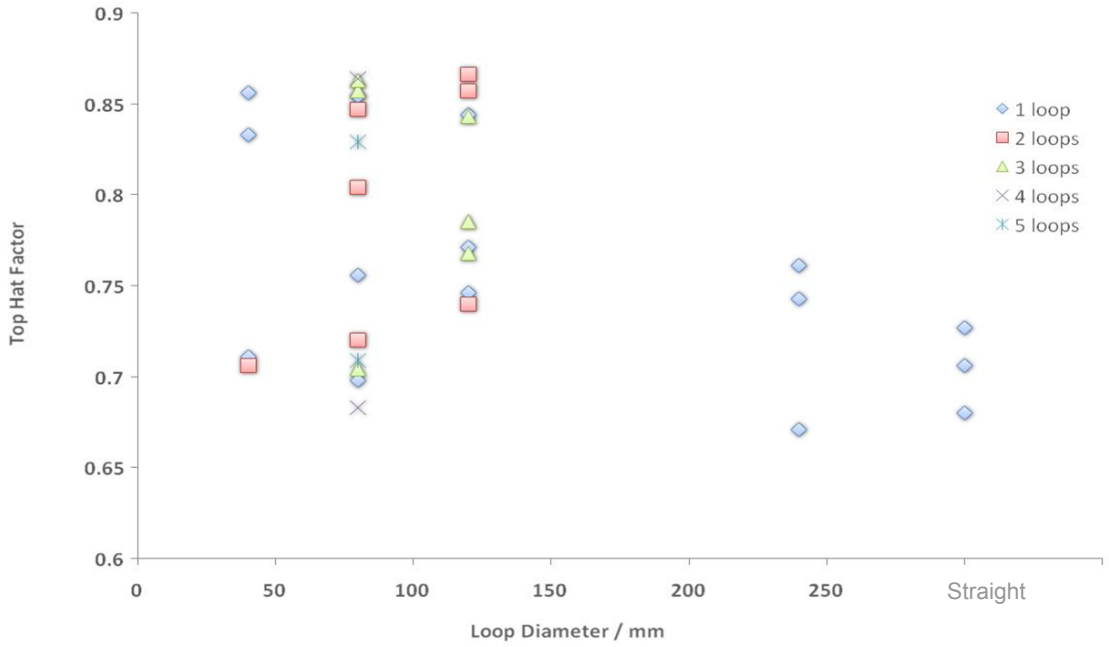

Figure 45 - Effect of Fibre Looping on Beam Profile for 3m Fibres

A tapered fibre may be expected to raise the top hat factor by the same method as a loop i.e. by increasing the angle the light rays make with the core/cladding interface, higher order modes are promoted. Thus for a tapered fibre, it would be expected that the higher the ratio between input and output diameters, and hence the larger the angle, the greater the effect would be. From the limited data, this is supported by the observation that top hat factor increases with decreased output face diameter (for a constant input diameter), as seen in Figure 46.

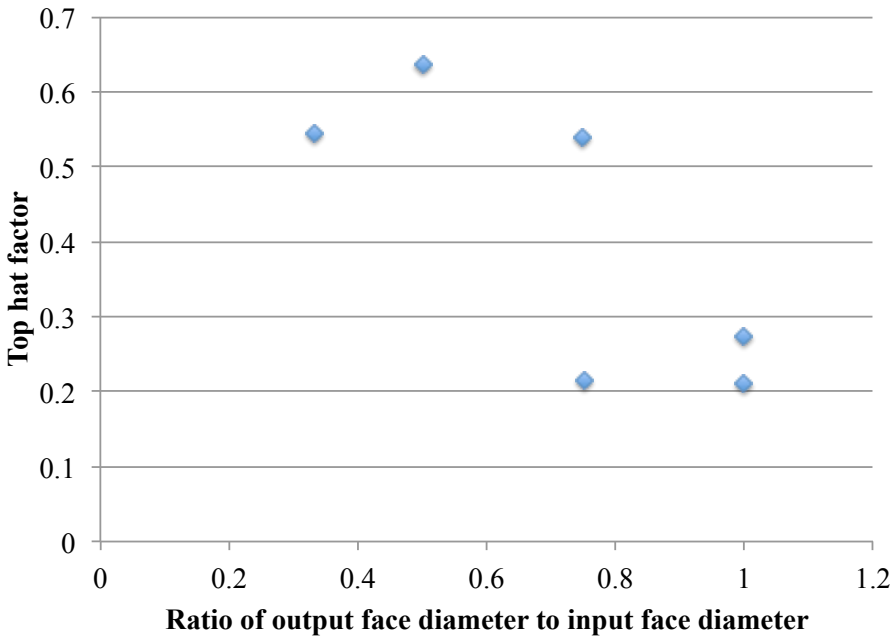

Figure 46 - Effect of tapered fibres on beam profile

The beam profiles of the taper side-fire fibres are difficult to measure because of the mechanical construction of the fibre connector. It was particularly difficult for the smaller side fire fibres. The 533-400 µm side fire fibres incorporated an up-taper before the machined bevel to increase the efficiency of the right-angled turn. The beam profiles of these fibres were over-sized and had poor beam uniformity, as seen in Figure 47. In contrast, the 300 µm side fire fibres had a uniform beam profile, albeit with a rectangle shape. The reason for this difference is not clear, but may be due to the polishing method (laser polished for the 533-400 µm side fire fibres, mechanically polished for the 300 µm side fire fibres).

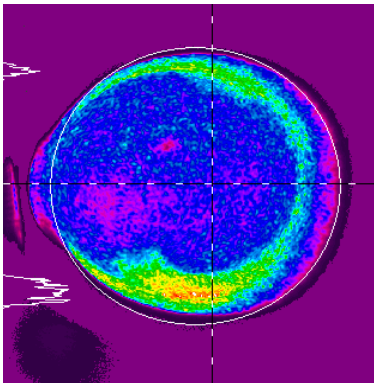

Figure 47 - Beam profile for 533 µm side-fire fibre

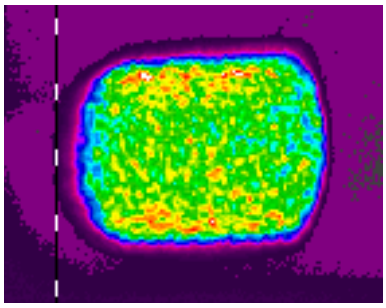

Figure 48 - Beam profile for 300 µm side fire fibre

5.3.4. Effect of Coupling Method on Tapered Optical Fibre Performance

The effect of the coupling method of the fibre performance was investigated. The bulk of this work positioned the fibre after the focal point of the beam, to eliminate the possibility of damage due to focusing in the fibre. The fibre was moved to the other side of the focal point, i.e. focusing into the fibre, as shown in Figure 49. The beam profile was similar at both locations. Three types of fibre were tested: the baseline fibre; a 400 to 200 µm tapered fibre; and a 400 to 200 µm fibre.

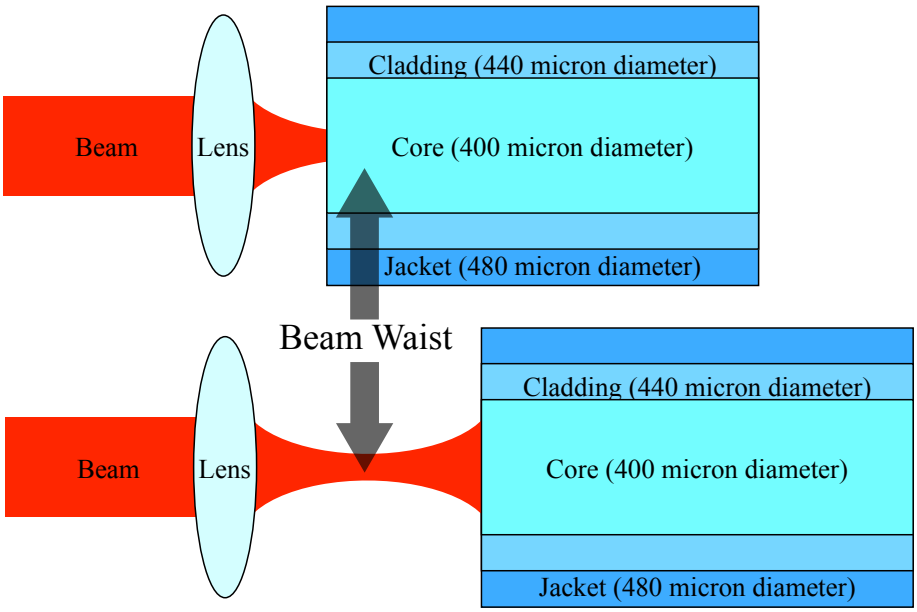

Figure 49 - Illustration of coupling methods

Moving the focal point inside the fibre was expected to increase the transmission of tapered fibres, as the angle that the rays make with the taper wall is increased, reducing the losses of higher order, and hence higher angle, modes. The results are shown in Figure 50. It can be seen that for a 400 to 200 μm taper, moving the focal point inside the fibre almost doubles the transmission, increasing to the level of a standard fibre. It is also apparent that moving the focal point inside the fibre increases the transmission of the laser polished baseline fibre also, to close to the theoretical maximum. This supports the earlier hypothesis that the glass sleeve around the fibre input induces coupling out of the fibre. With the focal point inside the fibre it is likely that the light rays do not contact the cladding in the region of the sleeve. An increase in transmission for the 400 to 200 μm side-fire is also observed, though this increase is not as dramatic. It is evident that the coupling method does not affect transmission losses through the side-fire section.

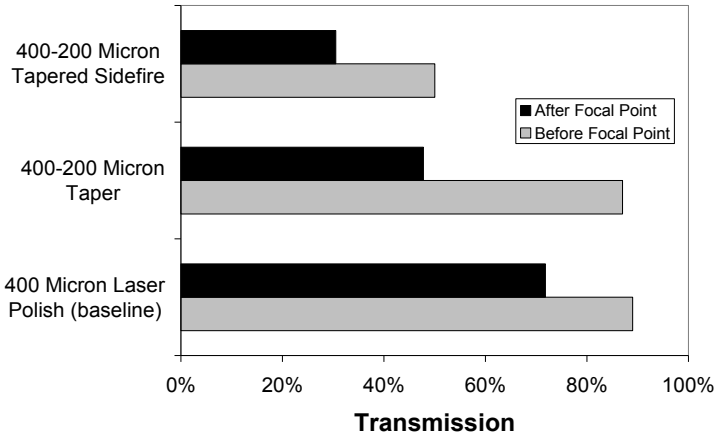

Figure 50 - Effect of Coupling Method on Transmission of tapered fibres

It would expected that moving the focal point of the beam to within the fibre would lower damage thresholds, as the focusing of the beam may increase the energy density beyond that which the fibre can withstand. This effect is evident in Figure 51. It can be seen that in all cases, the damage threshold was lower for this coupling method. For the baseline fibre and the side-fire fibre, the reduction in damage threshold is approximately 50%. The effect is lesser for the tapered fibre, with a loss of approximately 33%. This may be due to the limited number of fibres tested here. This is somewhat at odds with the increased transmission inherent with this coupling method. However, it is evident

that the damage due to the focusing within the fibre is more severe than that caused by the energy lost in the taper.

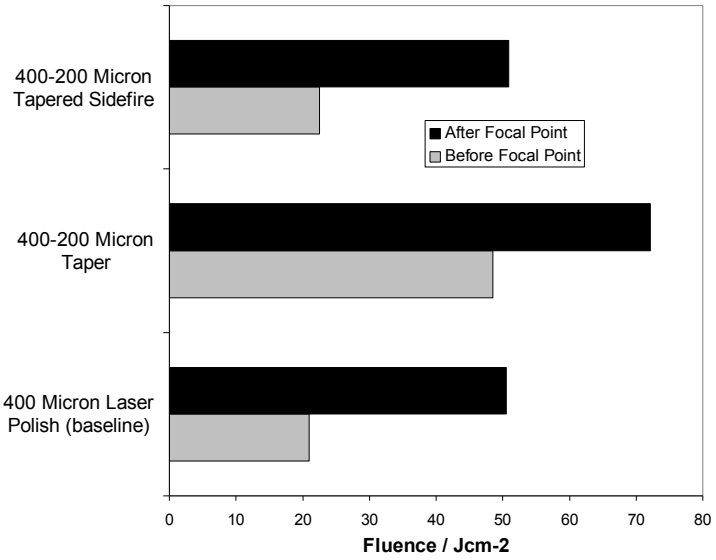

Figure 51 - Effect of coupling method on damage threshold of tapered fibres

5.3.5. Discussion of Novel Optical Fibres

A large variety of optical fibre designs have been characterised and a baseline fibre for use in laser detonators established. The measured damage threshold for both bare fibres and the baseline connectorised fibre compare well to other results published in this field.

The "side-fire" fibres tested have both an adequate damage threshold and beam quality, though not yet in the same design. The larger "side-fire" fibres are not suitable for laser detonators, as their output beam diameter would raise the firing energy, and hence the fluence incident on the input face, beyond the damage threshold of the fibre. The smaller fibres, whilst having a greatly improved beam profile, did not have an adequate damage threshold. It is believed this is due to both the mechanical finish and the input taper design.

The larger fibre tapers tested showed that a tapered fibre does not have a reduced damage threshold. However, the larger input face on these fibres offers no real benefit, and whilst they are suitable for use, their increased cost precludes their use. The smaller fibres are capable of transmitting sufficient energy for initiation, though they currently

have a greatly reduced transmission compared to the baseline fibre and the larger tapers. The larger fibre tapers show that it is possible to design a taper without a significant transmission loss.

These results suggest that the mechanically polished connectorized fibres offer the best combination of damage threshold, transmission and beam profile. Whilst the bare fibres outperform them, the difficulties of aligning and integrating a bare fibre make them unsuitable for use.

The effect of coupling method on fibre performance has been examined. For fibres where significant losses are introduced at the input face, such as glass-sleeved fibres or fibre tapers, it is possible to increase the transmission by moving the focal point inside the fibre. However, this increase comes with a consummate reduction in damage thresholds.

5.4. Use of Fibre Optic Tapers to Increase Connector Tolerance

There are two main interfaces to be considered within a laser detonator system. Firstly, the laser to fibre connection, and secondly, the fibre to detonator interface. The fibre to detonator interface typically comprised either a coated substrate placed at the output of the fibre, or a coated fibre. This interface does not have particularly tight tolerances, and for the purposes of this paper, will be disregarded.

The laser to fibre connection has significantly tighter tolerances. Misalignment of the laser to the fibre can at best result in a loss of transmission, at worst, catastrophic failure of the fibre. It is therefore desirable to understand the effect of misalignment of this interface, and to develop methods to increase the tolerances. Increased tolerances can both reduce cost and increase reliability of a laser detonator system.

A selection of optical fibres was evaluated (shown in Table 17), including both tapered and non-tapered fibres. All fibres evaluated were high purity silica fibres from a variety of vendors. For the purposes of this study a reference fibre and injection method has been defined. This is a Polymicro FIP400440480 400 μm core diameter fibre with mechanically polished standard SMA 905 connectors, shown in Figure 52, using a lenslet array with a primary lens to give a 320 μm diameter focussed spot. Two connectors designed for high-power usage were also investigated. The first uses a well-tip connector, shown in Figure 53, with the first 1-2 mm of fibre suspended in free space, minimizing the material exposed to the laser energy. The second uses a silica sleeve around the input of the fibre, shown in Figure 54. In both cases the 480 micron diameter polyimide buffer is removed leaving only the core and cladding. In Figure 52, Figure 53 and Figure 54 the laser is incident from the top of the diagram.

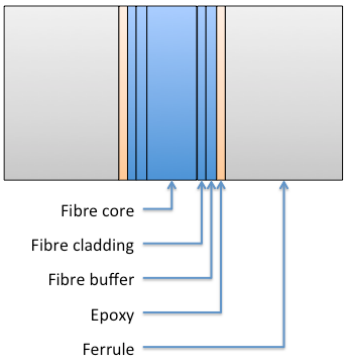

Figure 52 - Standard fibre optic connector

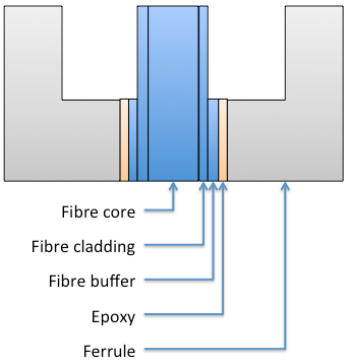

Figure 53 - Well-tip fibre optic connector

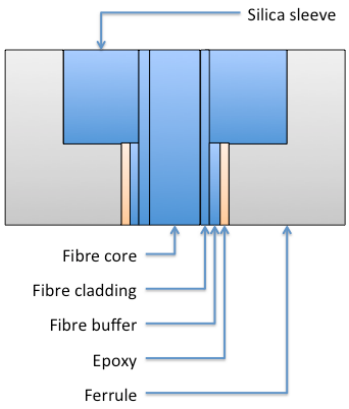

Figure 54 - Silica sleeved fibre optic connector

The fibres and injection methods are assessed for their ability to reduce the sensitivity of the fibre transmission to misalignment.

Input face diameter, µm	Output face diameter, µm	Taper length, mm	Connector type
533	400	2-3	Silica sleeve around input fibre face
400	300	50	Standard connector
400	200	50	Standard connector
800	300	2000	Standard connector
400	400		Well-tip input connector
400	400		Silica sleeve around input fibre face
400	400		Standard connector

Table 17 - Optical fibres evaluated to assess the use of tapered optical fibres to increase connector tolerance

Two techniques were used to focus the laser pulse into the optical fibre: a 100 mm focal length plano-convex lens to produce a spot size of 320 µm; or, a lenslet array was used with a 19 mm focal length lens to obtain a beam diameter of 320 µm.

The fibre was firstly aligned for maximum transmission using the beam profiler camera and the thermal sensors, by adjusting the fibre mount in the X and Y axis. The fibre

mount was then adjusted in the X axis to reduce the transmission to approximately 20-30%.

The fibre mount was then adjusted in the X axis in 10 μm increments, in the direction of increasing transmission. In each position, the incident laser energy was recorded by an thermal sensor placed in front of the fibre input, and then the transmitted energy recorded by a thermal sensor at the fibre output. The transmission was then calculated. This process was repeated until the transmission was seen to rise to a maximum and then return to the starting value of approximately 20-30%.

To maximize damage thresholds (the energy a fibre can transmit without suffering damage) it is desirable to use a beam profile with a high degree of spatial uniformity. This minimizes any local "hot-spots" and reduces the peak intensity relative to the average intensity. A typical laser beam profile is shown in Figure 55. It can be seen that the beam has reasonable uniformity, with a degree of asymmetry, most likely due to the pumping configuration of the laser cavity, resulting in a non-uniform gain within the laser rod. Figure 56 shows the beam as focused to a 320 μm spot using a 100 mm focal length plano-convex lens. This profile is not of particularly high quality. It is likely this profile would result in relatively low damage thresholds. Figure 57 illustrates the spatial profile of the beam focused using the lenslet array in conjunction with a 19 mm focal length lens. This has substantially improved the beam profile, with a high degree of symmetry and uniformity. The lenslet array produces multiple images of the beam, which are then overlapped by the 19 mm focal length lens, averaging the beam profile. Little relation was observed between the original beam profile and the conditioned beam profile, suggesting that the lenslet array focusing method is suitable for lasers with poor i.e. non-uniform beam profiles.

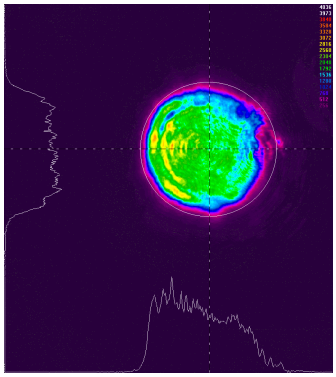

Figure 55 - Laser beam without beam conditioning

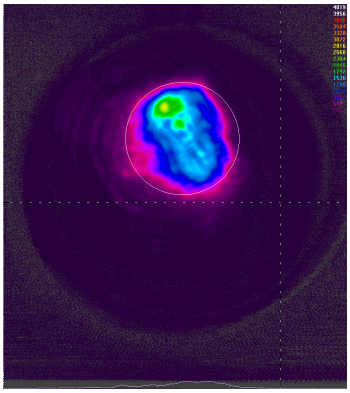

Figure 56 - Beam focused to a 320 µm spot using a 100 mm focal length lens

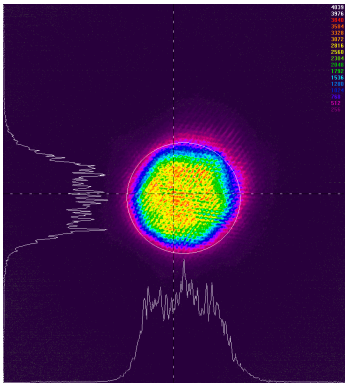

Figure 57 - Beam focused to a 320 µm spot using lenslet array and 19 mm focal length lens

By intentionally misaligning the fibre relative to the injected beam, it is possible to investigate the effect of fibre misalignment on output beam spatial intensity profile. For laser detonators using flyer initiation, the output beam profile is of critical importance, as it can be directly correlated to flyer shape. A uniform spatial intensity profile, to launch a flat, planar flyer, is desirable to maximize the shock imparted to the explosive.

The beam was coupled into a 5 m length, 400 µm fibre with the lenslet array. Figure 58 illustrates the results. A beam profile (left) was first captured with the fibre significantly misaligned (approximately 25% transmission). The fibre alignment was then optimized, and a second beam profile captured (centre). Finally, the fibre was misaligned in the opposite direction, and a final beam profile captured.

It can be seen that the beam profile remains constant, with the expected reduction in intensity due to the reduced transmission. Assuming that the transmitted energy still exceeds that required, moderate fibre misalignment is unlikely to cause significant problems.

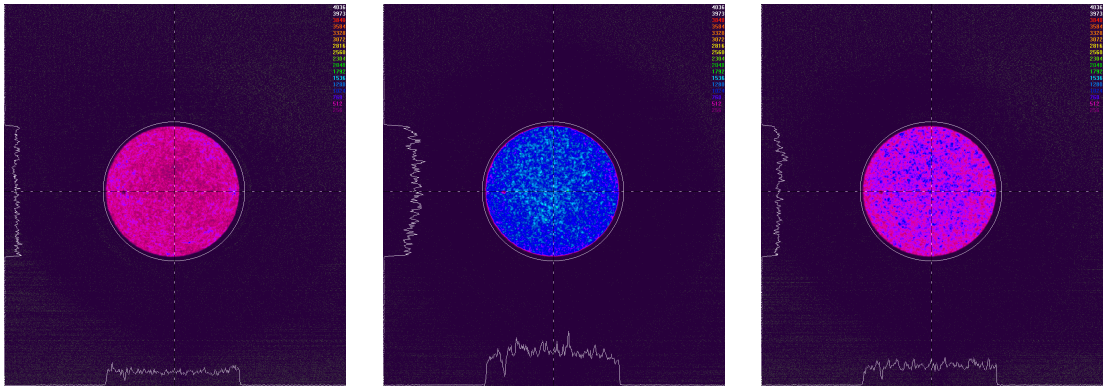

Figure 58 - Effect of misalignment of laser beam relative to optical fibre on beam profile. A beam profile (left) was first captured with the fibre significantly misaligned (approximately 25% transmission). The fibre alignment was then optimized, and a second beam profile captured (centre). Finally, the fibre was misaligned in the opposite direction, and a final beam profile captured.

Acceptable transmission losses will vary from system to system. The displacement required to produce both a 10% and 20% loss relative to the maximum transmission has therefore been measured for each fibre and injection method. It would also be possible to compare these losses relative to a standard transmission for all fibres and injection methods. However, a fibre optic taper reduces the overall acceptance angle of the fibre. As the lenslet injection method has a high angle of incidence upon the fibre face, the tapered fibres have reduced transmission relative to the non-tapered fibres when evaluated with the lenslet array. It is therefore not possible to make a comparison of all fibres and injection methods. It is possible to eliminate this effect by careful design of the lenslet array and focusing lens. By evaluating the loss relative to the maximum transmission for the particular fibre and injection method under test, this effect may be disregarded.

Table 18 summarizes the results. It can be seen that the reference fibre (underlined) has a tolerance of 140 μm for a 10% loss, and 200 μm for a 20% loss.

Fibre Type	Injection Method	Max. Trans.	Displacement (μm) for	
			10% loss	20% loss
400 μm, well-tip connector	100 mm lens, 320 μm spot	83%	180	250
400 μm, well-tip connector	Lenslet array, 320 μm spot	83%	130	200
400 μm, silica sleeved connector	100 mm lens, 320 μm spot	83%	190	270
400 μm, silica sleeved connector	Lenslet array, 320 μm spot	75%	130	180
400 μm, standard connector	100 mm lens, 320 μm spot	85%	240	260
400 μm, standard connector	Lenslet array, 320 μm spot	83%	140	200
400/300 μm tapered fibre	100 mm lens, 320 μm spot	84%	180	230
400/300 μm tapered fibre	Lenslet array, 320 μm spot	65%	140	200
400/200 μm tapered fibre	100 mm lens, 320 μm spot	83%	180	220
400/200 μm tapered fibre	Lenslet array, 320 μm spot	47%	120	200
533/400 μm tapered fibre	100 mm lens, 320 μm spot	88%	320	400
533/400 μm tapered fibre	Lenslet array, 320 μm spot	82%	220	300
800/300 μm tapered fibre	100 mm lens, 320 μm spot	93%	520	640
800/300 μm tapered fibre	Lenslet array, 320 μm spot	38%	NA	NA

Table 18 - Summary of experiment results for the use of tapered optical fibres to increase connector tolerance. The reference fibre is underlined.

It should be noted that in a system, misalignment may be present in several components. For example, the laser may be misaligned relative to the laser output connector, and the fibre may also be misaligned relative to the fibre connector. These are likely to be the main areas of concern. Fibre connector to output connector tolerances are likely to be very tight, and hence can essentially be disregarded. Care must be taken to ensure that all component tolerances are considered together to achieve similar results to those presented here.

A summary of the experimental results is shown in Figure 59. This shows the transmission of each test configuration as a function of the displacement of the laser spot relative to the fibre core in microns.

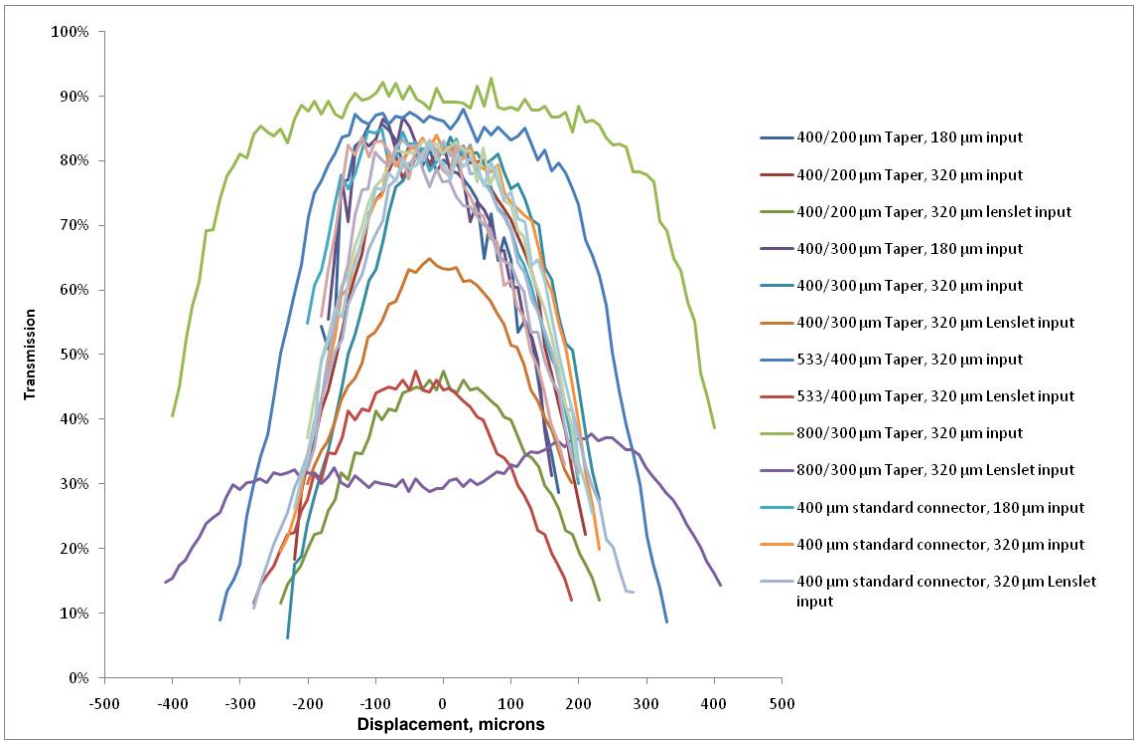

Figure 59 - Transmission data for all fibres and coupling methods

5.4.1. The Effect of Injection Method on Transmission

Figure 60 and Figure 61 illustrate the results obtained for the 400 µm diameter non-tapered fibres, for each of the two injection methods. Figure 60 and Figure 61 include the reference fibre (400 micron, standard connector) and injection method (lenslet array) as a comparison.

For the 320 µm input spots produced using the 100 mm lens, it is evident there is no difference between the three connector types detailed in Table 17. However, when we examine the 320 µm lenslet data, it is obvious that the silica-sleeved connector has a transmission some 8% lower than the other fibres (this connector is similar to the well-tip connector except the fibre is surrounded by a silica sleeve for the first 1-2 mm). This is due to the lenslet array having a high angle of incidence upon the fibre face, resulting in the light rays reflecting on the fibre/cladding interface in the region where the silica sleeve is present. It appears that the silica sleeve induces losses from the fibre in this region. The buffer is removed from the fibre in this region, and the manufacturing process may induce stress in the cladding, modifying the refractive index and hence

reducing the NA. This hypothesis is supported by previous experience of using fibres of this type at higher energies. A diffuse flash was often observed within the silica sleeve, distinctly different from the plasma formation characteristic of high energy laser-induced breakdown. It is likely this flash is due to energy deposition into the region.

The average displacement for a 10% and 20% loss is shown in Table 19. It can be seen that the 100 mm lens have a greater tolerance to misalignment than the lenslet array. Using the 100 mm lens with a 320 μm spot increases the tolerance by 60-80 μm compared to the lenslet array. This increased tolerance could both increase coupling reliability whilst reducing cost. It should be noted that the damage threshold for each injection method has not been determined, and is expected to be lower for the 100 mm lens, due to the decreased spatial uniformity.

Coupling Method	10% loss, μm	20% loss, μm
320 μm spot, 100 mm lens	203	260
320 μm spot, lenslet array	133	193

Table 19 - Displacement for transmission losses of 10% and 20% as measured for 400 μm fibres

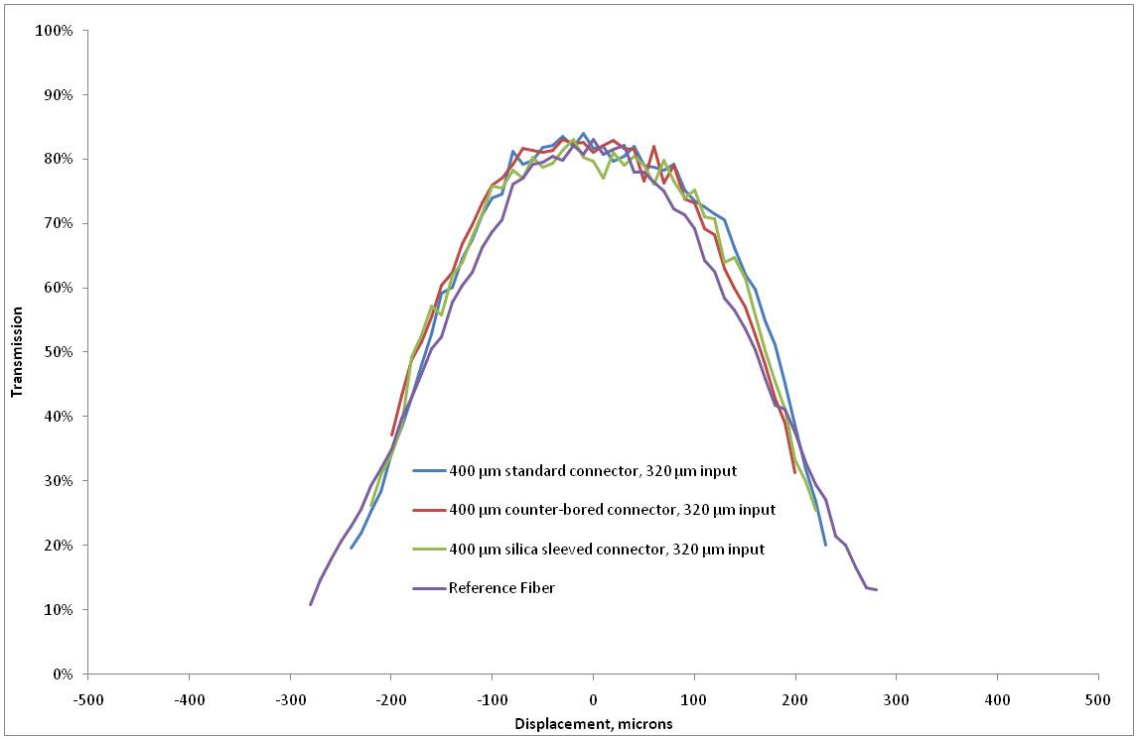

Figure 60 - Plot of transmission vs. displacement of laser beam relative to fibre for 400 µm fibres with 320 µm input

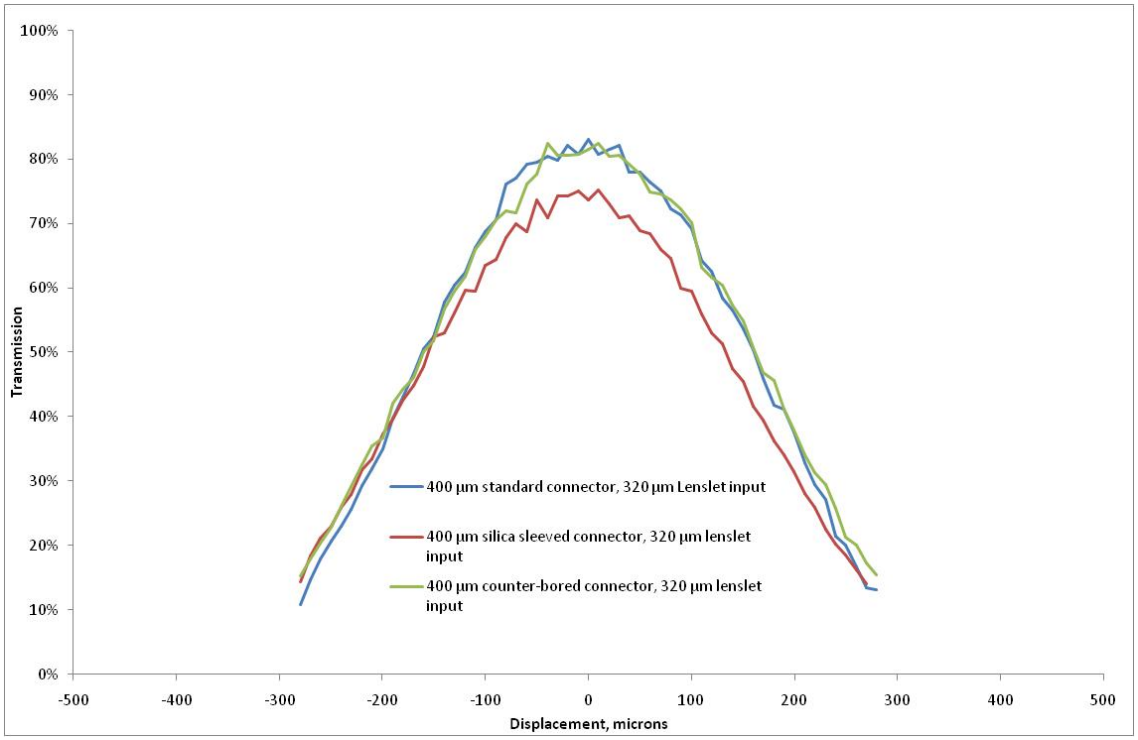

Figure 61 - Plot of transmission vs. displacement of laser beam relative to fibre for 400 µm fibres with 320 µm lenslet input

5.4.2. The Effect of Tapered Fibres on Transmission

Several tapered fibres designs were evaluated, investigating the effect of both taper length and input diameter to output diameter ratio. Figure 62 shows the results for a 320 µm input diameter beam produced by the 100 mm lens.

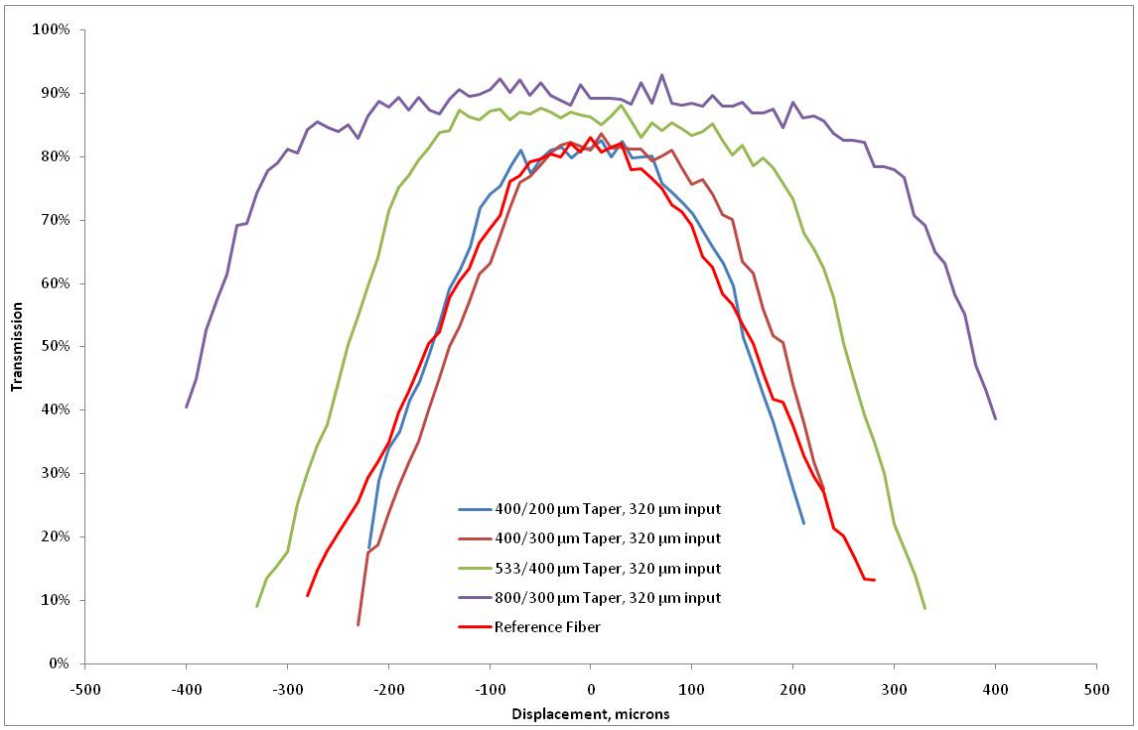

Figure 62 – Plot of transmission vs. displacement of laser beam relative to fibre for tapered fibres with 320 µm input

The two tapers with 400 µm input gave identical results, with a maximum transmission of around 84%. Both gave a displacement of 180 µm for a 10% loss, an improvement of 40 µm over the reference fibre. For a 20% loss, the average displacement was 225 µm, compared to 200 µm for the reference fibre.

The 533 to 400 µm taper gave slightly higher transmission, with a maximum of 88% transmission. The displacements for a 10% and 20% loss respectively were 320 and 400 µm. This offers a 200% improvement over the reference fibre, a substantial improvement. For a system utilizing a simple lens injection method similar to that used here, this taper could replace a 400 µm fibre and significantly ease tolerances.

The lenslet array was then used to couple the beam into the tapered fibres, with the results shown in Figure 63. It can be seen that all the fibres suffered a dramatic loss in transmission relative to the reference fibre, with peak transmission as low as 38% for the 800 to 300 µm taper. Clarkin et al [81] reported that losses in tapered optical fibres occur as a result of numerical aperture compression.

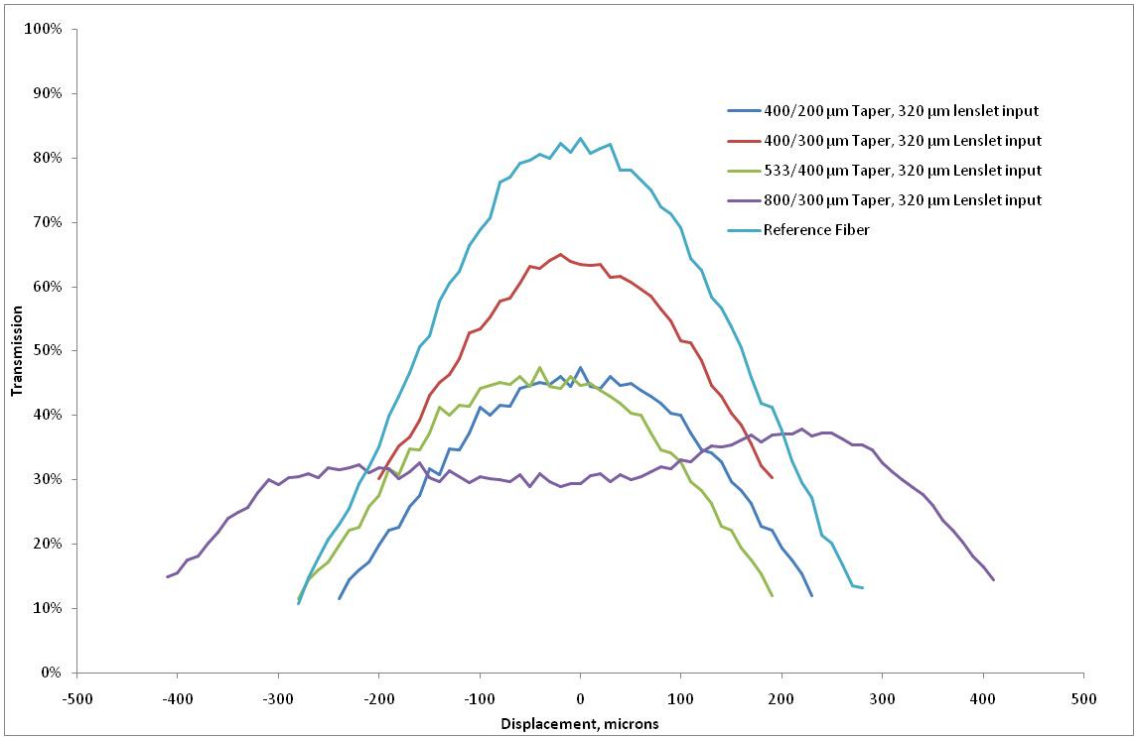

Figure 63 - Plot of transmission vs. displacement of laser beam relative to fibre for tapered fibres with 320 µm lenslet input

An optical fibre has a maximum angle below which light will be coupled into and conducted. Any light incident upon a fibre that exceeds this angle will be rejected. This is related to a fibre NA by the following equation:

$$NA = n.\sin\theta$$

Equation 10

where θ is the half-angle and n the refractive index outside the fibre (for air, n = 1).

A tapered optical fibre effectively reduces the numerical aperture as per the following equation:

$$NA = NA_o \frac{D_2}{D_1}$$

Equation 11

where NA is the effective numerical aperture, NA_0 the numerical aperture of the fibre composition (0.22 for all fibres tested here), D_2 the smallest fibre face diameter, and D_1 the largest fibre face diameter.

The effective NA of the injection optics can be calculated by calculating the angle subtended by the injection optics (as illustrated in Figure 64) and substituting into Equation 10 to give :

$$NA_{eff.} = n.\sin\left(\tan^{-1}\frac{D}{2L}\right)$$

Equation 12

which can be approximated to:

$$NA_{eff.} \approx n\frac{D}{2L}$$

Equation 13

where D is the beam diameter and L the focal length of the primary lens as

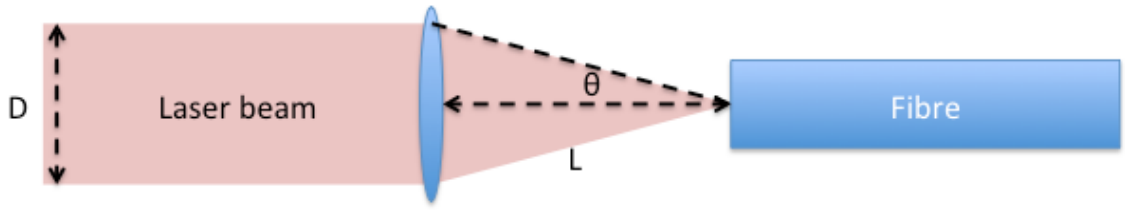

Figure 64 - Illustration of effective NA calculation

For the 100 mm lens with a beam diameter of 6 mm, we obtain an NA of 0.03, and for the lenslet array, an NA of 0.16.

By applying Equation 11 to the tapered fibres, the effective NA can be calculated, as shown in Table 20. These results broadly agree with the findings of Clarkin et al, that when the injection NA exceeds the effective NA, light is lost, and that this loss increases with the disparity between the NA's. However, for the two fibres with identical NA's, identical transmission is not observed. It could be expected that longer tapers would have higher transmission than shorter tapers, as the angle the core/cladding interface makes with the incoming light will be smaller. However, the opposite is observed, with the longer taper having lower transmission. We do not know the position of the taper within the fibre length, and it is possible that this varies between the two fibres. If there is any higher-order mode promotion prior to the taper, due to coils or bends, then a fibre with the tapered section some distance from the input may present a higher effective NA to the tapered section than that of a fibre with the tapered section close to or immediately at the input face.

Input Face Diameter, µm	Output Face Diameter, µm	Taper Length, mm	Effective NA	Max. Trans.
533	400	2-3	0.165	82%
400	300	50	0.165	65%
400	200	50	0.11	47%
800	300	2000	0.08	38%

Table 20 - Transmission losses in tapered fibres

It is difficult to avoid some higher-order mode promotion, and hence if a tapered fibre is used in this manner, it is desirable that the tapered section be located close to, or at, the input face, to ensure a correctly-matched injection NA is presented to the tapered section.

A curious result is observed with the largest taper, an 800-300 µm taper as seen in Figure 63. The displacement versus transmission curve has an obvious "m" shape, with a central minimum. This was not evident with the 100 mm lens (Figure 62), and it is logical to conclude this is due to the greater injection NA. The other substantial difference is that the taper in this fibre occurs over the entire fibre length. The fibre routing was not controlled due to the fibre length relative to the optical table upon

which the experiment was performed; hence loops, coils and other bends were present. For the other fibres, the tapered section is unlikely to experience significant curvature, being of much shorter length. With a continuous taper, the tapered section is likely to experience significant curvature, and this may explain this unusual result, though the exact mechanism is unknown.

5.4.3. Discussion on the Use of Tapered Optical Fibres to Increase Connector Tolerance

There are two main interfaces to be considered in a laser detonator system. Firstly, the laser to fibre connection, and secondly, the fibre to detonator interface. The fibre to detonator interface is likely to be less sensitive to misalignment; any misalignment at this interface may result in an off-centre initiation of the explosive fill, which is likely to be smoothed over the length of the fill. This interface is likely also to be permanently bonded, to provide an environmental seal and minimise volume. This has an important consequence, that is, the fibre/detonator component cannot easily be actively aligned to the laser. Therefore, the tolerances at the fibre/laser interface must be controlled to eliminate the need for active alignment.

It is possible to incorporate methods within the laser to enable alignment to the laser fibre connector, such as alignment wedges. These can essentially compensate for larger tolerances within the laser components, and the beam can thus be accurately aligned relative to the laser fibre connector. The critical tolerance then becomes that of the fibre concentricity. The data presented here effectively assesses the acceptable tolerance of the fibre concentricity.

The baseline configuration of a lenslet array injecting a 320 μm diameter spot into a 400 μm diameter fibre with standard connectors has a displacement of 140 μm for a 10% loss, and hence a required concentricity of 70 μm. These fibres are typically specified with a concentricity of 50 μm, within the acceptable range. However, increasing this concentricity may reduce the cost of these fibres.

By replacing the lenslet array with a simple 100 mm focal length plano-convex lens, the required concentricity is increased to 120 μm, a substantial improvement. However, this

injection method has a significantly larger volume, and presents a less uniform beam profile, which is likely to result in reduced fibre damage thresholds.

Tolerances may also be increased by replacing the 400 μm diameter fibre with a tapered fibre, presenting a larger area to the incident beam. By increasing the input face to 533 μm diameter, the concentricity could be increased to 160 μm and 260 μm with an 800 μm input face.

The use of tapered fibres with a lenslet array, or other high NA injection method introduces significant problems. A substantial loss in transmission is observed due to the reduction in NA of the fibre. It is possible to reduce this loss by increasing the focal length of the lenslet array and focusing lens. To match the NA of the 800-300 μm taper, the focal length would double from 19 mm to 38 mm. This is not a large increase in volume. However, this does not take into account any mode promotion within the fibre, and thus may require a longer focal length lens.

5.5. A High-energy Fibre to Fibre Connection

A high-energy fibre to fibre connection offers a significant advantage for the practical application of a laser detonator system. By separating the optical fibre into two sections, the free-space beam produced by the laser fireset can be actively aligned to an optical fibre which then forms part of the laser fireset. This fibre can also form part of an environmental seal for the fireset, preventing contamination of the laser.

A fibre-to-fibre connection system for a laser detonator system is proposed as follows. Firstly, a microlens array is used to image the laser beam into multiple beamlets, which are then collapsed to a single overlapping beam using a short (15-40 mm) focal length lens. This homogenizes the spatial intensity of the beam whilst dissipating any beam waists that could otherwise result in fibre damage. The resulting beam, is focused to a diameter of 400-450 μm onto the input face of a tapered optical fibre 2 m in length, with a 600 μm diameter input face. The output is tapered down to 300 μm diameter over the final 50 mm of the fibre length. The output face is proximity coupled to a vacuum-compatible fibre feed-through, which contains a short (~50 mm) length of 320 μm diameter optical fibre. This mitigates any misalignment between the two fibre faces as a result of the concentricity of each fibre ferrule. The output of this feed-through is then proximity coupled to the final, disposable fibre, typically part of the laser detonator. This fibre is 365 μm diameter with a length of 0.2-1.0 m. Again, the increase in fibre diameter ensures that the fibre faces remain aligned with the concentricity of the fibre ferrules.

5.5.1. Experimental Method for the Testing of a High Energy Fibre to Fibre Connection

A Big Sky CFR400 Nd:YAG laser operating at the fundamental wavelength of 1064 nm was used with a maximum output energy of 400 mJ at a pulse length of 12 ns. The beam diameter was approximately 6 mm.

Two micro-lens arrays were used with short focal length (30 & 40 mm) primary lenses to obtain beam diameters of 400 μm and 450 μm, 66-75% of the tapered fibre input core

diameter of 600 µm. An Ophir thermal energy sensor was used to determine the energy loss through the fibre injection optics.

A schematic of the experimental setup is shown in Figure 65.

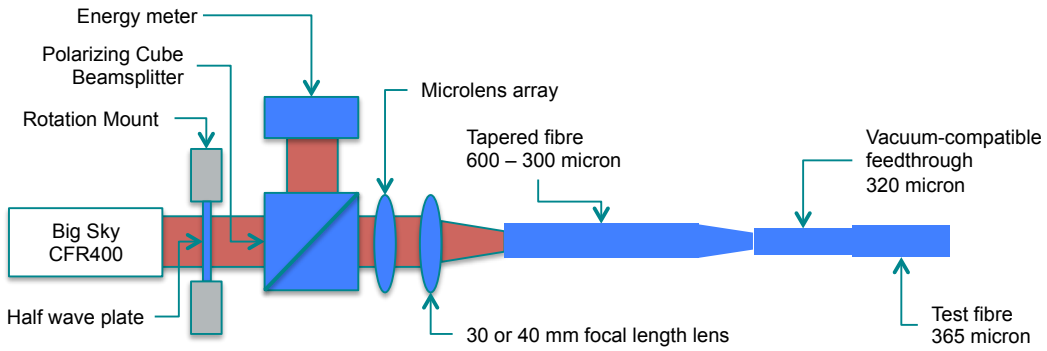

Figure 65 - Experimental setup for the testing of a high-energy fibre to fibre connection

5.5.2. Transmission and Damage Threshold of Tapered Fibres

The transmission and damage threshold for three identical tapered fibres (serial numbers E-12-031/07, E-12-31/02 and E-31-31/11) were measured to establish a baseline for the fibre-to-fibre connection study. The 30 mm focal length lens was used to match the acceptance angle of the tapered fibre. The numerical aperture (NA) of a tapered fibre is reduced by the ratio of the fibre face diameters as per Section 5.4, resulting in this case in a reduction from 0.22 to 0.11. The acceptance angle can be calculated using Equation 10 to give an acceptance angle of 6.32° is obtained. For a 6 mm diameter beam, the angle that the beam makes with the fibre is 5.71°. This ensures that the laser pulse is coupled into the tapered fibre with maximum efficiency.

The average transmission, calculated as the average of the first five shots on each fibre, is shown in Table 21. The maximum theoretical transmission of an optical fibre is 92.2%, accounting for Fresnel reflections (4%) at each interface. The discrepancy from theory is attributed to energy in the laser beam outside of the focussed spot that does not impinge on the optical fibre core, and is therefore not transmitted. This energy is measured by the larger diameter energy meter, but is of insufficient intensity to be visible on the beam profiling system. Additionally, scattering from microscopic imperfections at each fibre face will result in energy loss. The transmission obtained is

comparable to that of non-tapered fibres, suggesting that the numerical aperture and acceptable angle matching was successful.

	Transmission	Standard Deviation
Tapered fibre 1	79.4%	1.2%
Tapered fibre 2	82.3%	1.8%
Tapered fibre 3	80.5%	0.8%
Average	80.7%	1.8%

Table 21 – Transmission of tapered fibres

The damage testing results on the tapered fibres is shown in Figure 66, Figure 67 and Figure 68. The incident and transmitted energies are plotted, along with the transmission. Damage to the fibre is shown as a reduction in transmission, as a result of energy absorption by plasma formed on one or more fibre faces.

The maximum energy transmitted before damage was 40.3 mJ, 41.4 mJ and 79.8 mJ for tapered fibre 1, 2 & 3 respectively, corresponding to fluences (energy density) of 57.0 $J.cm^{-2}$, 58.6 $J.cm^{-2}$ and 112.9 $J.cm^{-2}$ at the 300 µm diameter output face. This is comfortably in excess of the 35 $J.cm^{-2}$ required for detonator initiation. No pre-conditioning, where plasma formation at lower fluences allows for subsequent transmission at higher fluences, was observed, with catastrophic damage occurring on the first plasma formation. Images of the damage to the fibre faces, obtained using a Westover fibre inspection microscope, are shown in Figure 69, Figure 70 and Figure 71. The greater loss of transmission for tapered fibre 1 can be correlated to the greater damage to the output face, with a large area of material ablated from the fibre face. No damage was observed to the input faces and plasma formation was not observed at the input face.

Tapered fibre 3 was able to transmit approximately twice the energy (79.8 mJ vs. 40.9 mJ) without damage compared to tapered fibres 1 & 2. Examination of the damage to tapered fibre 3 reveals moderate damage to the output face, and plasma formation was observed at the input face. A small region of damage was observed on the fibre input face, which is believed to be the limiting case for energy transmission for this fibre. It is not clear why tapered fibre 3 did not suffer catastrophic damage at the output face as per

tapered fibres 1 & 2. Output face damage is believed to have been caused by Fresnel reflections and scattering increasing the energy density immediately prior to the output face, resulting in internal breakdown and ejection of material. It is possible that a higher-quality finish was achieved for this fibre, minimising any increase in energy density at the output face. It should also be noted that the tapered fibres had well-tip ferrules (with the fibre levitated in free-space) and hence cleaning was problematic. This may have resulted in contamination of the fibre faces with dust or debris, forming energy absorption sites and hence premature plasma formation.

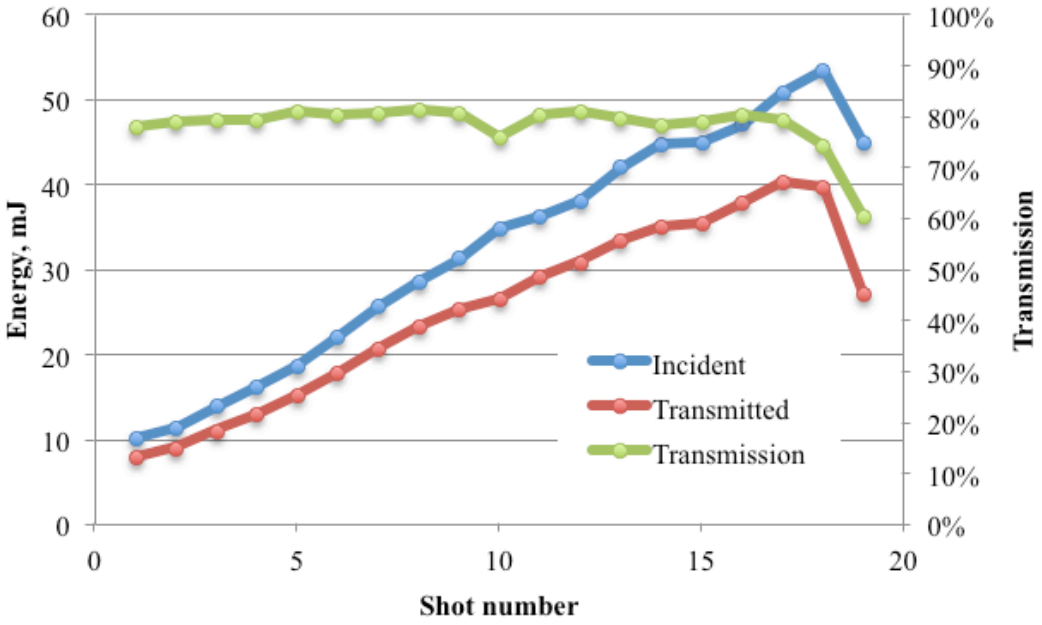

Figure 66 - Damage testing results for tapered fibre 1

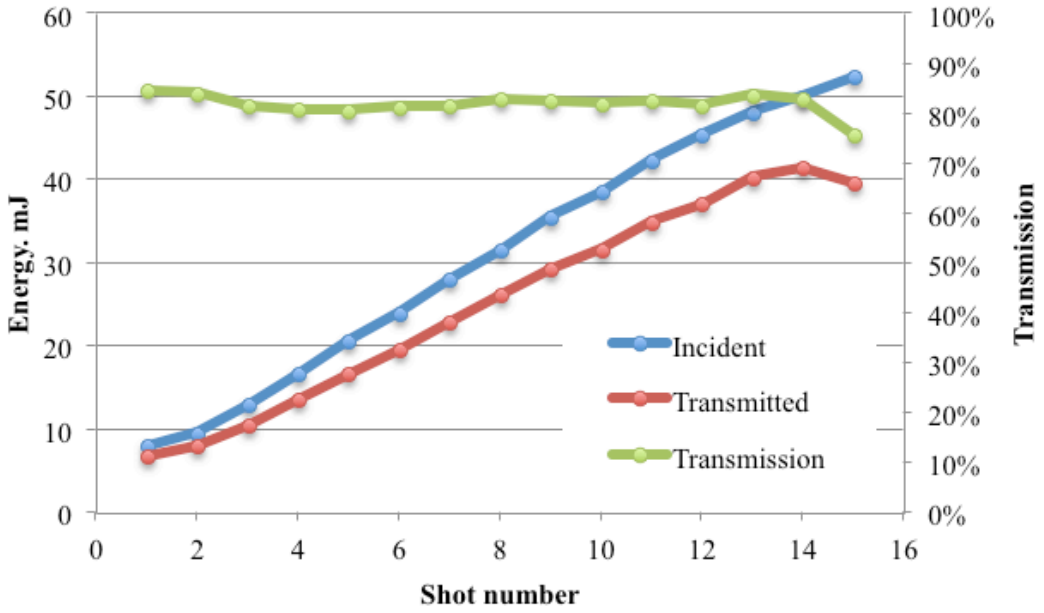

Figure 67 - Damage testing results for tapered fibre 2

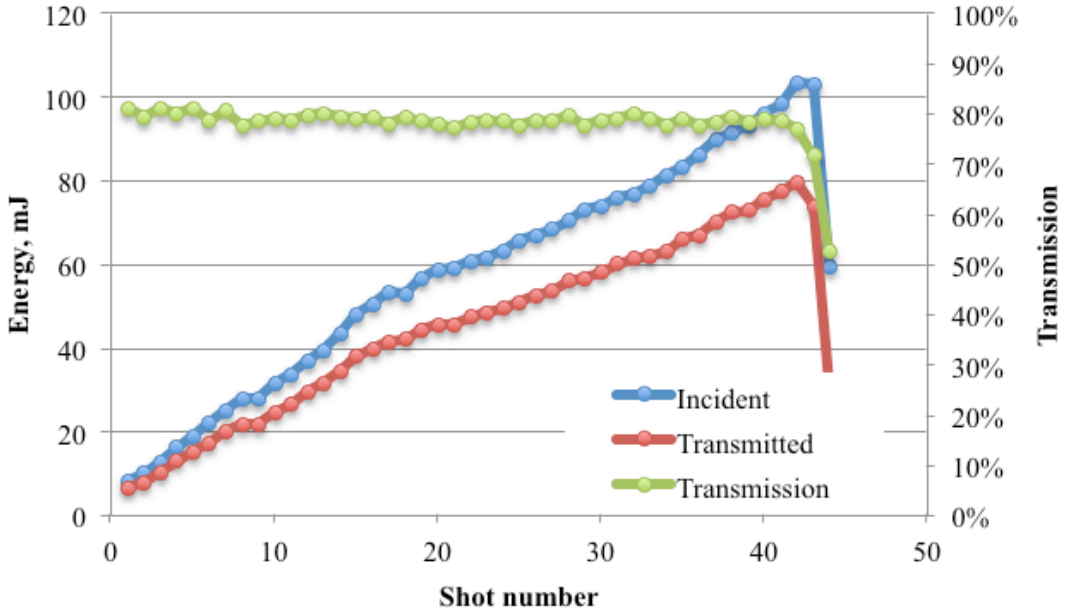

Figure 68 -Damage testing results for tapered fibre 3

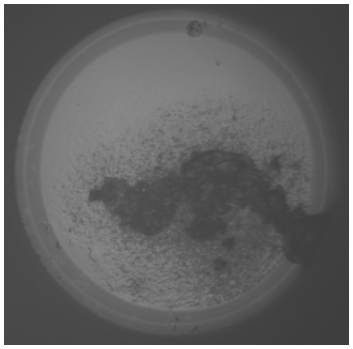

Figure 69 - Output face of tapered fibre 1

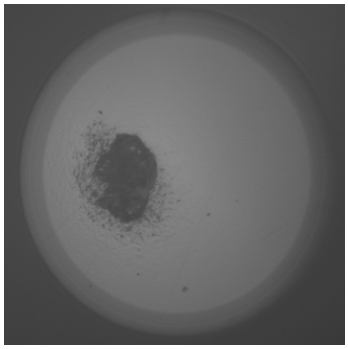

Figure 70 - Output face of tapered fibre 2

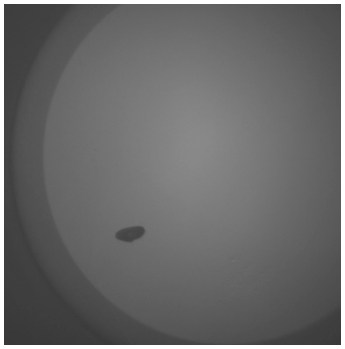

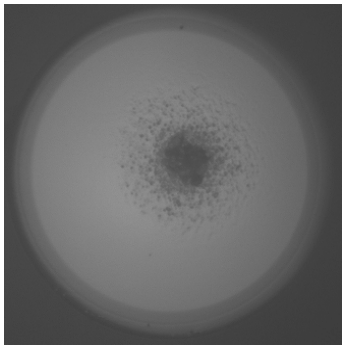

Figure 71 - Input face (top) and output face (bottom) of tapered fibre 3

5.5.2.1. Transmission and Damage Threshold of Tapered Fibre with Vacuum Feedthrough and Test Fibre

The next configuration tested was the intended design solution as described above: a tapered fibre proximately coupled to a vacuum fibre feedthrough, which was then connected to a disposable test fibre.

A fresh tapered fibre (serial number E-12-31/03) was connected to a vacuum fibre feedthrough (serial number 1084) and a disposable test fibre. The transmission of the tapered fibre was first measured at 85.6%. The transmission of the complete assembly was then measured as 46.7%. The maximum theoretical transmission, accounting for Fresnel reflection, is 78.3% (0.96^6 x 100%), assuming a fibre/air/fibre interface at each connection and complete collection of the input energy by the tapered fibre. Accounting

for the measured transmission of the tapered fibre, the maximum theoretical transmission becomes 72.7% (0.96^4 x 0.856 x 100%).

The damage testing results are shown in Figure 72. Shot 1 represents the tapered fibre only, without the vacuum feedthrough or test fibre. A drop in transmission, corresponding to a plasma formation event, is observed at an incident energy of 41.0 mJ. In contrast to the tapered fibres, discussed earlier, this did not result in catastrophic damage and energy could still be transmitted with no subsequent loss of transmission. A second drop in transmission, at an incident energy of 40.0 mJ, was then observed. This resulted in catastrophic damage. Inspection of the tapered fibre output revealed a loss of material over some 25% of the fibre core. It was not possible to inspect the input face of the vacuum feedthrough with the instruments available, as the fibre face is recessed within the SMA ferrule.

The combination of tapered fibre, vacuum feedthrough and test fibre was able to transmit an average of 17.2 mJ without damage, corresponding to a fluence of 24.3 $J.cm^{-2}$ at the tapered fibre output. This is below the fluence of 35 $J.cm^{-2}$ required for detonator initiation. It was suspected that the inability to clean and inspect vacuum feedthrough faces prior to use contributed to this result. To investigate this hypothesis, it was decided to test a tapered fibre to test fibre configuration, omitting the vacuum feedthrough, as the test fibre can be cleaned and inspected.

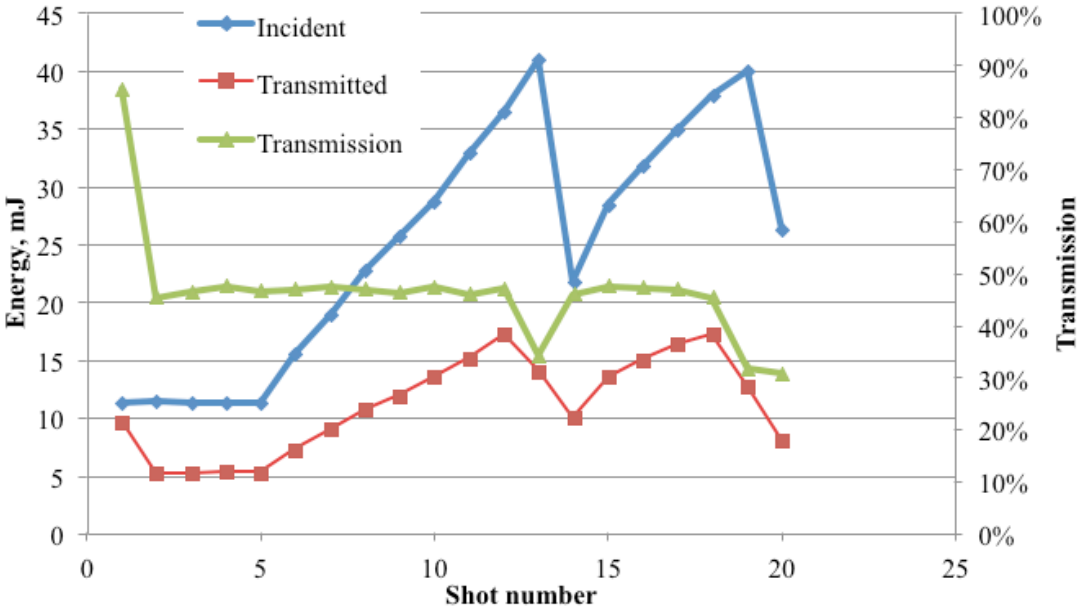

Figure 72 - Damage threshold testing for tapered fibre / vacuum feedthrough / test fibre

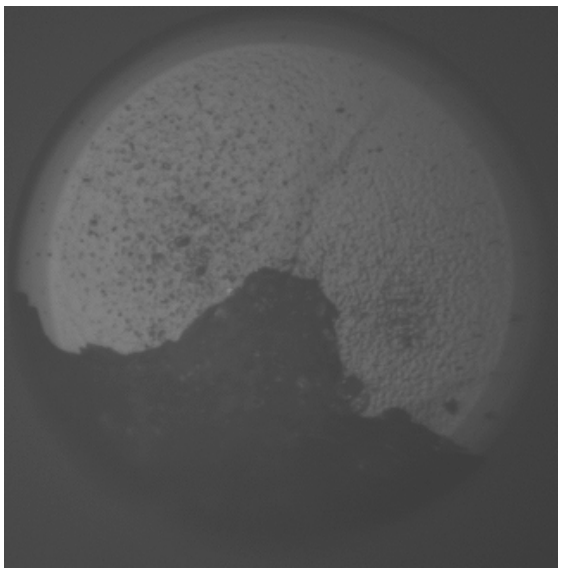

Figure 73 - Damage to output face of tapered fibre

5.5.2.2. Transmission and Damage Threshold of Tapered Fibre with Test Fibre

This configuration omitted the vacuum feedthrough to investigate the performance of a simple fibre-to-fibre connection. As stocks of the 365 μm core diameter test fibres were limited, and to eliminate the possibility of lateral misalignment, a 400 μm core diameter test fibre was used. An SMA/SMA sleeve connector was used to join the two fibres.

The damage testing results can be seen in Figure 74, with the first 3 data points represented the fresh tapered fibre (serial number E-12-031/10) only. The transmission of the tapered fibre was first measured at 87.4%. The transmission of the complete assembly was then measured as 46.7%. The maximum theoretical transmission, accounting for Fresnel reflection, is 85.0% (0.96^4 x 100%), assuming a fibre/air/fibre interface at each connection and complete collection of the input energy by the tapered fibre. Accounting for the measured transmission of the tapered fibre, the maximum theoretical transmission becomes 80.5%.

This configuration was able to transmit 20.2 mJ without damage corresponding to a fluence at the tapered fibre output of 28.6 $J.cm^{-2}$.

Catastrophic damage was observed at an incident energy of 37.0 mJ. Inspection of the fibre faces, Figure 75 & Figure 76, revealed significant damage to both faces, with material removed from approximately 50% of the tapered fibre output face and cracking and material removal from the test fibre input. It is likely that plasma formation on the tapered fibre output resulted in the damage to the test fibre input.

Removal of the vacuum feedthrough resulted in a significant improvement in transmission, but no improvement in damage threshold, with catastrophic damage occurring at the same location, the tapered fibre output, and at approximately the same incident energy.

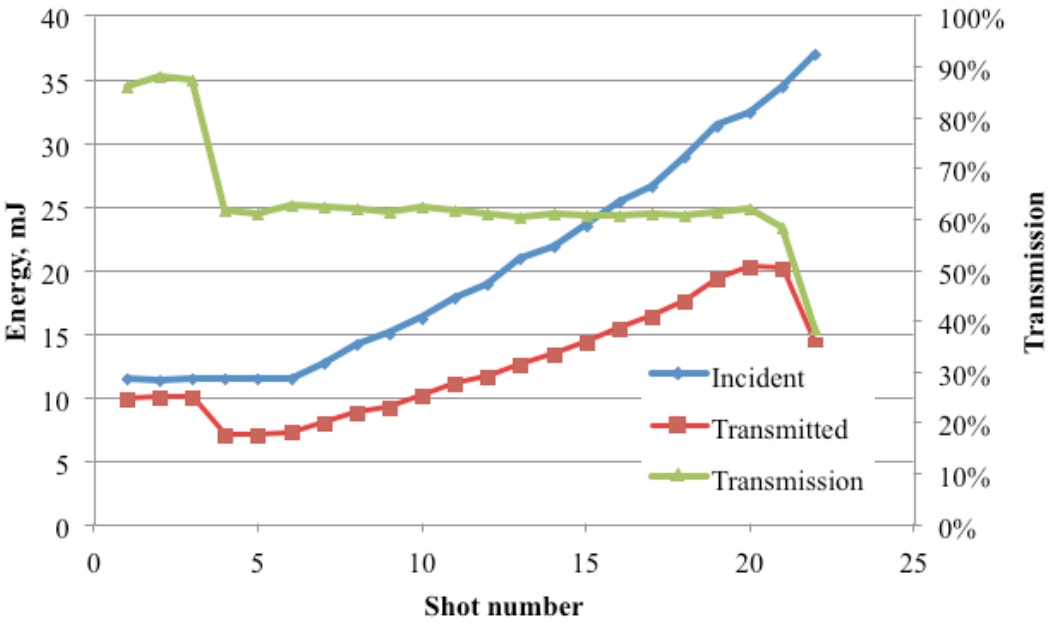

Figure 74 - Damage testing results for tapered fibre and test fibre

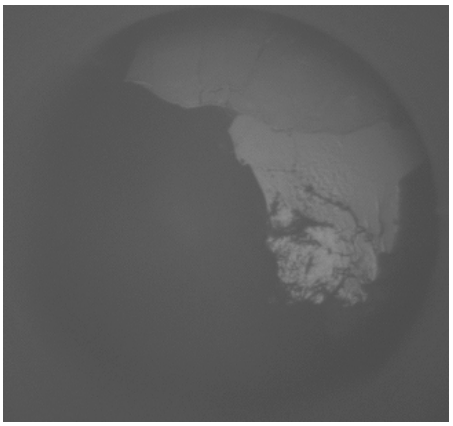

Figure 75 - Output face of tapered fibre

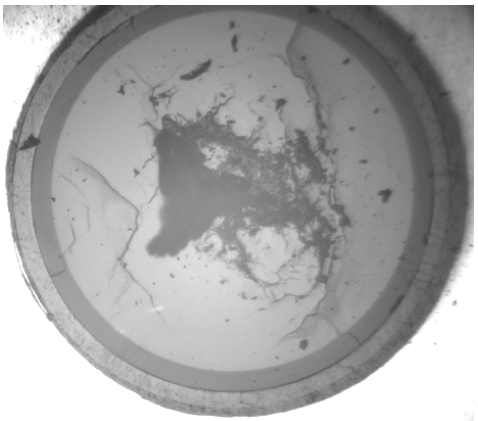

Figure 76 - Input face of test fibre

It was hypothesised that the taper location, at the output of the tapered fibre, was the cause of the low damage threshold and transmission. As the injection method was designed to closely match the overall numerical aperture of the tapered fibre, bends within the non-tapered section of the tapered fibre could result in the promotion of higher order modes, which could not be propagated by the taper. These higher order modes would be coupled into the fibre cladding where they would interact with the interface between the cladding, the air and the subsequent fibre (the vacuum

feedthrough or test fibre). The fibre cladding diameter is 360 μm, large enough to impinge on the epoxy surrounding the vacuum feedthrough and result in plasma formation. This hypothesis is supported by inspection of the tapered fibre output (Figure 73), where the region of damage can be seen to extend to the fibre/cladding interface.

To investigate this hypothesis, a second primary lens was used for the injection into the tapered fibre, with a 40 mm focal length lens. This results in an injection angle of 4.29°, well below the acceptance angle of the fibre, 6.32°. This would minimise any energy loss into the cladding as the result of mode promotion within the non-tapered section.

5.5.3. Comparison of Tapered Fibre Output for 30 mm and 40 mm Focal Length Lenses

Beam profiles were obtained for tapered fibre outputs with both 30 mm and 40 mm focal length lenses, shown in Figure 77 and Figure 78. It can be seen there is a reduction in the energy intensity in the cladding (seen as the lower intensity region surrounding the core) relative to the energy intensity in the core for the 40 mm focal length lens compared to the 30 mm focal length lens.

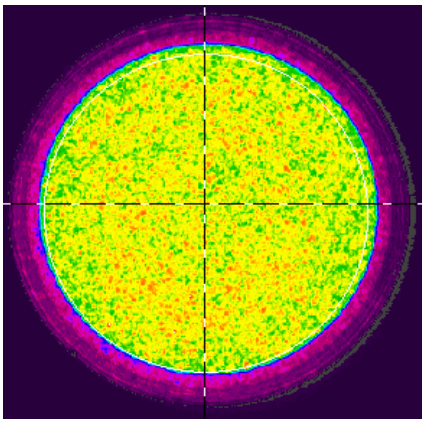

Figure 77 - Tapered fibre output beam profile with 30 mm focal length lens

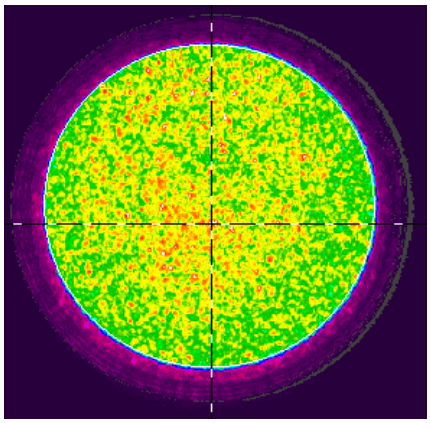

Figure 78 - Tapered fibre output beam profile with 40 mm focal length lens

It is evident that closely matching the numerical aperture of the injection optics to the tapered fibre results in energy coupling into the cladding when the taper is located at the

output of the fibre. Mode promotion within the non-tapered section results in modes that cannot be propagated by the tapered section, and are coupled into the cladding. As the cladding is larger in diameter than the vacuum feedthrough fibre core, this results in energy impinging upon the cladding and epoxy surrounding the vacuum feedthrough fibre core, resulting in damage and a loss of transmission. This can be reduced by increasing the focal length of the injection optics, reducing the number of modes injected into the taper.

5.5.3.1. Transmission and Damage Threshold of Tapered Fibre with Test Fibre, 40 mm Focal Length Lens

This configuration omitted the vacuum feedthrough to investigate the performance of a simple fibre-to-fibre connection, and used a 40 mm focal length lens to investigate the hypothesis that energy loss into the cladding was adversely affecting performance. The previously used 400 μm diameter fibre may have gathered light from the 360 μm diameter cladding of the tapered fibre output, thus the 365 μm core test fibre (serial B-12-079/3) was used to minimise any cladding transmission. An SMA/SMA sleeve connector was used to join the two fibres. As before, the transmission of the tapered fibre only was measured, at 81.2%, comparable to that previously measured, indicating the change of lens focal length had no effect on transmission.

To preserve the limited stocks of tapered fibres remaining, it was decided to attempt to avoid destructive testing, by limiting the transmitted energy to 25 mJ, approximately 25 $J.cm^{-2}$ at the output of the 365 μm diameter test fibre. The damage testing results can be seen in Figure 79, with the results for the 30 mm lens shown for comparison.

The transmission of the tapered fibre was first measured at 81.2%. The transmission of the complete assembly was then measured as 69.0%. The maximum theoretical transmission, accounting for Fresnel reflection, is 85.0% (0.96^4 x 100%), assuming a fibre/air/fibre interface at each connection and complete collection of the input energy by the tapered fibre. Accounting for the measured transmission of the tapered fibre, the maximum theoretical transmission becomes 74.8%.

The measured transmission, 69.0%, is substantially higher than for the 30 mm focal length lens configuration, which averaged 62.2% with a larger diameter (400 µm) test fibre. 10 successive shots with a transmitted energy in excess of 25 mJ without damage were performed, again substantially higher than with a 30 mm focal length lens, which was able to transmit 20.2 mJ before damage.

These results appear to confirm the hypothesis that mode promotion within the non-tapered section of the tapered fibre results in energy loss into the cladding, resulting in subsequent loss of transmission and premature damage.

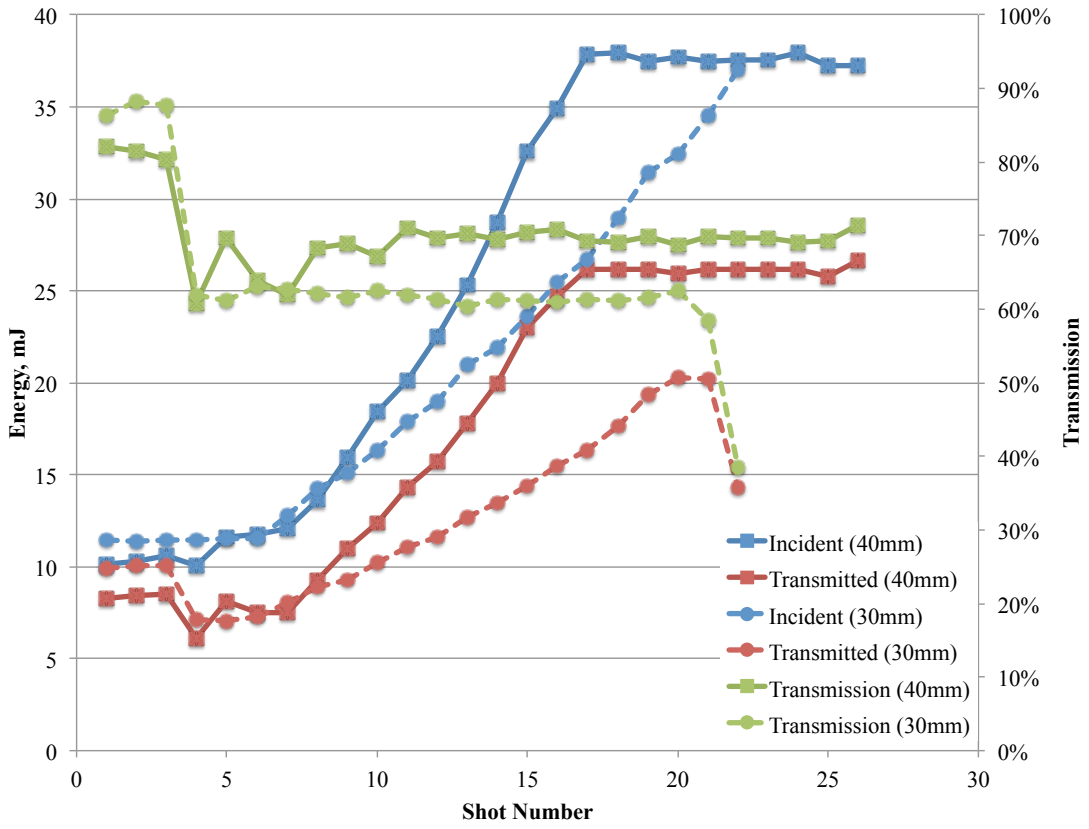

Figure 79 - Damage testing results for tapered fibre with test fibre and 40 mm focal length lens (solid lines), and 30 mm focal length lens (dashed lines).

Following this result, it was decided to test the tapered fibre, vacuum feedthrough, and test fibre configuration with the 40 mm focal length, to investigate whether a similar increase in performance was obtained.

5.5.3.2. Tapered Fibre with Vacuum Feedthrough and Test Fibre, 40 mm Focal Length Lens

The next configuration tested was the intended design solution as described above: a tapered fibre proximately coupled to a vacuum fibre feedthrough, which was then connected to a disposable test fibre. The 30 mm lens used for this configuration previously was replaced with a 40 mm lens.

A fresh tapered fibre (serial number E-12-31/04) was connected to a vacuum fibre feedthrough (serial number 1087) and a 400 μm diameter core test fibre (serial 1040). The stocks of 365 μm diameter core test fibres had been exhausted, necessitating the change to a 400 μm core test fibre. However, damage previously occurred at the tapered fibre / vacuum feedthrough interface, so this change should have minimal effect on the result.

The transmission of the tapered fibre was first measured at 89.8%. The transmission of the complete assembly was then measured as 60.2%. The maximum theoretical transmission, accounting for Fresnel reflection, is 78.2% (0.96^6 x 100%), assuming a fibre/air/fibre interface at each connection and complete collection of the input energy by the tapered fibre. Accounting for the measured transmission of the tapered fibre, the maximum theoretical transmission becomes 76.3%.

In the previously tested configuration with a 30 mm focal length lens, a transmission of 46.7% was obtained. This supports the hypothesis that mode promotion within the non-tapered section of the tapered fibre results in energy loss into the cladding, resulting in subsequent loss of transmission and premature damage.

Losses of transmission were observed on several shots with the 40 mm focal length lens, as seen in Figure 80 (where the 30 mm focal length data is shown also for comparison), which did not result in catastrophic damage, with transmission recovering upon a reduction in energy. Conditioning, or annealing, of the fibre assembly was observed, with each successive loss of transmission occurring at a higher energy. Catastrophic damage was observed at an incident energy of 39.9 mJ, with an energy of 22.0 mJ successfully transmitted on the previous shot.

It is possible to estimate the energy transmitted by the tapered fibre, as the transmission of the tapered fibre alone was measured, by scaling the measured incident energy by the average transmission of the tapered fibre alone. The tapered fibre was able to transmit approximately 36 mJ prior to damage. This compares favourably to the tapered fibres damage tested earlier, where tapered fibres 1 & 2 were able to transmit an average of 40.9 mJ prior to damage.

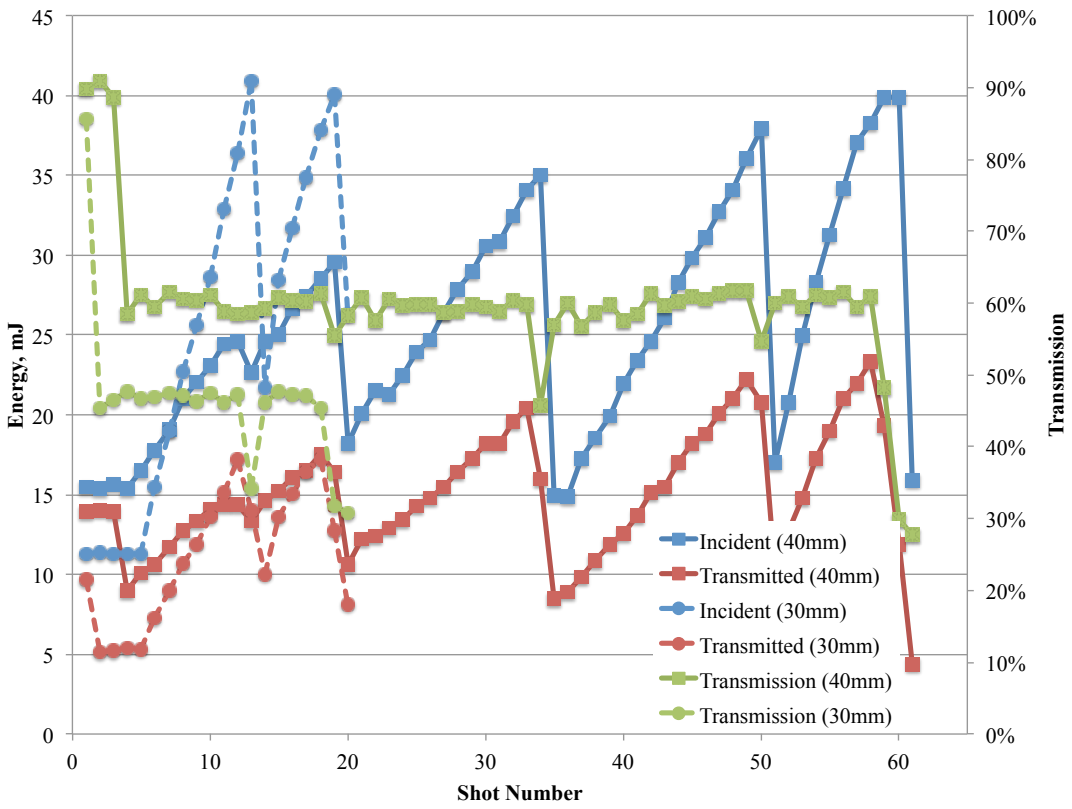

Figure 80 - Damage testing results for tapered fibre, vacuum feedthrough and test fibre, with 40 mm focal length lens (solid lines), and 30 mm focal length lens (dashed lines).

Inspection of the tapered fibre output face, Figure 81, revealed a large area of material, located centrally on the fibre face, with no material removal extending to the core/cladding interface. The input face of the test fibre, Figure 82, shows no evidence of damage. As before, it was not possible to inspect the faces of the vacuum feedthrough.

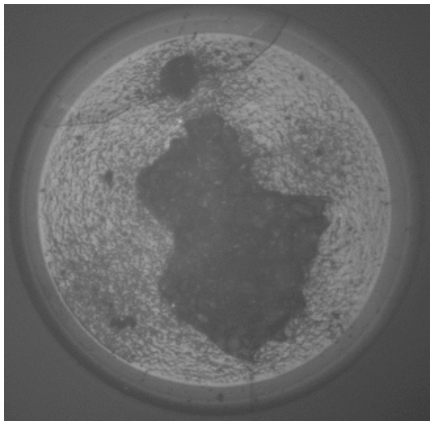

Figure 81 – Output face of tapered fibre

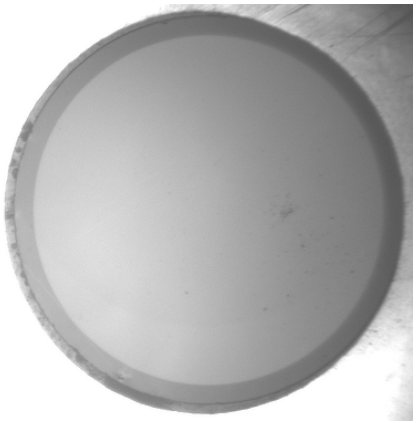

Figure 82 – Input face of 400 μm test fibre

5.5.4. Discussion on a High-energy Fibre to Fibre Connection

Several configurations of a high-energy fibre-to-fibre connection for use in laser detonator systems have been evaluated, with varying degrees of success. All configurations tested use a microlens array to focus the laser into a tapered fibre, which reduces the fibre diameter below that of the test fibre, which is proximity-coupled to the output of the tapered fibre. This allows the beam to diverge into the test fibre.

Two configurations show promise for practical implementation, both using a 40 mm focal length lens to initially underfill the tapered fibre, to allow for mode promotion. Firstly, a simple fibre-to-fibre connection between the tapered fibre and a test fibre was able to transmit in excess of 25 mJ (23.9 $J.cm^{-2}$ at the 365 μm diameter output) without damage, though the damage threshold was not established. This configuration is suitable for simple applications that do not require an environmental or vacuum seal between the laser fireset and the detonator. Secondly, a fibre-to-fibre connection with a vacuum feedthrough between the tapered fibre and the test fibre was able to transmit 22.0 mJ (21.0 $J.cm^{-2}$ at the 365 μm diameter output) prior to damage. Whilst this is not sufficient for practical applications, further refinement of the component designs to permit inspection and cleaning should allow this damage threshold to be increased to an adequate level.

It is clear that the capability to inspect and clean all fibre faces within the system is critical, and as such, receptacle-type connections should be avoided where possible. Instead, male fibre ferrules should be joined using mating sleeves, to allow easy inspection and cleaning of the fibre faces.

5.6. Summary of Optical Fibre Coupling

Previous research, as discussed in Section 2.1, has been limited to maximising the damage threshold of non-connectorised fibres. This is not suitable for incorporation into a laser detonator system.

Several areas have been studied to aid the development of a optical fibre suitable for use in a laser detonator system.

A variety of polishing methods were evaluated to determine which method had the highest damage threshold, for zirconia and steel ferrules. It was found that each ferrule type required a different polishing method, due to the differences in hardness between the silica fibre, the ferrule material and the polishing media. Both ferrule types were able to transmit a fluence in excess of 50 $J.cm^{-2}$ without damage, in excess of the estimated fluence required for explosive initiation of 20 $J.cm^{-2}$.

Novel optical fibres were evaluated as they may offer advantages for laser detonator system design. Tapered optical fibres, which increase the area into which the laser energy is coupled were tested. The damage threshold and transmission of tapered optical fibres was found to be highly dependant upon the coupling method used, in particular, focussed before the fibre, or focussing within the fibre. Side-fire optical fibres, with a shaped output face to direct the output at 90 degrees, allow for greater flexibility in the design of the detonator, by allowing the fibre to enter from the side of the detonator, instead of from the rear. Two designs of side-fire optical fibres were found to have acceptable damage thresholds and output beam quality, but a design that offered both has not been determined.

The use of tapered optical fibres to increase the tolerances required for the coupling of the laser into the optical fibre was evaluated, using both a lenslet array coupling method and a plano-convex lens coupling method. A non-tapered fibre using a lenslet array coupling method had a required tolerance of 70 μm. Tapered optical fibres were able to increase this to 260 μm.

A high-energy fibre to fibre connection was developed, offering a significant advantage for the practical application of a laser detonator system. By separating the optical fibre

into two sections, the free-space beam produced by the laser fireset can be actively aligned to an optical fibre which then forms part of the laser fireset. This fibre can also form part of an environmental seal for the fireset, preventing contamination of the laser. To aid this, the lenslet array injection method was optimised for tapered fibres by matching the reduced NA of the tapered fibres, increasing the transmission to 80%, comparable to that of non-tapered fibres. Two designs were produced. The first design, with a simple fibre to fibre connection, had a damage threshold of 23.9 $J.cm^{-2}$. This design is suitable for applications where an environmental seal between the laser fireset and detonator is not required. The second design, with a vacuum feedthrough between the two fibres, had a damage threshold of 21.0 $J.cm^{-2}$. Whilst both designs have a damage threshold above the estimated fluence required for explosive initiation (20 $J.cm^{-2}$), the margin is inadequate. Methods for improving the damage threshold were proposed.

The baseline optical fibre was changed from Polymicro FIP400440480 to Thorlabs FG365UEC. The specifications of each fibre are shown in Table 22. A schematic of Thorlabs FG365UEC is shown in Figure 83. This optical fibre has a damage threshold in excess of 50 $J.cm^{-2}$ when used with a steel ferrule and a lenslet array coupling method.

Manufacturer	Part number	Core diameter, µm	Cladding diameter, µm	Buffer or 2nd cladding diameter, µm	Jacket diameter, µm
Polymicro	FIP400440480	400 ± 8	440 ± 9	480 ± 7	
		Fused silica	Fluorine-doped silica	Polyimide	
Thorlabs	FG365UEC	365 ± 14	400 ± 8	425 ± 10	730 ± 30
		Fused silica	Fluorine-doped silica	TEQS	Tefzel

Table 22 - Optical fibre specifications

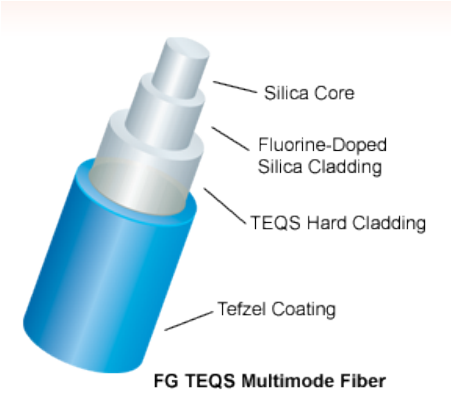

Figure 83 - Schematic of Thorlabs FG365UEC optical fibre

This change was made for several reasons:

1. The reduction in core diameter from 400 µm to 365 µm reduces the estimated energy required for initiation (a fluence of 20 $J.cm^{-2}$) from 25 mJ to 21 mJ, a 17% reduction. This can reduce the laser energy required.
2. The Tefzel jacket offers increased robustness. Experience from handling both fibre types during experimental work confirms this.
3. FG365UEC has reduced transmission losses in ionizing radiation environments, that may be experienced in use [78; 82].

CHAPTER 6: FLYER LAUNCH AND CHARACTERISATION

6.1. Introduction

In order to improve flyer performance, in particular velocity, multi-layer flyer plates were used, as this allowed the retention of a well-characterized impactor layer, whilst varying the absorption, ablation and insulating layers. The flyers evaluated here comprised up to four layers. A first absorption layer of a few nanometres provided an initial interface for the laser energy to be absorbed at. A second ablation layer was used to contribute to the driving plasma. A third layer was used to insulate the impactor layer from the driving plasma, reducing the risk of compromising flyer integrity.

6.2. Initial Flyer Composition

An initial flyer composition was chosen to allow development of experimental techniques to determine flyer velocity and to provide data for model development. A total flyer thickness of 4 μm was chosen, as this was a commonly investigated size in the published literature. An ablation layer of aluminium, 0.25 μm thickness, and an aluminium oxide layer, 0.25 μm thickness, were selected as the published literature indicated substantial increases in flyer velocity and integrity over a single-layer aluminium flyer. An aluminium impactor layer, 3.5 μm thickness, was selected, based upon the published literature. The flyer composition was coated onto fused silica substrates. Fused silica is readily transparent at the laser wavelength of 1064 nm, and allows a straightforward translation to flyers coated directly onto the fused silica optical fibres to be made.

6.3. Characterisation of Initial Flyer Composition

Flyers were launched using the technique detailed in section 3.2.6. The laser fluence was gradually increased from 1.5 $J.cm^{-2}$ to 32.5 $J.cm^{-2}$ and the terminal velocity determined. The results are shown in Figure 84. It should be noted that the laser fluence reported is corrected for the loss from the uncoated substrate surface, measured at 3%.

Flyer motion was not observed below 2.2 J.cm^{-2}. Below this, deformation of the surface, or ejection of discrete particles, was observed, but not a distinct flyer. Once flyer motion is attained, the terminal velocity increased gradually with fluence to approximately 5000 m.s^{-1}.

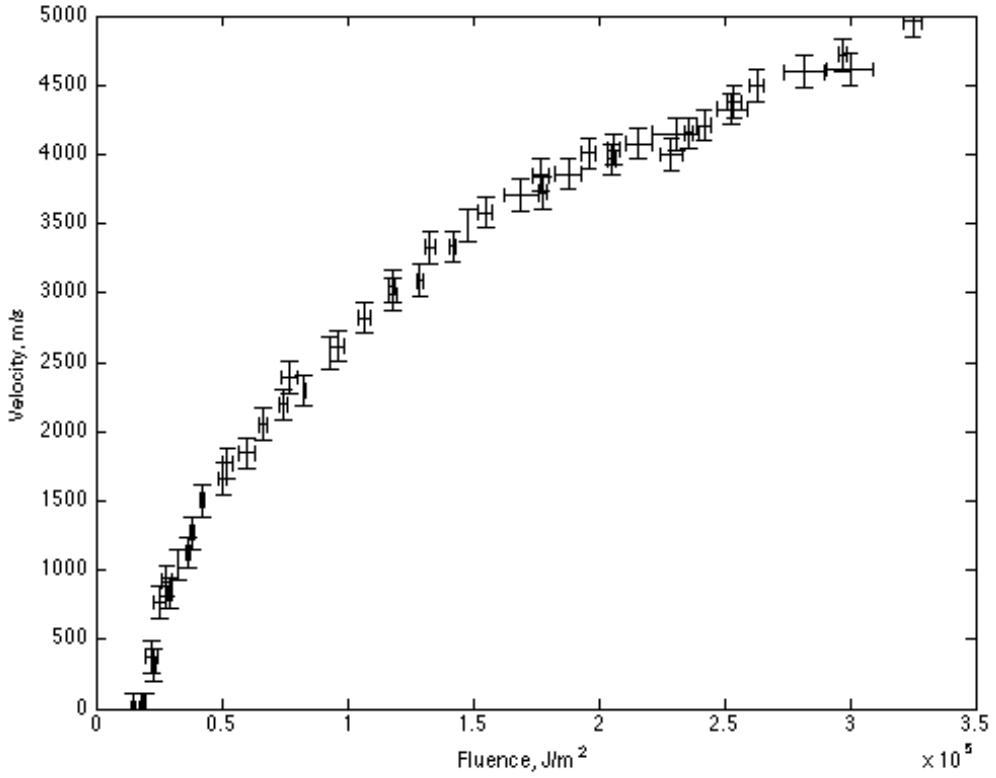

Figure 84 – Terminal velocity of initial flyer composition as a function of laser fluence. Horizontal error bars are 3 standard deviations of fluence. Vertical error bars are 3 frequency windows. Fluence is reported as calculated incident upon the substrate/flyer interface.

6.4. Modelling of Initial Flyer Composition

A simple one-dimensional, time-dependent model of the flyer motion was constructed. The model made the following calculations:

1. The absorbed intensity of the laser pulse by the ablation layer was calculated, accounting for the reflection from the uncoated surface of the substrate and the temperature-dependant reflectivity of the ablation layer. This was integrated with respect to time to give the absorbed fluence, as shown in Equation 14.

$$F_a = \int_0^{\mathrm{t}} r.I\,.a(T)\,dt$$

Equation 14

2. The temperature rise of the ablation layer was calculated using the specific heat capacity as shown in Equation 15.

$$\Delta T = \frac{\Delta F_a}{\rho_A C_p}$$

Equation 15

3. When the melt temperature was reached, the temperature was fixed until sufficient fluence was been absorbed to melt the ablation layer. Once complete, the temperature was allowed to rise again.
4. When the vaporisation temperature was reached, the temperature was fixed and the ablation depth was calculated by comparing the absorbed fluence to that required to fully ablate the ablation layer.
5. Once gas was formed, the flyer velocity was calculated using Equation 16, which was solved by the Euler method as per Equation 17. Equation 16 was adapted from that derived by Maheswaren [83] for the acceleration of electrically-driven flyers.

Equation 16

$$\dot{v}_f = \frac{\left[\left(F_{mod} - \frac{\left(\rho_{A(f)} + \frac{\rho_{A(g)}}{3}\right)v_f^2}{2}\right)(\gamma - 1) - \frac{\rho_{A(g)}v_f^2}{3} - \alpha\lambda_{m(air)}v_f^2\right]}{\left(\rho_{A(f)} + \frac{\rho_{A(g)}}{3}\right)x_f}$$

Equation 17

$$v_{n+1} = \mathrm{h}\frac{\left[\left(F_{mod} - \frac{\left(\rho_{A(f)} + \frac{\rho_{A(g)}}{3}\right)v_f^2}{2}\right)(\gamma - 1) - \frac{\rho_{A(g)}v_f^2}{3} - \alpha\lambda_{m(air)}v_f^2\right]}{\left(\rho_{A(f)} + \frac{\rho_{A(g)}}{3}\right)x_f} + v_n$$

6. The temperature of the gas, once the ablation layer was fully vaporised, was calculated by Equation 15, with the specific heat capacity for an ideal gas, and scaled by the change in volume assuming constant pressure i.e. isobaric.

The model makes the following assumptions:

- The thermal diffusion timescale (estimated as $\tau \approx l^2/K$, where l is the ablation layer thickness, and K the thermal diffusivity) was small compared to the laser pulse duration, therefore thermal diffusion could be ignored. For a 250 nm thickness aluminium ablation layer, the thermal diffusion timescale is 0.65 ns, much less than the typical 12 ns laser pulse duration.
- The heat capacity, C_p, was constant with temperature for each material phase.
- The laser pulse had a Gaussian time profile.
- The substrate upon which the flyer composition is coated formed a massive, immobile tamper and did not form part of the thermal system.
- No heat flow into the insulator layer occurred.
- The gas obeyed the ideal gas laws.
- Ionisation of the ablation layer was not considered.
- The reflectivity of the flyer coating decreased linearly from the textbook value at ambient temperature until the vaporisation temperature is reached, above which it remains constant.

The following conventions are used in the above equations:

F_i = incident fluence, in $J.m^{-2}$

F_a = absorbed fluence, in $J.m^{-2}$

C_p = specific heat capacity, in $J.(kg \cdot K)^{-1}$

F_{mod} = absorbed fluence in excess of that required to vaporise the ablation layer, in $J.m^{-2}$

$\rho_{A(f)}$ = areal density of flyer, in $kg.m^{-2}$

$\lambda_{m(air)}$ = linear density of air, in $kg.m^{-1}$

v_f = flyer velocity, in $m.s^{-1}$

γ = ratio of specific heats, unitless

$\rho_{A(g)}$ = areal density of gas, in $kg.m^{-2}$

x_f = flyer position or displacement, in metres

h = calculation time step, in seconds

α = drag co-efficient, unitless

The model predicted the following time-dependant outputs, as illustrated in Figure 85: intensity incident upon the ablation layer; fluence incident upon the ablation layer; fluence absorbed by the ablation layer, temperature of the ablation layer; and flyer velocity. The phase changes within the ablation layer can be seen, within the onset of flyer motion coincident with the onset of gas formation.

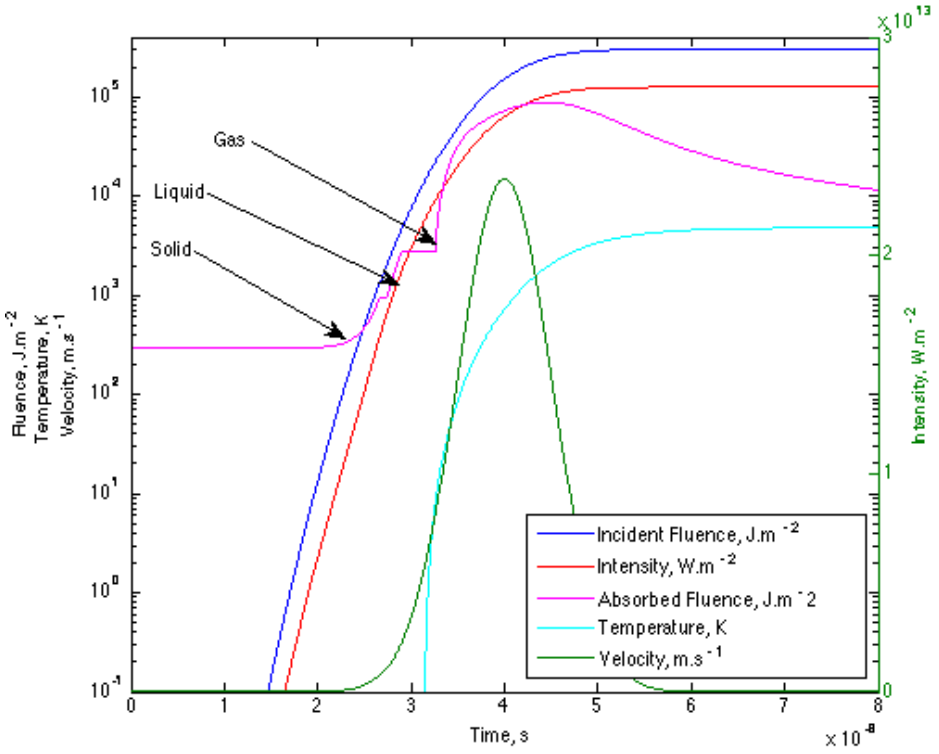

Figure 85 - Plot of outputs of flyer model. Material phases are labelled.

6.4.1. Comparison of Modelled Flyer Velocity to Experimental Flyer Velocity

The model was used to calculate the terminal velocity of the initial flyer composition as a function of fluence. A comparison between the calculated terminal flyer velocity and the experimental terminal flyer velocity is shown in Figure 86. A close agreement can be seen, with a slight over-prediction low fluences, less than $5x10^4$ $J.cm^{-2}$, close to the threshold for flyer launch. At these fluences, the majority of the absorbed fluence is required to vaporise the ablation layer, and it is likely that the coarse assumptions made above are not valid.

This result is impressive given the simplicity of the model, with the exclusion of phenomena such as ionisation. Three values are used to fit to experimental data:

1. α, the drag co-efficient. This determines the late time flyer velocity history, and is typically set to a value of 2. This was determined by fitting to velocity-time histories at a range of fluences.
2. γ, the ratio of specific heats. This determines the early time flyer velocity history and the peak flyer velocity. A value of 1.75 was used for all results reported here. This was determined by fitting to velocity-time histories at a range of fluences, and is comparable to that for a monatomic ideal gas, ≈ 1.67.
3. The reflectivity at the vaporisation temperature. This determines the coupling efficiency of the flyer, and varies for each material. For aluminium, a value of half the ambient reflectivity is used. Temperature-dependent reflectivities are not readily available and this is a source of potential error in the model. This is the only fit parameter which is changed between materials.

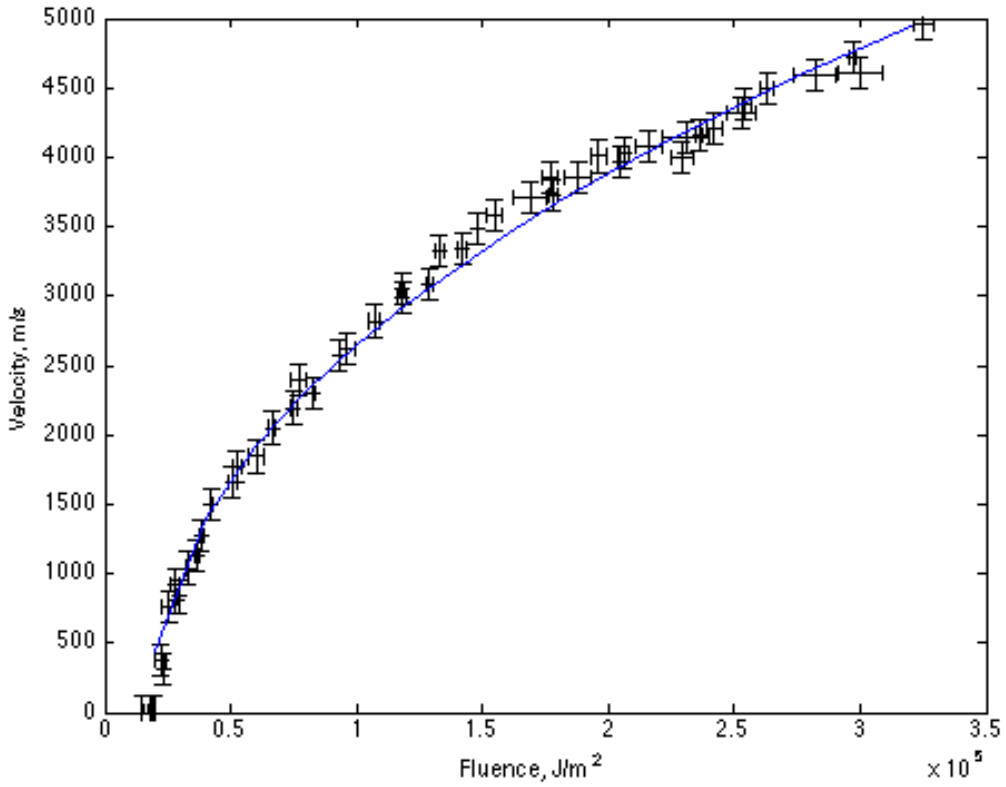

Figure 86 - Comparison of modelled (line) and experimental (points) terminal velocities as a function of fluence for a $Al/Al_2O_3/Al$, 250/250/3500 nm flyer. Horizontal error bars are 3 standard deviations of fluence, vertical error bars are 3 analysis window widths.

The model was also compared to time-dependant experimental velocity histories. Several fluences were investigated, covering the range of experimental data gathered: $2.94x10^4$, $7.70x10^4$, $1.55x10^5$, $2.05x10^5$, $2.53x10^5$ and $3.00x10^5$ $J.m^{-2}$.

To eliminate the requirement to time-correlate the experimental and modelled velocity histories, the velocity as a function of distance, or displacement, was compared. Figure 87 shows the comparison between modelled and experimental velocity histories. As noted previously, the model slightly over-predicts the flyer velocity at low fluences. However, close agreement is observed for other fluences. It should be noted that the fluctuations in the experimental velocity histories are due to regions of low signal-to-noise ratio.

This simple, one-dimensional model was capable of predicted both the terminal velocity and the time-dependent velocity history with a high level of accuracy, and can be used as a design tool to evaluate alternate flyer thicknesses and materials.

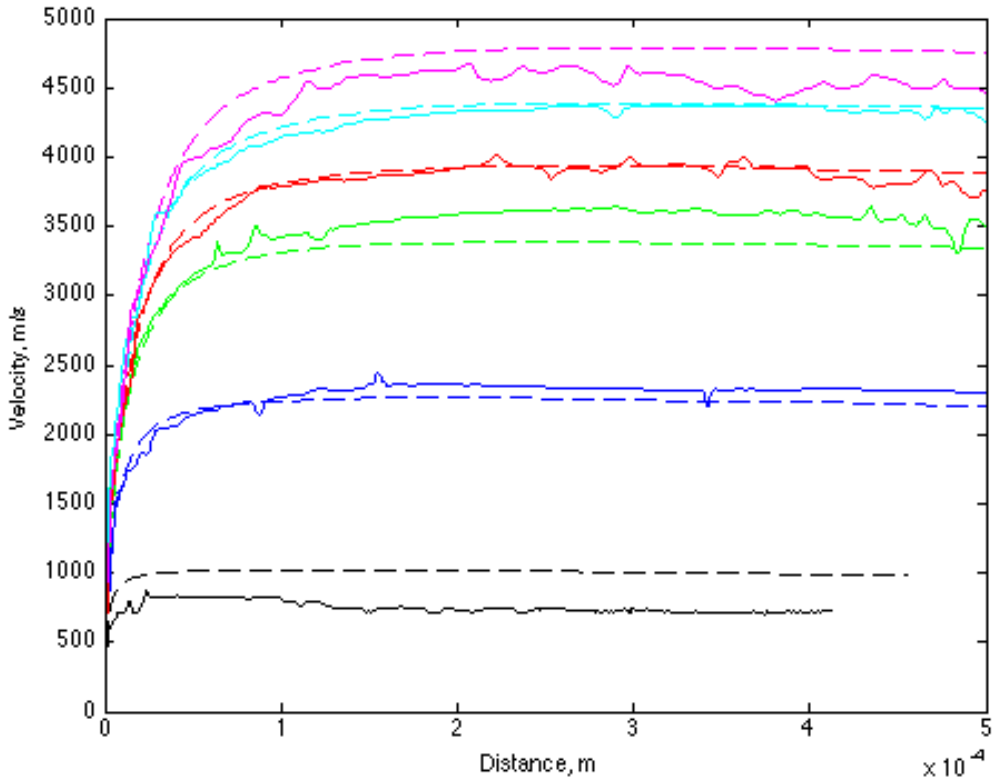

Figure 87 - Comparison of modelled (solid line) and experimental (dashed line) velocities histories for a $Al/Al_2O_3/Al$, 250/250/3500 nm flyer. Fluences are (from bottom to top) $2.94x10^4$, $7.70x10^4$, $1.55x10^5$, $2.05x10^5$, $2.53x10^5$ and $3.00x10^5$ $J.m^{-2}$.

To assess the accuracy of this model, it is useful to compare it to a published model, such as the Lawrence and Trott [40] model, as described in Section 2.3.3.1.

Lawrence and Trott showed this model accurately modelled terminal flyer velocity over a range of fluences and flyer thickness, for pure aluminium flyers. The model was modified for the multi-layer flyers investigated here, as part of this study.

The calculated ablated thickness x_d was limited to the ablation layer thickness. Farnsworth [50] has shown that a thin dielectric layer as used here confines the ablation and the impactor layer remains below the melt temperature. Once the calculated ablated

thickness reached the ablation layer thickness, the vaporisation energy, ε_d was increased to limit the calculated ablation thickness. This represents increasing ionization of the layer. Additionally, the constant k, which appears to be a fitting constant, was set to a value of 1.

A comparison of the experimental terminal velocity, and the terminal velocity calculated by the Bowden model and the Lawrence and Trott model is shown in Figure 88. Extremely close agreement can be seen above 0.5×10^5 J.m^{-2}, with the Bowden model developed in this study fitting the experimental data slightly better below this. The Bowden model is capable of predicting time-dependant velocity and thus is more useful as a design tool.

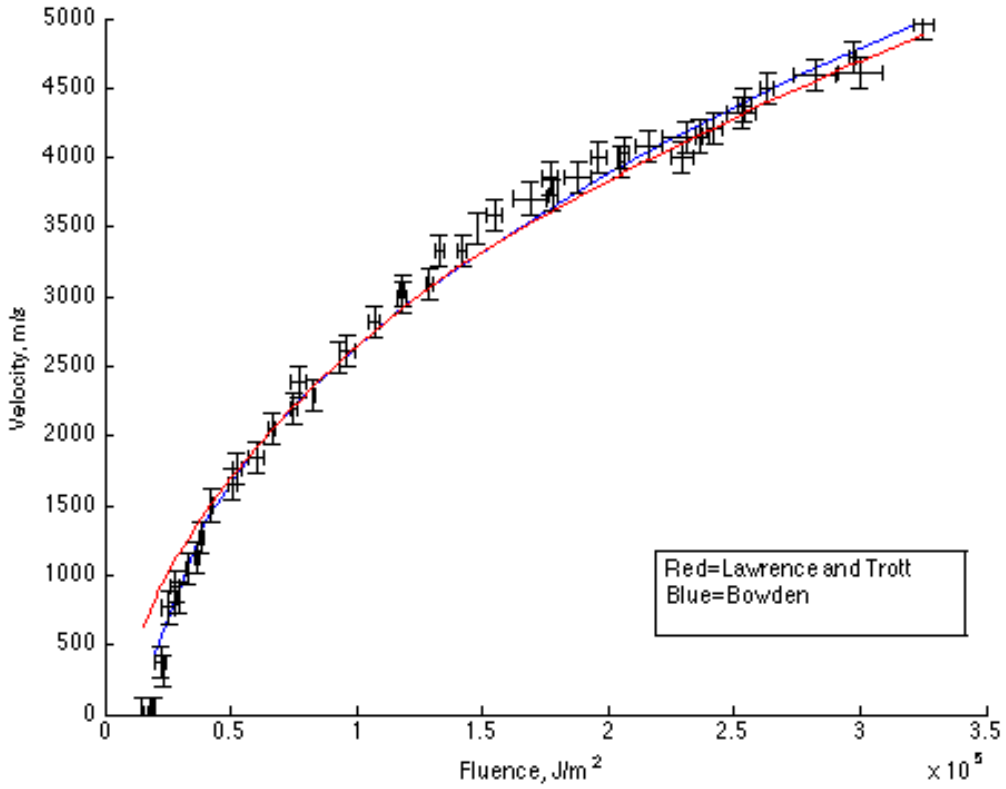

Figure 88 - Comparison of modelled (blue line = Bowden model, red line = Lawrence & Trott model) and experimental (points) terminal velocities as a function of fluence for a Al/Al_2O_3/Al, 250/250/3500 nm flyer. Horizontal error bars are 3 standard deviations of fluence, vertical error bars are 3 analysis window widths.

6.5. Optimisation of Absorption Layer Thickness

The addition of a thin (10-50 nm thickness) titanium layer between the substrate and the aluminium albation layer was investigated. Titanium has a lower reflectivity (0.55) than aluminium (0.95) at a wavelength of 1064 nm, and should reduce the energy reflected before an absorbing plasma is formed.

Flyers with a 3 μm aluminium impactor layer, and titanium absorption layers of 0, 10, 25 and 50 nm thickness were launched with laser fluences of 1 to 30 $J.cm^{-2}$, and the flyer velocity measured. The experimental data is shown in Figure 89. A logarthmic fit is made through each data set to aid visualisation of the data. The velocity at a fluence of 20 $J.cm^{-2}$, as determined from the fits, is shown in Table 23.

It can be seen that the addition of a 10 or 25 nm titanium layer has a negligible effect on velocity, less than 2%. In contrast, a 50 nm titanium layer reduces the flyer velocity by almost 10%. This result cannot be explained by the simple model described in Section 6.4, and an adequate explanation is likely to require knowledge of the change in reflectivity of aluminium and titanium with temperature, and a high-fidelity numerical model including radiation transport.

The threshold of hexanitrostilbene (HNS) with a surface area of 8.3 $m^2.g^{-1}$ impacted by a flyer with a 3.5 μm aluminium impactor layer (with no absorption layer) was determined by the author in a previous study [84] as 22.92 $J.cm^{-2}$. In this study, the threshold of the same HNS impacted by a flyer with a 3.5 μm aluminium impactor layer (and a 10 nm titanium absorption layer) was determined to be 16.79 $J.cm^{-2}$, a reduction in threshold of approximately 27%. This does not correlate with the flyer velocity results reported above. Titanium is frequently used as an adhesion layer between silica, as used in the substrate for the flyer coating, and other metals. It is possible that this increased adhesion results in a cleaner launch of the flyer, resulting in a flyer with increased planarity. This two dimensional effect would not be measured by the one dimensional diagnostics, such as PDV, used here.

A 10 nm absorption layer was chosen for the optimised flyer, based upon the positive evidence that it reduces initiation thresholds, as reported above. A 25 nm titanium layer may offer further improvements, and is worthy of further investigation.

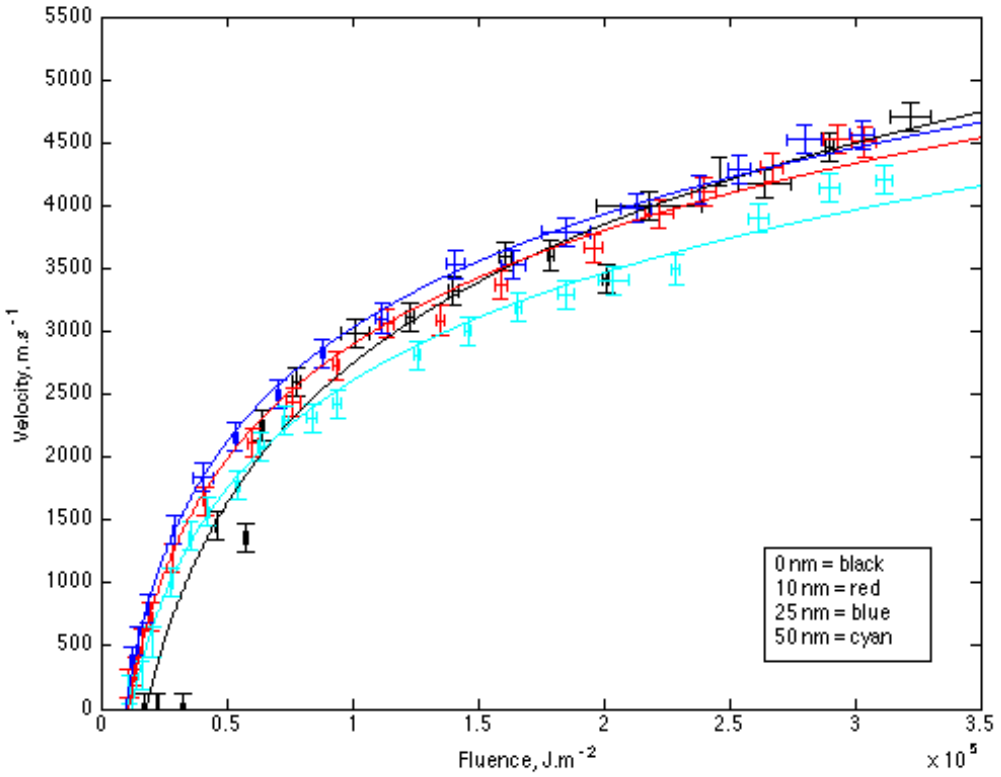

Figure 89 - Variation in terminal velocity as a function of fluence with absorption layer thickness, at a distance of 75 μm. Fits are logarthmic fits. Horizontal error bars are 3 standard deviations of fluence, vertical error bars are 3 analysis window widths.

Titanium thickness, nm	Flyer batch	Velocity, $m.s^{-1}$	Change in velocity (relative to 0 nm titanium)
0	10374	3845	0
10	10173	3800	0.99
25	10168	3927	1.02
50	10157	3460	0.91

Table 23 - Mean velocity at a fluence of 20 $J.cm^{-2}$ for varying absorption layer thicknesses.

6.6. Optimisation of Ablation and Insulator Layer Thickness

The flyers evaluated here were comprised of four layers (Figure 90). An absorption layer of titanium, 10 nm thickness, provided an initial interface to absorb the laser energy. An ablation layer of aluminium was used to contribute to the driving plasma. An insulator layer of alumina was used to insulate the impactor layer from the driving plasma, reducing the risk of compromising flyer integrity. Finally, a thicker aluminium impactor layer formed the final flyer plate. Ablation and insulator layer thicknesses of 100, 250 and 500 nm were used, with an impactor layer thickness of a few μm. For varying ablation layer thicknesses, the insulator layer was held at 250 nm, and for varying insulator layer thicknesses; the ablation layer was held constant at 250 nm.

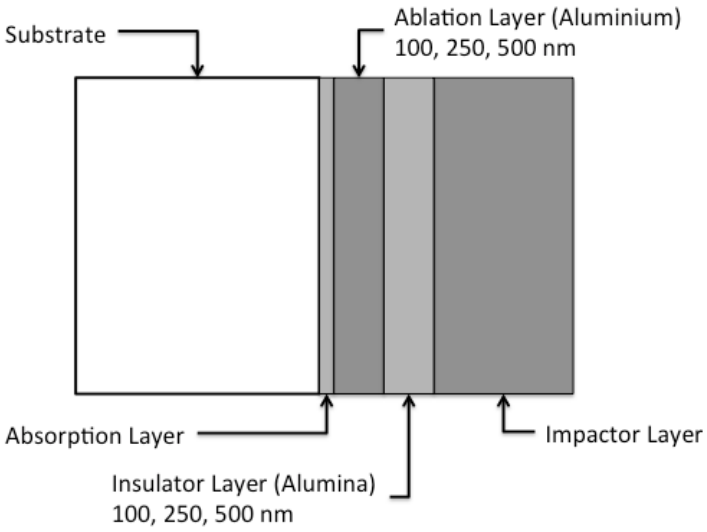

Figure 90 – Schematic of coated substrate with multiple layers

6.6.1. Results and Discussion

Two primary metrics were chosen to quantify the performance of the flyer plates studied. Firstly, the distance the flyer plates travelled before the flyer integrity was compromised was determined. PDV was used to measure the flyer velocity history, as discussed in Section 3.2.6. The spectrograms of each flyer launched were studied for evidence of loss of flyer integrity. This was indicated by the velocity trace becoming weak, intermittent or broader. A broader trace is evidence of a large velocity range across the flyer plate, or fragmentation. Once this degradation was identified, the

velocity against time data was extracted, and then integrated to provide velocity and distance against time.

The second metric, velocity, was examined at two points: 75 μm displacement, a point at which 90% of terminal velocity is typically reached, and at the point of flyer degradation. The terminal velocity was not used in case some flyers did not reach terminal velocity.

Varying the ablation and insulator thickness would increase the mass of the flyer plate, potentially decreasing the flyer plate velocity for a given laser pulse energy. It was therefore vital to quantify any flyer velocity change as the layer thicknesses are changed.

6.6.1.1. Ablation Layer Thickness

Three ablation layer thickness were studied: 100, 250 and 500 nm. The results are summarized in Table 24, with the distance and velocity against time data in Figure 91, Figure 92 and Figure 93. The standard deviation of each data set was comparable, with a slightly reduced variation for increased ablation layer thicknesses. The velocity at a displacement of 75 μm did not vary with ablation layer thickness, with a slight increase in velocity at the point of degradation. This can be explained by examining the displacement at the point of degradation, which increases with ablation layer thickness from 120 μm to 182 μm, thus the flyers with thicker ablation layers have a greater distance over which to accelerate.

	Velocity at 75 μm displacement, $km.s^{-1}$		Velocity at point of flyer degradation, $km.s^{-1}$		Displacement at point of flyer degradation, μm	
Ablation layer thickness, nm	Mean	σ	Mean	σ	Mean	σ
100	3.056	0.146	3.079	0.443	120	62
250	3.135	0.132	3.194	0.224	139	38
500	3.059	0.104	3.278	0.024	182	10

Table 24 - Ablation layer performance

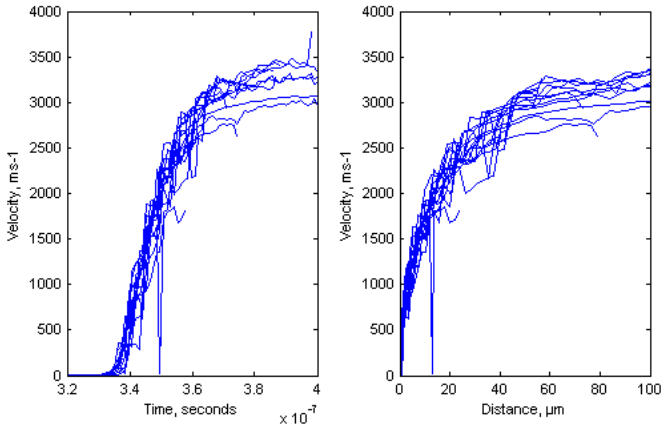

Figure 91 – Performance of 100 µm ablation layer

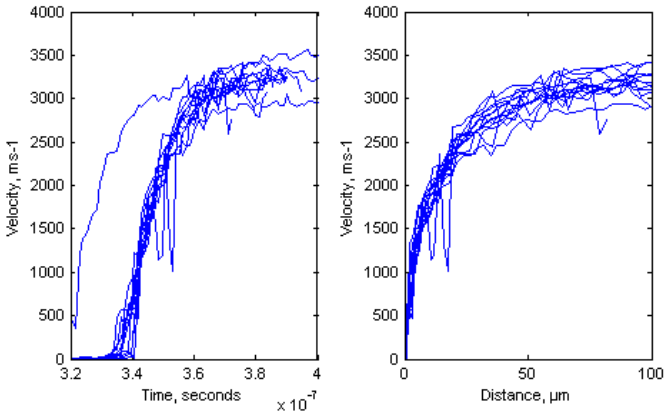

Figure 92 – Performance of 250 µm ablation layer

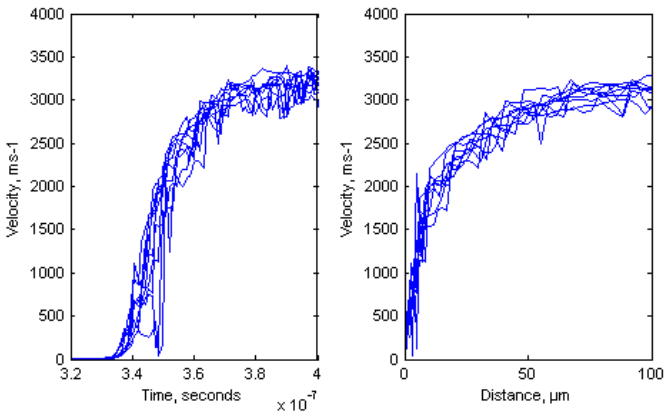

Figure 93 - Performance of 500 µm ablation layer

Lee et al [49] modelled the performance of comparable flyers using the 1-dimensional hydrocode LASNEX, with ablation layer thicknesses of 0, 250 and 500 nm. They found that for a 250 nm thickness ablation layer, the melt temperature of the impact layer was exceeded in 55 ns, increasing to 70 ns for a 500 nm thickness ablation layer. The flyer velocity was reduced by 5%, though the distance at which this was calculated was not reported. Melt of the impactor will occur prior to flyer degradation, hence the calculated times are somewhat shorter than those measured here. The comparison between the time to degradation and the time to melt is shown in Table 25. A comparable increase in time with increasing ablation layer thickness is seen for both cases. A velocity reduction of 2.4% at the point of degradation for 500 nm ablation layers relative to 250 nm ablation layers was measured experimentally in this study, agreeing closely with the 5% calculated reduction by Lee.

Figure 94 shows a qualitative comparison between an experimental velocity history from this study and a calculated velocity history reported by Lee [49]. A good agreement can be seen, further confirming the validity of the calculated data. The addition of material to the ablation layer will delay the onset of melt and degradation of the impactor layer, but will also increase the mass of the flyer, decreasing velocity.

Ablation layer thickness (nm)	Time to degradation (ns)	Time to melt (from Lee) (ns)[5]
100	54	Not reported
250	77	55
500	110	70

Table 25 - Comparison of flyer performance to Lee et al [49].

[5] Reported for time interval from start of laser pulse. Corrected by 15 ns to compare to data presented here. Time interval of experimental data is from a displacement of 100 nm to the point of degradation.

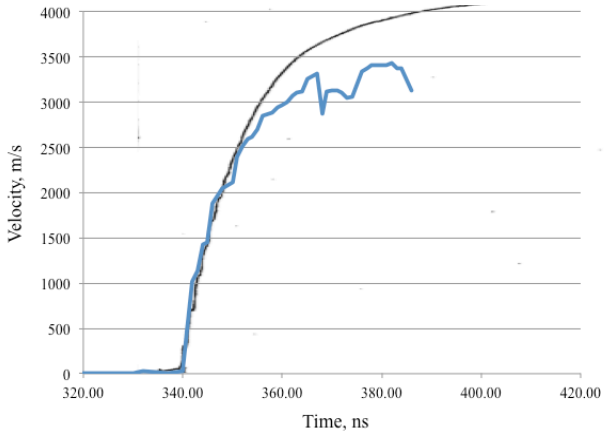

Figure 94 - Comparison of experimental and calculated [49]velocity

6.6.1.2. Insulator Layer Thickness

Three insulator layer thicknesses were evaluated: 100, 250 and 500 nm. The results are summarized in Table 26, with the distance and velocity against time data in Figure 95, Figure 96 and Figure 97. It can be seen that there was a slight increase in flyer velocity at 75 micron and also at the point of flyer degradation with increasing insulator layer thickness. There was a significant increase in the point of flyer degradation with increasing insulator thickness, from 82 µm to 338 µm.

	Velocity at 75 µm displacement, $km.s^{-1}$		Velocity at point of flyer degradation, $km.s^{-1}$		Displacement at point of flyer degradation, µm	
Insulator Layer Thickness, nm	Mean	σ	Mean	σ	Mean	σ
100	2.941	0.136	2.849	0.343	82	34
250	3.135	0.126	3.194	0.224	139	38
500	3.145	0.104	3.298	0.290	338	101

Table 26 – Summary of insulator layer performance

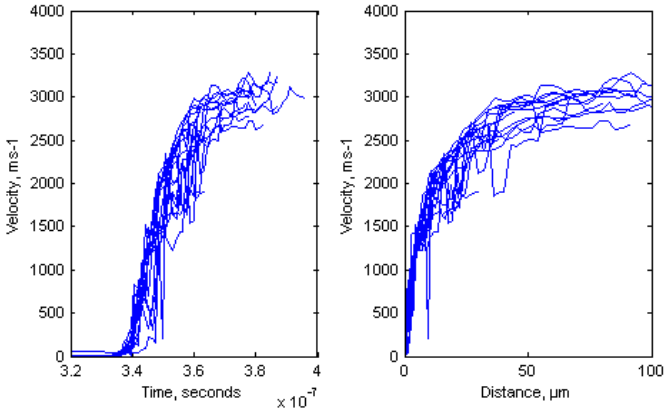

Figure 95 - Performance of 100 µm insulator layer

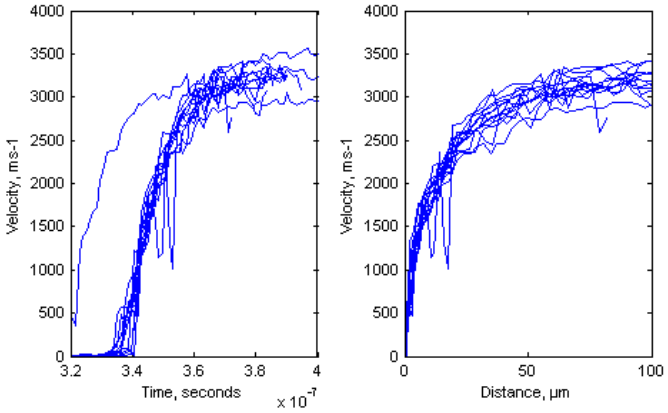

Figure 96 - Performance of 250 µm insulator layer

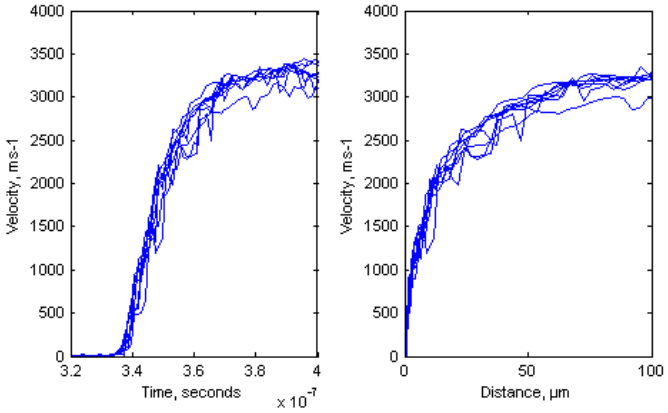

Figure 97 - Performance of 500 µm insulator layer

The insulator layer acts to confine the accelerating plasma as it has a lower thermal conductivity (30 $W.m^{-1}\cdot K^{-1}$ for aluminium oxide, 237 $W.m^{-1}\cdot K^{-1}$), reducing heat losses to the flyer plate, relative to a single layer aluminium. It is likely that the thicker insulator layer, the higher the plasma temperature and thus the higher the velocity attained.

The insulator layer delays the melt of the impactor by decreasing the rate of thermal diffusion through the flyer plate. This can be seen in Figure 98, where modelling reported by Labaste [85] shows the temperature distribution through the flyer plate.

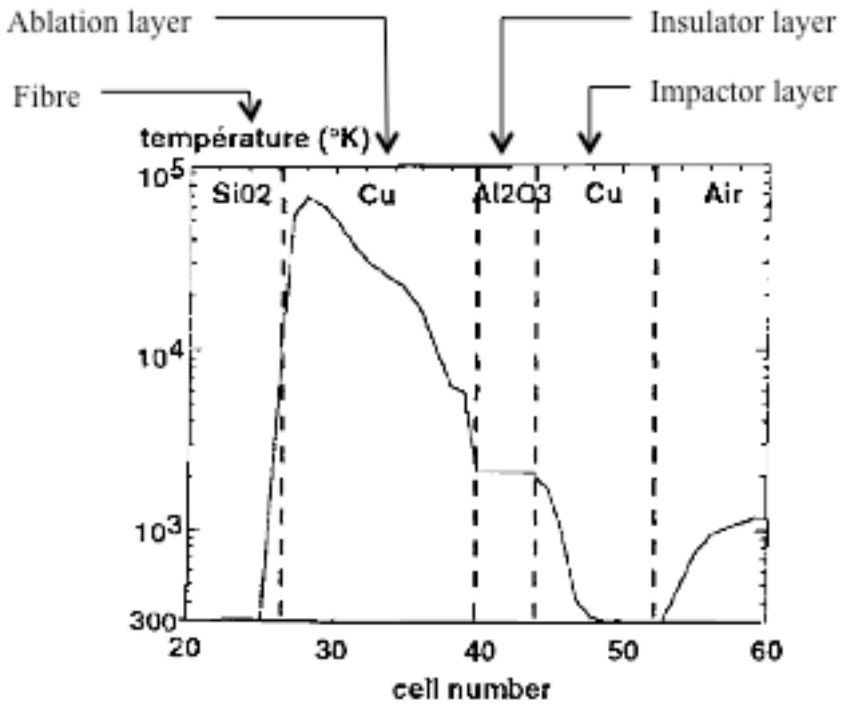

Figure 98 – Modelled temperature distribution through flyer plate [85]

The time taken to reach the melt temperature of the impactor layer increases with increasing insulator layer thickness, evidenced by the significant increase in the displacement at the point of flyer degradation with insulator layer thickness seen in Table 26. There will be a limiting case for thicker layers where the increased insulator layer offers no additional thermal confinement or insulation on the flyer flight timescales, and the increased insulator layer thickness adds to the mass of the flyer, offsetting the increase in acceleration and thus decreasing velocity.

The survival rate of each insulator layer thickness for 25 µm distance intervals is shown in Figure 99, clearly illustrating the dramatic improvement offered by the 500 nm insulator layer. The survival rate represents the proportion of flyer plates that travelled at least the specified distance.

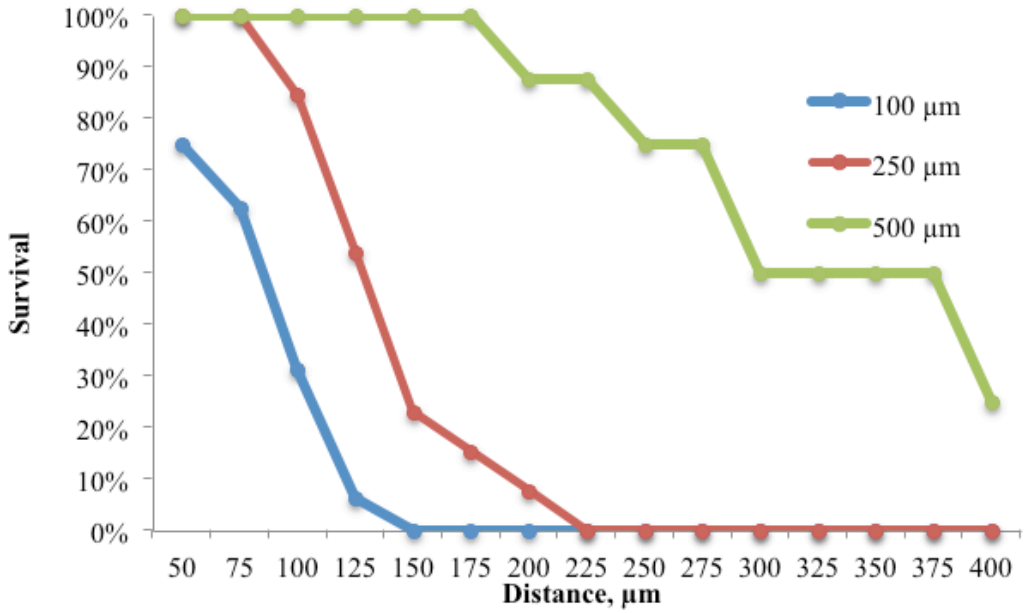

Figure 99 - Flyer Survival vs. Displacement

6.6.1.3. Profilometry of Flyer Launch Sites

Surface maps of the coated substrates were obtained using an ADE Phase Shift MicroXAM optical surface profilometer to examine the flyer plate launch sites. An example surface map is shown in Figure 100, with a dimensioned line profile shown in Figure 101. Four features are observed.

Firstly, a region corresponding to the fibre diameter, 365 µm, is seen to exhibit an ablation pattern consistent with the spatial energy distribution on the fibre output, shown in Figure 102. It is evident that a portion of the accelerating plasma is formed of the fibre itself, as the height of the fibre in this region is effectively negative. Trott [86] reported silica emission lines from the accelerating plasma along with aluminium lines, for an aluminium coating on a fused silica window.

Secondly, a region extending to a diameter of approximately 630 µm with a gradual increase in height to approximately 250 nm above the central region is seen. This is likely to be the ablation layer, in this case a 250 nm thickness of aluminium. This layer appears to be strongly adhered to the substrate, as the layers above it, the insulator layer and impactor layer, are missing.

A third region, approximately 500 nm in thickness with a diameter of 865 µm, is likely to be the insulator layer.

Fourthly, outside of the apparent petalling or peeling, is the impactor layer, closely corresponding to the impactor layer thickness. The mechanism for the erosion of the layers radially outwards from the central region, where the laser energy is deposited, is unknown, but radial expansion of the driving plasma is a potential mechanism. If this erosion occurs on timescales corresponding to the early acceleration of the flyer plate, then this may reduce the coupling efficiency of the plasma energy to the flyer kinetic energy.

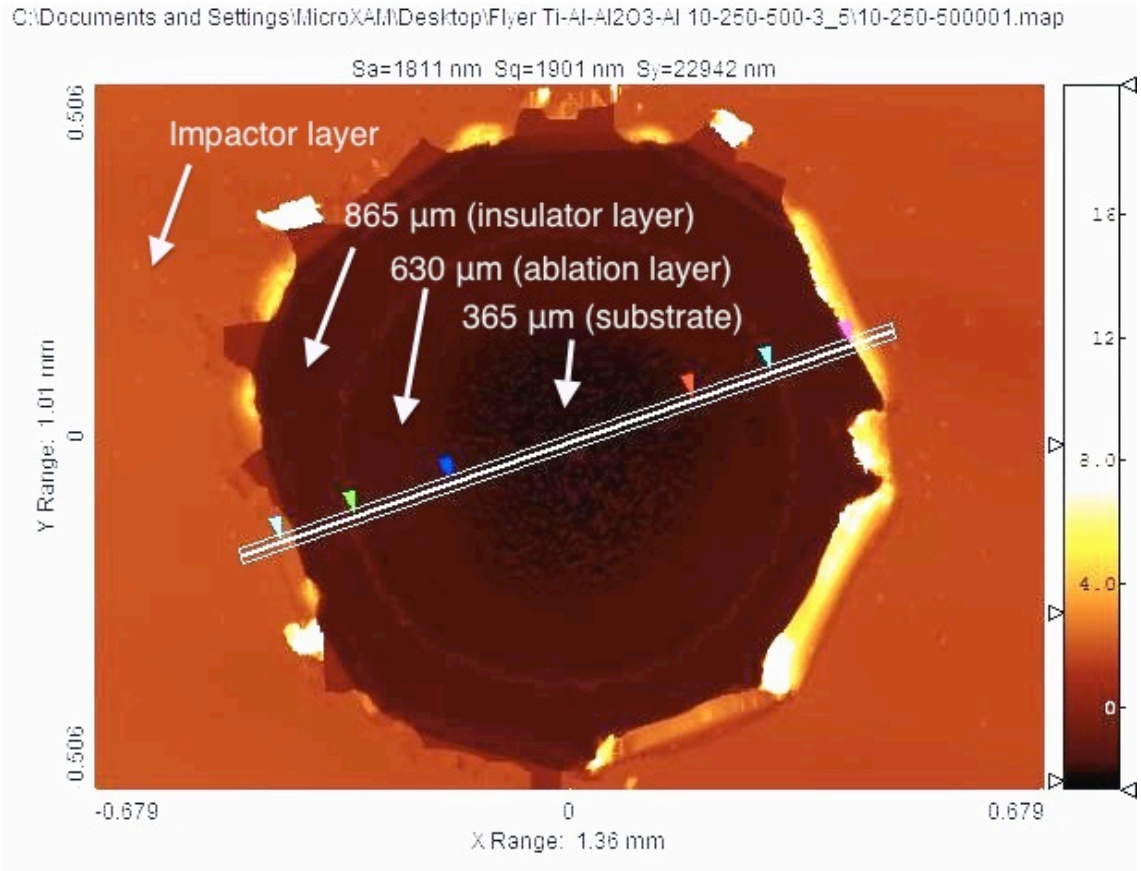

Figure 100 - Surface map of ablated coating

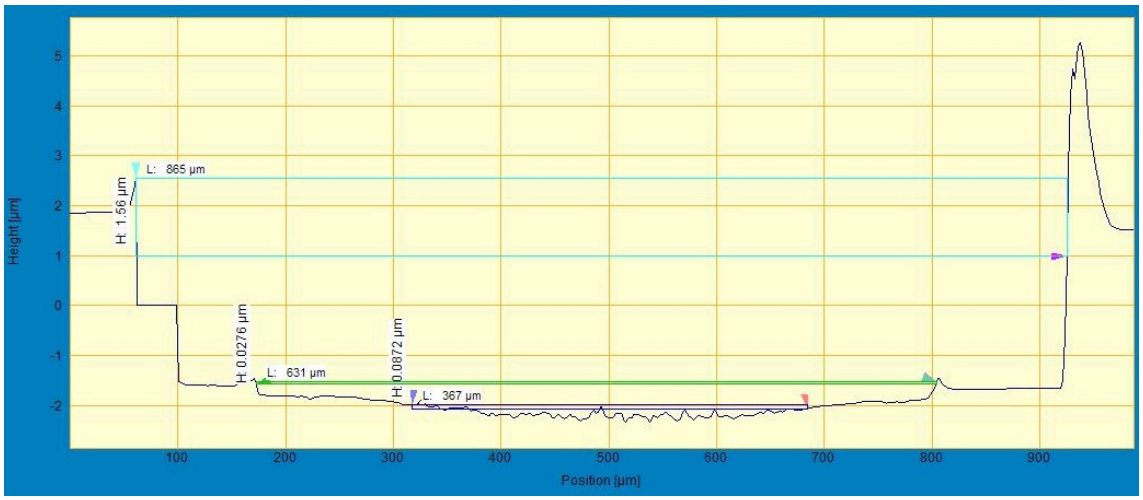

Figure 101 - Measurements of Ablated Coating

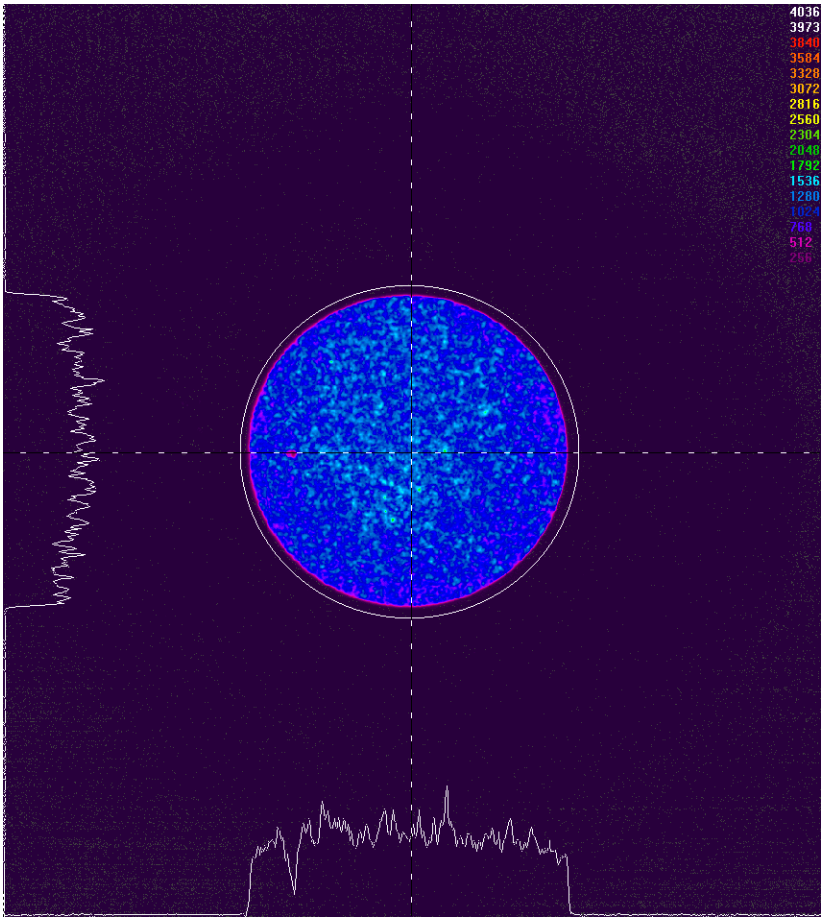

Figure 102 - Typical spatial energy distribution of fibre output

6.6.2. Summary of Optimisation of Ablation and Absorption Layer Thickness

The mean velocity attained at 75 μm for each ablation and insulator layer thickness is shown in Figure 103, as obtained from Table 24 and Table 26. The optimal layer thickness to maximise the flyer velocity at 75 μm is 250 nm for the ablation and 500 nm for the insulator layer. However, increasing the ablation layer to 500 nm increases the point of flyer degradation from 139 μm to 182 μm, whilst having a negligible effect on the flyer velocity. It is therefore prudent to conclude that the optimal layer thickness is 500 nm for both ablation and insulator layers.

There is a clear benefit in increasing the ablation and insulator layer thicknesses. For the baseline case, 250 nm thickness ablation and insulator layers, the distance at which degradation was observed (139 μm) was almost twice that at which 90% of terminal velocity is typically reached (75 μm). It was decided not to change the ablation or insulator thicknesses, as some explosive experiments had been performed with a 250 nm insulator layer thickness.

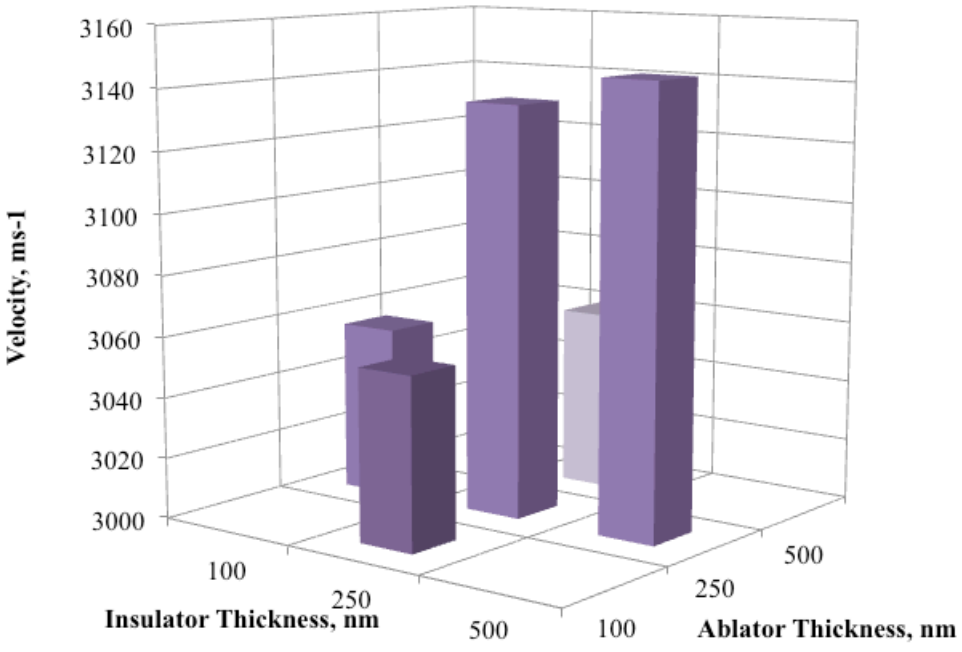

Figure 103 - Velocity at 75 μm displacement for all ablation and insulator layers

6.7. Characterisation of Optimised Flyer

The optimised flyer is defined in Table 27. The titanium absorption layer has been shown to reduce explosive initiation thresholds significantly (see Section 6.5), whilst the ablation and insulation layer thicknesses have been shown to be near-optimal (see Section 6.6). The impactor layer thickness gave the minimum threshold energy when tested with HNS (see Section 7.3.1).

Layer	Material	Thickness, nm
Substrate	Fused silica	0.5 (mm)
Absorption	Titanium	10
Ablation	Aluminium	250
Insulation	Aluminium oxide	250
Impactor	Aluminium	3500

Table 27 - Optimised flyer composition

It is important to thoroughly characterise the optimised flyer, for two reasons. Firstly, it provides a benchmark against which to measure any future variations in flyer composition. Secondly, it provides a well-characterised impactor that imparts a known pressure magnitude and duration to explosives.

To complete the characterisation, two parameters were determined using PDV: flyer velocity on impact, and the duration of the shock generated on impact. The experimental results are detailed in Annex A, Table 46, and discussed here.

6.7.1. Velocity Measurement

The flyer velocity was measured as a function of fluence as described in Section 3.2.6 The flyers were launched from 400 μm diameter optical fibres, using a Big Sky CFR400 Nd:YAG laser with a pulse length of 12 ns. Three measurements were made of the energy transmitted through the optical fibre immediately prior to the flyer launch, and the mean fluence (for a 400 μm diameter) and standard deviation calculated.

Fluences from 1.3 $J.cm^{-2}$ to 33.5 $J.cm^{-2}$ were used. This bracketed the fluences typically used for explosive initiation and probed the threshold fluence required for flyer launch.

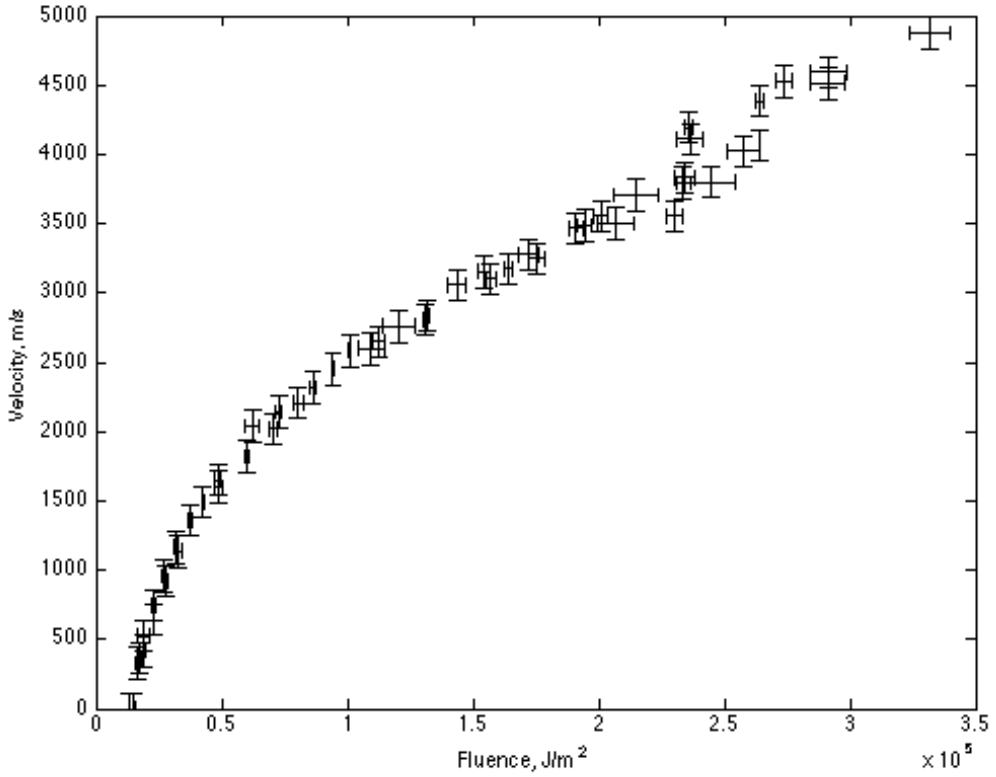

Figure 104 - – Terminal velocity of baseline flyer composition as a function of laser fluence. Horizontal error bars are 3 standard deviations of fluence. Vertical error bars are 3 frequency windows. Fluence is reported as calculated incident upon the substrate/flyer interface.

6.7.2. Measurement of Imparted Pulse Duration

In order to characterise the shock initiation of an explosive by a flyer plate impact, two parameters must be known: the shock pressure imparted to the explosive, and the duration for which this pressure is maintained. The shock pressure can be easily calculated from the flyer velocity at impact. The duration however, is harder to determine. It is traditionally assumed to be equal to the time taken for the shock reflected into the flyer plate to reach the rear surface of the flyer plate, reflect, and return to the flyer plate-explosive interface, and is given by Equation 18, where τ is the shock duration, U_{flyer} is the shock velocity in the flyer, and x is the thickness of the flyer.

$$\tau = \frac{U_{flyer}}{x}$$

Equation 18

The shock velocity is easily calculated from the flyer velocity at impact. The flyer thickness at impact however, must be determined. Given that the flyer launch process is extremely violent, with accelerations in excess of 10^9 g, and the flyer is accelerated by plasma formed from the flyer plate itself, it is reasonable to expect that the flyer plate is eroded during flight, resulting in a reduced thickness at impact. The anticipated shock duration is extremely short, less than one ns, and durations of this brevity are extremely challenging to measure. It was hypothesised that the flyer thickness on impact was equivalent to the final layer (the impactor layer) only.

The flyer plate velocity was determined using PDV with high quality data obtained during the majority of the velocity history. This alone is significant, as PDV is typically applied to experiments with durations exceeding 1 μs, rather than the tens of ns investigated here. Successfully applying PDV to measure events under 1 ns in duration has not been reported in the literature.

The flyer plates were launched across an air gap of approximately 150 μm, into lithium fluoride windows, as described in Section 3.2.6. The flyer plates tested were the baseline flyer, comprising a 10 nm titanium absorption layer, a 250 nm aluminium ablation layer, a 250 nm aluminium oxide insulator layer, and a 3500 nm aluminium impactor layer.

The PDV signal was recorded using a Miteq fibre optic receiver with a bandwidth of 12 GHz connected to a Tektronix DPO71254C digital oscilloscope, with a bandwidth of 12.5 GHz and a sampling rate (on two channels) of 100×10^9 samples.s^{-1}, i.e. data acquisition every 20 ps.

The resulting signal was analysed using SIRHEN, with an STFT analysis window of 1 ns, a slide between windows of 20 ps, and zero padding to 1024 points.

A numerical model of the experiment was implemented in a hydrocode by Matthew Maisey (AWE), to predict the velocity of the aluminium-lithium fluoride interface.

Data during the flyer impact into the window was obtained for 6 experiments, shown in Table 28.

Experimental Reference	Impact Velocity, $km.s^{-1}$
121121_102208	2.527
121121_155447	2.993
121121_155226	3.105
121122_111952	3.173
121122_113548	3.222
121122_114919	3.257

Table 28 - Impact velocities for pulse duration determination experiments

The modelled flyer velocity was then compared to the PDV analysis, along with the velocity extracted from the PDV analysis, shown in Figure 105, Figure 106, Figure 107, Figure 108, Figure 109 & Figure 110.

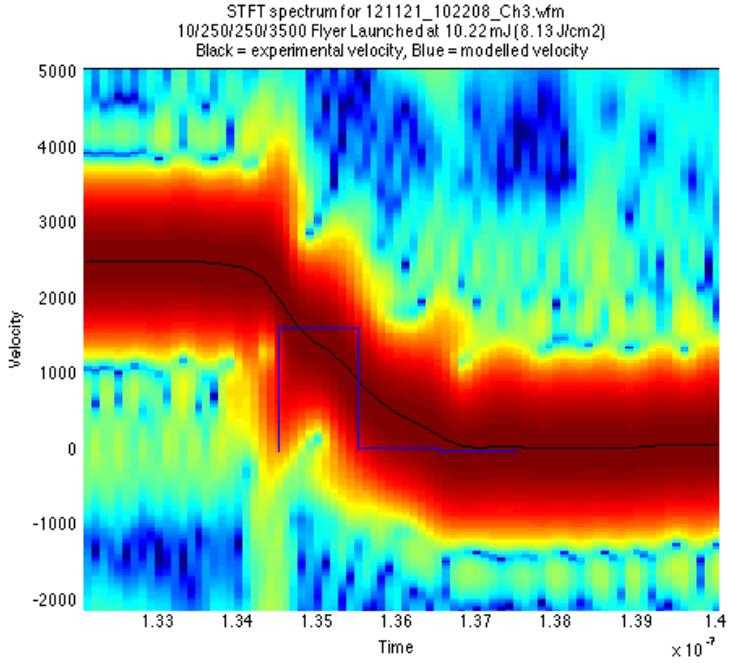

Figure 105 - PDV Analysis for aluminium flyer impacting lithium fluoride at 2.527 km.s^{-1}. Black line is extracted experimental velocity, blue line is modelled velocity of aluminium / lithium fluoride Interface

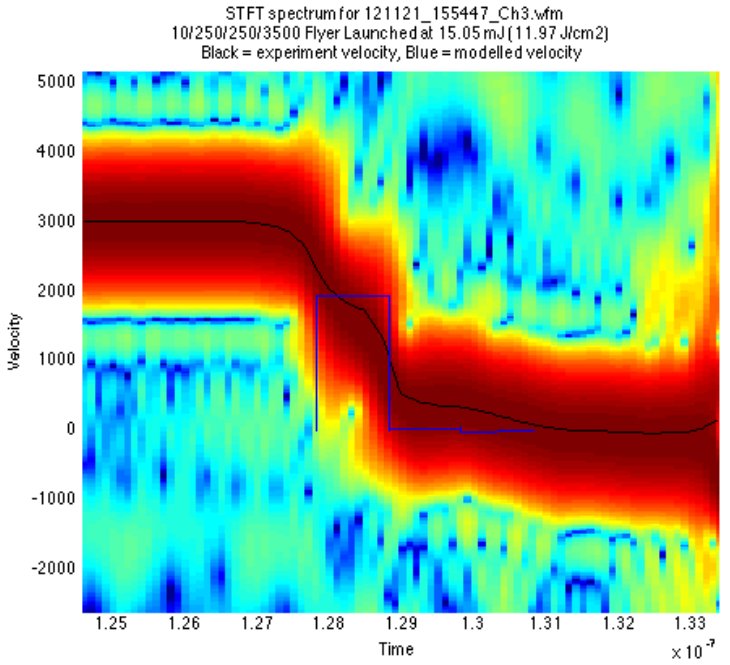

Figure 106 - PDV Analysis for aluminium flyer impacting lithium fluoride at 2.993 km.s^{-1}. Black line is extracted experimental velocity, blue line is modelled velocity of aluminium / lithium fluoride Interface

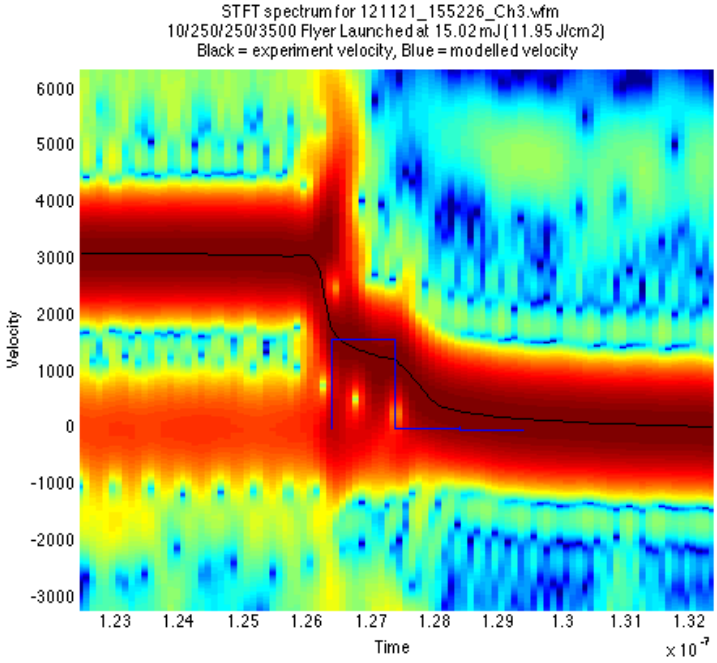

Figure 107 - PDV Analysis for aluminium flyer impacting lithium fluoride at 3.105 km.s^{-1}. Black line is extracted experimental velocity, blue line is modelled velocity of aluminium / lithium fluoride Interface

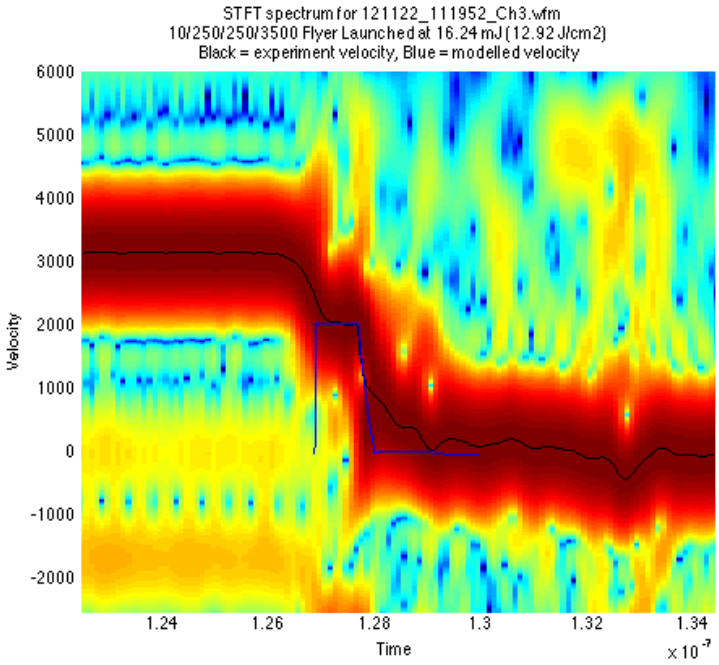

Figure 108 - PDV Analysis for aluminium flyer impacting lithium fluoride at 3.173 km.s^{-1}. Black line is extracted experimental velocity, blue line is modelled velocity of aluminium / lithium fluoride Interface

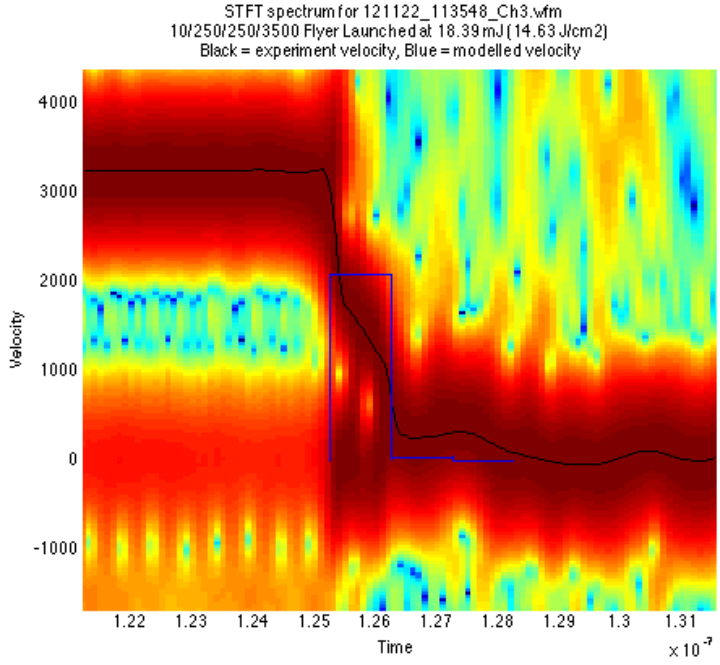

Figure 109 - PDV Analysis for aluminium flyer impacting lithium fluoride at 3.222 km.s^{-1}. Black line is extracted experimental velocity, blue line is modelled velocity of aluminium / lithium fluoride Interface

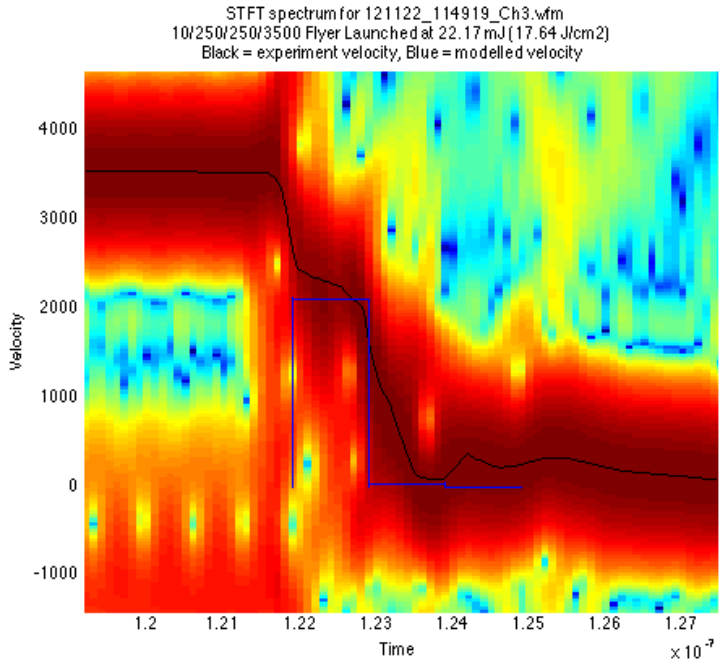

Figure 110 - PDV Analysis for aluminium flyer impacting lithium fluoride at 3.257 km.s^{-1}. Black line is extracted experimental velocity, blue line is modelled velocity of aluminium / lithium fluoride Interface

The experimental and modelled results are tabulated in Table 29. A reasonable match between the experimental and modelled interface velocities was obtained, with the modelled velocity 13% higher on average.

Impact velocity, $m.s^{-1}$	Experimental interface velocity, $m.s^{-1}$	Modelled interface velocity, $m.s^{-1}$	Interface velocity error	Experimental pulse duration, s	Modelled pulse duration, s	Pulse duration error
2527	1182	1293	109%	$0.90x10^{-9}$	$0.99x10^{-9}$	110%
2993	1320	1531	116%	$0.80x10^{-9}$	$0.96x10^{-9}$	120%
3105	1154	1588	138%	$1.10x10^{-9}$	$0.94x10^{-9}$	85%
3173	1593	1622	102%	$0.86x10^{-9}$	$0.93x10^{-9}$	108%
3222	1399	1647	118%	$0.90x10^{-9}$	$0.93x10^{-9}$	103%
3257	1797	1665	93%	$0.90x10^{-9}$	$0.93x10^{-9}$	103%

Table 29 - Comparison of experimental and modelled results for pulse duration determination

The modelled interface velocity history was calculated using a 3500 nm aluminium flyer, i.e. the impactor layer. It can be seen that the modelled pulse duration closely matches the experimental pulse duration, with the modelled pulse duration 5% greater on average. This implies that the impactor layer has not significantly decreased in thickness during the launch and flight process. It is assumed that the absorption, ablation and insulation layers have been ablated. This result is important, as it allows the accurate characterisation of the explosive initiation process. For all calculations in Chapter 6, the flyer thickness is assumed to be that originally deposited on the substrate as the impactor layer.

The duration of the events measured here using PDV are the shortest reported in the literature, and are made possible by a highest optimised probing arrangement and the extremely high bandwidth PDV system developed as part of this investigation.

6.8. Summary of Flyer Launch and Characterisation

An initial flyer composition was chosen to allow development of experimental techniques to determine flyer velocity and to provide data for model development. A total flyer thickness of 4 μm was chosen, as this was a commonly investigated size in the published literature. An ablation layer of aluminium, 0.25 μm thickness, and an aluminium oxide layer, 0.25 μm thickness, were selected as the published literature indicated substantial increases in flyer velocity and integrity over a single-layer aluminium flyer. An aluminium impactor layer, 3.5 μm thickness, was selected, based upon the published literature. The flyer composition was coated onto fused silica substrates.

A simple one-dimensional, time-dependent model of the flyer motion was constructed. This simple, one-dimensional model was capable of predicted both the terminal velocity and the time-dependent velocity history with a high level of accuracy, and can be used as a design tool to evaluate alternate flyer thicknesses and materials.

The ablation and insulator layers were investigated to determine the optimal layer thicknesses. The optimal layer is 500 nm for both ablation and insulator layers. There was a clear benefit in increasing the ablation and insulator layer thicknesses. For the baseline case, 250 nm thickness ablation and insulator layers, the distance at which degradation was observed (139 μm) was almost twice that at which 90% of terminal velocity is typically reached (75 μm). It was decided not to change the ablation or insulator thicknesses, as some explosive experiments had been performed with a 250 nm insulator layer thickness.

An optimised flyer was determined, shown in Table 27, and characterised, with the terminal velocity determined as a function of laser fluence.

The optimised flyer was impacted into lithium fluoride windows, and the interfacial velocity measured using a high-bandwidth PDV system. By comparing the experimental results to a model of the experiment, the flyer thickness at impact was estimated. The flyer thickness was found to correspond to the impactor layer, provided

an accurate determination of the shock duration that would be subsequently imparted to the explosive, essential for accurate characterisation of the explosive response.

CHAPTER 7: EXPLOSIVE INITIATION

It is evident from the literature review that there are several criteria that must be met in order to initiate energetic materials using laser-driven flyer plates. These can be divided into those concerning the explosive, and those concerning the flyer plates, with the caveat that they are often interrelated. Whilst there are many parameters of interest, those presented here represent the most critical parameters for successful initiation of energetic materials.

7.1. Critical parameters for Explosive Initiation

7.1.1. Critical Energy Criteria

In order to establish detonation, an energetic material requires a stimulus which exceeds a certain critical energy fluence, E_c a function of the input shock pressure, P, shock duration, τ, shock velocity, U and explosive density, ρ, traditionally linked by the relationship developed by Walker and Wasley [87] for flat plate impacts onto energetic materials:

$$E_c = \frac{P^2\tau}{\rho_0 U}$$

Equation 19

The James Criterion [88] is an extension of the original Walker-Wasley criterion. It possesses all the applicability of the Walker-Wasley criterion but applies to a wider range of both impactor shapes and energetic materials. The James Criterion is given by

$$\frac{E_c}{E} + \frac{\Sigma_c}{\Sigma} = J$$

Equation 20

where E_c and Σ_c are constants for a given explosives. Σ is given by $\frac{U^2}{2}$, and E by:

$$E = \frac{P^2 \tau}{\rho_0 U}$$

Equation 21

The 50% probability for initiation is given by J=1, with successful initiation occurring for J>1 and unsuccessful initiation occurring for J<1.

Both the Walker-Wasley and James Criteria are applicable for one dimensional shocks only.

7.1.1.1. Calculation of Pulse Duration

Two shock parameters must be known to characterise the initiation of an explosive charge: the shock pressure imparted to the explosive, and the duration over which this pressure is sustained. The pressure can be calculated from the measured flyer velocity. The pulse duration is extremely difficult to measure experimentally, due to its extreme brevity. Historically, it is has been approximated as the shock reflection time within the flyer, given by:

$$\tau = \frac{2x}{U_s}$$

Equation 22

where x is the flyer thickness, and U_s is the shock velocity in the explosive.

7.1.2. Critical and Initiation Diameter

The energetic material must be able to develop and sustain a detonation over a diameter accessible to laser-driven flyers i.e. less than 1 mm. Though flyers in excess of this diameter can be launched, the availability of optical fibres with diameters above 1 mm is severely limited [76], and their minimum bend radius restrictively large.

The concept of a critical diameter for an energetic material is well established as the diameter at which an unconfined material can propagate a steady-state detonation. This ranges from several millimetres for TATB to sub-mm for HNS and PETN. It can be affected by various parameters such as density, confinement and particle size. It is a

matter of debate as to whether a separate “initiation diameter” exists for initiation conditions. The initiation diameter can be defined as the minimum diameter over which an energetic material can be shocked to establish a steady-state detonation. It can be argued that the confinement of the shocked region by the surrounding material will permit initiation by flyers of less than the critical diameter. Reflections from the free surface of the unconfined material act to quench the reactions at this interface, increasing the curvature of the detonation wave and decreasing the detonation velocity to a point at which the detonation fails, at the critical diameter. For a confined material, with a shock diameter less than the critical diameter, these reflections are not present, and energy release from the material outside the shock diameter may in fact aid the growth to detonation process.

Initiation by flyer plates at diameters below the published critical diameter has been reported for HNS and PETN [89]. However, these flyer plates were electrically launched polyimide flyer plates, possessing significant curvature. Upon impact, these will impart a diverging shock wave. It is likely that this shock will diverge to a diameter equal to that and greater than the critical diameter where, assuming sufficient shock pressure, detonation will be established. Laser-driven flyers, due to their planar nature, offer a valuable technique to probe this relationship. Welle [60] has measured the critical diameter of HNS as approximately 300 μm, and it is possible threshold flyer velocity will increase with decreasing flyer diameter towards this value, with initiation below it impossible. However, initiation at smaller diameter may be possible if the confinement provided by the explosive surrounding the initiation region is sufficient to reduce the critical diameter by reducing the energy losses at the edge of the shocked region.

7.1.3. Run to Detonation Distance

The run to detonation distance is a function of the shock pressure, with higher-pressure shocks resulting in a shorter run to detonation distance [90]. The relationship between shock pressure and run distance, for an infinite duration shock (where the release waves from the rear of the flyer do not attenuate the growth to detonation) is known as the Pop plot, after Popalato of Los Alamos Scientific Laboratory.

Laser-driven flyers are typically limited in thickness, and hence shock duration, so it is necessary to have a short run to detonation distance, i.e. less than the available maximum one-dimensional shock length in the energetic material for a given pressure, given by the time taken for the rarefaction wave in the flyer plate to travel back to the flyer / energetic material interface. If the run distance for a given pressure is greater than the shocked length, then the run to detonation can be extended [91] or fail entirely.

7.1.4. Particle Size

Shock initiation of heterogeneous explosives, such as PETN and HNS, relies on the creation of localised areas of incresed temperautre, known as “hot spots”. These hot spots can be caused by compression of the voids between particles, collapse of the void resulting in jetting of the surrounding material, or mechanical fracture of the particles. The temperature of the hot spots induces reaction in the surrounding material (ignition), releasing energy and raising the temperature further. As the reaction grows to detonation, these “hot spots” grow and coalesce until the reaction has reached a steady-state detonation. The rate of this growth is dependant upon the particle size and hence surface area; small particles with a high specific surface area will react faster than large particles with a low specific surface area. For a given shock pressure, the hot spot temperature is higher for large particles, and hence large hot spots, than for small particles with small hot spots.

For long duration shocks, large particle size materials with low specific surface area will be more sensitive, as the pressure required to attain a critical temperature is lower. However, for short duration shocks, the temperature is reduced by the rearfaction waves before the large particles are able to fully burn and react. Although small particle size and high specific surface area materials require a higher shock pressure to attain a critical temperature, the small particles are able to burn and fully react before the rearfaction waves reduce the temperature. For short duration shock therefore, small particles size materials are more sensitive.

A limiting case may be reached for very small particle size materials, which begin to approach a homogeneous material. The material may considered to be uniformly heated

by the shock, and the bulk temperature is significantly lower than that of a smaller particle size material, requiring a higher pressure for initiation.

For the short duration shocks generated by laser-driven flyer plates, there is likely to be an optimal particle size, where the hot spot temperature is great enough for ignition of the material, and the particle size small enough that the reaction can grow before it is quenched by the rearfaction waves.

7.1.5. Flyer Plate Criteria

The flyer plate must deliver a shock that satisfies the above Critical energy criterion given in Section 7.1.1, whilst exceeding the critical diameter. In order to achieve this, the flyer must meet certain criteria.

7.1.5.1. Flyer Velocity

The flyer must have sufficient velocity to impart the required shock pressure in order for the explosive to run to detonation within the available shock duration. From the critical energy criterion it can be seen it is more efficient to increase the shock pressure, and hence flyer velocity, than to increase the shock duration and hence flyer thickness.

7.1.5.2. Flyer Integrity

The flyer must remain in a solid or semi-solid state, in order to maintain the shock pressure over the required diameter. Voids in the flyer area, perhaps from penetration by the accelerating plasma, will result in the effective diameter of the flyer being reduced.

7.1.5.3. Flyer Thickness

The flyer must be sufficiently thick to impart a shock of the required duration for a given flyer velocity and hence shock pressure. To some degree, given a limited flyer thickness, the required duration can be reduced by increasing the shock pressure, though a limiting condition may well be imposed by the reaction zone thickness, which for materials such as PETN and HNS may be comparable to typical shock durations generated by laser-driven flyers.

7.1.5.4. Flyer Diameter

The flyer must be of sufficient diameter to exceed the critical diameter of the energetic material, as discussed in Section 7.1.2. This is typically less than 1 mm for materials such as PETN and HNS, but can exceed several mm for materials such as TATB, making the successful initiation of such materials unlikely. The optical fibre used to deliver the laser pulse typically defines the flyer diameter, and these are generally limited to a maximum of 1 mm diameter for practical applications.

7.1.6. Shock Initiation by Thin Flyer Plates

The process of shock initiation of energetic materials by thin flyer plates, where the thickness of the flyer is small relative to its diameter, has been extensively studied.

Two competing mechanisms act to attenuate the shock imparted to the material. Firstly, upon impact, a shock is reflected backwards into the flyer. Upon reaching the rear, free surface of the flyer, the shock is reflected as a rarefaction wave. This wave travels faster through the material compressed by the shock, eventually catching the shock and attenuating it. If detonation is not established by the time this occurs, it is likely to quench the reaction. Simplistically, it is possible to determine the maximum 1D shock length (in time and distance) imparted to the explosive by considering the round trip time in the flyer plate. Secondly, for a planar flyer, the diameter of the shock will decrease with time due to edge losses. These effects are shown in Figure 111.

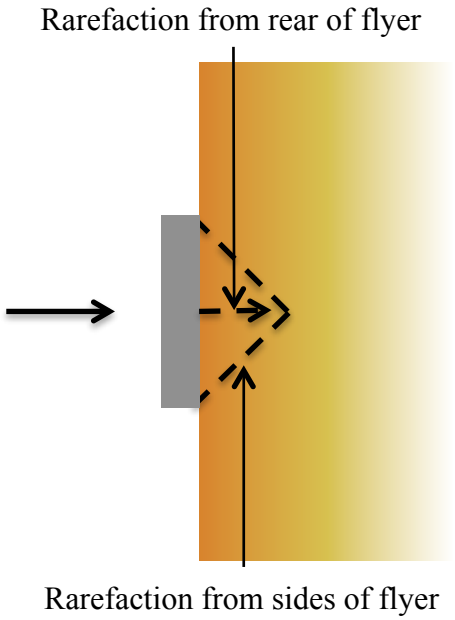

Figure 111 - Shock attenuation by flyer impact

There is a well-studied relationship between shock pressure and run distance i.e. the distance over which the reaction grows to detonation, with higher shock pressures inducing shorter run distances, as discussed in Section 7.1.3. The regime where shock pressure approaches the detonation pressure (CJ pressure) has not been studied.

The majority of flyer plate initiation experiments have used dielectric flyers such as polyimide, typically 12-50 μm in thickness. These impart a shock of approximately 10-15 GPa with shock durations of approximately 20 ns. In comparison, aluminium flyers impart shocks in excess of 20 GPa, with shock durations of approximately 1 ns. This is comparable to the CJ pressure of HNS & PETN [92; 93]. The initiation of HNS & PETN at these shock pressures has not been extensively investigated. The reactive zone length of HNS & PETN is estimated at less than 5 ns [94].

It is possible that initiation by aluminium flyer plates is analogous to initiation by a steady-state detonation i.e. the run distance tends towards the reaction zone thickness. Below a certain flyer thickness, the shock length will be less than the reaction zone thickness. The chemical reactions responsible for maintaining the detonation wave occur in the reaction zone, and if the rearfaction waves attenuate these reactions and limit the subsquent maintanence of the detonation wave, the detonation may fail.

Determining this critical flyer thickness may provide a means to determine the reaction zone thickness of PETN and HNS. The effects of a higher-than-detonation shock pressure in this regime are not well studied i.e. can it drive the reaction zone length shorter than that in a steady state detonation? If so, it may be not be possible to measure reaction zone thickness by this method.

7.2. Pentaerythritol Tetranitrate (PETN)

7.2.1. PETN Tested

Four batches of PETN have been studied. The PETN powders were produced by the same method, with the precipitation rate varied to produce differing particle sizes and hence surface areas. The specific surface area of these batches ranged from 12,700 to 25,100 $cm^2.g^{-1}$, as measured by gas adsorption. The batches tested are detailed in Table 30. Figure 112, Figure 113, Figure 114 & Figure 115 show scanning electron microscope images of the batches. It can be seen that the batches shared a common particle morphology, varying in surface area only.

Batch	Specific surface area, $cm^2.g^{-1}$
A3U	25,100
A4	20,600
C2	15,300
A6	12,700

Table 30 - PETN Powders Tested

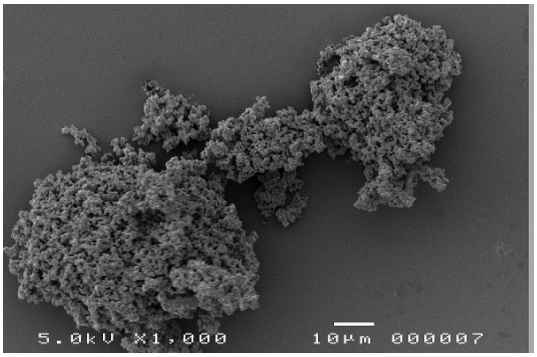

Figure 112 –A3U SEM

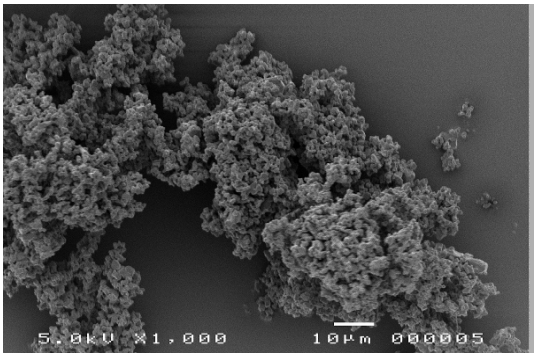

Figure 113 - A4 SEM

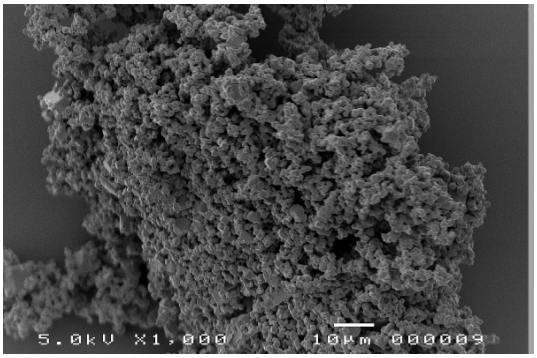

Figure 114 – A6 SEM

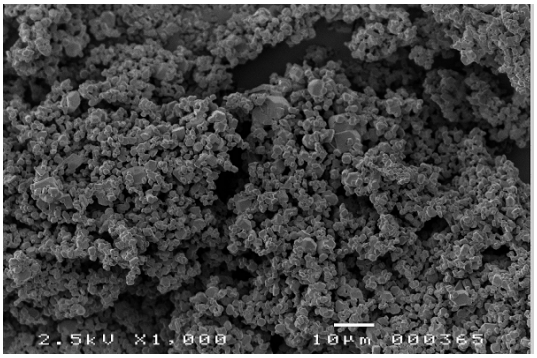

Figure 115 - C2 SEM

7.2.2. Initiation of Pentaerythritol Tetranitrate

PETN powders as detailed in Section 7.2.1 were pressed into 6 mm diameter by 3 mm length pellets at a density of 1.6 g.cm^{-3}. These pellets were then impacted by flyers with 3 µm thickness aluminium impactor layers and the energy required for a 50% probability of detonation determined using a Neyer D-optimal method [95]. Using PDV, the flyer velocity at threshold was then determined. The relationship between laser energy and flyer velocity is shown in Figure 116.

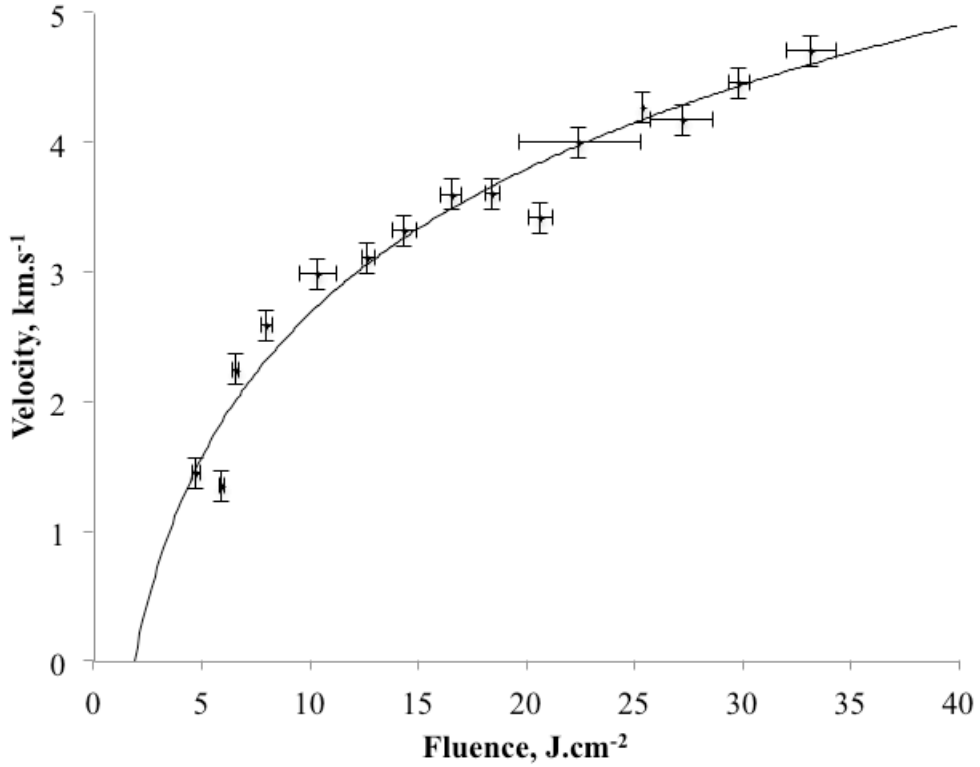

Figure 116 - Laser fluence vs. flyer velocity. Fluence error bars are 3σ. Velocity error bars are three frequency windows. Trend line is a logarithmic fit.

7.2.3. Effect of Surface Area on Threshold

All PETN powders tested were successfully initiated. This was surprising, as it was expected that as surface area decreased, the threshold energy would increase to a level unachievable with the experimental configuration. Table 31 shows the thresholds for each batch. These values are plotted in Figure 117. It can be seen that, as surface area increases, the threshold decreased. There was a strong dependence of threshold on surface area. This is consistant with the results of Waschl [89], who reported that the threshold of PETN reduced with increasing surface area above 7,500 $cm^2.g^{-1}$. This is explained in Section 7.1.4.

Two powders had threshold fluences under 25 $J.cm^{-2}$, the 20,600 and 25,100 $cm^2.g^{-1}$ powders, less than half the fibre damage threshold of 50 $J.cm^{-2}$. Although the all-fire fluence was not determined, there should significant margin between the all-fire fluence and the fibre damage threshold. A surface area of greater than 20,000 $cm^2.g^{-1}$ is

therefore considered necessary for a laser detonator such as those investigated in this study.

PETN Batch	Specific surface area, $cm^2.g\text{-}1$	Threshold, ± 1 σ, $J.cm^{-2}$	Threshold Flyer Velocity, $km.s^{-1}$
A3U	25,100	20.4	3.83
A4	20,600	23.9 ± 1.0	4.08
C2	15,300	35.3	4.71
A6	12,700	41.1 ± 5.1	4.95

Table 31 - Threshold data for PETN

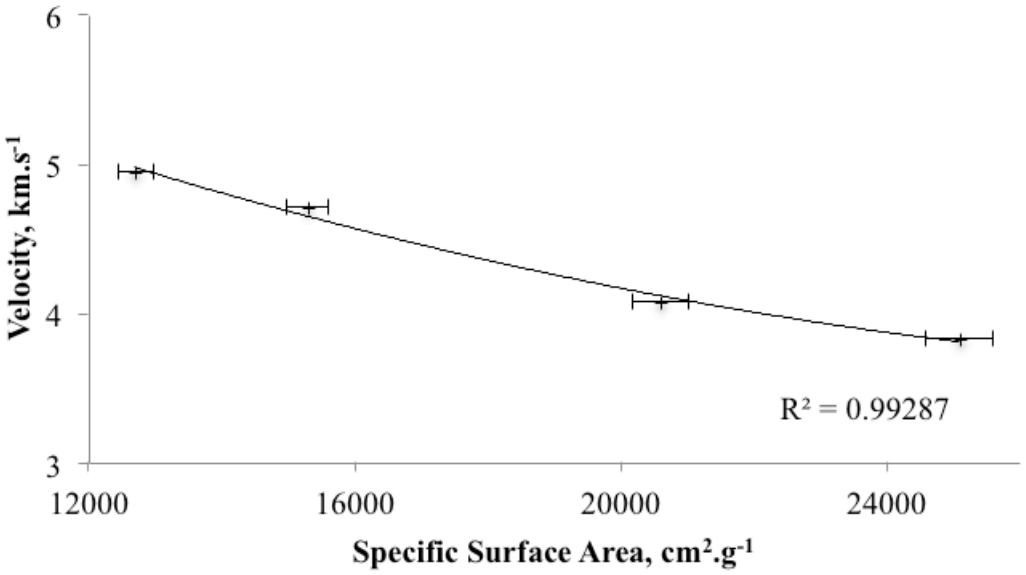

Figure 117 – Specific surface area vs. threshold flyer velocity for PETN. Specific surface area error bars are 5%, velocity error bars are 1σ. Trend line is a polynomial fit.

7.2.4. Effect of Firing Energy on Function Time and Detonation Velocity

Exploding Bridgewire (EBW) detonators exhibit a reduction in transit time[6] with increasing firing energy [61; 96], due to the increased shock pressure imparted to the explosive reducing the run distance. The shock imparted to the explosive has a velocity less than the steady-state detonation velocity. By comparing the transit time to that expected if the explosive detonated at the steady-state detonation velocity, an excess transit time can be calculated, as seen in Figure 118.

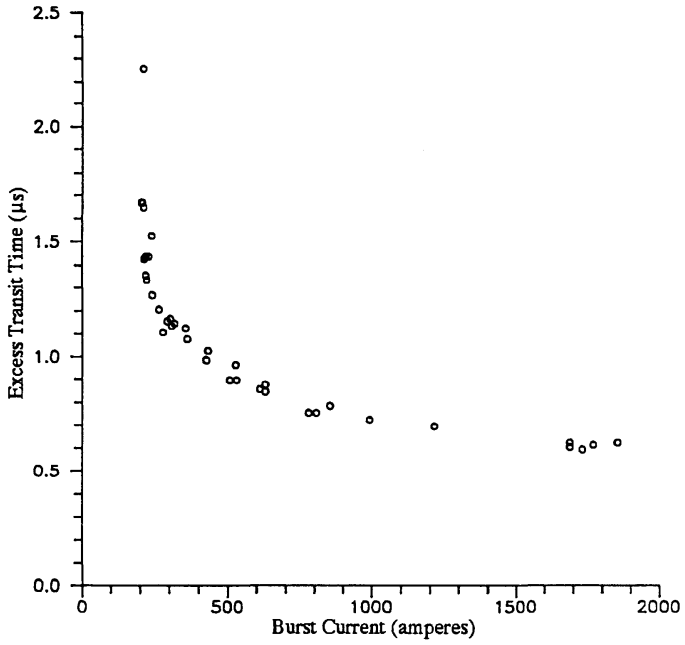

Figure 118 - Excess transit time for an EBW detonator [96]

In comparison to EBW detonators, the flyers used in this investigation impart a shock to the PETN with a shock velocity in excess of 7.5 km.s^{-1}, comparable to the detonation velocity of PETN, 7.75 km.s^{-1}. Therefore, the excess transit time observed in EBW detonators, resulting from the run to detonation, should be minimal.

It can been seen in Figure 119 that the function, or transit time does not vary with flyer velocity. The run distance in PETN at these pressures, >28 GPa is less than 8 µm [61],

[6] Defined as the time between flyer impact and explosive output.

although this is a significant extrapolation from the experimental data, which is limited to 2 GPa.

There are two possible mechanisms for lack of variation in transit time with flyer velocity. Firstly, the run to detonation distance at these shock pressures is extremely short, less than the shock length in the explosive, approximately 5 μm; the shock appears to be of infinite duration to the reaction The majority of the pellet length then detonates at the steady-state detonation velocity. Secondly, the run to detonation distance is longer than the shock length in the pellet, and the run distance is extended by the rarefaction waves from the rear of the flyer. However, in this case, the shock velocity is extremely close to the steady-state detonation velocity. It is not possible to determine which mechanism is responsible for the lack of excess transit time.

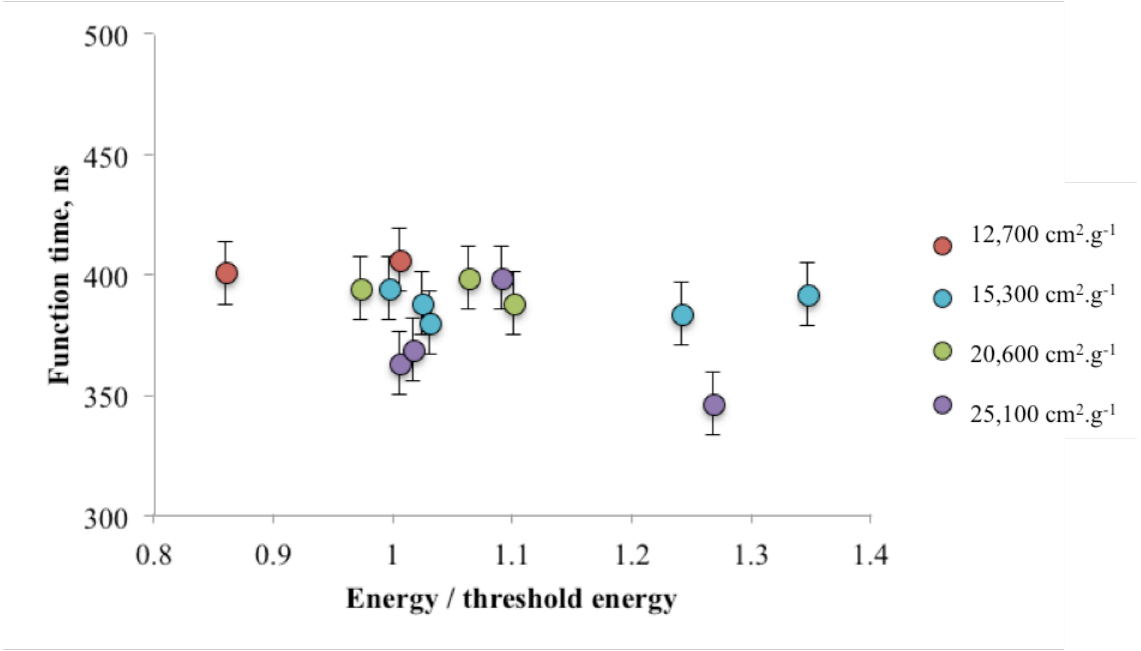

Figure 119 – Function time vs. threshold energy. Error bars are the variation in function time given by a ± 0.1mm variation in pellet length at the published detonation velocity. The function time is corrected for flyer plate flight time.

The lack of excess transit time enables the velocity of detonation to be accurately determined from the overall functioning time. The measured velocities of detonation as shown in Table 32 are consistent with the published value of 7.75 $km.s^{-1}$ for PETN at 1.6 $g.cm^{-3}$ [92]. It is interesting to note that published detonation velocities are typically

taken from cylinder test data, where the reaction has a significant length scale over which to stabilise. The close match of the detonation velocities measured here to the published values may indicate that a steady state reaction is reached extremely quickly.

PETN Batch	Surface area / $cm^2.g^{-1}$	Detonation velocity / $km.s^{-1}$	σ / $km.s^{-1}$
A3U	25,100	7.98	0.39
A4	20,600	7.62	0.10
C2	15,300	7.75	0.12
A6	12,700	7.44	0.07
	Mean detonation velocity	7.70	0.23

Table 32- Function time and detonation velocity for PETN. Outlier value with a function time of 346 ns for batch A3U not included in analysis.

7.2.5. Estimation of Critical Energy Fluence for PETN

The critical energy fluences as calculated from Equation 19 for the four batches of PETN are tabulated in Table 33 and plotted against specific surface in Figure 120. For PETN, and the range of specific areas considered, the critical energy fluence decreases with increasing specific surface area. As discussed in previous sections, this result can be rationalized in terms of the increase in reaction rates with increasing specific surface area.

Published values of E_c for PETN range from 0.140 $MJ.m^{-2}$ by Schwarz [97] to 0.167 $MJ.m^{-2}$ by Cooper [90]. This is higher than the values reported here, and suggests that the PETN used by Cooper and Schwarz had a lower surface area., due to the dependance of critical energy fluence on surface area.

PETN Batch	Specific surface area, $cm^2.g^{-1}$	Pressure, GPa	Shock duration, ns	Shock velocity, $km.s^{-1}$	Critical Energy Fluence, E_c, $MJ.m^{-2}$
A3U	25,100	28.7	0.80	7.49	0.055
A4	20,600	31.7	0.77	7.84	0.061
C2	15,300	39.9	0.69	8.71	0.079
A6	12,700	43.2	0.66	9.03	0.086

Table 33 - Shock calculations for PETN initiation

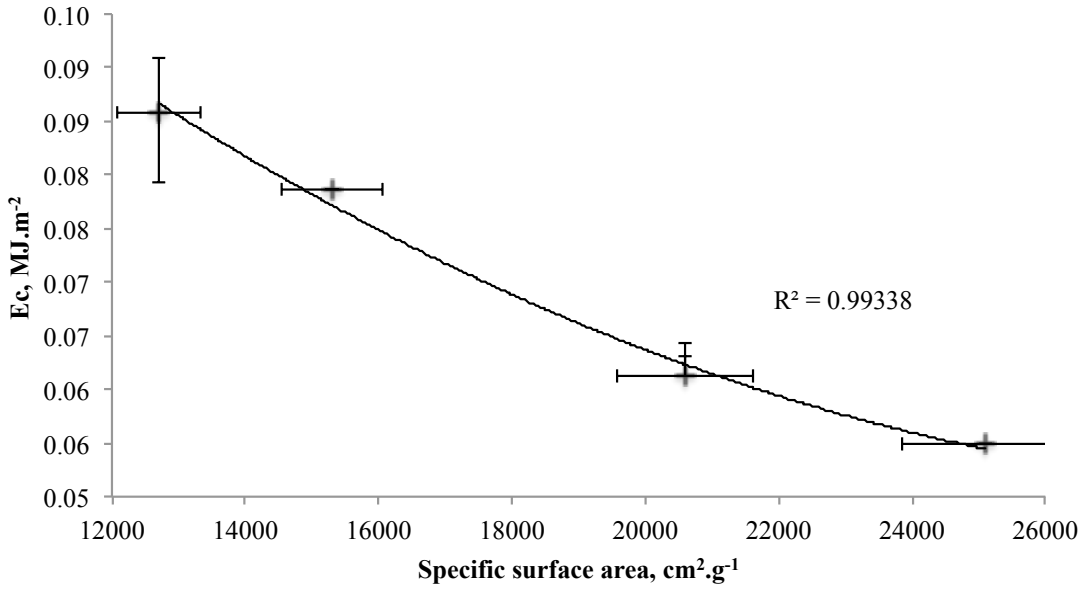

Figure 120 - Variance of critical energy fluence with surface area for PETN. Specific surface area error bars are 5%, E_c error bars are 1σ. Trend line is a polynomial fit.

7.2.6. Partial Reactions in PETN

Some unusual results were obtained when detonators filled with batch A6 were tested. This batch had the highest threshold of the batches we examined. It was observed that some shots appeared to be partial reactions. No audible reaction was noted, and the timing fibre at the pellet output did not record any light emission, yet upon examination of the fired detonator, disruption of the explosive pellet was evident around the flyer impact site In these shots the detonator body was observed to be intact, suggesting a limited violence to the reaction.

One shot in particular merits closer examination. The detonator body was split in two by the reaction, as seen in Figure 121. It appears that the end cap, which held the timing fibre, provided sufficient confinement for pressure from the gas produced by the partial reaction to build up, resulting in significant disruption to the detonator body. However, the explosive pellet remained largely intact, allowing for post-shot analysis.

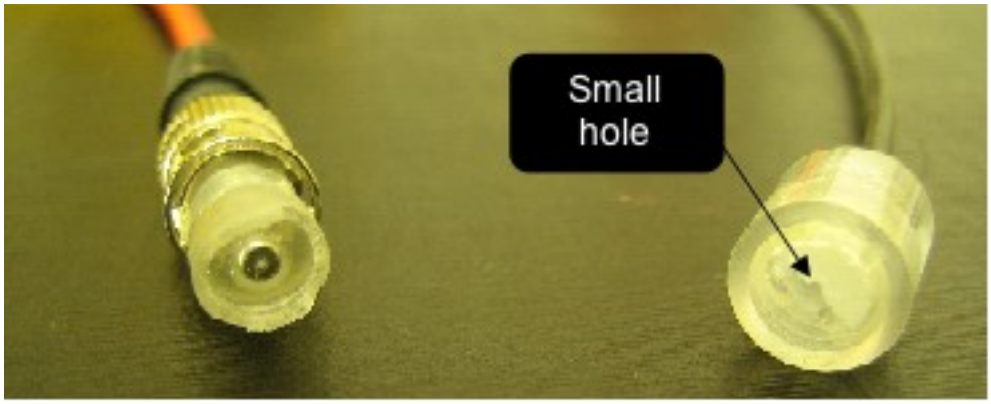

Figure 121 - Disrupted Detonator

A small hole, approaching the size of the flyer plate, is evident in the centre of the pellet. It is believed a reaction begun here, but was not sustained. It is likely that in the other shots, insufficient confinement was available to allow pressure build up, and hence only the explosive pellet itself was disrupted.

Waschl [89] noted similar results in PETN powders of a similar surface area initiated with small electrically driven flyer plates, where some shots resulted in excessive function times and evidence of a lower-order reaction. He did not recover any intact

explosive and hence was unable to make a detailed assessment. He suggests that the critical initiation diameter is variant with surface area, increasing as surface area decreases.

The hole-boring in the remains of the PETN pellet in the disrupted pellet is characteristic of the response of HNS and TATB compositions when subjected to shock loading over an area below the critical initiation diameter. Batch A6 had the lowest surface area, and would therefore be expected to have the longest run distance for a given shock pressure. It is possible that the rarefaction waves from the rear of the flyer have extended the run distance to a point where the lateral release waves from the sides of the flyer reduce the shocked region to below the critical diameter, and the run to detonation is interrupted.

7.3. Hexanitrostilbene (HNS)

The HNS evaluated was supplied by BWXT Pantex and pressed into pellets by QinetiQ. The pellets were 6.25 mm in diameter, 3 mm in length with a density of 1.6 $g.cm^{-3}$. This HNS has a surface area of 13.9 $m^2.g^{-1}$, as measured by gas adsorption.

7.3.1. Initiation of Hexanitrostilbene

The energy required for a 50% probability of initiation was determined for two detonator systems: Exploding Foil Initiators (EFI), with polyimide flyers 380 μm by 380 μm square, with a thickness of 25 μm; Laser Slapper Detonators, with 400 μm diameter aluminium flyers, ranging in thickness from 3 to 5 μm. These flyer diameters were well in excess of the critical failure diameter for HNS, approximately 250 μm [60], with a diameter much greater than their thickness, allowing a one-dimensional treatment of the initiation, as the lateral release waves from the sides of the flyer could be ignored.

The threshold flyer velocities were measured using PDV. The velocity histories for 3.5 μm thickness aluminium flyers fired at the threshold energy are shown in Figure 122. The velocity histories are extremely consistent and repeatable. Shot 110608_112313 has the lowest velocity on impact, and also the noisiest trace. It is likely that the slightly low velocity extracted is due to the noisy signal.

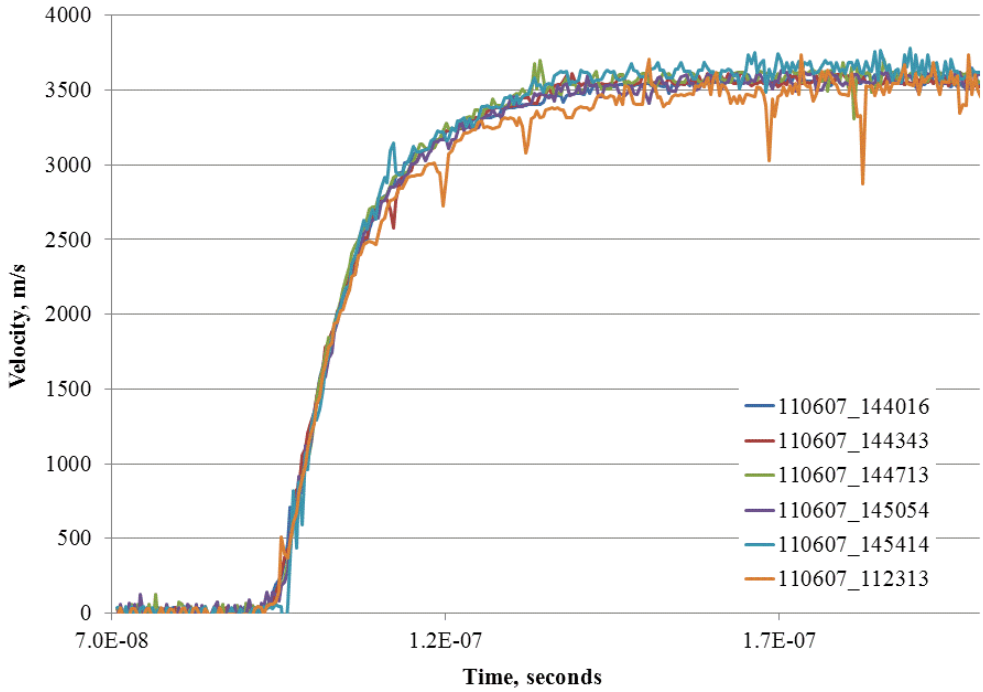

Figure 122 - 3.5 µm thickness aluminium flyer velocity histories

Flyer batch	Thickness, µm	Number of shots	Mean velocity, ± 1 σ, $km.s^{-1}$	Laser fluence, ± 1 σ, $J.cm^{-2}$
10607	3	3	3.66 ± 0.13	16.95 ± 0.08
10626	3.5	6	3.33 ± 0.05	16.87 ± 0.16
10616	4	8	3.16 ± 0.11	16.95 ± 0.08
10609	4.5	8	2.92 ± 0.17	18.06 ± 0.72
10613	5	10	2.81 ± 0.23	18.62 ± 0.64

Table 34 - Extracted aluminium flyer velocities on impact for HNS initiation

The velocity histories for four polyimide flyers at the same threshold capacitor voltage are shown in Figure 123. The histories can be seen to be repeatable and consistent. The flyer velocities on impact are detailed in Table 35. The variation in the data is due to noise in the extracted velocity histories. The variation may be reduced slightly by taking a 3 point average around the velocity profile, but as the flyers are still accelerating at impact, this would introduce some error into the measurement.

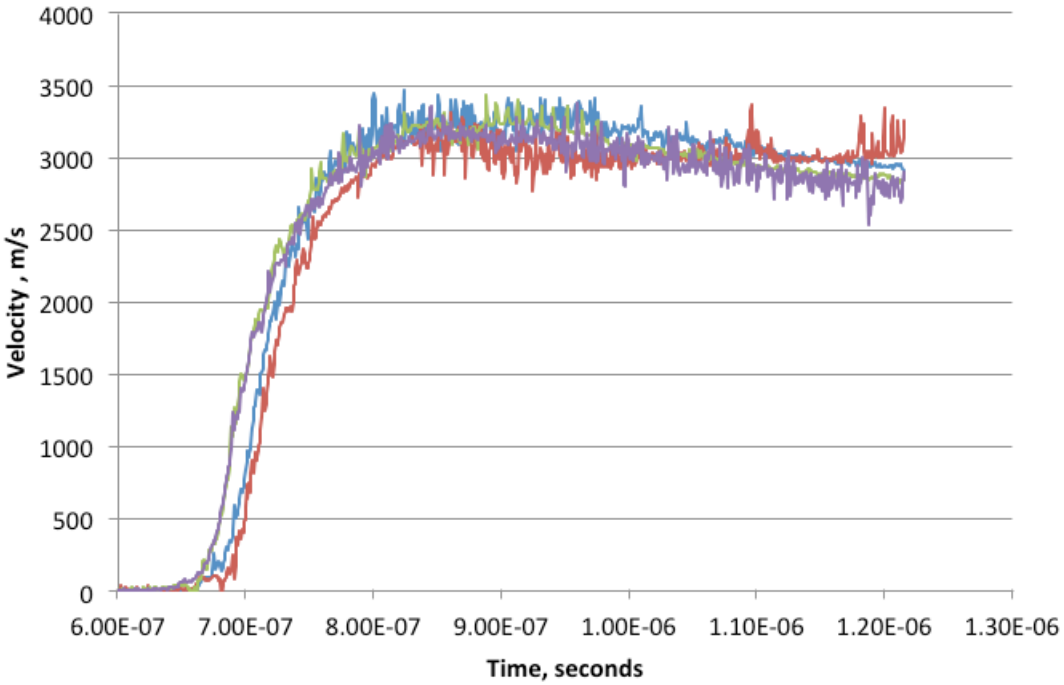

Figure 123 - Polyimide flyer velocity histories

Shot	Velocity, $km.s^{-1}$
110616_155918	3.09
110616_160237	2.87
110616_160854	2.84
110616_161311	3.02
Mean	2.96
Standard Deviation	0.12

Table 35 - Extracted polyimide flyer velocities at impact

The material properties used for all analysis in this section are shown in Table 36. The HNS Hugoniot was selected as the work performed in [98] included the specific HNS used in this report. A range of aluminium Hugoniots were used in the analysis and no significant variation was observed. The Kapton Hugoniot was selected on the basis of having been established at the higher stresses than other available Hugoniots (~20 GPa); albeit still lower than the stress regimes investigated here.

The experimental results are tabulated in Table 37. Two other threshold data sets for HNS are available. The first, from Schwarz [99], is for two HNS powders with a surface area of 2.5 $m^2.g^{-1}$ and 10 $m^2.g^{-1}$, at pressures of 3.9 to 10.4 GPa. The second, from Damm [100], is for a HNS with a surface area of 6 $m^2.g^{-1}$, at pressures of 8.2 to 21.5 GPa. Waschl [101] and Harris [102]reported that the threshold of HNS is independent of surface area from 5 to 20 $m^2.g^{-1}$. It is therefore considered appropriate to consider this data alongside the data reported here.

Material	Density, $g.cm^{-3}$	C_0, $km.s^{-1}$	s
HNS [98]	1.6	1.43	2.630
Al 2024 [61]	2.785	5.370	1.290
Kapton [61]	1.410	0.93	1.640

Table 36 - Material properties used for HNS initiation calculations

Flyer thickness, μm	Flyer material	Threshold flyer Velocity, $km.s^{-1}$	Shock Pressure, GPa	Shock duration, ns	Energy fluence, $MJ.m^{-2}$
3.0	aluminium	3.66	27.1	1.6	0.096
3.5	aluminium	3.33	23.1	1.9	0.092
4.0	aluminium	3.16	21.6	2.2	0.096
4.5	aluminium	2.92	19.1	2.6	0.092
5.0	aluminium	2.81	17.7	2.9	0.092
25	polyimide	2.96	11.1	9.9	0.152

Table 37 – Initiation thresholds for HNS with a surface area of 13.9 $m^2.g^{-1}$ as a function of flyer thickness

7.3.2. Critical Energy Fluence Determination for HNS

Walker and Wasley [87] proposed that initiation of an explosive could only occur when the energy fluence imparted to the explosive exceeded a certain critical value, given by Equation 19. The critical energy fluence as a function of pressure for the HNS investigated here, along with the data from Schwarz and Damm is shown in Figure 124. Although the HNS powders presented differ in surface area (2.5, 6, 10 and 13.9 $m^2.g^{-1}$), clear trends are observed in Figure 124. An asymptote at 3.6 GPa, as reported by Schwarz, below which initiation cannot occur, is apparent, with the required energy

fluence increasing as this pressure is approached. Above this pressure, the energy fluence decreases, approaching a constant value at around 15 GPa. It is interesting to note that this is close to the CJ pressure of HNS, 21.5 GPa [90]. The shock duration for initiation at these high pressures is 2-3 ns (from Table 37), less than the reaction zone duration reported for PETN (<10 ns)[103]. It is possible that the initiation process is comparable to that of a steady state detonation wave, as the pressure and duration are both comparable.

There is some dependance on surface area evident, with the lower surface area HNS able to be initiated at lower pressures than the higher surface area HNS. At higher pressures, this trend reverses, with the higher surface area HNS having a lower critical energy fluence than the lower surface area HNS. This is consistent with the explanation detailed in Section 7.1.4.

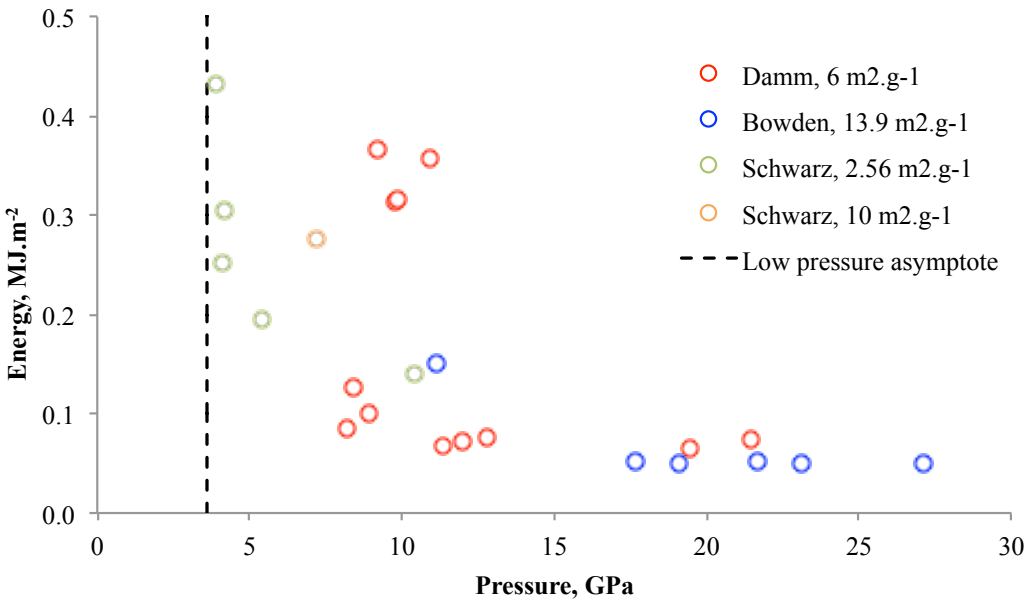

Figure 124 - Energy fluence variance with pressure for HNS of varying surface areas

7.3.3. Calculation of the James Initiation Parameters

The James Criterion [88] is an extension of the original Walker-Wasley criterion. It possesses all the applicability of the Walker-Wasley criterion but applies to a wider range of both impactor shapes and explosives. Further details are given in Section 7.1.1. The James criterion is given by

$$\frac{\Sigma_C}{\Sigma} + \frac{E_C}{E} = 1$$

Equation 23

where Σ_C and E_C are constants for a given explosive.

As the thresold of HNS is independent of surface area from 5 to 20 $m^2.g^{-1}$ [101; 102], the three highest surface area HNS powders (6, 10 and 13.9 $m^2.g^{-1}$) may be considered as a single data set. The composite data is presented in Figure 125, along with the fitted James curve. The values of E_C and Σ_C are 0.0356 $MJ.kg^{-1}$ and 0.5797 $MJ.m^{-2}$ respectively, determined by fitting to the experimental data. It can be seen that a good fit is obtained to the composite data, with little variance between the three data sets. Confidence in this data may be extended further by determining the threshold for the 6 $m^2.g^{-1}$ HNS at higher pressures, with aluminium flyers, and the threshold for the 13.9 $m^2.g^{-1}$ at lower pressures, to increase the overlap of the data.

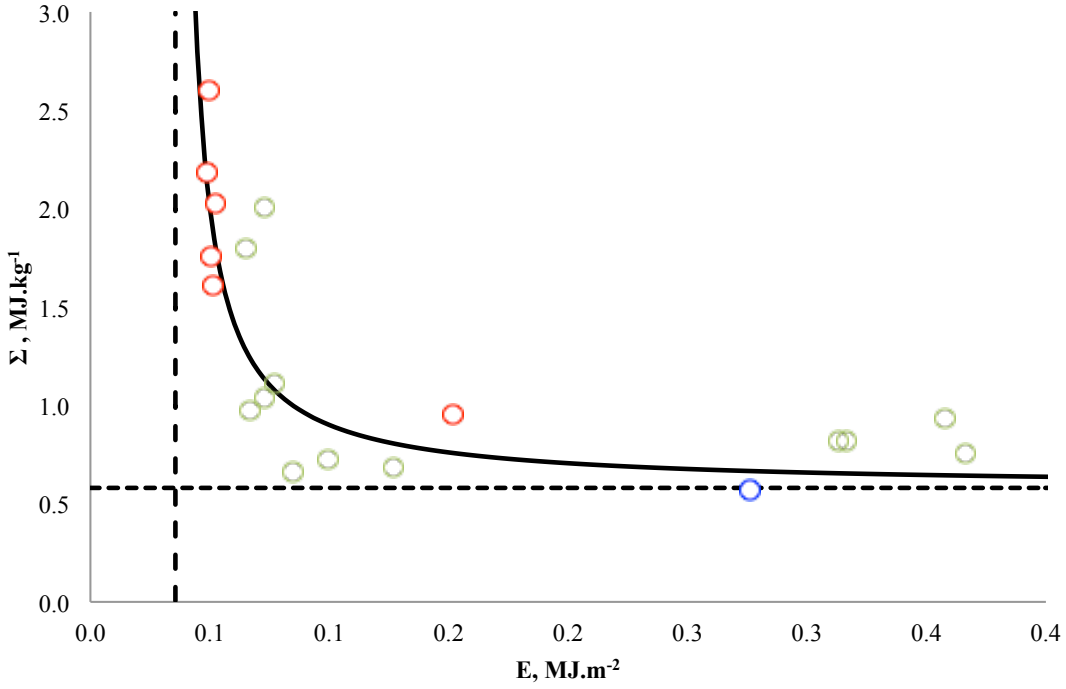

Figure 125 - James Criterion for HNS. Blue circles are Schwarz data, red circles are Bowden data, green circles are Damm data, solid line is J=1 (threshold), and dashed lines are E_C and Σ_C

7.3.4. Effect of Surface area and Solvent Content on Initiation

High surface area HNS is typically produced by crash precipitation from a solvent solution [104]. This can produce powders with a variety of surface areas and solvent content. Five such powders were available for this study, detailed in Table 38. Surface areas from 4.5 to 13.9 $m^2.g^{-}1$ were measured by gas adsorption. The main solvent contaminant was dimethylformamide (DMF), the concentation of which increased with surface area.

HNS Batch	Specific Surface Area, $m^2.g^{-1}$	Residual Solvent Content	
91143-07DT-01	4.5	Trace dioxane	
01123-07PFP-001B	8.3	0.45wt% DMF	Trace MeOH
96095-07PFP-001	9.9	0.61wt% DMF	0.04%wt MeOH
94082-07PFP-01B	10.76	0.63wt% DMF	0.05%wt MeOH
97121-07PFP-001B	13.9	0.74wt% DMF	Trace MeOH

Table 38 - Properties of HNS powders

The HNS evaluated was supplied by BWXT Pantex and pressed into pellets by QinetiQ. The pellets were 6.25 mm in diameter, 3 mm in length with a density of 1.6 $g.cm^{-3}$. Scanning electron micrographs of the HNS powders are shown in Figure 126, Figure 127, Figure 128, Figure 129 and Figure 130.

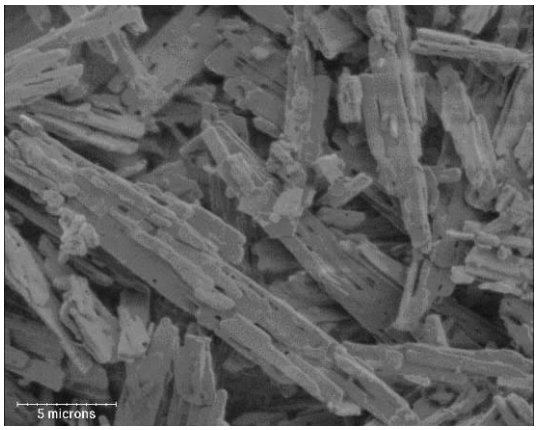

Figure 126 – Scanning electron micrograph of HNS, surface area 4.5 $m^2.g^{-1}$

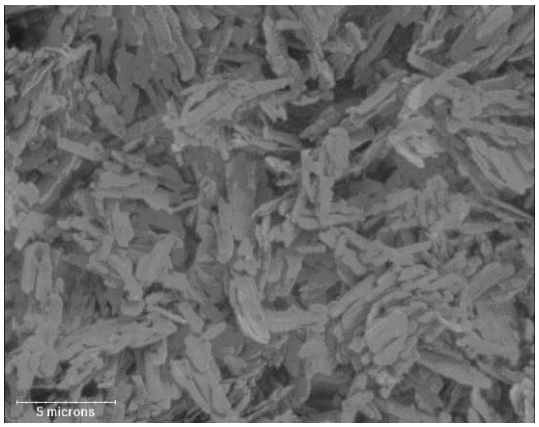

Figure 127 - Scanning electron micrograph of HNS, surface area 8.3 $m^2.g^{-1}$

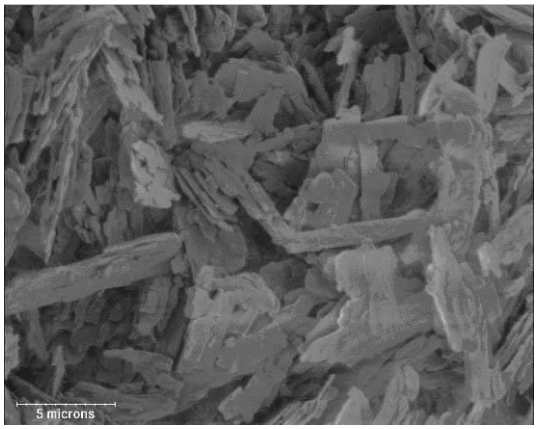

Figure 128 - Scanning electron micrograph of HNS, surface area 9.9 $m^2.g^{-1}$

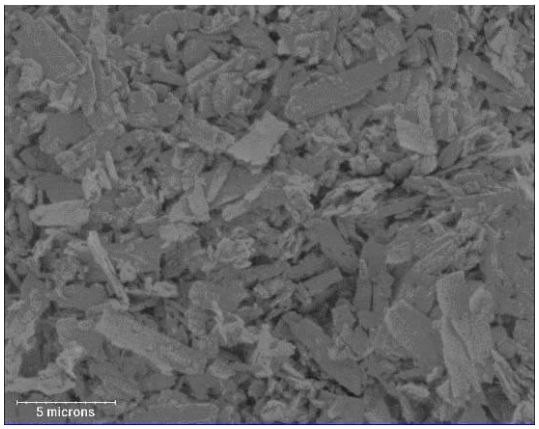

Figure 129 - Scanning electron micrograph of HNS, surface area 10.76 $m^2.g^{-1}$

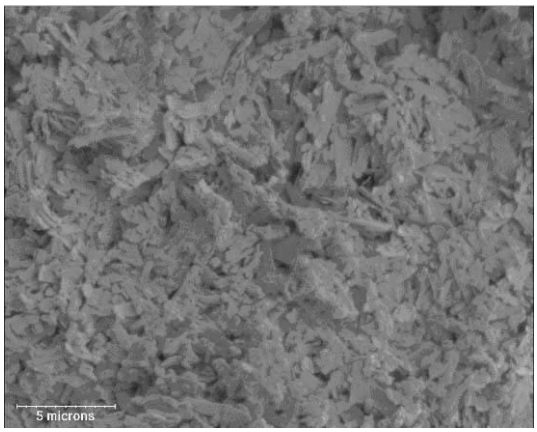

Figure 130 - Scanning Electron Micrograph of HNS, surface area 13.9 $m^2.g^{-1}$

The HNS pellets were impacted with 3.5 μm thickness aluminium flyer plates and the fluence required for a 50% probability of initiation determined using a Neyer D-optimal method [95]. The flyer velocity required for a 50% probability of initiation was then determined from Figure 104. The results are tabulated in Table 39, with the variation in threshold flyer velocity with surface area shown in Figure 131. The 8.3 $m^2.g^{-1}$ powder was initiated with flyers from a second coating run, to investigate the run-to-run variability of the flyers.

SSA, $m^2.g^{-1}$	Number of Shots	Threshold Fluence, ± 1σ, $J.cm^{-2}$	Threshold Velocity, ± 1 σ, $m.s^{-1}$	All-fire fluence, $J.cm^{-2}$, 0.99 probability at 50% confidence
4.5	17	18.82 ± 2.16	3414 ± 150	29.71
8.3	15[7]	16.79 ± 0.20	3273 ± 15	17.60
8.3	15[8]	17.05 ± 0.23	3292 ± 17	18.04
9.9	15	16.79 ± 0.84	3273 ± 63	20.74
10.76	11	17.06 ± 0.97	3293 ± 72	24.82
13.9	12	21.23 ± 7.85	3562 ± 567	200.60

Table 39 - Threshold results for HNS powders

[7] First coating run

[8] Second coating run

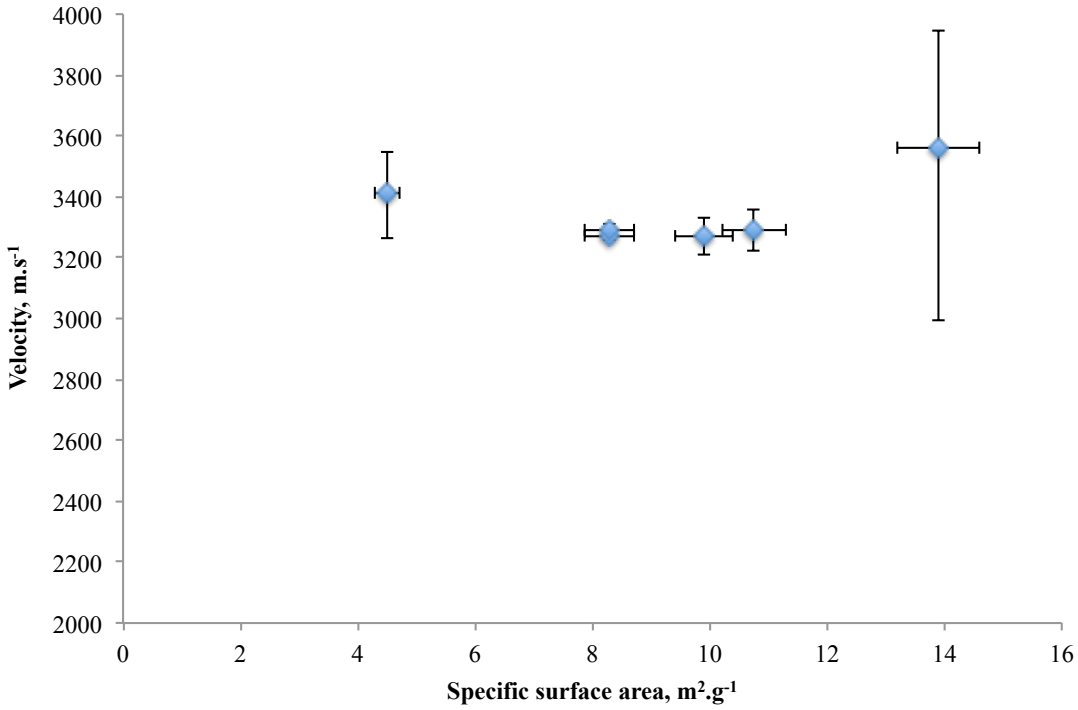

Figure 131 - Threshold flyer velocity vs. surface area for HNS powders tested. Velocity errors bars are 1 σ, surface area error bars are 5%.

Two observations can be made. Firstly, there is no significant correlation of threshold with surface area, over the range of surface areas tested, in agreement with the literature [99; 105]. Secondly, the two extremities, 4.5 and 13.9 $m^2.g^{-1}$, have a significantly higher standard deviation than the other powders, as high as 37% for the highest surface area powder. Visual inspection of the 13.9 $m^2.g^{-1}$ pellets revealed a mottled finish, with brown spots. It was suspected that these spots were concentrations of the DMF contaminant. As it was not possible to control the flyer impact site, relative to the pellet, the high standard deviation may result from the flyer impacting sites of high DMF concentration. The source of the high standard deviation for the 4.5 $m^2.g^{-1}$ pellets is not evident. As these thresholds were determined from a relatively small number of experiments (15-17), it may simply be a statistical outlier.

The two flyer coating runs tested on the 8.3 $m^2.g^{-1}$ pellets produced thresholds within the standard deviation of each other, indicated no statistically significant difference. This suggests that multiple flyer coating runs can be considered as one lot.

Three powders had all-fire fluences under 25 $J.cm^{-2}$, the 8.3, 9.9 and 10.76 $m^2.g^{-1}$ powders, less than half the fibre damage threshold of 50 $J.cm^{-2}$ (see Section 5.6.). There is significant margin between the all-fire fluence and the fibre damage threshold. These three powders had a DMF content of less than 0.63 wt.%, and this may therefore considered an acceptable upper limit for DMF content.

7.3.5. HNS Run Distance and Pop Plot

Run distance data for HNS is very sparsely reported in the literature. Kipp and Setchell [106] reported the run distance for a high surface area (8 $m^2.g^{-1}$, compared to that studied here, 13.9 $m^2.g^{-1}$) HNS for sustained shocks from 4 to 12 GPa. The data indicates a "kink" in the run distance data at approximately 7 GPa. They also present experimental data for thin[9] (25 and 75 μm) polyimide flyer initiation, from 7 to 12 GPa. This data is shown in Figure 132. It can be seen that as the flyer velocity is increased, the shock length relative to the run distance for a sustained shock increases, and the run distance trends towards that for a sustained shock.

[9] A thin flyer is one that imparts a shock duration to the explosive less than the run to detonation duration for a sustained shock at a given pressure.

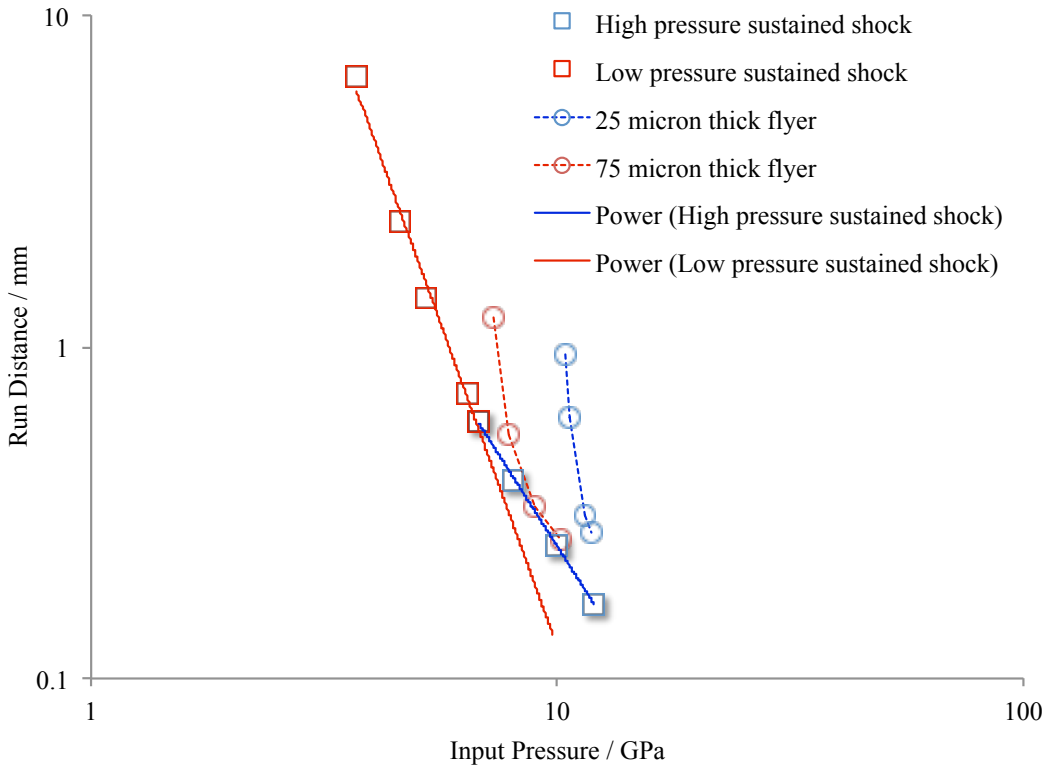

Figure 132 - Kipp and Setchell Run distance data for HNS, shock pressures 4 to 12 GPa

It is possible to calculate the pulse duration of the shock imparted to the explosive, given the pressure (and hence flyer velocity) and flyer thickness, from Equation 22. This can then be compared to the run distance predicted by the Pop plot at that pressure, to determine whether a particular flyer is “thin” or “thick”. A “thick” flyer has sufficient thickness that the detonation is established before the rarefaction waves from the rear of the flyer are able to interact with the growth to detonation. A thick flyer, disregarding 2 dimensional effect (minimal in this case, as the flyer diameters are significantly above the critical diameter for HNS (~250 μm)), will result in a run distance as per that predicted by the Pop plot i.e. it appears as an infinite duration shock. For thin flyers, the rarefaction waves begin to interact with the growth to detonation before it is complete, and will result in a loss of pressure and hence energy at the rear of the reaction. This will result in an extended run distance.

The boundary between thin and thick flyers is simple to calculate, but the effect on the run distance less so. Gittings [91] reported that where the shock duration/run time to detonation ratio exceeds 0.3, the excess transit time is close to zero i.e. the run distance

is that given by the Pop plot, and is not extended In this case, the rarefaction waves do not extend the run distance.

Kipp and Setchell's data is tabulated in Table 40, along with the pulse duration, shocked length, and the run distance as predicted by the Pop plot. It can be seen that all the 25 μm thickness flyers have a shock duration/run time less to 0.3. Therefore, the run distance should be extended relative to the Pop plot.

Flyer thickness, μm	Pressure, GPa	Pulse duration, ns	Shocked length, μm	Pop Plot run distance, μm	Shocked length / Pop plot run distance	Measured run distance, μm	Run distance extension, unitless
25	10.39	10.19	50.0	230	0.22	956	4.16
25	10.65	10.08	50.0	218	0.23	611	2.81
25	11.41	9.79	50.0	187	0.27	310	1.66
25	11.86	9.64	50.0	172	0.29	275	1.60
75	7.32	35.23	150.0	497	0.30	1221	2.45
75	7.89	34.19	150.0	422	0.36	542	1.29
75	8.94	32.50	407.5	320	1.27	332	1.04
75	10.14	30.87	407.0	243	1.68	262	1.08

Table 40 - Kipp and Setchell experiment data [106]

It can be seen that the flyers with a ratio of shocked length to Pop plot run distance less than approx. 0.30 have a significant extension to the run distance. This effect is shown in Figure 133, where the extension to the Pop plot run distance is shown as a function of how "thin" the flyer is i.e. the ratio of shocked length to the Pop plot run distance for 25 μm and 75 μm thickness flyers.

A simple one dimensional treatment of the initiation is inadequate at this point, as the rarefaction waves from the sides of the flyer will begin to interact with the shock as the run distance is extended. This likely results in the dramatic extension of the run distance at for thinner flyers, as the lateral rarefaction waves have a greater opportunity to interact with the growth to detonation. This complex relationship suggests that this effect must be characterised for each flyer diameter of interest.

The 75 μm polyimide flyer data is a useful verification of the Pop plot as measured at higher pressures i.e. above 7 GPa, as it can be seen in Figure 132 that the run distance trends to the Pop plot run distance as the flyer velocity, and shock length, is increased.

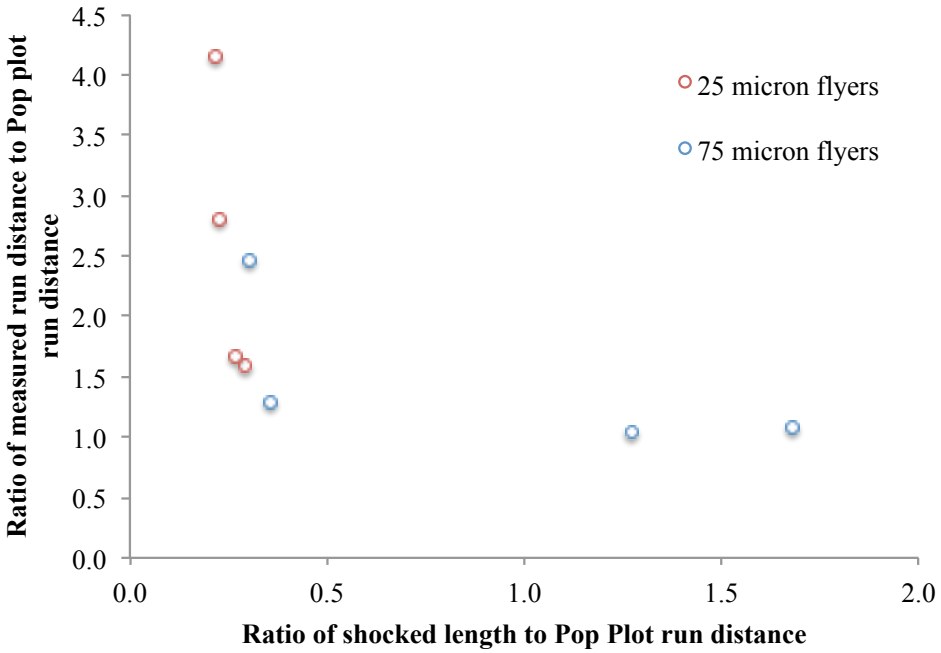

Figure 133 - Run Distance Extension by Thin Flyers

There remains a question as to the role of lateral rarefaction waves in extended run distance initiation scenarios, where the reaction has not yet grown to completion before the rarefaction waves can interact with the growth. It is likely that the lateral rarefaction waves quench the reaction growth when they approach the critical diameter of HNS (approximately 250 μm), as illustrated in Figure 134. Above this diameter, the reaction can still grow to detonate, and subsquently diverge.

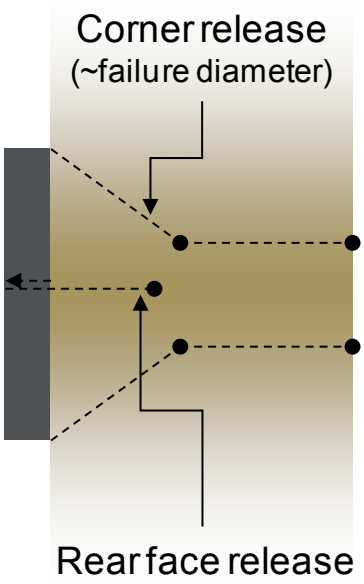

Figure 134 - Rarefaction Waves

This distance may be estimated by taking the pulse duration, τ_{rod}, for a rod-type impactor [107]:

$$\tau_{rod} = \frac{D}{2c_0}$$

Equation 24

where D is the flyer (or rod) diameter, and c_0 the sound speed in the explosive, correcting for the critical diameter and multiplying by the shock velocity in the explosive to give x_{rod}, the distance at which the diameter of the shocked region has converged to the critical diameter,

$$x_{rod} = \frac{(D - D_c)u_s}{2c_0}$$

Equation 25

where D is the flyer diameter, u_s the shock speed in the HNS, D_c the critical diameter, and c_e the sound speed in the shocked explosive.

The shocked length for a flyer is given by x_f:

$$x_f = \frac{2xU_{HE}}{U_f}$$

Equation 26

where x is the flyer thickness, U_{HE} is the shock velocity in the explosive, and U_f is the shock velocity in the flyer.

Five impactor types can therefore be defined, where x_{pp} is the run distance given by the Pop plot:

1. $x_{rod} < x_f < x_{pp}$ (narrow, thin rod), where lateral and rear rarefaction waves result in substantially extended run distances. The lateral rarefaction waves interact with the growth to detonation first.
2. $x_f < x_{rod} < x_{pp}$ (thin, narrow flyer), where lateral and rear rarefaction waves result in substantially extended run distances. The rear rarefaction waves interact with the growth to detonation first.
3. $x_f < x_{pp} < x_{rod}$ (thin flyer), where rear rarefaction waves result in close to those predicted by the Pop plot, if the ratio of shock length to Pop plot run distance exceeds 0.3, as discussed earlier.
4. $x_{pp} < x_f$ *or* x_{rod} (thick flyer or rod), resulting in run distances predicted by the Pop plot.
5. $xr_{od} < x_{pp} < x_f$ (rod), where lateral rarefaction waves result in extended run distances.

The data shown in Figure 133 can then be replotted by impactor type, in Figure 135. Table 41 shows the calculated shock lengths for each flyer, along with the type of impactor. It should be noted that for the thin, narrow flyer there is little difference between the rod shock length and flyer shock length. Where the Pop plot run distance is in excess of the longest shock length, significantly extended run distances are observed, as the rear rarefaction waves extend the run distance to a point where the lateral release waves can further extend it. If the Pop plot run distance is between the flyer and rod shock lengths, then run distances close to that predicted by the Pop plot are achieved.

Flyer thickness, µm	Flyer diameter, µm	Pressure, GPa	Shock length (flyer), µm	Shock length, (rod), µm	Pop Plot run distance, µm	Measured run distance, µm	Type of impactor
25	381	10.39	50.0	224.8	230	956	Thin, narrow flyer
25	381	10.65	50.0	227.2	218	611	Thin flyer
25	381	11.41	50.0	233.8	187	310	Thin flyer
25	381	11.86	50.0	237.6	172	275	Thin flyer
75	1016	7.32	150.0	1140.3	497	1221	Thin flyer
75	1016	7.89	150.0	1175.0	422	542	Thin flyer
75	1016	8.94	407.5	1236.1	320	332	Thick flyer
75	1016	10.14	407.0	1301.5	243	262	Thick flyer

Table 41 - Impactor Types

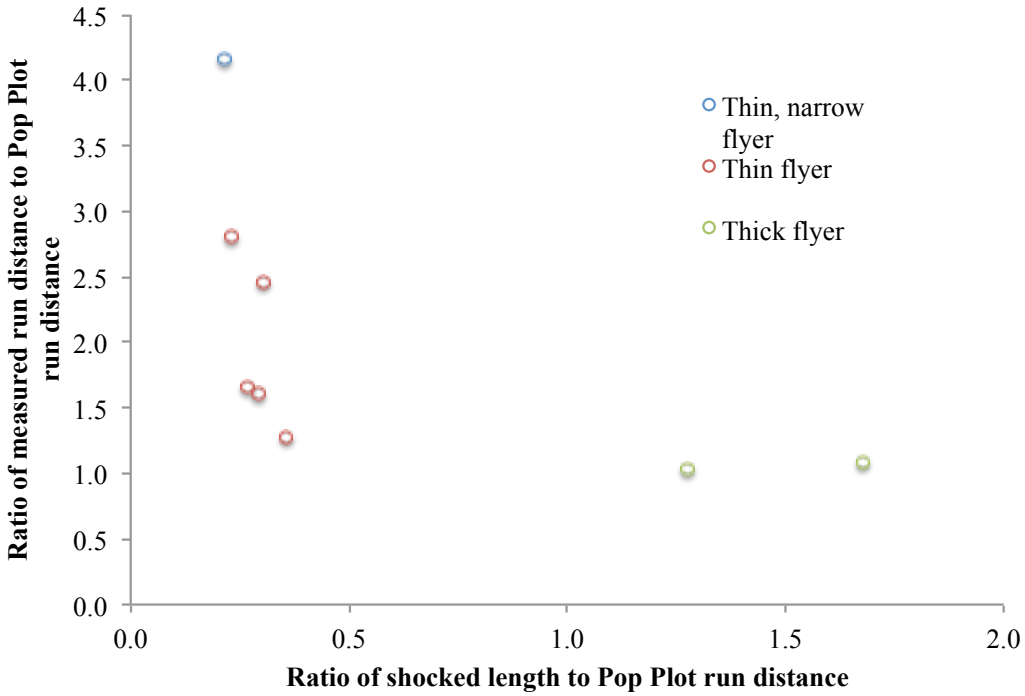

Figure 135 - Run distance extension by various flyer types

It is then possible to determine the impactor type for the aluminium and polyimide flyers used in this study. All flyers are thin flyers, i.e. $X_f < X_{PP} < X_{rod}$. The run distances can then be estimated from Kipp and Setchell's data, by fitting an exponential law

through the thin flyer data points, as shown in Figure 136. The estimated run distances are given in Table 42. It is noteworthy that the predicted run distance for the 25 μm polyimide flyer exceeds the rod shock length, and may therefore be further extended. There are large uncertainties in this prediction due to the limited number of data and significant extrapolation, so care should be taken in the application of this prediction.

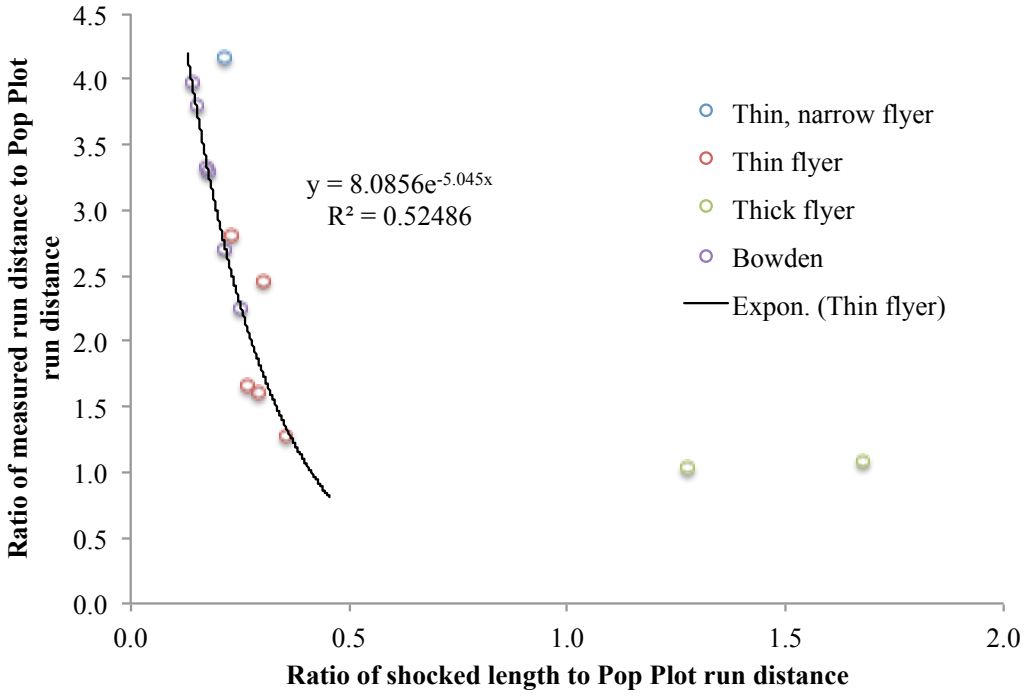

Figure 136 - Run distance extension prediction

Flyer thickness, μm	Flyer diameter, μm	Pressure, GPa	Shock length (flyer), μm	Shock Length, (rod), μm	Pop Plot run distance, μm	Estimated run distance, μm
3	400	27.1	6.0	390	28	75
3.5	400	23.1	7.0	363	39	129
4	400	21.6	8.0	353	46	152
4.5	400	19.1	9.0	334	60	227
5	400	17.7	10.0	323	71	283
25	380	11.1	50.0	230	198	445

Table 42 - Determination of impactor types and run distance estimation

It may be possible to verify these calculated run distances by consideration of the excess transit time i.e. the additional time for the reaction to propagate through the explosive charge due to the growth to detonation process. In the case of the 5 μm aluminium flyer in Table 42, the calculated run distance is 283 μm. If we assume that the growth to detonation proceeds at the shock speed in the HNS (6.15 $km.s^{-1}$), then the reaction will grow to detonation in 65.4 ns. The remaining length of the charge will detonate at the steady state detonation velocity, 6.8 $km.s^{-1}$. For a 1 mm length charge, this equates to a transit time of 151.5 ns, giving an excess transit time of 4.4 ns. Clearly, this would be challenging to measure. Another method for verifying the calculated run distance would be to attempt the initiation of a very short pellet, approximately 200 μm. If complete detonation is observed, then the run distance has not been extended by the thin flyer. Conversely, if incomplete reaction is observed, then the run distance is in excess of the pellet length. The extent of reaction can be determined by measuring the interface velocity between the explosive and a window, such as lithium fluoride, using PDV.

This analysis has defined several new impactor types for shock initiation of explosive, in addition to the traditional rod and flyer impactors. This has allowed for the development of a method for predicting run distance extension for non-sustained shocks. This method, if validated, provides a valuable design tool to enable design margins to be quantified and improved.

7.4. Characterisation of Explosive Output

A detonator is an explosive device used to convert a non-explosive energy source, such as electrical energy stored in a capacitor, into an explosive output. This explosive output is generally used to initiate further explosive charges. It is therefore desirable characterize the output of detonators, in particular output pressure. This allows for reliable detonation systems to be designed. There are two methods available for measuring the output pressure of an explosive charge, using PDV. Firstly, by measuring the interface velocity between the explosive and a window of known impedance, such a lithium fluoride. Secondly, by measuring the velocity of a flyer plate placed in contact with the explosive and subsequently accelerated. In this study, flyer plates were used due to the experience gained in the characterisation of laser-driven flyer plates.

7.4.1. Experimental Results and Discussion for Characterisation of Explosive Output

The laser detonator test body described in Section 3.2.7 was filled with the HNS powders tested in Section 7.3.4, pressed into pellets at a density of 1.6 $g.cm^{-3}$, for a total of 147 mg of explosive. As this test body has a bare explosive output, an aluminium disk of 125 μm thickness was bonded to the explosive using a cyanoacrylate adhesive.

The detonator test bodies were mounted in a polycarbonate experimental fixture, with the PDV probes held at approximately 3-4 mm standoff from the output face of the detonator of interest. No alignment of the probe relative to the surface was performed, primarily due to safety concerns relating to high power laser impingement upon explosives. A typical PDV data trace is shown in Figure 137, with the corresponding spectrogram shown in Figure 138.

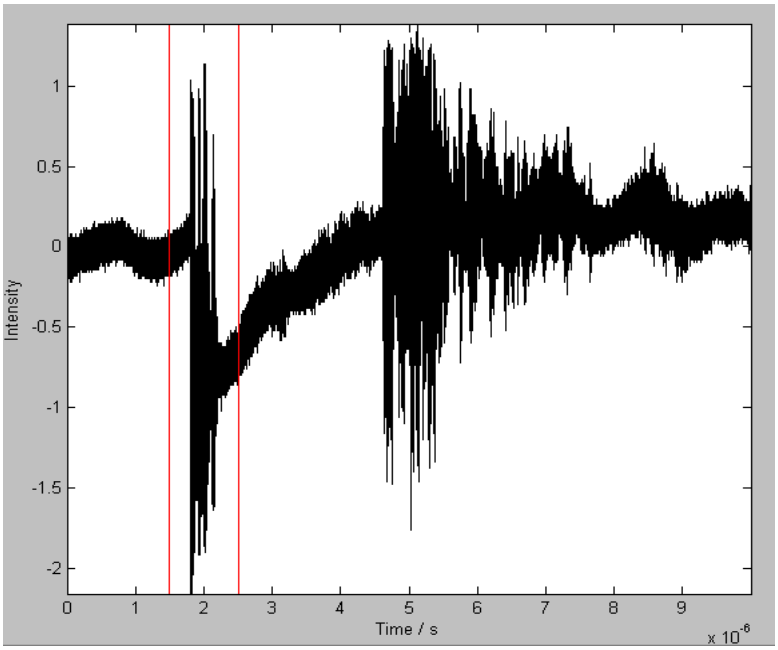

Figure 137 – Typical PDV Raw Signal for HNS Pellet

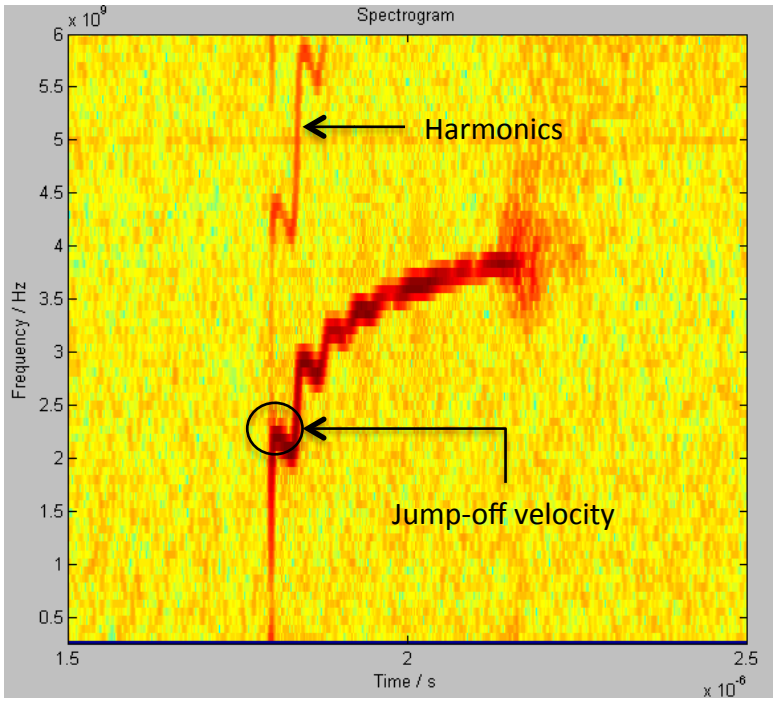

Figure 138 – Typical Time Frequency Representation of Jump Off Signal for HNS Pellet

Once a velocity history was obtained the jump-off velocity was determined from the velocity history, as shown in Figure 138. The detonation was then modelled using the CTH hydrocode (Sandia National Laboratories), and the detonation pressure required to

accelerate the flyer to the recorded velocity was determined. A range of equations of state were used for both the aluminium and the HNS to ensure that material parameters did not adversely affect the results. The HNS parameters were taken from Goveas et al, [98] whilst the aluminium parameters were taken from the library of materials provided with the CTH hydrocode.

All of the shots showed the same predominant features of a very rapid acceleration to a "jump-off" velocity followed by shock reverberation induced acceleration to a steady velocity, seen in Figure 139. The results of these shots are summarized in Table 43.

Shot Number	Specific Surface Area, $m^2.g^{-1}$	Jump-off Velocity, $km.s^{-1}$	Calculated Pressure, GPa
1	9.9	1.76	21.0
2	8.3	1.94	25.0
3	8.3	1.88	23.9
4	4.5	1.76	21.0
5	4.5	1.76	21.0
6	10.76	2.00	30.0
7	10.76	1.82	23.1
8	13.9	1.82	23.1
9	13.9	1.93	25.6
	Mean	1.85	23.74
	σ	0.09	2.91

Table 43 – Summary of results for HNS output measurements

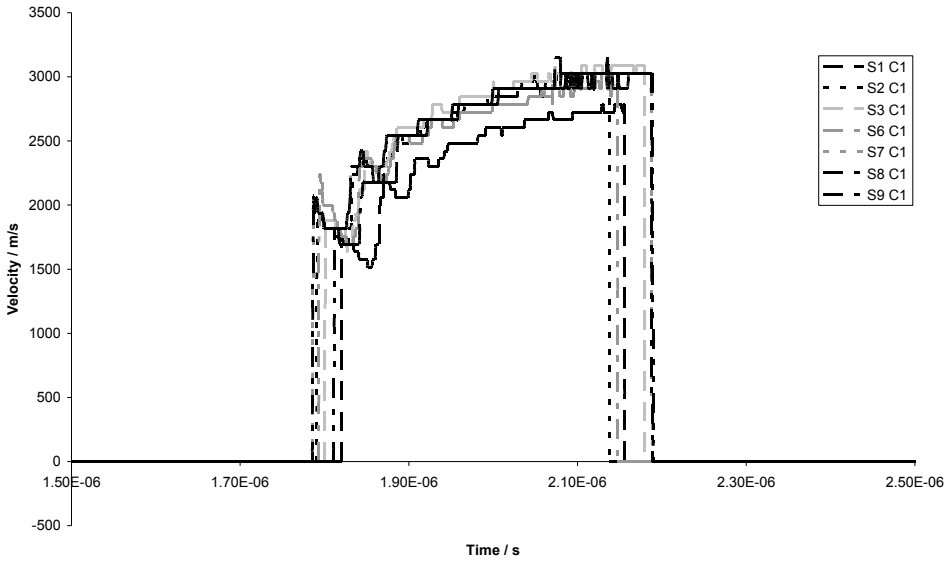

Figure 139 - Selected Time-Velocity Profiles for HNS

The average pressure determined, 23.74 GPa, is somewhat higher than the published value for HNS, 21.5 GPa [92]. The outlier value for shot 6, 30 GPa, is due to the PDV-peak finding algorithm struggling to separate the true velocity from the harmonics observed in Figure 138. It is possible that the time resolution of the PDV system, around 1 ns, is adequate to partially resolve the Neumann spike at the front of the reaction zone., not previously measured. There is no correlation of HNS detonation pressure with surface area as expected.

The use of PDV for non-contact velocity measurements to measure the early time velocity of explosively driven thin foils has been demonstrated. This technique provides a simple method to investigate both the performance of detonators, and detonics properties such as the detonation pressure. Further refinement of the technique, by replacing the aluminium flyer with a lithium fluoride window, may allow direct measurement of the explosive reaction zone.

Measurement of the detonation pressure allows for the design of an integrated initiation train, comprising a detonator, booster charge and a main charge, by allowing the initiation of the booster charge by the detonator to be modelled.

7.5. Summary of Explosive Initiation

Two explosive materials have been initiated with laser-driven aluminium flyer plates: pentaerythritol tetranitrate (PETN) and hexanitrostilbene (HNS).

A strong dependence of threshold on surface area was found for PETN, with the minimum surface area for use in laser detonators found to be 20,000 $cm^2.g^{-1}$. The critical energy for initiation was determined, <0.086 $MJ.m^{-2}$ for PETN with a surface area greater than 12,700 $cm^2.g^{-1}$, and found to be lower than that reported in the literature, most likely due to the high surface area of the PETN powders tested. Due to the high shock velocities generated within the PETN, the detonation velocity could be accurately determined as 7.70 $km.s^{-1}$, in close agreement with the literature value of 7.75 $km.s^{-1}$. For low surface area powders, 12,700 $cm^2.g^{-1}$, partial reactions were observed, believed to be due to long run distances allowing the lateral release waves from the sides of the flyer to quench the growth of reaction.

The threshold of HNS was not found to be dependant on surface area over the range studied, but was dependant on the concentration of a contaminant, DMF, with the value of <0.63 wt.% required.. The critical energy for HNS with a surface area of 13.9 $m^2.g^{-1}$ was determined to be 0.05 $MJ.m^{-2}$, and the James Criteria was also evaluated for high surface area HNS, with values of E_C = 0.036 $MJ.m^{-2}$ and Σ_C =0.570 $MJ.kg^{-1}$ determined.

HNS and PETN are both suitable for use in laser detonators, with all-fire fluences of less than 25 $J.cm^{-2}$, providing significant margin when compared to the optical fibre damage threshold of 50 $J.cm^{-2}$.

The efficiency of the flyer initiation can be calculated by comparing the laser fluence to the energy fluence imparted to the explosive, given by Equation 19. The results are shown in Table 44. It can be seen that the initiation is very efficient, with around 25% of the laser fluence, as measured at the fibre output, imparted to the explosive.

Material	Surface area, $m^2.g^{-1}$	Laser fluence, $MJ.m^{-2}$	Critical energy fluence, $MJ.m^{-2}$	Efficiency
PETN	1.27	0.411	0.086	0.21
PETN	1.53	0.353	0.079	0.22
PETN	2.06	0.239	0.061	0.26
PETN	2.51	0.204	0.055	0.27
HNS	13.9	0.172	0.092	0.28

Table 44 - Efficiency of flyer initiation for PETN and HNS

The relationship between sustained shock pressure and run distance was discussed for HNS, and the extension of the run distance by non-sustained shocks estimated. A relationship between flyer parameters, such as diameter and thickness, and the degree of run distance extension was proposed.

Finally, the use of Photonic Doppler Velocimetry to determine explosive material parameters such as output pressure and reaction zone length was investigated. The output pressure of HNS was measured as 23.74 GPa, somewhat higher than the published value of 21.5 GPa. It was proposed that this discrepancy was due to resolution of previously unrecorded features of the reaction zone within the explosive.

CHAPTER 8: THE LASER DETONATOR SYSTEM

The baseline laser detonator system, as defined in Section 2.6, can be revised following the work reported in this studies. The system parameters are specified in Table 45.

Parameter	Specification	Justification
Laser type	Nd:YAG, 1064 nm	Most common laser type reported in literature. Commercially available. Fundamental wavelength (1064 nm) is most efficient
Laser energy	>26 mJ	365 µm core diameter fibre (Section 5.6) 25 J.cm^{-2} at fibre output (Section 7.5) 80% fibre transmission (Section 5.4.1) 90% transmission through coupling optics
Laser pulse width	11.5 – 14 ns	Most commonly reported in literature for fibre injection
Injection method	Microlens array with primary lens	Damage threshold greater than 50 J.cm^{-2} (5.2.6)
Fibre core diameter	365 µm	Section 5.6
Fibre length	<30 m	30 m length fibres were able to transmit laser pulses without degradation [78]
Fibre type	Thorlabs FG365UEC	Section 5.6
Fibre ferrule	Steel	Section 5.2.5.3
Fibre polishing method	See Section 5.2.6	
Flyer plate composition	0.5 mm fused silica window 10 nm titanium absorption layer 0.25 µm aluminium ablation layer 0.5 µm alumina insulator layer 3.5 µm aluminium impactor layer	Section 6.7

Barrel length[10]	75 μm	90% of terminal velocity attained by 75 μm, 100% by 100 μm (Section 6.7)
Explosive material	HNS	Lower thresholds than PETN (Section 7.5)
Explosive density	90% TMD	Successful initiation reported by laser-driven flyer plates [21; 54-57]
Explosive surface area	8.3 – 10.76 $m^2.g^{-1}$ surface area (for HNS)	Lowest thresholds and standard deviations (Section 0)
Explosive solvent content	Less than 0.63 wt.% DMF (for HNS)	Lowest thresholds and standard deviations (Section 0)

Table 45 - The laser detonator system

These parameters produce an optimised system, with a thorough understanding of the operating principles and processes, suitable for use with commercially available laser systems. Although further integration is necessary for a fieldable system, the system developed within this study is a robust, well understood design concept.

[10] Separation between flyer plate and explosive

CHAPTER 9: CONCLUSION

From a review of the literature a baseline laser detonator system was defined. Whilst these parameters should produce a usable system, it will not be optimised, nor will a full understanding of the processes involved be available.

Starting with the baseline system, each component and interfave was studied to gain an understanding of the underlying principles and processes, to aid in the design of an optimised system.

A variety of optical fibre polishing methods were evaluated to determine which method had the highest damage threshold, for zirconia and steel ferrules. It was found that each ferrule type required a different polishing method, due to the differences in hardness between the silica fibre, the ferrule material and the polishing media. Both ferrule types were able to transmit a fluence in excess of 50 $J.cm^{-2}$ without damage, in excess of the estimated fluence required for explosive initiation of 20 $J.cm^{-2}$.

Novel optical fibres were evaluated as they may offer advantages for laser detonator system design. Tapered optical fibres, which increase the area into which the laser energy is coupled were tested. The damage threshold and transmission of tapered optical fibres was found to be highly dependant upon the coupling method used, in particular, focussed before the fibre, or focussing within the fibre. Side-fire optical fibres, with a shaped output face to direct the output at 90 degrees, allow for greater flexibility in the design of the detonator, by allowing the fibre to enter from the side of the detonator, instead of from the rear. Two designs of side-fire optical fibres were found to have acceptable damage thresholds and output beam quality, but a design that offered both has not been determined.

The use of tapered optical fibres to increase the tolerances required for the coupling of the laser into the optical fibre was evaluated, using both a lenslet array coupling method and a plano-convex lens coupling method. A non-tapered fibre using a lenslet array coupling method had a required tolerance of 70 μm. Tapered optical fibres were able to increase this to 260 μm.

A high-energy fibre to fibre connection was developed, offering a significant advantage for the practical application of a laser detonator system. By separating the optical fibre into two sections, the free-space beam produced by the laser fireset can be actively aligned to an optical fibre which then forms part of the laser fireset. This fibre can also form part of an environmental seal for the fireset, preventing contamination of the laser. To aid this, the lenslet array injection method was optimised for tapered fibres by matching the reduced NA of the tapered fibres, increasing the transmission to 80%, comparable to that of non-tapered fibres. Two designs were produced. The first design, with a simple fibre to fibre connection, had a damage threshold of 23.9 $J.cm^{-2}$. This design is suitable for applications where an environmental seal between the laser fireset and detonator is not required. The second design, with a vacuum feedthrough between the two fibres, had a damage threshold of 21.0 $J.cm^{-2}$. Whilst both designs have a damage threshold above the estimated fluence required for explosive initiation (20 $J.cm^{-2}$), the margin is inadequate. Methods for improving the damage threshold were proposed.

The damage threshold of the optimised fibre design was determined to be 50 $J.cm^{-2}$.

A simple one-dimensional, time-dependent model of the flyer motion was constructed. This simple, one-dimensional model was capable of predicted both the terminal velocity and the time-dependent velocity history with a high level of accuracy, and can be used as a design tool to evaluate alternate flyer thicknesses and materials.

The ablation and insulator layers were investigated to determine the optimal layer thicknesses. The optimal layer is 500 nm for both ablation and insulator layers. There was a clear benefit in increasing the ablation and insulator layer thicknesses. For the baseline case, 250 nm thickness ablation and insulator layers, the distance at which degradation was observed (139 μm) was almost twice that at which 90% of terminal velocity is typically reached (75 μm). It was decided not to change the ablation or insulator thicknesses, as some explosive experiments had been performed with a 250 nm insulator layer thickness.

The optimised flyer was characterised, with the terminal velocity determined as a function of laser fluence.The optimised flyer was impacted into lithium fluoride

windows, and the interfacial velocity measured using a high-bandwidth PDV system. By comparing the experimental results to a model of the experiment, the flyer thickness at impact was estimated. The flyer thickness was found to correspond to the impactor layer, provided an accurate determination of the shock duration that would be subsequently imparted to the explosive, essential for accurate characterisation of the explosive response.

Two explosive materials have been initiated with laser-driven aluminium flyer plates: pentaerythritol tetranitrate (PETN) and hexanitrostilbene (HNS).

A strong dependence of threshold on surface area was found for PETN, with the minimum surface area for use in laser detonators found to be 20,000 $cm^2.g^{-1}$. The critical energy for initiation was determined, <0.086 $MJ.m^{-2}$ for PETN with a surface area greater than 20,000 $cm^2.g^{-1}$, and found to be lower than that reported in the literature, most likely due to the high surface area of the PETN powders tested. Due to the high shock velocities generated within the PETN, the detonation velocity could be accurately determined as 7.70 $km.s^{-1}$, in close agreement with the literature value of 7.75 $km.s^{-1}$. For low surface area powders, 12,700 $cm^2.g^{-1}$, partial reactions were observed, believed to be due to long run distances allowing the lateral release waves from the sides of the flyer to quench the growth of reaction.

The threshold of HNS was not found to be dependant on surface area, but was dependant on the concentration of a contaminant, DMF, with the value of <0.63 wt.% required.The critical energy for HNS with a surface area of 13.9 $m^2.g^{-1}$ was determined to be 0.05 $MJ.m^{-2}$, and the James Criteria was also evaluated for a generic high surface area HNS, with values of E_C = 0.036 $MJ.m^{-2}$ and Σ_C =0.570 $MJ.kg^{-1}$. The threshold of HNS was found

Both HNS and PETN are practical for use in laser detonators, with all-fire fluences of less than 25 $J.cm^{-2}$, providing significant margin when compared to the optical fibre damage threshold of 50 $J.cm^{-2}$.

The relationship between sustained shock pressure and run distance was discussed for HNS, and the extension of the run distance by non-sustained shocks estimated. A

relationship between flyer parameters, such as diameter and thickness, and the degree of run distance extension was proposed.

Finally, the use of Photonic Doppler Velocimetry to determine explosive material parameters such as output pressure and reaction zone length was investigated. The output pressure of HNS was measured as 23.74 GPa, somewhat higher than the published value of 21.5 GPa. It was proposed that this discrepancy was due to resolution of previously unrecorded features of the reaction zone within the explosive.

An optimised laser detonator system, with a thorough understanding of the operating principles has been developed. This system has robust margins, and offers significant safety advantages over electrical detonators, with immunity from electrical threats such as electrostatic discharge.

CHAPTER 10: FUTURE WORK

A laser detonator system has been developed, with a thorough scientific understanding gained of the processes involved in each component and stage of operation. There remains some areas where further work would deepen the understanding and lead to further refinements of the design.

10.1. Fibre to Flyer Coupling

Side-firing fibres: It is considered desirable for the optical fibre to enter the detonator body from the side, i.e. non-axial. Some work has been conducted on the development and characterisation of side-firing fibres, but a design has not yet been achieved to optimise beam quality and damage threshold. This will investigate designs and the operation thereof to achieve acceptable performance of both these parameters. Window coatings vs. fibre coatings: current work has used flyer coatings on a substrate in close proximity to the fibre end. It is expected that by directly coating the fibre end with the flyer coating, an increase in efficiency can be obtained.

10.2. Explosive Initiation

The initiation of explosive materials at ultra-high pressures (~P_{CJ}) and ultra-short lengths and durations (~reaction zone) is not well understood. This could be investigated, and phenomena such as run to detonation distance, homogenous vs. heterogeneous initiation, and extension of run distances studied. The relationship between critical diameter and initiation diameter may be determined, and a History-Variable Reactive Burn (HVRB) model developed.

10.3. Explosive Output

The Von Neumann pressure of HNS and PETN has not been accurately measured, along with the reaction zone thickness or detonation wave profile. Improvements to the PDV technique may allow this measurement. The wave curvature from initiation by thin, planar, high pressure shocks could also be studied, and relationship between detonation wave curvature and velocity established. This will allow accurate modelling of small detonator charges.

REFERENCES

1. Wikipedia, *Optical Fiber*. Available from: <http://en.wikipedia.org/wiki/Optical_fibre%3E. [11/06/2013].

2. Allison, SW, Gillies, GT, Magnuson, DW & Pagano, TS 1985, 'Pulsed laser damage to optical fibers', *Applied Optics*, vol. 24, p. 3140.

3. Allison, SW & Cates., MR 1986, *Pulsed-power-handling capability of optical fibers*, CONF-860680--2, Oak Ridge Gaseous Diffusion Plant, Oak Ridge, TN, USA.

4. Trott, WM & Meeks, KD 1990, 'High-power Nd:Glass laser transmission through optical fibers and its use in acceleration of thin foil targets', *Journal of Applied Physics*, vol. 67, no. 7, pp. 3297-3301.

5. Setchell, RE, Meeks, KD & Trott, WM 1990, 'High-power transmission through step-index, multimode fibers', in *Laser-Induced Damage in Optical Materials*, SPIE, pp. 61-70.

6. Su, D, Boechat, AAP & Jones, JDC 1992, 'Beam delivery by large-core fibers: effect of launching conditions on near-field output profile', *Applied Optics*, vol. 31, no. 27, pp. 5816-5821.

7. Klingsporn, PE 1992, *Surface preparation and characterizaion of a 400 micron diameter fused silica optical fiber for direct optical initiation (DOI) applications*, KCP-613-4969, Allied-Signal Aerospace Company, Kansas City, MO, USA.

8. Carlson, NM & Johnson, JA 1993, 'Pulsed laser energy through fiberoptics for generation of ultrasound', *Journal of Nondestructive Evaluation*, vol. 12, no. 3, pp. 187-192.

9. Sweatt, WC & Farn, MW 1993, 'Kinoform/lens system for injecting a high power laser beam into an optical fiber', in *25th Boulder Damage Symposium*, SPIE, pp. 82-86.

10. Reng, N, Beck, T & Ostermeyer, M 1994, 'Comparison of different types of fibers for high-power cw Nd:YAG lasers', in *High-Power Gas and Solid State Lasers*, pp. 443-454.

11. Setchell, RE 1995, *Very high intensity fiber transmission systems*, CONF-960378--1, Sandia National Laboratories, Albuquerque, NM, USA.

12. Setchell, RE 1996, 'An optimized fiber delivery system for Q-switched, Nd:YAG lasers', *Laser-Induced Damage in Optical Materials*.

13. Setchell, RE 1997, 'End-face preparation methods for high-intensity fiber applications', in *Laser-Induced Damage in Optical Materials*, SPIE, pp. 390-399.

14. Frank, AM, Wilkins, PR, Honig, JN, Moss, M & Gillespie, CH 2000, 'High-energy laser pulse multiplexing into a fused silica fiber array', in *Laser Beam Shaping*, SPIE, pp. 85-97.

15. Honig, J 2004, *A 1-Joule laser for a 16-fiber injection system*, UCRL-CONF-203419, Lawrence Livermore National Laboratory, Livermore, CA, USA.

16. Greenaway, MW, Proud, WG, Field, JE, Goveas, SG & Drake, RC 2000, 'The effect of surface finish on the high power transmission characteristics of fused-silica optical fibres', in *32nd Annual Boulder Damage Symposium*, SPIE, pp. 599-607.

17. Clarkin, JP, Timmerman, RJ & Shannon, JH 2004, 'Shaped fiber tips for medical and industrial applications', in *Optical Fibers and Sensors for Medical Applications IV*, SPIE, pp. 70-80.

18. Brown, DM, Dickey, FM & Thomes, WJ 2005, 'Design considerations for multi-fiber injection', in *Optical Technologies for Arming, Safing, Fuzing and Firing*, SPIE, pp. 41-52.

19. Sheffield, SA & Fisk, GA 1983, 'Particle velocity measurements in laser irradiated foils using ORVIS', in, United States, p. Pages: 5.

20. Sheffield, SA & Fisk, GA 1983, 'Particle velocity measurements in laser irradiated foils using ORVIS', in *Shock Waves in Condensed Matter*, pp. 243-246.

21. Paisley, DL 1989, 'Laser-driven miniature flyer plates for shock initiation of secondary explosives', *Shock Compression of Condensed Matter*.

22. Paisley, DL, Montoya, NI, Stahl, DB & Garcia, IA 1991, 'Interferometry, streak photography, and stereo photography of laser-driven miniature flying plates', in, ed. WWF Peter, SPIE, pp. 760-765.

23. Paisley, DL 1991, *Laser-driven flyer plate*, United States Patent US 5046423 ;A; Pat. Priority: US 7-502956.

24. Paisley, DL & Stahl, DB 1992, 'Subnanosecond optical diagnostics of laser-material interaction and dynamic microstructure of materials', in *20th International Congress on High Speed Photography and Photonics*, eds JM Dewey & RG Racca, SPIE, Victoria, BC, Canada, p. 880.

25. Paisley, DL, Warnes, RH & Stahl, DB 1994, 'Experimental techniques for subnanosecond resolution of laser-launched plates and impact studies', in, eds AK George & RS Donald, SPIE, pp. 167-172.

26. Watson, S & Field, JE 2000, 'Measurement of the ablated thickness of films in the launch of laser-driven flyer plates', *Journal of Physics D: Applied Physics*, no. 2, p. 170.

27. He, H, Kobayashi, T & Sekine, T 2001, 'Time-resolved measurement on ablative acceleration of foil plates driven by pulsed laser beam', *Review of Scientific Instruments*, vol. 72, no. 4, pp. 2032-2035.

28. Rupp, TD, Gehr, RJ, Bucholtz, SM, Robbins, DL, Stahl, DB & Sheffield, SA 2004, 'Stereo Camera System for Calibration and Analysis of Small Laser-Driven Flyer Plates', in, eds DF Michael, MG Yogendra & WF Jerry, AIP, pp. 1405-1408.

29. Kohler, D, Seitz, W, Loree, T & Gardner, S 1974, 'Speckle reduction in pulsed-laser photographs', *Optics Communications*, vol. 12, no. 1, pp. 24-28.

30. Paisley, DL 1991, *Fiber optic mounted laser driven flyer plates*, United States Patent US 5029528 ;A; Pat. Priority: US 7-502960.

31. Trott, WM 1991, 'Studies of laser-driven flyer acceleration using optical fiber coupling', in, United States, p. Pages: (17 p).

32. Paisley, DL, Warnes, RH & Kopp, RA 1991, 'Laser-driven flat plate impacts to 100 GPA with sub-nanosecond pulse duration and resolution for material property studies', in, United States, p. Size: Pages: (5 p).

33. Frank, AM & Trott, WM 1994, 'Stop Motion Microphotography of Laser Driven Plates', in *Proceedings of SPIE Ultrahigh- and High-Speed Photography, Videography, and Photonics, Vol. 2273*, pp. 196-206.

34. Trott, WM 1995, *High-speed optical studies of the driving plasma in laser acceleration of flyer plates*.

35. Stahl, DB & Paisley, DL 1994, *Carbon-assisted flyer plates*, United States Patent US 5301612; A; Other: PPN: US 8-068032.

36. Farnsworth, AVJ 1995, *Laser acceleration of thin flyers*, SAND--95-0827C; CONF-950846--17; Other: ON: DE95016754; TRN: TRN: AHC29524%%92.

37. Trott, WM 1994, 'Investigation of the dynamic behavior of laser-driven flyers', in, eds SC Schmidt, JW Shaner, GA Samara & M Ross, AIP, pp. 1655-1658.

38. Labaste, JL, Doucet, M & Joubert, P 1996, 'Shocks induced by laser driven flyer plates 1-experiments', in, eds SC Schmidt & WC Tao, AIP, pp. 1213-1215.

39. Hatt, DJ & Waschl, JA 1996, 'A study of laser-driven flyer plates', in, eds SC Schmidt & WC Tao, AIP, pp. 1221-1224.

40. Lawrence, RJ & Trott, WM 1993, 'Theoretical analysis of a pulsed-laser-driven hypervelocity flyer launcher', *International Journal of Impact Engineering*, vol. 14, pp. 439-449.

41. Paisley, DL & Stahl, DB 1996, *Optical techniques for determining dynamic material properties*.

42. Labaste, JL, Doucet, M & Brisset, D 1999, 'Initiation optique: optimisation de la mise en vitesse d'un projectile initie par laser', *25th International Pyrotechnics Seminar*.

43. Trott, WM, Setchell, RE & Archie V. Farnsworth, J 2001, 'Development of Laser-Driven Flyer Techniques for Equation-of-State Studies of Microscale Materials', in, eds DF Michael, NT Naresh & H Yasuyuki, AIP, pp. 1347-1350.

44. Trott, WM, Setchell, RE, Castaneda, JN & Berry, DM 2001, 'Evaluation of a diffractive microlens-array beam shaper for use in acceleration of laser-driven flyers', in, eds MD Fred, CH Scott & LS David, SPIE, pp. 166-177.

45. Greenaway, MW, Proud, WG, Field, JE & Goveas, SG 2003, 'A Laser-accelerated Flyer System', *International Journal of Impact Engineering*, vol. 29, pp. 317-321.

46. Farnsworth, AVJ & Lawrence, RJ 1991, 'Numerical and analytical analysis of thin laser-driven flyer plates', in, United States, p. Pages: (5 p).

47. Gurney, RW & Laboratory, USABR 1943, *The Initial Velocities of Fragments from Bombs, Shell, Grenades*, Ballistic Research Laboratories.

48. Cazalis, B, Boissiere, C & Sibille, G 1996, 'Shocks induced by laser driven flyer plates 2-numerical simulations', in, eds SC Schmidt & WC Tao, AIP, pp. 1217-1220.

49. Lee, RS, Colvin, J, Frank, A, Fried, L & Reaugh, J 2001, *Final report: flight dynamics and impact characteristics of thin flyer plates driven by laser-and electrically-produced plasmas*, UCRL-ID-142522.

50. Farnsworth, AVJ, Trott, WM & Setchell, RE 2002, 'A Computational Study of Laser Driven Flyer Plates', in, eds DF Michael, NT Naresh & H Yasuyuki, AIP, pp. 1355-1358.

51. Swift, DC 2004, *Simulations of laser-launched flyers*, Los Alamos National Laboratory, Los Alamos, NM, USA.

52. Paisley, DL 1989, *Laser-driven miniauture flyer plates for shock initiation of secondary explosives*, LA-UR-89-2723, Los Alamos National Laboratory, Los Alamos, NM, USA.

53. Chengwei, S, Chunyan, W, Yonghua, Y, Changling, L & Yuanzheng, G 1999, 'Shock initiation of explosives impacted by laser-driven flyers', in *Proceedings of the 26th International Pyrotechnics Seminar* pp. 490-497.

54. Watson, S, Gifford, MJ & Field, JE 2000, 'The initiation of fine grain pentaerythritol tetranitrate by laser-driven flyer plates', *Journal of Applied Physics*, vol. 88, no. 1.

55. Greenaway, MW, Gifford, MJ, Proud, WG, Field, JE & Goveas, SG 2001, 'An Investigation into the Initiation of Hexanitrostilbene by Laser-driven Flyer Plates', *Shock Compression of Condensed Matter*.

56. Zhuowei, G, Chengwei, S, Jianheng, Z & Ning, Z 2004, 'Experimental and numerical research on shock initiation of pentaerythritol tetranitrate by laser driven flyer plates', *Journal of Applied Physics*, vol. 96, no. 1, pp. 344-347.

57. Parker, A, Claridge, RP, Hamid, J & Proud, WG 2008, 'Particle Size Modification of Thermally Stable Secondary Explosives for IM Applications', *Propellants, Explosives, Pyrotechnics*, vol. 33, no. 1, pp. 55-59.

58. Parker, A, Claridge, R & Hamid, J 2008, 'Particle Size Modification of Thermally Stable Secondary Explosives for IM Applications', *Propellants, Explosives, Pyrotechnics*, vol. 33, no. 1.

59. Akinci, A, Thomas, K, Munger, A, Nunn, L, Clarke, S, Johnson, M, Kennedy, J & Montoya, D 2005, 'On the development of a laser detonator', *Optical Technologies for Arming, Safing, Fuzing, and Firing*.

60. Pahl, RJ, Muenchausen, RE, Welle, EJ, Tappan, AS & Palmer, JA 2006, 'Diameter effects on detonation performance of HNS and CL-20'.

61. Cooper, PW 1996, *Explosives engineering*, Wiley-VCH.

62. Morelli, GL & Bright, MR 2008, 'A Comparison of Two Prototype Laser-Optical Firing Systems', in *Optical Technologies for Arming, Safing, Fuzing, and Firing IV*, eds FM Dickey & RA Beyer, SPIE, San Diego, CA, USA, p. Medium: ED.

63. Morelli, GL 2009, *Assembly and Characterization of a Prototype Laser-Optical Firing System*.

64. Bright, M 2008, 'Post mortem results of a Laser-Optical system packaged for use in harsh environments', *Optical Technologies for Arming, Safing, Fuzing and Firing IV*.

65. Morelli, G 2007, 'Design and Assembly Strategies for Two Laser-Optical Firing Systems', *Optical Technologies for Arming, Safing, Fuzing and Firing*.

66. Bright, M & Morelli, G 2006, 'Characterization of optical components for use in harsh environments', *Optical Technologies for Arming, Safing, Fuzing, and Firing II*.

67. Barker, LM 2000, 'The development of the VISAR, and its use in shock compression science', *AIP Conference Proceedings*, vol. 505, no. 1, pp. 11-18.

68. Bloomquist, DD & Sheffield, SA 1983, 'Optically Recording Velocity Interferometer System (ORVIS) For Subnanosecond Particle Velocity Measurements In Shock Waves', pp. 523-528.

69. Strand, OT, Berzins, V, Goosman, DR, Kuhlow, WW, Sargis, PD & Whitworth, TL 2005, 'Velocimetry Using Heterodyne Techniques', in *26th International Congress on High-Speed Photography and Photonics*, SPIE, pp. 593-599.

70. Frank, AM, Gillespie, CH & Trott, WM 1996, *High speed imaging of Raleigh-Taylor instabilities in laser driven plates*.

71. Bowden, MD & Maisey, MP 2007, 'The development of a heterodyne velocimeter system for use in sub-microsecond time regimes', *Optical Technologies for Arming, Safing, Fuzing, and Firing III*.

72. Dolan, DH 2010, 'PDV Modifications', *5th Annual PDV Users Conference*.

73. Dolan, DH, III & Ao, T 2010, *SIRHEN : a data reduction program for photonic Doppler velocimetry measurements*, SAND2010-3628; TRN: US201019%%607.

74. Thorlabs Inc., *Datasheet for Thorlabs FG365UEC Optical Fibre*. Available from: <http://www.thorlabs.com/thorproduct.cfm?partnumber=FG365UEC%3E. [16/06/2013].

75. Greenaway, MW, Proud, WG, Field, JE & Goveas, SG 2002, 'The development and study of a fiber delivery system for beam shaping', *Review of Scientific Instruments*, vol. 73, no. 5, pp. 2185-2189.

76. Polymicro-Technologies, Tue, 08 Jul 2008, *Optical Fiber Power Transmission*, Polymicro Technologies. Available from: <http://www.polymicro.com/catalog/2_19.htm%3E. [29/07/2010].

77. Bowden, MD, Singleton, CA & Drake, RC 2006, 'Characterization of novel optical fibers for use in laser detonators', *Optical Technologies for Arming, Safing, Fuzing and Firing II*.

78. Akinci, A, Bowden, MD, Cheeseman, MC, Knowles, SL, Meister, DC, Pecak, SN & Potter, KS 2009, 'The effect of high dose rate transient gamma radiation on high-energy optical fibers', *Optical Technologies for Arming, Safing, Fuzing, and Firing V*.

79. American-Elements, *Zirconia Information Center*. Available from: <http://www.americanelements.com/newpage3.htm%3E. [29/07/2010].

80. Akinci, A 2010, *Optical Fiber Polishing Recipe*, M Bowden.

81. Clarkin, JP, Timmerman, RJ & Shannon, JH 2004, 'Shaped fiber tips for medical and industrial applications', *Optical Fibers and Sensors for Medical Applications IV*.

82. Cheeseman, MC & Bowden, MD 2008, 'An assessment of a variety of optical fibers in ionizing radiation environments for use in a high-power optical system', *Optical Technologies for Arming, Safing, Fuzing, and Firing IV*.

83. Maheswaren, M-A & Whitehorn, LJ 2011, *Development of a Semi-Analytic Model for Slapper Detonators*, AWE Plc.

84. Bowden, MD, Drake, RC, Maisey, MP, Richardson, J, Whitehorn, LJ & Williams, AR 2006, 'The initiation of fine particle hexanitrostilbene using laser driven flyer plates', *13th International Detonation Symposium*.

85. Labaste, JL, Doucet, M & Joubert, P 1996, 'Shocks Induced by Laser Driven Flyer Plates', in *Shock Compression of Condensed Matter*, American Physical Society.

86. Trott, WM 1996, 'High-speed optical studies of the driving plasma in laser acceleration of flyer plates', in *Shock Compression of Condenser Matter*, American Physical Society.

87. Walker, FE & Wasley, RJ 1969, 'Critical energy for shock initiation of heterogeneous explosives', *Explosivstoffe*, vol. 17, no. 1.

88. James, HR 1996, 'An Extension to the Critical Energy Criterion used to predict shock initiation thresholds', *Propellants, Explosives, Pyrotechnics*, vol. 21, no. 1, pp. 8-13.

89. Waschl, JA 1998, 'An investigation of PETN sensitivity to small scale flyer plate impact', *Journal of Energetic Materials*, vol. 16, no. 4, pp. 279-288. [2011/11/12].

90. Cooper, PW & Kurowski, SR 1996, *Introduction to the technology of explosives*.

91. Gittings, EF 1965, 'Initiation of a solid explosive by a short duration shock', in *4th International Detonation Symposium*.

92. Dobratz, BM & Crawford, PC 1985, *LLNL Explosives Handbook - Properties of Chemical Explosives and Explosive Simulants*, Lawrence Livermore National Laboratory.

93. Tarver, CM, Breithaupt, RD & Kury, JW 1997, 'Detonation waves in pentaerythritol tetranitrate', *Journal Name: Journal of Applied Physics; Journal Volume: 81; Journal Issue: 11; Other Information: PBD: Jun 1997*, pp. Medium: X; Size: pp. 7193-7202.

94. Tarver, CM 2005, *Detonation Reaction Zones in Condensed Explosives*.

95. Neyer, BT 1994, 'AD-Optimality-Based Sensitivity Test', *Technometrics*, vol. 36, no. 1, pp. 61-70.

96. Cooper, PW, Owenby, RN & Stofleth, JH 1990, *Excess transit time as a function of burst current in an exploding bridgewire detonator*, SAND-89-2327C; CONF-900254--1; Other: ON: DE90007168.

97. Schwarz, AC 1975, *New technique for characterizing an explosive for shock initiation sensitivity. [PETN, RDX, HNAB, HNS-I, NONA, HNS-SF, HNS-II]*, SAND-75-0314 United States10.2172/7299650Thu Mar 24 09:20:24 EDT 2011Dep. NTISSNL; ERA-01-07267English.

98. Goveas, SG, Millett, JCF, Bourne, NK & Knapp, I 2006, 'One-Dimensional Shock and Detonation Characterization of Ultrafine Hexanitrostilbene', *AIP Conference Proceedings*, vol. 845, no. 1, pp. 1065-1068.

99. Schwarz, AC 1981, *Study of factors which influence the shock-initiation sensitivity of hexanitrostilbene (HNS)*, SAND-80-2372, United States.

100. Damm, DL 2012, *Critical Energy Values for HNS (unpublished work)*.

101. Waschl, J & Richardson, D 1991, 'Effect of specific surface area on the sensitivity of hexanitrostilbene to flyer plate impact', *Journal of Energetic Materials*, vol. 9, no. 4, pp. 269-282. [2013/07/03].

102. Harris, SM, Klassen, SE, Quinlin, WT, Cates, DM & Thorpe, R 2001, 'Hexanitrostilbene (HNS) Development for Modern Slapper Detonators', *International Annual Conference (32nd) of ICT*.

103. Green, L & Lee, E 2006, 'Detonation Pressure Measurements on PETN', in *Proceedings of 13th International Detonation Symposium*.

104. Singh, B & Malhotra, RK 1983, 'Hexanitrostilbene and Its Properties', *Defence Science Journal*, vol. 33, no. 2, pp. 165-176.

105. Hasman, E, Gvishi, M & Solomonovici, A 1987, 'The Initiation Threshold Sensitivity of HNS Explosive as a Function of its Grain Size', *Propellants, Explosives, Pyrotechnics*, vol. 12, no. 4, pp. 130-132.

106. Kipp, ME & Setchell, RE 1989, *A shock initiation model for fine-grained hexanitrostilbene*, SAND-88-2385C;, Sandia National Laboratories.

107. Haskins, PJ & Cook, MD 2010, 'A Modified Criterion for the Prediction of Shock Initiation Thresholds for Flyer Plate and Rod Impacts', *14th International Detonation Symposium*.

ANNEX A: THE PHYSICS OF PHOTONIC DOPPLER VELOCIMETRY

PDV is based upon two physical processes; these being the Doppler effect and Optical Mixing, i.e. heterodyning. When a laser signal is reflected from the surface of a moving target the wavelength alters, the degree of change being dependent upon the velocity of the target. This is the Doppler effect, and for a medium-independent wave, such as light, the change in wavelength is:

$$f_2 = f_1\sqrt{\frac{c-v}{c+v}}$$

Equation 27

where f_1 and f_2 are wavelengths, and v the velocity of interest. The return signal is then heterodyned with the original signal. Assuming simple sine wave form signals the return signal is

$$I(t) = A_1 \sin(f_1 t) + A_2 \sin(f_2 t + \phi)$$

Equation 28

Where A_1 and A_2 are amplitudes, t is time, υ_1 and υ_2 are frequencies and ϕ is the phase. Assuming that the amplitude of the return signal is separable, and applying a simple trigonometric identity

$$I(t) = 2A_1 \cos\left(\frac{f_1 - f_2}{2}t - \frac{\phi}{2}\right)\sin\left(\frac{f_1 + f_2}{2}t - \frac{\phi}{2}\right) + A_3 \sin(f_2 t + \phi)$$

Equation 29

It is possible to separate out the phase component of the second signal, yielding;

$$I(t) = 2A_1 \cos\left(\frac{f_1 t - f_2 t}{2}\right)\sin\left(\frac{f_1 t + f_2 t}{2}\right) + f(f_2, t, \phi)$$

Equation 30

The heterodyning process thus produces three frequency responses. A beat frequency that is the difference between the two signals, a high frequency equal to the sum of the frequencies and a remainder component due to the differences between the amplitudes.

Due to the difference in frequency between the laser and sampling rate of the scope, the remainder signal and the summated frequency are extremely heavily aliased. Further, analogue to digital converter (ADC) within the oscilloscope used to digitize the optical signal acts both as an integrator and a low-pass filter. Thus the remainder term $f(f_2, t, \phi)$ is considered to be constant.

The only term of consequence is therefore the difference of the two frequencies: the beat frequency.

$$f_b = f_1 - f_2$$

Equation 31

As cosine is symmetric the effect of this frequency is independent of the direction of travel of the target, and only the magnitude need be considered. Expanding Equation 27 as a power series and applying it twice, required as the signal is Doppler shifted on absorption by the target and then upon detection by the receiver, yields

$$f_2 = f_1\left(1 - \frac{2v}{c} + second\ order\ terms\right)$$

Equation 32

Non-linear terms can be ignored, as the ratio of the target velocity to the speed of light is so small, typically in the region of 2 x 10^{-5}. The beat frequency is thus related to the velocity by:

$$f_b = \frac{2v}{c} f_0$$

Equation 33

With this relation for the beat frequency we can use the Nyquist-Shannon Sampling Theorem to determine the required bandwidth, *B* of a system to accurately evaluate a

given velocity. For a band-limited signal to be fully reconstructable the sampling frequency f_s, must fulfil the relationship $f_s \geq 2B$.

Using Equation 33 we find

$$f_s \geq \frac{4v}{\lambda}$$

Equation 34

Given a velocity of 5 km.s^{-1}, and a laser frequency of 1.9 x 10^5 GHz it can be shown that the beat frequency is of the order of 6.5 GHz, whilst the summated frequency is of the order of 4 x 10^5 GHz. The remainder term will have a frequency very close to that of the laser frequency.

Thus in order to track a flyer up to 5 km.s^{-1} a system with a bandwidth in excess of 13 GHz is required to optimally record the velocity. It is necessary to extract the beat frequency from the returned signal in order to determine the velocity.

ANNEX B: EXPERIMENTAL DATA FOR BASELINE FLYER CHARACTERISATION

Energy, mJ					Fluence, $J.cm^{-2}$	Filename	Velocity at 75 um, $m.s^{-1}$
1	2	3	Shot	SD			
2.06	2.03	2.04	2.04	0.02	1.63	121121_095338	463.932
2.98	2.96	2.98	2.97	0.01	2.37	121121_095845	1003.55
4.04	4.01	4.02	4.02	0.02	3.20	121121_100029	1248.82
5.24	5.28	5.22	5.25	0.03	4.17	121121_100230	1471.08
5.98	6.01	6.02	6.00	0.02	4.78	121121_100443	1711.92
7.08	7.10	7.09	7.09	0.01	5.64	121121_100851	2017.69
8.06	8.14	8.09	8.10	0.04	6.44	121121_101054	1981.84
9.14	9.22	9.20	9.19	0.04	7.31	121121_101311	2284.87
10.21	10.26	10.22	10.23	0.03	8.14	121121_101641	2319.52
10.22	10.46	10.44	10.37	0.13	8.25	121121_101817	2363.80
10.24	10.36	10.35	10.32	0.07	8.21	121121_102044	2335.95
10.18	10.20	10.28	10.22	0.05	8.13	121121_102208	2452.34
12.07	12.15	12.05	12.09	0.05	9.62	121121_143744	2530.17
13.07	13.02	13.01	13.03	0.03	10.37	121121_144313	2547.03
14.18	13.96	14.08	14.07	0.11	11.20	121121_144747	2633.05
15.21	15.23	15.26	15.23	0.03	12.12	121121_145356	2713.57
15.15	14.96	14.94	15.02	0.12	11.95	121121_155226	2991.32
14.85	15.31	14.99	15.05	0.24	11.97	121121_155447	2922.65
14.94	14.97	15.12	15.01	0.10	11.94	121121_155718	2932.41
16.64	16.55	16.56	16.58	0.05	13.19	121122_101538	2989.79
16.33	16.51	16.60	16.48	0.14	13.11	121122_103012	2625.56
16.55	16.57	16.56	16.56	0.01	13.18	121122_111711	2899.10
16.17	16.18	16.36	16.24	0.11	12.92	121122_111952	3090.20
15.98	16.35	16.26	16.20	0.19	12.89	121122_112342	3097.33
16.02	16.28	16.33	16.21	0.17	12.90	121122_112610	3201.36
16.02	16.12	15.97	16.04	0.08	12.76	121122_113339	2994.14
18.39	18.44	18.33	18.39	0.06	14.63	121122_113548	3085.47
17.82	18.14	17.74	17.90	0.21	14.24	121122_113802	2843.11
19.69	19.79	19.63	19.70	0.08	15.68	121122_114209	3190.92

Energy, mJ					Fluence, J.cm^{-2}	Filename	Velocity at 75 um, m.s^{-1}
1	2	3	Shot	SD			
19.62	19.69	19.70	19.67	0.04	15.65	121122_114443	3163.70
19.71	19.86	19.90	19.82	0.10	15.77	121122_114648	3098.60
22.00	22.20	22.30	22.17	0.15	17.64	121122_114919	3378.63
23.40	23.80	23.70	23.63	0.21	18.80	121122_115145	3459.69
24.40	24.30	24.50	24.40	0.10	19.41	121122_120259	3270.68
24.30	24.50	24.80	24.53	0.25	19.52	121122_120539	3531.02
25.10	25.40	25.50	25.33	0.21	20.16	121122_135216	3687.90
30.10	29.80	29.50	29.80	0.30	23.71	121122_140501	3670.69
26.20	26.30	26.20	26.23	0.06	20.87	121122_144243	3465.32
27.00	27.10	27.10	27.07	0.06	21.54	121122_145300	3651.28
28.40	28.60	28.60	28.53	0.12	22.70	121122_150126	3904.16

Table 46 - List of shots for baseline flyer characterisation

ANNEX C: PAPERS PUBLISHED DURING THE THESIS STUDY

The development of a heterodyne velocimeter system for use in sub-microsecond time regimes

M. D. Bowden* and M. P. Maisey

Atomic Weapons Establishment, Aldermaston, Reading, Berkshire, RG7 4PR, United Kingdom

ABSTRACT

Recent advances over the last five years in high-speed digitizing oscilloscopes and high-bandwidth photodiodes, driven primarily by the telecommunications industry, have enabled the development of a new type of interferometer for measuring high velocities, such as those found in detonics experiments.

The heterodyne velocimeter can be visualized as a fiber-based Michelson interferometer. The beam from a single-mode fiber laser at 1550 nm is passed through a circulator, acting to separate bi-directional light. The beam is then reflected via free-space optics from the surface of interest, and then focused back into the same fiber. This reflected light is mixed with an approximately equal amount of non-reflected light, and the resulting interference is recorded using a high-bandwidth photodiode and oscilloscope. In contrast to more traditional velocimetry techniques such as VISAR, only a single data channel is required per probe.

The uses of heterodyne velocimetry have, to date, been primarily in the multi-microsecond time regime, i.e. explosively-driven metal plates. In this paper, we present a four-channel, ultra-high bandwidth system designed for use in the sub-microsecond time regime, and present the results obtained from laser-driven flyer plates traveling in excess of 3 km s^{-1}. We have developed analysis software suited to use in this time regime, where a relatively small displacement is recorded.

The original heterodyne velocimeter relied on back-reflectance from the probe to obtain the non-reflected light. This limits both the flexibility of the system and the efficiency of the probes. We have overcome this issue by introducing a beam splitter into the system prior to the circulator. This allows the probing system to be designed for maximum efficiency, and we are then able to tune the non-reflected light on a shot-to-shot basis.

"The development of a heterodyne velocimeter system for use in sub-microsecond time regimes", *Proc. SPIE* 6662, Optical Technologies for Arming, Safing, Fuzing, and Firing III, 66620B (September 13, 2007)

Laser initiation of energetic materials: a historical overview

M. D. Bowden*, M. Cheeseman, S. L. Knowles and R. C. Drake

Atomic Weapons Establishment, Aldermaston, Reading, Berkshire, RG7 4PR, United Kingdom

1. ABSTRACT

Laser initiation of energetic materials has been a topic of interest almost since the invention of the first laser in 1960. Since then, a wide range of lasers, and an even wider range of energetic materials, ranging from sensitive primary explosives such as lead azide, to very insensitive explosives such as Triamino Trinitrobenzene (TATB) have been investigated. With the continuous reduction in laser size, and increase in laser energies and powers, using lasers to initiate energetic materials is becoming easier and more practical to implement in a system environment.

In this paper we examine the development of the concept of laser initiation, from its early days using large Ruby lasers, to the more modern use of Nd:YAG lasers. We collate and present here the open source literature published in this field in order to produce a concise and accurate historical overview of the research published to date, and make a prediction of future trends where possible. We also examine research presented in enabling technologies, such as laser-driven flyer plates and high-energy optical fibers.

"Laser initiation of energetic materials: a historical overview", *Proc. SPIE* 6662, Optical Technologies for Arming, Safing, Fuzing, and Firing III, 666208 (September 13, 2007)

The initiation of high surface area Pentaerythritol Tetranitrate using fiber-coupled laser-driven flyer plates

M. D. Bowden* and R. C. Drake

Atomic Weapons Establishment, Aldermaston, Reading, Berkshire, RG7 4PR, United Kingdom

ABSTRACT

A system for launching flyer plates using a Q-switched Nd:YAG laser has been developed for shock initiation of secondary explosives. Flyer plates have been launched at velocities exceeding 4 km s^{-1}. These flyers produce sub-nanosecond duration shocks in excess of 30 GPa on impact.

Flyer planarity and integrity have been studied by impacting polymethylmethacrylate (PMMA) windows and using a high-speed streak camera to record the light generated. Analysis of this data has provided an insight of the key mechanisms and enabled the system attributes to be controlled and optimized for explosive initiation.

Pentaerythritol Tetranitrate (PETN) has been tested with specific surface areas (SSA) ranging from 12,700 $cm^2 g^{-1}$ to 25,100 $cm^2 g^{-1}$ and the effect of SSA on initiation threshold in this extremely short duration shock regime is examined. A minimum surface area size for initiation is evident. Calculations show that the pulse width is on the order of the particle size. We observed partial reactions in some firings, and we propose a mechanism to explain this.

We then evaluate $P^2\tau$ for PETN initiated by laser driven flyer plates. The critical energy fluence calculated is compared to published values and discussed for similar systems.

Keywords: Pentaerythritol Tetranitrate, PETN, laser detonator, laser-driven flyer plates

"The initiation of high surface area Pentaerythritol Tetranitrate using fiber-coupled laser-driven flyer plates", *Proc. SPIE* 6662, Optical Technologies for Arming, Safing, Fuzing, and Firing III, 66620D (September 13, 2007)

Use of Fiber Optic Tapers to Increase Connector Tolerance for DOI Systems

M. D. Bowden[1]

Atomic Weapons Establishment, Aldermaston, Reading, Berkshire, RG7 4PR, United Kingdom

ABSTRACT

Direct Optical Initiation (DOI) of explosives offers significant safety advantages over traditional electrical initiation of explosives, primarily by removing the electrically conducting pathway to the explosive material. A firing system typically consists of three main components: the fireset, which provides the energy to initiate the explosive; the cable, which transmits or conducts this energy; and the detonator, which uses this energy to initiate the explosive charge.

Electrical firing systems used to fire secondary explosives typically use voltages of 500 volts and upwards, with currents of 500 amps and upwards. The technology to transmit such signals over the short distances required is mature and well-proven. However, an optical initiation system requires optical powers in excess of 10 MW, and the technology to deliver such powers is relatively immature. Optical fibers are used to transmit the firing energy, which require very high tolerances to ensure the beam is successfully coupled into the fiber without damage. Fiber optic tapers offer a method to relax these tolerances, and hence reduce system cost and complexity, by providing a larger area into which to couple this beam. We present here our initial results from a series of tests aimed at establishing the feasibility of using tapered optical fibers for this purpose. The transmission loss and beam profiles are reported as a function of the beam position on the input face of the optical fiber.

Keywords: DOI, Optical Fibers, Tolerance, Tapered Optical Fibers

"Use of fiber optic tapers to increase connector tolerance for DOI systems",*Proc. SPIE* 7070, Optical Technologies for Arming, Safing, Fuzing, and Firing IV, 70700J (September 03, 2008)

Characterization of Detonator Performance Using Photonic Doppler Velocimetry

M. P. Maisey and M. D. Bowden[1]

Atomic Weapons Establishment, Aldermaston, Reading, Berkshire, RG7 4PR, United Kingdom

ABSTRACT

Detonators are used to convert electrical or other energy into an explosive output. This output can then be used to initiate further explosive charges. To aid in the development of explosive systems, it is important to characterize the output of detonators, in particularly the pressure produced.

Recent advances over the last five years in high-speed digitizing oscilloscopes and high-bandwidth photodiodes, driven primarily by the telecommunications industry, have enabled the development of a new type of interferometer for measuring high velocities, such as those found in detonics experiments. The Photonic Doppler Velocimeter (PDV) can be visualized as a fiber-based Michelson interferometer. The light from a single-mode fiber laser at 1550 nm is passed through a circulator, which acts to separate bi-directional light. The beam is then reflected via free-space optics off the surface of interest, and then focused back into the same fiber. This reflected light is then mixed with an approximately equal amount of non-reflected light, and the resulting interference is recorded using a high-bandwidth photodiode and oscilloscope. In contrast to more traditional Velocimetry techniques such as VISAR, only a single data channel is required.

We have used our PDV system to investigate the performance of optical and electrical detonators. The detonators examined are the commercially available RISI RP-80, and an AWE DOI (Direct Optical Initiation) detonator. The RP-80 is an exploding bridgewire (EBW) detonator, utilizing Pentaerythritol Tetranitrate as the initiating explosive and a RDX output pellet. The DOI detonator uses an aluminum flyer to initiate a Hexanitrostilbene (HNS) pellet. Both detonators are canned in aluminum and the velocity of the can was measured, and from this, the output pressure of the detonator has been determined. This is compared to calculated values.

"Characterization of detonator performance using photonic Doppler velocimetry", *Proc. SPIE* 7070, Optical Technologies for Arming, Safing, Fuzing, and Firing IV, 70700P (September 03, 2008)

Determination of Critical Energy Criteria for Hexanitrostilbene Using Laser-driven Flyer Plates

M. D. Bowden, M. P. Maisey

Atomic Weapons Establishment, Aldermaston, Reading, Berkshire, RG7 4PR, United Kingdom

ABSTRACT

Laser-driven flyer plates comprise of one or more thin layers forming a foil coated onto a transparent substrate. Irradiation of the foil/substrate interface with a Q-switched laser pulse produces a plasma, the expansion of which forms a flyer plate, which can reach velocities in excess of 5 km/s. These plates impart shocks in excess of 50 GPa, with duration of less than a nanosecond. This shock is sufficient to initiate secondary explosives such as Hexanitrostilbene (HNS) and Pentaerythritol Tetranitrate (PETN).

Thresholds of detonators based on laser-driven flyer plates are typically measured in terms of energy. By using a Photonic Doppler Velocimeter (PDV) we measure the velocity of the flyer plate at the threshold energy. This allows calculation of the shock pressure and duration imparted to the explosive.

By initiating HNS with a variety of flyer thicknesses, from 3 to 5 μm, we are able to evaluate $P^n\tau$ in this extreme shock regime. The calculated value of n is compared to published values and discussed for similar systems. We are also able to use the James Criterion to analyze the initiation, with values of E_c and $\sum_c$ being determined from experimental data, providing a predictive capability to model other configurations such as different flyer thicknesses and materials.

"Determination of critical energy criteria for hexanitrostilbene using laser-driven flyer plates", *Proc. SPIE* 7070, Optical Technologies for Arming, Safing, Fuzing, and Firing IV, 707004 (September 03, 2008)

Optimisation of Laser-driven Flyer Velocity Using Photonic Doppler Velocimetry

M. D. Bowden and S. L. Knowles

Atomic Weapons Establishment, Aldermaston, Reading, Berkshire, RG7 4PR, United Kingdom

ABSTRACT

Laser-driven flyer plates offer a convenient, laboratory-based method for generating extremely high pressure shocks, in excess of 30 GPa, in a variety of materials. They comprise of one or more thin layers forming a foil, coated onto a transparent substrate. By irradiating the interface between foil and substrate with a moderate-energy, short-duration laser pulse, it is possible to form a flyer plate, which can reach velocities in excess of 5 km/s. These flyer plates have several applications, from micrometeorite simulation to initiation of secondary explosives.

The flyer plates considered here have up to four layers: an absorption layer, to absorb the laser energy; an ablation layer, to form a plasma; an insulating layer; and a final, thicker layer that forms the final flyer plates.

By careful selection of both layer material and thickness, it is possible to increase the maximum velocity achieved for a given laser pulse energy by increasing the proportion of laser energy coupled into flyer kinetic energy. Photonic Doppler Velocimetry (PDV) is used to measure the flyer velocity.

"Optimisation of laser-driven flyer velocity using photonic Doppler velocimetry",*Proc. SPIE* 7434, Optical Technologies for Arming, Safing, Fuzing, and Firing V, 743403 (August 28, 2009)

Optimal Polishing Methods for High Energy Optical Fibers

M. D. Bowden, S. L. Knowles and M. C. Cheeseman

Atomic Weapons Establishment, Aldermaston, Reading, Berkshire, RG7 4PR, United Kingdom

ABSTRACT

Direct Optical Initiation (DOI), uses a moderate energy Q-switched Nd:YAG laser to shock initiate secondary explosives, via either a flyer plate or exploding metal foil. DOI offers significant performance and safety advantages over conventional electrical initiation. Optical fibers are used to transport the optical energy from the laser to the explosive device.

Energy densities in the region of 35 J cm^{-2} are required for initiation, significantly above the damage threshold of typical optical fibers. Laser-induced damage is typically caused by laser absorption at the input face due to imperfections in the surface polishing. To successfully transmit energy densities for DOI, a high quality fiber end face finish is required.

Fiber assemblies were prepared by C Technologies Inc, NJ, USA, with Innovaquartz FG365UEC optical fiber, using a variety of polishing methods, with both steel and zirconia ferrules. The quality of the fiber end faces was assessed using non-contact optical profilometry. The damage threshold for each polishing method was then determined using a Q-switched Nd:YAG laser and the optimal polishing method determined for each ferrule material. Significant performance differences between zirconia and steel ferrules were observed, and a physical cause of this difference is proposed.

Energies in excess of 35 J/cm^2 were successfully transmitted through all fibers without damage, with a higher laser-induced damage threshold observed for zirconia ferrule fiber assemblies.

"Optimal polishing methods for high-energy optical fibers", *Proc. SPIE* 7795, Optical Technologies for Arming, Safing, Fuzing, and Firing VI, 77950D (September 03, 2010)

CHARACTERISATION OF LASER-DRIVEN FLYER PERFORMANCE USING PHOTONIC DOPPLER VELOCIMETRY

M. D. Bowden, S. L. Knowles and M. P. Maisey

Atomic Weapons Establishment, Aldermaston, Reading, Berkshire, RG7 4PR, United Kingdom

ABSTRACT

Laser-driven flyer plates offer a convenient, laboratory-based method for generating extremely high-pressure shocks, in excess of 30 GPa, in a variety of materials. They comprise of one or more thin layers forming a foil, coated onto a transparent substrate. By irradiating the interface between foil and substrate with a moderate-energy, short-duration laser pulse, it is possible to form a flyer plate, which can reach velocities in excess of 5 km/s. These flyer plates have several applications, from micrometeorite simulation to initiation of secondary explosives.

The flyer plates considered here have up to four layers: an absorption layer, to absorb the laser energy; an ablation layer, to form a plasma; an insulating layer; and a final, thicker layer that forms the impactor plate. Three thicknesses of ablation and insulator layers were investigated to develop a highly robust, optimised flyer composition.

A Q-switched Nd:YAG laser operating at a fixed energy was used to launch test flyers of varying compositions. The velocities were measured using twin-laser Photonic Doppler Velocimetry (PDV) and the point at which flyer degradation occurred during flight was identified. From the data it was possible to compare the performance of each batch and determine which composition produced the highest velocity robust flyer.

"Characterisation of Laser-driven Flyer Performance Using Photonic Doppler Velocimetry", 37th International Pyrotechnic Seminar, 2011.

SHOCK INITIATION OF HEXANITROSTILBENE AT ULTRA-HIGH SHOCK PRESSURES AND CRITICAL ENERGY DETERMINATION

M. D. Bowden, M.P. Maisey, and S. L. Knowles

Atomic Weapons Establishment, Aldermaston, Reading, Berkshire, RG7 4PR, United Kingdom

Abstract. Hexanitrostilbene (HNS) is a secondary explosive with attractive properties for detonator usage, including thermal stability, good safety properties and easy initiability. It is desirable to characterize the shock initiation of detonator explosives to enable optimization of system parameters. HNS is a suitable explosive for use in electrical and optical slapper detonators, where shock pressures generated by the flyer plates used can exceed 30 GPa. This extreme shock regime can be explored by initiating HNS with a variety of flyer thicknesses, from 3 to 25 microns at velocities of several km/s. Thresholds for optical and electrical slapper detonators were evaluated, and Photonic Doppler Velocimetery used to determine the flyer velocity at threshold. The flyer diameters are in excess of the critical diameter for HNS, allowing a one-dimensional treatment of the initiation. Calculated values for pressure and shock duration are used to evaluate the critical energy criteria $P^2\tau$. The James Criterion is used to analyse the initiation, with values of E_C and Σ_C being determined from experimental data, providing a predictive capability to model other configurations such as different flyer thicknesses and materials.

Keywords: HNS, Hexanitrostilbene, flyer plate, detonator, laser, electrical, James Criterion, shock initiation, Direct Optical Initiation.
PACS: 82.33.Vx, 82.40.Fp.

"Shock initiation of hexanitrostilbene at ultra-high shock pressures and critical energy determination", *SHOCK COMPRESSION OF CONDENSED MATTER - 2011: Proceedings of the Conference of the American Physical Society Topical Group on Shock Compression of Condensed Matter. AIP Conference Proceedings, Volume 1426, pp. 615-618 (2012).*

A High-energy Fibre to Fibre Connection for Direct Optical Initiation Systems

M. D. Bowden & S. L. Knowles

Atomic Weapons Establishment, Aldermaston, Reading, Berkshire, RG7 4PR, United Kingdom

ABSTRACT

Direct Optical Initiation (DOI), uses a moderate energy laser to shock initiate secondary explosives, via either a flyer plate or exploding metal foil. DOI offers significant performance and safety advantages over conventional electrical initiation. Optical fibres are used to transport the optical energy from the laser to the explosive device.

A DOI system comprises of a laser, one or more optical fibres, and one or more laser detonators. Realisation of a DOI system is greatly eased by the use of fibre-to-fibre connections, allowing for easy integration into bulkheads or other interfaces, such as firing tanks and environmental test chambers. Fibres to fibre connectors capable of transmitting the required energy densities are not commercially available.

Energy densities in the region of 35 J cm^{-2} are required for initiation, above the damage threshold of typical optical fibres. Laser-induced damage is typically caused by laser absorption at the input face due to imperfections in the surface polishing. To successfully transmit energy densities for DOI, a high quality fibre end face finish is required.

A fibre-to-fibre connection utilizing micro-lens array injection into a large-core, tapered optical fibre, a hermetic fibre bulkhead feedthrough, and a disposable test fibre has been developed. This permits easy connection of test detonators or components, with the complex free-space to fibre injection simplified to a single operation. The damage threshold and transmission losses of the fibre-to-fibre connection have been established for each interface.

"A high-energy fibre-to-fibre connection for direct optical initiation systems",*Proc. SPIE* 8530, Laser-Induced Damage in Optical Materials: 2012, 853016 (December 4, 2012)